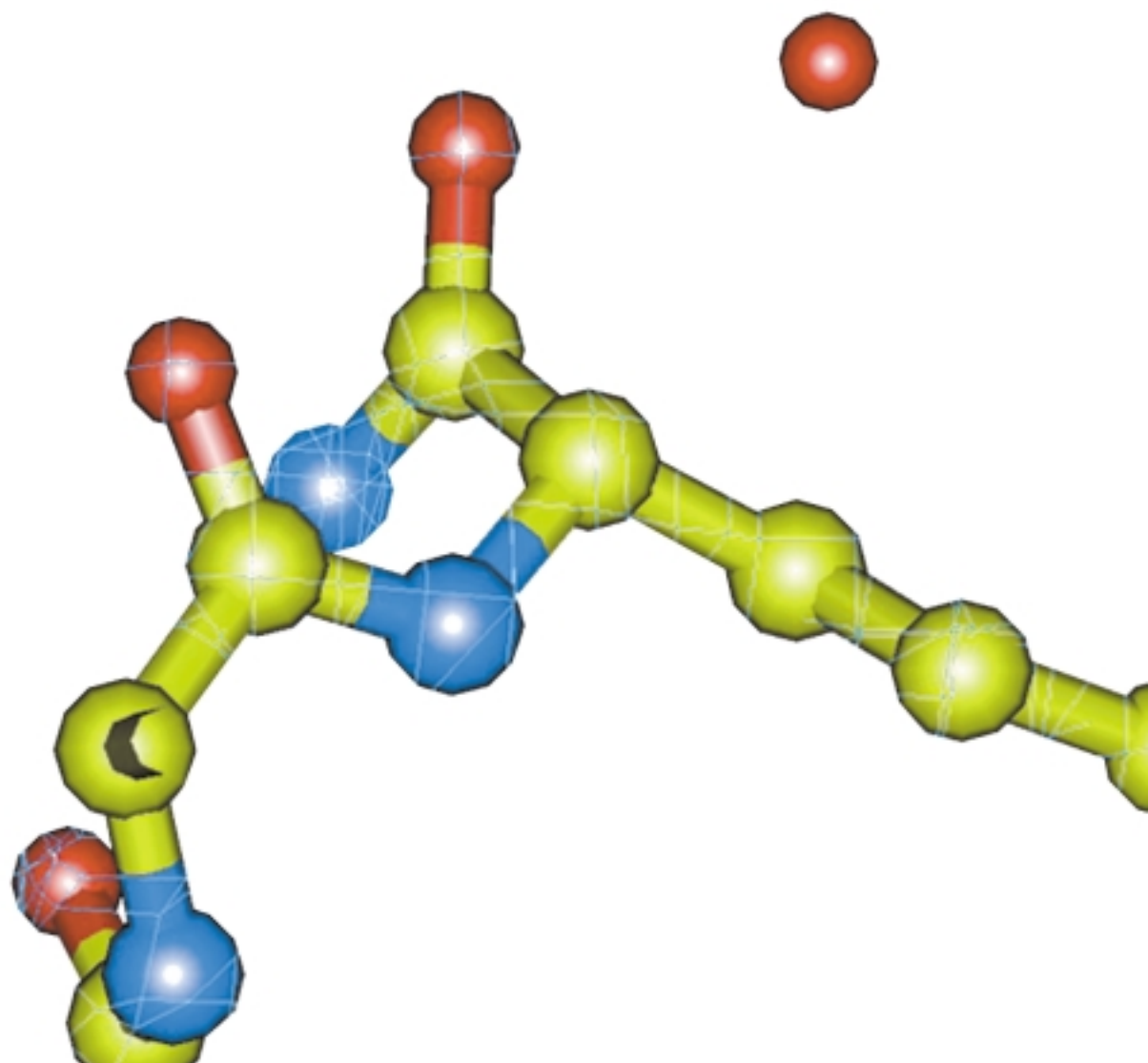


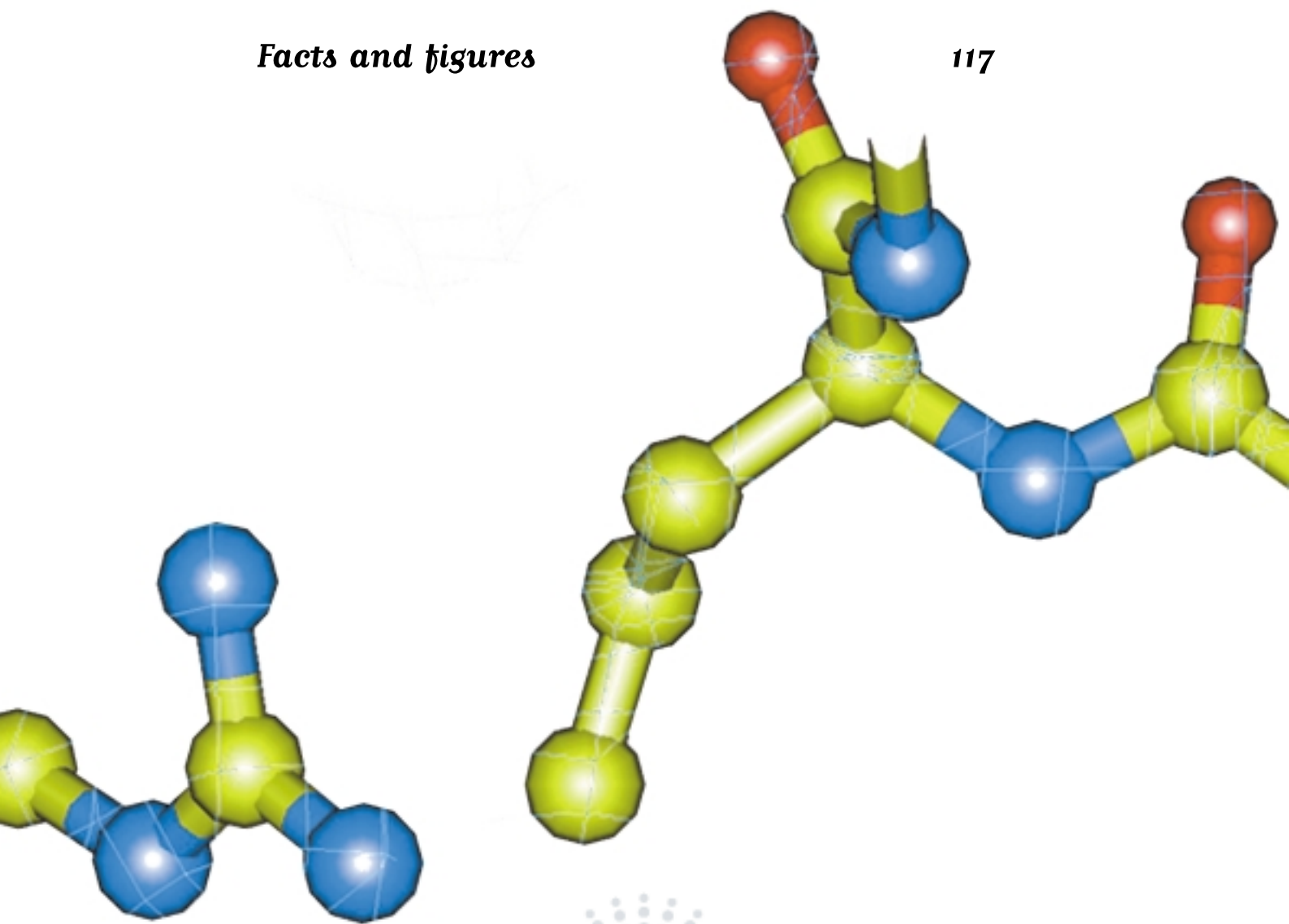
Highlights

1999





Introduction	4
Scientific highlights	5
<i>Life sciences</i>	<i>6</i>
<i>Chemistry</i>	<i>22</i>
<i>Surfaces and interfaces</i>	<i>38</i>
<i>Electronic states and lattice dynamics</i>	<i>45</i>
<i>Magnetism</i>	<i>56</i>
<i>High pressure</i>	<i>70</i>
<i>Materials</i>	<i>76</i>
<i>Applied and industrial research</i>	<i>83</i>
<i>Techniques and instrumentation</i>	<i>96</i>
The X-ray source	106
Facts and figures	117



Introduction

Previous Highlights covered the period from August through to July of the following year. This edition marks a change; the report corresponds to the experiments done between August 1998 and December 1999, so that from now onwards the Highlights will be able to encompass a calendar year.

As usual some of the experimental results have not yet been fully analysed, and therefore some scientists are reluctant to expose details of their results before publication in a scientific journal. Consequently the articles presented here give only a partial view.

The availability of the machine reached 95.4% in 1999. Users operation with very low emittance ($\epsilon_{\text{HOR}} = 3.8 \text{ nm.rad}$ and $\epsilon_{\text{VER}} = 10 \text{ pm.rad}$) has been tested for several weeks. The 1.6 metre in-vacuum undulator on beamline ID11 is delivering 2.10^{20} photons/s/mm²/mrad²/0.1%bw at 10 keV and still 10^{19} at 60 keV. In view of these results some of the other beamlines are going to be equipped with 2 x 2 metre in-vacuum undulators. Additionally, it is interesting to note that the machine is able to reach $\epsilon_{\text{HOR}} = 1.7 \text{ nm.rad}$ and $\epsilon_{\text{VER}} = 10 \text{ pm.rad}$ with 100 mA and a lifetime of 31 hours.

The number of countries participating at the ESRF has increased recently. Portugal joined as associate member in 1998, Israel in 1999. The Czech Republic also joined in 1999 and will form a consortium with Hungary and Poland in July 2000.

Today the 30 public beamlines are in full operation. In addition 10 CRG (Collaborating Research Groups) beamlines have been implemented and two more will start construction in 2000. If one adds the industrial beamline for microelectronics (MEDEA) and accounts for multiple end stations, this gives 52 simultaneous experiments instead of the 30 foreseen at the beginning of the ESRF.

The ESRF management is also pleased to report that Dr Paolo Carra (Theory group) has been awarded the Agilent Technologies Europhysics Award for the year 2000 in conjunction with Drs G. Schütz and G. van der Laan. This prestigious award (formerly known as the Hewlett Packard Europhysics Award) was awarded for the scientists' pioneering work in establishing the field of magnetic X-ray dichroism.

We would like to thank the ESRF staff and our users: their efforts have enabled us to obtain the results described in this report.

*G. Admans, W.E.A. Davies, J.-M. Filhol, C. Kunz, P.F. Lindley, Y. Petroff
(May 2000)*

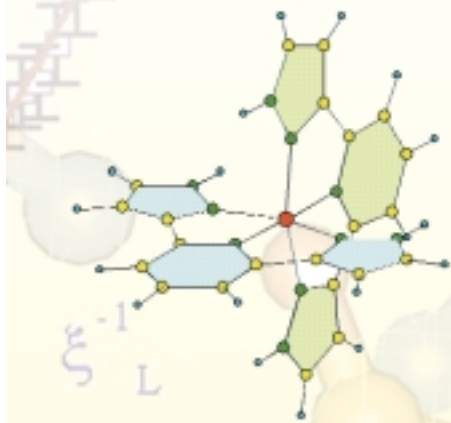


Pictured from left to right are G. van der Laan, G. Schütz and P. Carra after receiving the Agilent Technologies Europhysics Award.



Highlights
1999

Scientific highlights



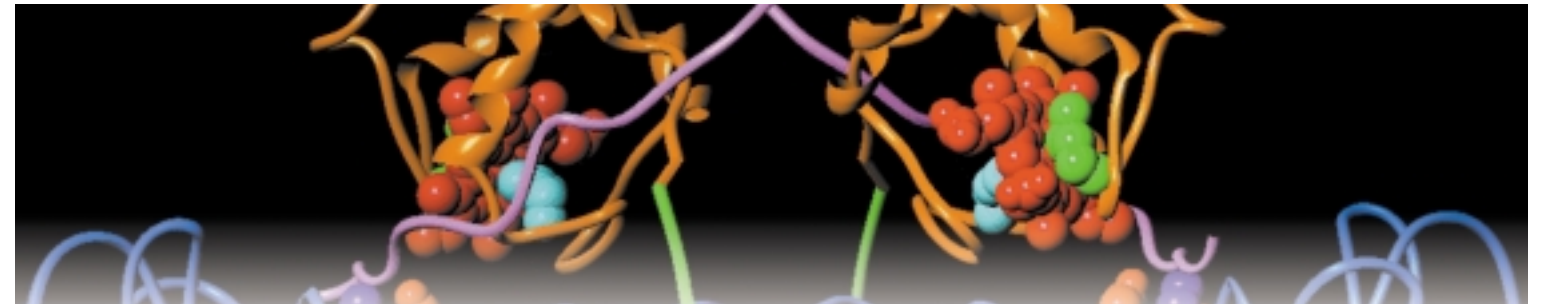
255 270

$$T_{CO} = 239.2$$

$$\nu \approx 1.08 \pm 0.1$$

ξ^{-1}

(H, K)



Life Sciences

Introduction

This year has been another highly productive period for the scientific programme in the Life Sciences and it is encouraging to see that although the field is currently dominated by macromolecular crystallography, other techniques are also beginning to play a significant role. Thus, this highlights section is able to include contributions on fibre diffraction using the microfocus beamline ID13, on the contraction of muscles using beamline ID2, and on the *in vivo* fluorescence microtomography of plants using a second microfocus beamline, ID22. The Medical Beamline, ID17, has continued to extend its research programme and highlights are included with respect to bronchography and the measurement of blood volumes in the brain. The angiography studies involving the first human patients suffered a frustrating delay before the proposed experimental protocol was accepted by the authorities and consequently the first patient could not be received before the end of January, 2000.

In the field of Macromolecular Crystallography, a survey of the journals, *Nature*, *Science*, *Cell*, *Nature Structural Biology*, *Structure*, *Acta Crystallographica D*, *Biochemistry*, *Journal of Molecular Biology*, *Journal of Biological Chemistry*, *EMBO Journal*, *Proteins: Structure, Function and Genetics*, *FEBS*, *RNA*, *Proceedings of the National Academy of Sciences (USA)* and the *Journal of Synchrotron Radiation*, for the year 1999 has revealed well over 100 structural papers where the use of the ESRF beamlines has been instrumental in undertaking a structural analysis. In addition there were several crystallisation papers and review or technical articles. Many of these papers cover work that was undertaken in 1998 (or earlier) and the beginning of 1999 when the Quadriga complex, ID14, was not fully operational. The number is therefore an underestimate compared to that which can be expected for the coming year. However, more significant than the quantity of structures is their quality and importance. Whilst it is inevitable that some of the data collected at

the ESRF could also be collected elsewhere, and many of the larger problems do involve data collected at several sources, there are some structures for which the use of the high brilliance, highly collimated characteristics are mandatory. This highlights section has chosen only a few examples of the structures that have been solved using ESRF data. The Multiple-wavelength Anomalous Dispersion (MAD) technique continues to play an important role in the elucidation of new structures with the use of both BM14 and ID14/4. The speed of structure solution using MAD continues to cause amazement with reports of three structures being solved in a day by the Marseille group using S-methionine substituted proteins, and an in-house experiment taking less than one hour from mounting the protein crystal to producing a fully interpretable electron density map. It seems that although the growth of suitable crystals is still the dominating rate-limiting step in macromolecular crystallography, the time that used to be spent on structure elucidation is now of necessity used to formulate the results as a scientific paper!

A number of technical developments have taken place during the year including the construction and commissioning of a micro-goniometer for use initially on the microfocus beamline ID13 (*Acta Crystallographica*, D55, 1765-70, 1999). The success of this joint EMBL-ESRF project will lead to the construction of similar goniometers for other macromolecular crystallographic beamlines. The emphasis in the future will be to use microbeams to produce usable diffraction data from microcrystals. A further project involves the construction of an automated sample exchanger for frozen protein crystals and a prototype has been tested. Clearly, for routine data collection purposes, the future will involve submitting protein samples by courier and running the data collection experiments remotely. In conjunction with this concept, software developments have also taken place to simplify and accelerate data collection for the external user community.

Fibre Diffraction of Biopolymers

In situ Studies of Forced Silking of Nephila Senigalensis Spiders

There is currently a considerable interest in dragline spider silk due to its exceptional mechanical qualities [1]. X-ray structural studies of silk have been limited to few spider species where sufficiently large quantities of spider silk could be obtained by the so-called forced silking technique [2]. ID13 has pioneered the development of single fibre diffraction techniques, which have allowed the collection of diffraction patterns from a variety of spider silks [3]. The development of artificial silk requires a detailed understanding of the structural processes occurring during the formation of the natural product. It is therefore of interest to apply the same *in situ* techniques, which have been developed for the study of extrusion processes of synthetic polymers, to extrusion from the living animal. Of course, given the size of a spider, an extreme miniaturisation of the setup was required.

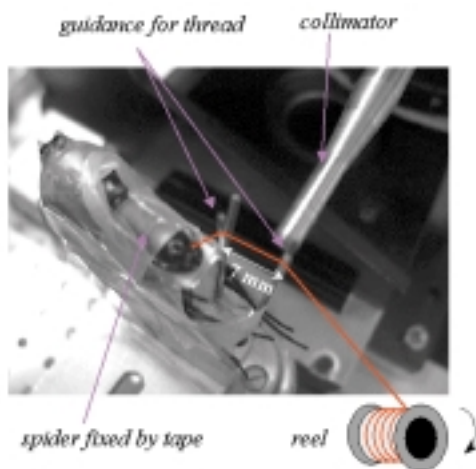


Fig. 1: *Nephila senigalensis* spider lying on its back and strapped by soft tape to a support structure. The silk fibre of about 4 µm diameter (red line) is guided by two pins and wound up by a motorised reel. The beam is guided through a 10 µm collimator.

Figure 1 shows the setup used for studying a *Nephila senigalensis* spider using a 10 µm sized beam at the ID13 beamline [4]. Forced silking can be maintained for several hours under these conditions and the spiders remain unharmed by this procedure. Figure 2 shows a typical scattering pattern obtained during the extrusion as recorded by a MAR CCD detector. The pattern reflects a mixture of small crystallites with the β-poly(L-alanine)

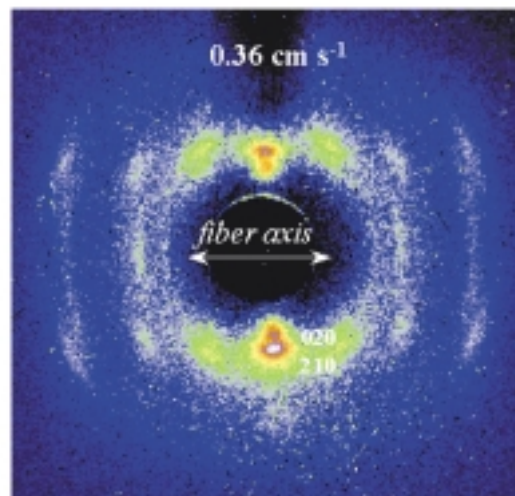


Fig. 2: Single fibre diffraction pattern recorded at a reeling speed of 0.36 cm s⁻¹ during forced silking with a CCD detector. The strongest equatorial reflections have been indexed.

structure in an oriented, amorphous matrix. For the *in situ* extrusion of synthetic polymers, the influence of parameters such as the extrusion speed on the microstructure can be studied. Of particular interest in future studies will be to find out the extent to which this biopolymer production line is influenced by environmental parameters such as temperature etc. This opens a window into the study of a fascinating biophysical process.

References

- [1] J.M. Gosline, M.E. DeMont, M.W. Denny, *Endeavour*, **10**(1), 37-43 (1986).
- [2] R.W. Work, P.D. Emerson, *J. Arachnol.*, **10**, 1-10 (1982).
- [3] C. Riekell et al., *Int. J. Mol. Biol.*, **24**(2-3), 187-195 (1999).
- [4] C. Riekell, M. Mueller, F. Vollrath, *Macromolecules*, **32**(13), 4464-4466 (1999).

Authors

C. Riekell (a), M. Mueller (a), F. Vollrath (b,c).

(a) ESRF

(b) Department of Zoology, University of Aarhus (Denmark)

(c) Department of Zoology, University of Oxford (UK)

X-ray Interference Reveals Angstrom-Scale Motions of Myosin in Intact Muscle Cells

Small-angle X-ray scattering (SAXS) can be used to study changes in protein conformation in the native environment of a living cell. The structural information obtained by SAXS is often complementary to that obtained by protein crystallography; SAXS has lower spatial resolution, but can reveal the dynamics of structural changes in relation to protein function.

Recent experiments carried out on **ID2** (SAXS beamline) have shown that it is possible to measure angstrom-scale motion of a protein by SAXS. This study probed the motion of myosin heads during contraction of single intact muscle fibres. The axial X-ray diagram from a muscle fibre shows reflections that index on the approximate 43 nm quasi-helical repeat of the myosin filaments (M1, M2, M3; **Figure 3**). The prominent M3 reflection comes from the regular 14.5 nm repeat of the motor domain of myosin (the myosin head) along the myosin filaments. Owing to the high brilliance and unprecedented collimation of the X-ray beam on ID2, it is shown that this reflection, during contraction, is composed of two closely-spaced sub-peaks (Figure 3a).

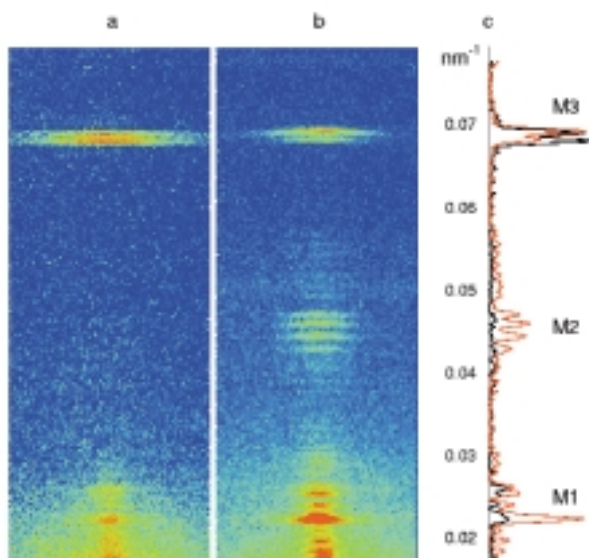


Fig. 3: Axial X-ray diffraction pattern recorded at ID2 from a single fibre isolated from frog muscle, during active contraction (a, 6s exposure) and in the absence of ATP (b, 60s exposure) and comparison of the respective axial intensity distributions (c; active, black; rigor, red).

These two sub-peaks are due to X-ray interference between the two arrays of myosins in each filament (**Figure 4**). The myosin filament (black) is bipolar; it is designed to pull neighbouring actin filaments (blue) towards

its centre, and this relative sliding between the actin and myosin filaments is responsible for muscle contraction. The centres of the two arrays of myosin heads in each filament are 870 nm apart during active contraction. This interference distance, corresponding to 59.5 repeats of the 14.5 nm axial periodicity, is maintained with atomic precision by interactions between the elongated tails of the myosins in the filament backbone.

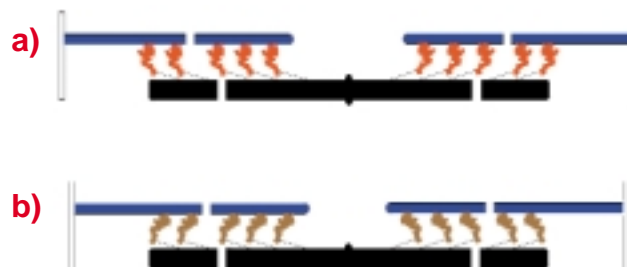


Fig. 4: The two arrays of myosin heads in each half of the myosin filament (black) in the conformation assumed during isometric contraction (a), and in the absence of ATP (b). Actin filaments shown in blue.

The interference distance changes when the myosin head binds to actin and drives filament sliding by tilting towards the centre of the myosin filament [1]. The interference effect gives a very precise measure of this motion, so that changes in the interference distance by about 1 Å can be measured from the relative intensities of the two sub-peaks of the M3 reflection. The method has already been used to measure the change in conformation of the myosin head between isometric contraction and the rigor state observed in the absence of ATP (Figures 3 and 4). By combining large area image plates and precise fast shuttering, this interference technique is now being used to characterise the sub-millisecond motion of the myosin heads that are responsible for force generation.

Reference

[1] I. Dobbie, M. Linari, G. Piazzesi, M. Reconditi, N. Koubassova, M.A. Ferenczi, V. Lombardi, M. Irving, *Nature*, **396**, 383-387 (1998).

Authors

V. Lombardi (a), M. Irving (b), G. Piazzesi (a), M. Linari (a), M. Reconditi (a), M.E. Vannicelli Casoni (a), I. Dobbie (b), T. Narayanan (c) P. Boesecke (c).
 (a) Università di Firenze (Italy)
 (b) King's College London (UK)
 (c) ESRF

Microdiffraction and Micro-Fluorescence Tomography

As indicated previously, there are a number of biological investigations where the use of microfocus technology is becoming crucial to maximising the information that can be obtained on the structure and behaviour of biological tissues. The following study is representative of the work carried out on beamlines ID22 and ID18F.

In vivo Fluorescence Microtomography of Plants

Plant physiologists and microbiologists are trying to link the macroscopic appearance to the molecular biology of a plant, especially with a view to understanding the influence of single genes on a plants large scale structure. The current research of the plant physiology group at the IBI, Forschungszentrum Jülich, Germany, includes the study of ion channels and their influence on the long range transport of ions through the plant [1]. To that end, valuable information is obtained from a determination of the ion concentrations inside the plant.

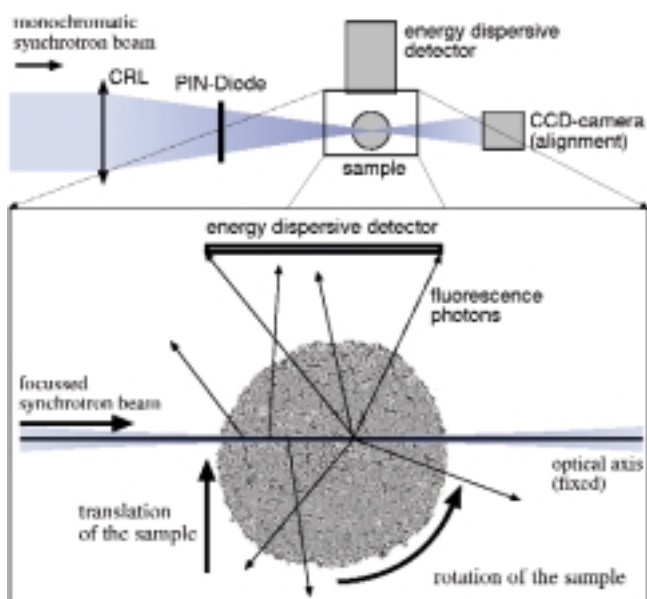
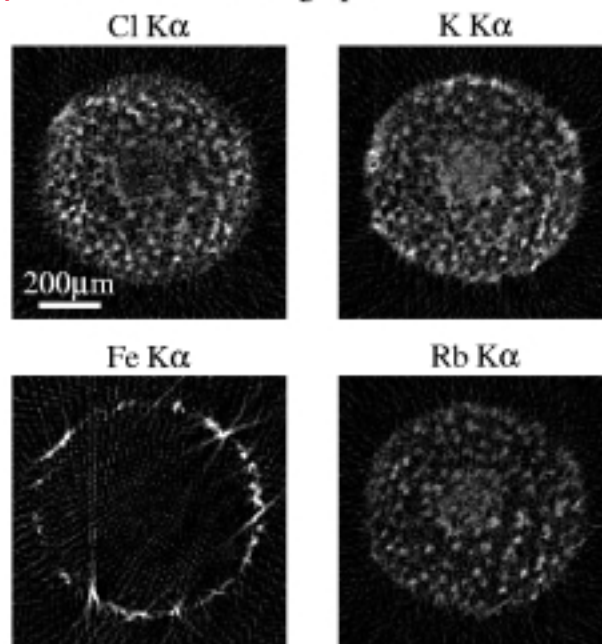


Fig. 5: Schematic setup for fluorescence microtomography. The sample is scanned through the microbeam for a large number of rotation angles between 0 and 360°. The fluorescence radiation is collected in the energy dispersive detector.

a) Fluorescence tomographs



b) Phase contrast tomograph

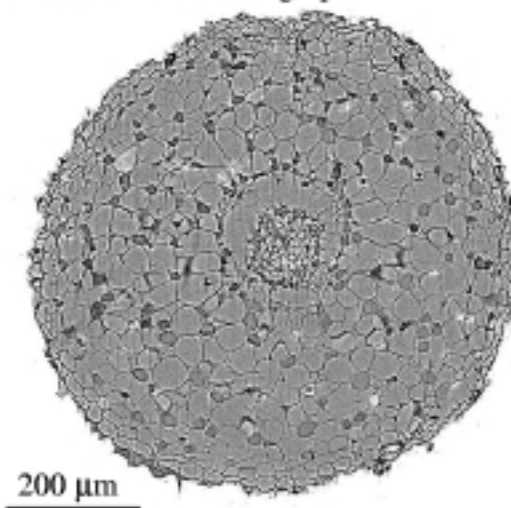


Fig. 6: (a) Fluorescence tomographs of the root of the mahogany plant (*Swietenia macrophylla*). Tomographic reconstructions (using filtered back projection) of the $K\alpha$ -lines for Cl, K, Fe, and Rb are shown. (b) Phase contrast tomograph of the mahogany root, showing the cellular structure.

In an experiment at beamline ID22/ID18F the concentration of physiologically relevant ions inside various plants has been determined by fluorescence microtomography. This method, currently under further development in collaboration with the University of Technology in Aachen, Germany, allows non-destructive determination of the element specific inner structure of a sample with a resolution in the micrometer range [2]. It is particularly suited to imaging the elemental distributions inside

biological bulk samples at a cellular level with a minimum of sample preparation. It does not require vacuum, thus allowing wet samples to be investigated. Since the fluorescence is excited with monochromatic X-rays rather than charged particles (such as electrons in EDXA), the signal to background ratio is high, and even small elemental concentrations can be detected.

As a scanning technique, fluorescence microtomography uses a microbeam of high intensity produced using a compound refractive lens for hard X-rays [3]. The monochromatic microbeam (19.5 keV) had a lateral size of 6 μm by 1.6 μm (horizontal by vertical FWHM) with a flux of 1.1×10^{10} photons/s. The sample is scanned through the microbeam. Inside the sample, the atoms along the path of the microbeam are excited and emit characteristic fluorescence radiation that is recorded by an energy dispersive detector (Figure 5). After a line scan, the sample is rotated by a small angle and the scanning is repeated. The whole procedure is continued until the sample has completed a full rotation. From this data, the distribution image for each element is reconstructed by computer tomographic techniques.

Figure 6a shows the fluorescence tomograph of a root of the mahogany plant (*Swietenia macrophylla*) without the surrounding soil. With a resolution of 7 μm the cellular structures of the plant are clearly resolved. The distribution of chlorine, potassium, iron, and rubidium is shown. While iron is not absorbed from the soil into the root and sticks to the roots surface, rubidium is incorporated by the plant in a similar way to potassium. However, it is about three orders of magnitude less concentrated than potassium. The reconstruction illustrates the high sensitivity of the method. In combination with other tomography techniques, such as phase contrast microtomography, the elemental distribution can be directly related to the structure of the sample. Figure 6b shows the phase contrast tomograph of the mahogany root.

Due to the small amount of sample preparation and its non-destructive character, fluorescence microtomography may become an important tool in many disciplines, including biomedicine, environmental and earth science, condensed matter physics, and chemistry.

References

- [1] W.H. Schröder, G.L. Fain, *Nature*, **309**, 268-270 (1984).
- [2] A. Simionovici, M. Chukalina, M. Drakopoulos, I. Snigireva, A. Snigirev, C. Schroer, B. Lengeler, K. Janssen, F. Adams, in *Developments in X-ray Tomography II*, Ulrich Bonse, Editor, *Proceedings of SPIE*, **3772**, 304-310 (1999).
- [3] B. Lengeler, C. Schroer, J. Tümmeler, B. Benner, M. Richwin, A. Snigirev, I. Snigireva, M. Drakopoulos,

Journal of Synchrotron Radiation, **6**(6), 1153-1167 (1999).

Authors

W. Schroder (a), C. Schroer (b), B. Lengeler (b), J. Tümmeler (b), F. Gunsler (b), A. Simionovici (c), A. Snigirev (c).

(a) IBI, Forschungszentrum, Jülich (Germany)

(b) RTWH, Aachen (Germany)

(c) ESRF

Macromolecular Crystallography

Examples of Macromolecular Structures Published During 1999 Using Data Collected on the ESRF Beamlines

The year 1999 produced many new structures with 6 papers in *Nature* and 7 in *Science*. In this context and with the limited space available, choosing highlight structures is very much a matter of taste. However, the following section should give a clear impression of the quality of the work that is produced through the use of the ESRF beamlines.

Fumarate Reductase from Wolinella Succinogenes

The membrane protein complex, fumarate reductase, couples the reduction of fumarate to succinate to the oxidation of quinol to quinone, in a reaction which is opposite to that catalysed by succinate dehydrogenase (SDH) in the related complex II of the aerobic respiratory chain. SDH is also the only membrane-bound enzyme in the citric acid cycle (Krebs' cycle). The structure of fumarate reductase from the anaerobic bacterium *Wolinella succinogenes* has been recently determined [1], using data collected at beamline **BM14**. The phases were determined by multiple isomorphous replacement with anomalous scattering (MIRAS). All data were collected at 277 K on only one crystal per data set. Since most derivatives contained only one heavy atom bound per fumarate reductase complex of 130 kDa, the reliable incorporation of anomalous differences was essential in order to include the contribution of the endogenous iron sites (11 Fe per fumarate reductase complex) in the calculation of phases. The phases were improved using a series of density modification methods, including solvent flattening,

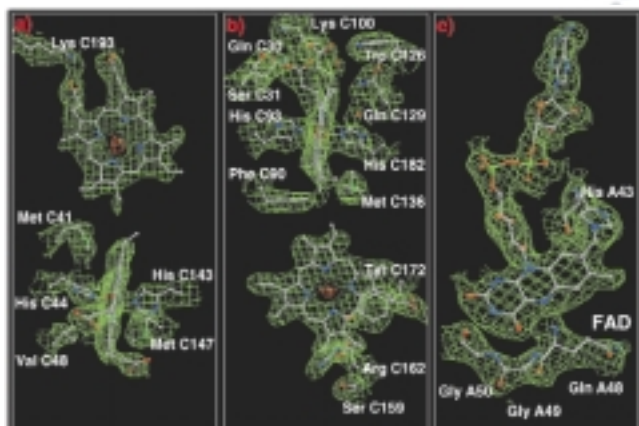


Fig. 7: Representative parts of the experimental electron density maps for crystal form A calculated with the MIRAS phases after density modification and phase extension to 2.2 Å resolution. Carbon, nitrogen, oxygen, phosphorous, and sulphur atoms are shown in grey, blue, red, light green and green, respectively, haem iron centres are shown in orange. Contour levels are 1.0 σ (green) and 9.0 σ (red) above the mean density of the map. a, b) the two haem b molecules and the side chains of some neighbouring residues in the transmembrane region. c) the covalently bound FAD prosthetic group.

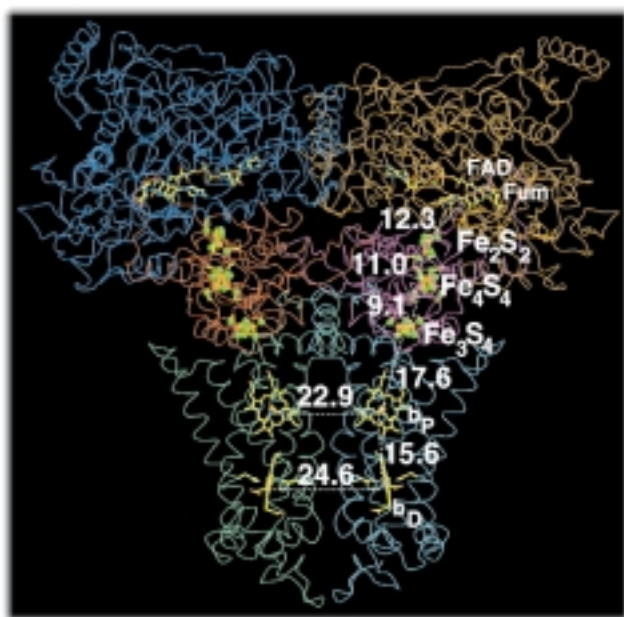


Fig. 8: The three-dimensional structure of the *Wolinella succinogenes* fumarate reductase dimer. The polypeptide backbones of the two A subunits are drawn in blue and brown, those of the two B subunits in red and pink and those of the C subunits in green and light blue. The prosthetic groups are displayed as atomic models with C in yellow, N in blue, O in red, P in light green, S in green and Fe in red-brown. The prosthetic groups of one monomer are labelled as heme groups b_D and b_P , and as iron-sulphur centres Fe_3S_4 , Fe_4S_4 , and Fe_2S_2 . Also labelled are the FAD group and the bound substrate fumarate as well as the indicated distances in Å units.

histogram matching, NCS averaging and phase extension to a resolution of 2.20 Å. Representative electron density maps are shown in Figure 7. The excellent quality of the experimental map allowed rapid model building for most of the structure. The two fumarate reductase complexes in the asymmetric unit of the crystal form a dimer, with each monomer containing the three different subunits A, B, and C (see Figure 8). The large hydrophilic subunit A contains the site of fumarate reduction and the covalently bound prosthetic group flavin adenine dinucleotide (FAD). The smaller hydrophilic subunit B contains three iron-sulphur centres. The quinol-oxidizing membrane-embedded subunit C binds two haem b groups. On the basis of the structure, a pathway of electron transfer can be traced from the two haem groups of subunit C via the three iron-sulphur centres and the FAD to the site of fumarate reduction. The structure has also enabled the suggestion of a catalytic mechanism for the reduction of fumarate to succinate with general relevance also to succinate dehydrogenases.

Reference

[1] C.R.D. Lancaster, A. Kröger, M. Auer, H. Michel, *Nature*, **402**, 377-385 (1999).

Authors

C.R.D. Lancaster (a), A. Kröger (b), M. Auer (a), H. Michel (a).
 (a) Max-Planck-Institut für Biophysik, Frankfurt am Main (Germany).
 (b) Institut für Mikrobiologie, J.W. Goethe-Universität, Frankfurt/M. (Germany).

A Triple β -spiral in the Adenovirus Fibre Shaft — a New Structural Motif for a Fibrous Protein

The human adenoviruses are responsible for a number of respiratory, gastroenteric and ocular infections. They also make good candidates as delivery vehicles for gene therapy applications and are therefore of intense interest among various biotechnology companies. They form icosahedral particles with 240 copies of the trimeric hexon protein arranged on the planes of the icosahedron and a penton complex at each of the twelve vertices. The penton comprises a pentameric base, implicated in virus internalisation, and a protruding trimeric fibre, responsible for the attachment of the virus to the receptor. The fibres are homo-trimeric proteins containing an amino terminal penton base attachment domain, a long thin central shaft, and a carboxy terminal cell attachment or head domain [1]. The primary sequence of the fibre shaft consists of a 15 residue pseudo-repeat unit and there are 22 repeats in both the serotype 2 and 5 of the human adenovirus. The shaft gives the virus a long reach to search for CAR (Coxsackievirus

and Adenovirus Receptor) receptors on cell surfaces. The CAR is lodged in the outer membrane of most human cells and has an antenna-like projection that extends outside the cell. Although CAR's function in healthy cells is still unknown, it has been recently shown that the receptor recognises the head domain of the adenovirus. When the virus approaches the cell, the fibre head binds to CAR as a first step in gaining access to the cell. It is also the link that will have to be broken if the adenovirus is to become a useful therapeutic tool, since it will be required to bind not to the majority, but only to the target cells.

Fig. 9: Adenovirus fibres are formed when three identical proteins fold into a long strand with a knotted head.

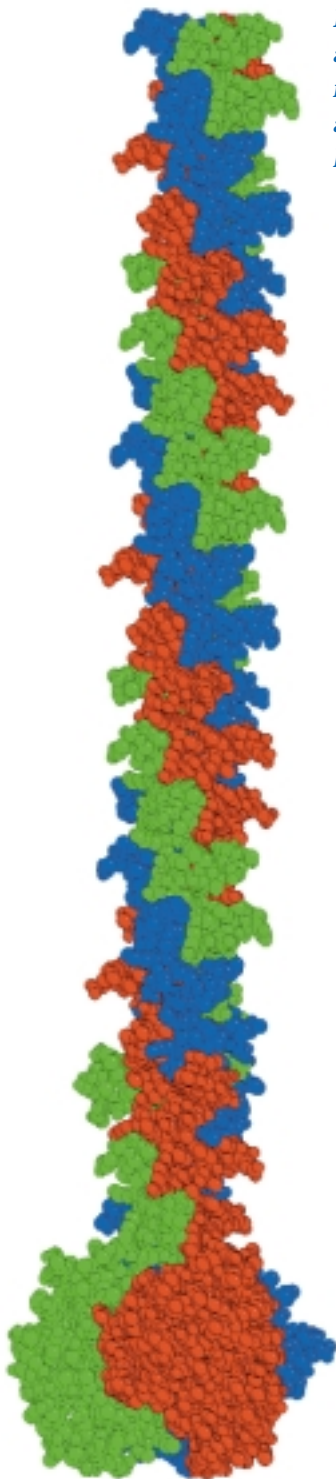
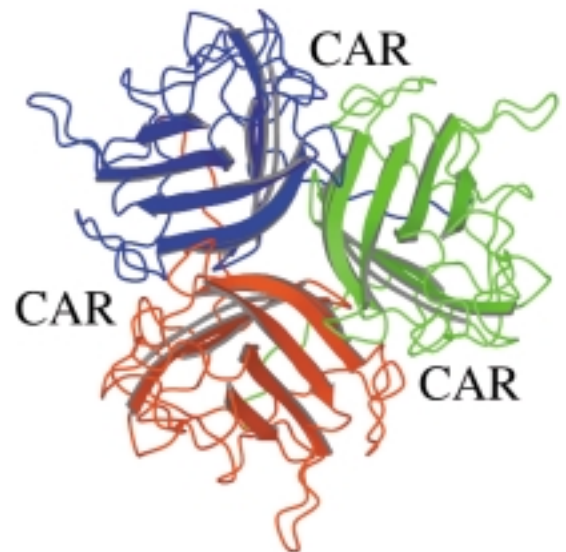


Fig. 10: The crystal shows how the three fibres meet at the fibre head (viewed from the top in this figure) forming grooves into which the CAR molecules can bind.



It has been possible to crystallise a recombinant protein comprising the four distal repeats of the adenovirus type 2 shaft plus the receptor-binding head domain. Using beamline **ID14/3**, data to a resolution of 2.4 Å was collected at 100 K and the structure solved by molecular replacement using the Ad2 fibre head structure alone [2].

The shaft structure reveals a new fold, termed the “triple β -spiral”, as shown in **Figure 9**. This is a regular, highly cross-linked structure which together with a high proportion of buried surface (one third of the solvent accessible surface of a shaft monomer is buried on trimer formation) gives a high rigidity and stability to the shaft. The average diameter of the shaft is some 15 Å, although surface loops give a maximum diameter of 22 Å and a model of the full length fibre, based on the four repeats in the current structure, indicates a total shaft length of some 300 Å. The stability and morphology of the adenovirus shaft have led to its use as a model for synthetic fibre design. As indicated in **Figure 10**, the three fibres meet at the fibre head and van Raaij and Cusack have been able to identify grooves between adjacent subunits where CAR molecules bind. This, in turn, has enabled them to propose mutations of amino acids which will alter or abolish the binding of CAR without interfering with the overall structure of the fibre. Such proposals are being investigated by genetic engineering enterprises.

References

- [1] M.J. van Raaij, N. Louis, J. Chroboczek, S. Cusack, *Virology*, **70**, 7071-8 (1996).
- [2] M.J. van Raaij, A. Mitraki, G. Lavigne, S. Cusack, *Nature*, **401**, 935-8 (1999).

Authors

- M.J. van Raaij (a), A. Mitraki, (b), J. Chroboczek (b), S. Cusack (a).
 (a) EMBL Grenoble Outstation (France)
 (b) IBS (CEA-CNRS), Grenoble (France)

Studies on Bacteriorhodopsin

Bacteriorhodopsin (bR) from *Halobacterium salinarum* is a proton pump, which converts the energy of light into a proton gradient that drives ATP synthesis. In vivo, the seven transmembrane helix protein is organised in purple patches, in which bR and lipids form crystalline two dimensional arrays. Upon absorption of a photon, the all trans retinal moiety, covalently bound to Lys216 via a Schiff base, is isomerised to a 13-cis, 15-anti configuration. This initiates a sequence of events, the photocycle, during which a proton is transferred from the Schiff base to Asp85, followed by proton release into the extracellular medium, and reprotonation from the cytoplasmic side of the membrane. The aim of these studies is to understand the structural basis for the proton transfer in bR, the simplest known photon-driven proton pump which as such provides a paradigm for the study of a basic function in bioenergetics.

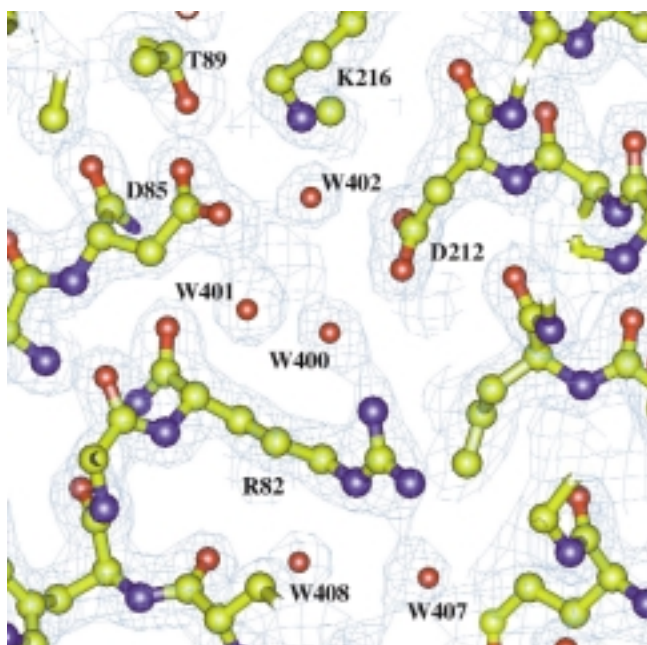


Fig. 11: Electron density map ($2F_o - F_c$, contoured at 1σ) in the vicinity of the Schiff base. The electron density map to 1.9 Å resolution is represented in blue, water molecules are represented as red spheres.

Following the pioneering work carried out on the microfocus beamline ID13 [1] from crystals grown in lipidic cubic phases, the structure of bR in the ground state was extended to 1.9 Å resolution from larger and non twinned crystals [2]. It revealed eight well ordered water molecules in the extracellular half of the putative proton translocation pathway (Figure 11). The water molecules form a continuous hydrogen bond network from the Schiff base nitrogen (Lys216) to Glu194 and Glu204 and includes residues Asp85, Asp212 and Arg82. This network is

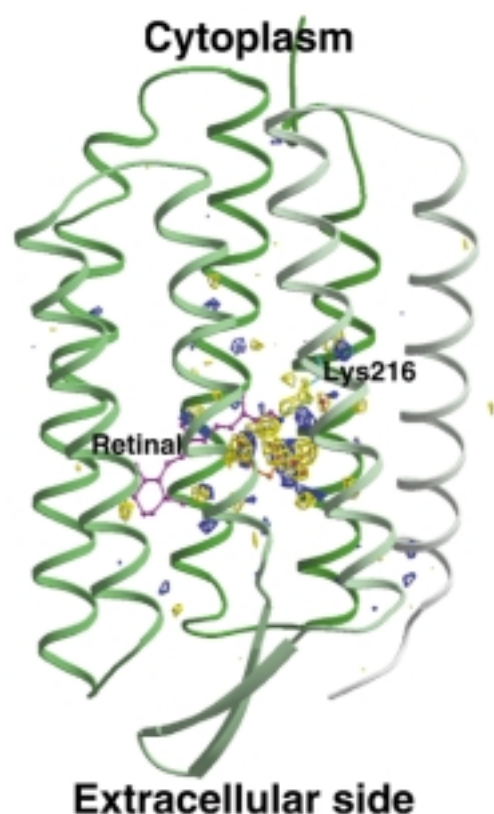


Fig. 12: Structural changes in bR resulting from photoexcitation at 110 K. Overview of the ($F_{exc} - F_{ground}$) difference electron density maps (yellow: negative, blue: positive density) contoured to 3.5σ ($\sigma = r.m.s.$ electron density for the unit cell) and overlaid on the ground state bR model. At this contour level most changes are clustered in the vicinity of the retinal.

involved in both proton translocation occurring during the photocycle as well as in stabilising the structure of the ground state. Nine lipid phytanyl moieties could also be modelled into the electron density maps. From all these elements and further analysis, the atomic resolution structure of bR, lipid and water molecules in the lipidic cubic phase grown crystals could be shown to represent the functional entity of the protein in the purple membrane of the bacteria [2].

The ground state structure of bR is however not sufficient to explain the entire mechanism of the proton translocation. In order to elucidate the initial structural changes coupled to the proton pumping mechanism, an early intermediate of the photocycle was trapped at low temperature within wild type bR crystals and diffraction data measured to 2.1 Å resolution [3]. The experiment was carried out on ID14/3.

The difference Fourier map between this new photoexcited state (F_{exc}) and the ground state (F_{ground}) described above shows clear movements of the protein, all located in the

vicinity of the chromophore (Figure 12). Changes in the orientation of the retinal moiety displace the key water molecule (W402 in Figure 11) which was bridging the Schiff base to the Asp85 in the ground state structure, enabling this latter residue to move towards the retinal. Displacement of main chain Lys216 locally disrupts the hydrogen bonding network of helix G, facilitating structural changes in later stages of the photocycle. Those results give some insights into how the proton is transferred from the Schiff base to the Asp85 and reveal the deformations of the protein related to the photocycle initiation [3].

In order to understand the complete proton transfer mechanism, the structural modifications during the further steps of the photocycle of bR will be studied.

References

- [1] E. Pebay-Peyroula, G. Rummel, J.P. Rosenbusch, E.M. Landau, *Science*, **277**, 1676-1681 (1997).
 [2] H. Belrhali, P. Nollert, A. Royant, C. Menzel, J.P. Rosenbusch, E.M. Landau, E. Pebay-Peyroula, *Structure*, **7**, 909-917 (1999).
 [3] K. Edman, P. Nollert, A. Royant, H. Belrhali, E. Pebay-Peyroula, J. Hajdu, R. Neutze, E.M. Landau, *Nature*, **401**, 822-826 (1999).

Authors

H. Belrhali (a), P. Nollert (b,c), A. Royant (a,d), C. Menzel (e), J.P. Rosenbusch (b), E.M. Landau (b), E. Pebay-Peyroula (d,f), K. Edman (g), J. Hajdu (g), R. Neutze (g).
 (a) ESRF
 (b) Biozentrum, University of Basel (Switzerland)
 (c) Current address: Department of Biochemistry and Biophysics, UCSF, (USA)
 (d) Université Joseph Fourier, Grenoble (France)
 (e) University of Münster (Germany)
 (f) Institut de Biologie Structurale, CEA-CNRS, Grenoble (France)
 (g) Department of Biochemistry, Uppsala University (Sweden)

Multi-wavelength Anomalous Dispersion (MAD) Studies

The multiple-wavelength anomalous dispersion technique for deriving phase information in the determination of the structures of biological macromolecules can be practised on both ID14/4 and BM14; the latter beamline will be superseded by ID29 during the course of 2000. During 1999 some 73 MAD experiments were undertaken on BM14 of which only one has been reported as unsuccessful. The edges covered (with number of structures in parentheses) include Se (44), Hg (5), Pt (3), Br (3), Pb (2), Fe (6), Zn (3), Cu (2), and one each for Ni, Gd,

Eu, Ho and W. ID14/4 only commenced a full user service for MAD in May 1999, but still some 32 successful experiments were performed for Se (24), U (2), Br (3), Hg (1), Pt (1) and As (1). These impressive numbers are in addition to the routine single wavelength data collection experiments. BM1 (SNBL) and BM30A (FIP) CRG beamlines have also undertaken successful MAD experiments. The speed of MAD experiments is also astonishing with reports of several new structures being solved per day by various groups. Figure 13 shows part of an electron density map derived from a three wavelength

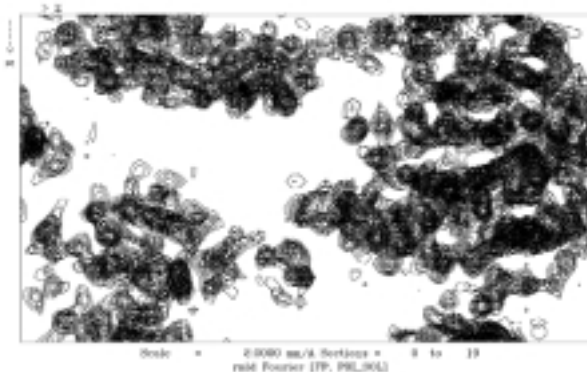


Fig. 13: Part of an electron density map of the protein L-rhamnose (J. Naismith and colleagues, St Andrews, Gordon Leonard, ESRF and Sean McSweeney, EMBL). This map was computed only some 50 minutes after the mounting of the sample on the beamline. It is clearly interpretable in terms of the molecular structure.

experiment on a seleno-methionine substituted protein. The map is clearly interpretable in terms of the polypeptide chain and its production was achieved only 50 minutes after the data collection was commenced. Each data set took only 5 minutes to collect using the ADSC Quantum 4 detector system on ID14/4, whereas the determination of the Se positions (4 Se per 32.6 kDa asymmetric unit) took some 24 minutes; some of the remaining minutes were occupied by computation, but one also suspects that the experimenters had time for a cup of coffee! Such speed in optimal circumstances is an indication of our capabilities for the immediate future, and with increasing automation of both data collection methods and phase determination, the ESRF should be able to cope with future needs in this area.

The NADP(H)-binding Component (dIII) of the Proton-translocating Transhydrogenase from Human-heart Mitochondria

Transhydrogenase is located in the inner membranes of animal mitochondria and the cytoplasmic membranes of bacteria. It couples the transfer of reducing equivalents of NAD(H) and NADP(H) to proton pumping. The protein has

a tripartite structure and its dII component spans the membrane. The dI and dIII components protrude outside the membrane and have binding sites for NAD⁺/NADH and NADP⁺/NADPH respectively. Proton pumping is probably coupled to changes in the binding affinities of dIII for NADP⁺ and NADPH.

Crystals have been obtained for the NADP(H)-binding component, dIII of human-heart transhydrogenase. Diffraction data were collected on a single cryo-cooled Se-Met crystal on beamline **ID14/4** to a resolution of 2.5 Å at three wavelengths corresponding to the inflexion point, peak and remote wavelength of the Se K-edge. Initially a 55° wedge of data was collected at each wavelength, followed by a second 40° wedge (space group P4₁22 with a = 58.1 Å and c = 250.8 Å). Each diffraction image on the ADSC Quantum 4 detector was a 1.0° oscillation with a 1 second exposure; the time to collect the complete data set was 62 minutes. The resolution was then extended to 1.9 Å using a second crystal. The program SOLVE [1] was used to locate 14 out of a possible 18 Se positions and subsequent phase determination and solvent flattening allowed the fitting of the polypeptide chain, followed by refinement of the structure.

The structure of the dIII component resembles the classical "Rossman" fold, **Figure 14** [2]. However, NADP⁺ binds to dIII with a reversed orientation. There is a Gly-X-Gly-X-X-Ala/Val fingerprint in the first β₁β₂β₃ motif of dIII, but it has a different function to the classical Rossman structure. The nicotinamide ring of NADP⁺ is located on a ridge where it is exposed to interaction with NADH on the dI subunit. Two distinctive features of the dIII structure are the helix-D/loop-D which projects from the β-sheet and loop-E which forms a lid over the bound NADP⁺.

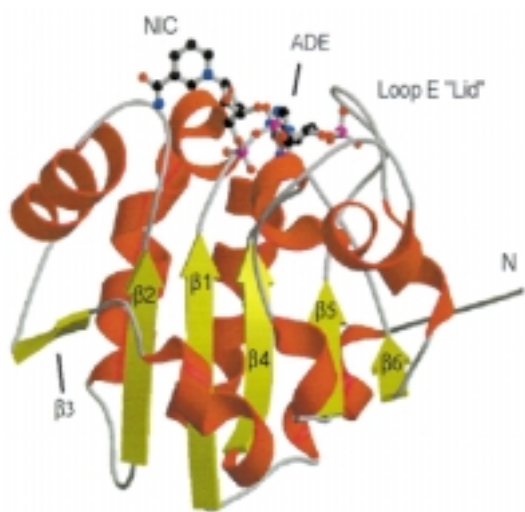


Fig. 14: A stereo-ribbon diagram of human transhydrogenase, dIII, showing the resemblance to the classical Rossman fold, the nicotinamide binding site and the position of the loop-E lid.

Thus the helix-D/loop-D interacts with the bound nucleotide, with loop-E and probably the membrane spanning second domain. Changes in the ionisation and conformation of the helix-D/loop-D resulting from proton translocation through dII may be responsible for the changes in affinity of dIII for NADP⁺ and NADPH, that drive the reaction.

References

- [1] T.C. Terwilliger, J. Berendzen, *Acta Cryst.*, **D55**, 849-861 (1999).
- [2] S.A. White, S.J. Peak, S. McSweeney, G. Leonard, N.P.J. Cotton, J.B. Jackson, *Structure*, **8**, 1-12 (2000).

Authors

S.A. White (a), S.J. Peak (a), S. McSweeney (b), G. Leonard (c), N.P.J. Cotton (a), J.B. Jackson (a).
 (a) School of Biosciences, University of Birmingham (UK)
 (b) EMBL Grenoble Outstation (France)
 (c) ESRF

A Novel Type of Catalytic Copper Cluster in Nitrous Oxide Reductase

Nitrous oxide (N₂O) is a greenhouse gas, the third most significant contributor to global warming [1]. As a key process for N₂O elimination from the biosphere, nitrous oxide reductase (N₂OR) catalyses the two-electron reduction of N₂O to N₂. This periplasmic enzyme is found in denitrifying bacteria which obtain metabolic energy by using nitrogen-oxidised compounds, instead of oxygen, as terminal electron acceptors in anaerobic respiration. Nitrous oxide reductase is a 1160 residue, homodimer, containing 2 copper centres called CuA and CuZ. The CuA centre is the electron entry site, and is structurally homologous to the CuA centre of cytochrome c oxidase [2]. The structure of the catalytic CuZ centre, however, is unknown. In order to solve the structure of N₂OR and thereby elucidate the structure of the CuZ centre, a MAD data collection was performed on **BM14**, exploiting the anomalous absorption of the copper K-edge. The coordinates of the twelve copper clusters were identified from low resolution anomalous Patterson syntheses. Phases were calculated from these twelve clusters and improved by solvent flattening. After iterative rounds of model building and six-fold, non-crystallographic symmetry averaging, the improved map enabled the complete polypeptide chain to be built. The copper centres were then constructed by refining the preliminary model against a 2.4 Å data set collected from **ID14-4**.

Each N₂OR monomer is composed of two distinct domains. The N-terminal domain (residues 10-443) adopts a 7-bladed β-propeller fold, with the CuZ centre located at one end of the propeller on the pseudo 7-fold axis. The C-terminal domain (residues 478-581) forms an anti-parallel

β -sandwich in the Greek key motif, and adopts a cupredoxin fold already seen in bovine cytochrome c oxidase, with the CuA centre located in a loop region between strands β 8 and β 9. In the dimer, the C-terminal domain of one monomer faces the N-terminal domain of the second monomer reminiscent of the phenomenon of 'domain-exchange' (Figure 15). Upon dimerisation 26% of the total surface area of each monomer is buried to a 1.6 Å radius probe.

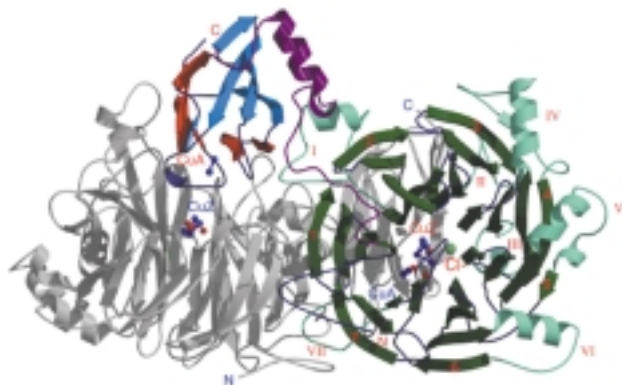


Fig. 15: Overall view of the crystal structure of the N_2OR dimer; one monomer is uniformly coloured grey while the other monomer is colour coded as a function of secondary structure. The labels of the coloured monomer (N- and C- termini, the copper centres, Cl^- ion, blade and insertion numbering) are in red; labels for the second monomer are in blue. Blades are numbered from 1 to 7. Seven insertions are identified: labelled I to VII.

The CuZ centre of N_2OR comprises four copper ions which adopt the shape of a distorted tetrahedron, and ten ligands (Figure 16): seven histidines residues and three hydroxide ions. Two histidine residues (His270 and His437) of the CuZ centre belong to the loops located on the top of the propeller domain and the remaining five (His79, His80, His128, His325, His376) belong to the inner-most strand of the blades (Figure 16). The seven His ligands are not part

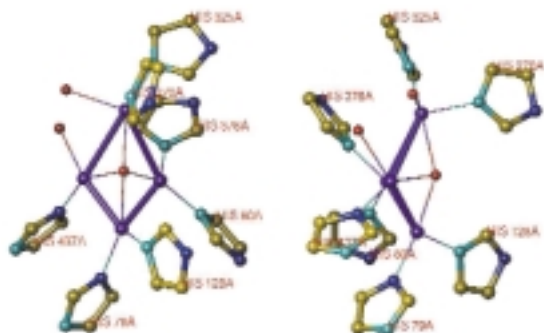


Fig. 16: Side and front representations of the CuZ centre; copper is in purple, OH^- in red, imidazole rings from the histidines are colour-atom coded, the $N\delta 1$ being dark blue, and the $N\epsilon 2$ light blue.

of a consensus sequence, the CuZ centre thus differs from other copper centres. As a result of the intermonomer 'domain-exchange', the CuA centre of one monomer is in close proximity (closest distance, 10.2 Å) to the CuZ centre of the second monomer.

The structure of the CuZ centre suggests that there is only one possible site for N_2O binding. The CuZ centre could behave as an electron buffer, three copper ions being reduced by the CuA centre prior to substrate processing. The catalytic copper would remain oxidised and, therefore, able to bind the substrate. This electron reservoir could favour a fast electron exchange and prevent the formation of dead-end products.

References

- [1] J. Reilly et al., *Nature*, **401**, 549-555 (1999).
- [2] J.A. Farrar, A.J. Thomson, M.R. Cheesman, D.M. Dooley, W.G. Zumft, *FEBS Lett.*, **294**, 11-15 (1991).

Authors

K. Brown (a), M. Tegoni (a), M. Prudêncio (b), A.S. Pereira (b), S. Besson (b), J.J. Moura (b), I. Moura (b), C. Cambillau (a).

(a) Architecture et Fonction des Macromolécules Biologiques, UPR 9039, CNRS, Marseille (France)

(b) Departamento de Química, Centro de Química Fina e Biotecnologia, Universidade Nova de Lisboa (Portugal)

Dihydroorotate Dehydrogenase from *Escherichia coli*

Dihydroorotate dehydrogenases (DHOD) catalyse the oxidation of (S)-dihydroorotate to orotate in the in vivo synthesis of UMP, the precursor of pyrimidine nucleotides, building blocks of both DNA and RNA. These enzymes have a flavin mononucleotide (FMN) cofactor in common, which is involved in the transfer of a hydride ion from the substrate to the electron acceptor. According to their amino acid sequences DHOD's can be divided into two main families [1]. Family 1 consists of cytosolic enzymes from Gram-positive bacteria, while DHOD's from eukaryotes and Gram-negative bacteria belong to family 2 and are membrane associated. Family 2 enzymes use long-chain ubiquinones as electron acceptors, and the electrons generated are delivered to the respiratory chain. The catalytically active residue in the family 1 enzymes is a cysteine, while in the family 2 enzymes it is a serine. DHOD is the rate limiting enzyme in the de novo pyrimidine biosynthetic pathway. Human DHOD belongs to family 2 and its inhibition by quinone analogues is currently investigated as a potential means of treating immune based diseases. Until recently only structures representative of family 1 enzymes were known.

A Se-edge MAD data set was collected at the **BM30A** (FIP) beamline on the Se-methionine substituted form of the *E. coli* DHOD, belonging to family 2. The protein (37 kDa) was co-crystallised with the reaction product orotate (crystal space group: $P4_12_12$, $a=b=119.7$ Å, $c=295.97$ Å). Due to the long *c*-axis, extreme care had to be taken to optimise the resolution and avoid spot overlaps by selecting the correct detector to crystal distance. The 2.5 Å resolution data were collected at 3 wavelengths with 120 s exposure per image (0.5° oscillation) on a MAR345 image plate detector. The data was integrated and scaled using DENZO and SCALEPACK (global $R_{\text{merge}} \sim 8\%$, $R_{\text{ano}} \sim 5\%$, completeness $\sim 97.5\%$). The positions for 24 out of the 28 expected Se-sites per asymmetric unit (4 molecules/a.u.) were localised using the program SOLVE and further refined by SHARP. The first maps calculated employing NCS-averaging and DM allowed the tracing of the complete structure except for the first two residues in the N-terminus. Refinement of the structure was completed using CNS ($R=17.9\%$, $R_{\text{free}}=21.9\%$, resolution range 20-2.5 Å). The α/β -barrel structure common to all other known DHOD structures is maintained, with the FMN group and orotate

Fig. 17: The structure of the *Escherichia coli* dihydroorotate dehydrogenase. The protein forms an α/β -barrel with two extra helices at the N-terminal lying on the side of the barrel, when compared with other DHOD structures. These helices are proposed to be the membrane associating part of the enzyme. The FMN group and the product orotate are represented as stick models (FMN, yellow; orotate, orange).



binding site situated on the top of the barrel. The structure has an extended N-terminal, which forms two helices situated on one side of the barrel (Figure 17), which are proposed as the membrane associated part of the protein. Though the sequence identity with DHOD's from family 1 is low, the active site and the orotate binding pattern is conserved. The substitution of the catalytic cysteine found in family 1 enzymes to a serine is confirmed, and an increase in the hydrophobic character of its environment is observed. This increase involves a substitution of a solvent oriented Glu (family 1 structures) into a Leu of which the side chain is turned inwards, shielding the active site serine.

Reference

[1] O. Björnberg, P. Rowland, S. Larsen, K.F. Jensen, *Biochemistry* **36**, 16197-16205 (1997).

Authors

S. Nørager (a), O. Björnberg (b), K.F. Jensen (b), S. Larsen (a).

(a) Centre for Crystallographic Studies, Department of Chemistry, University of Copenhagen (Denmark)

(b) Institute for Molecular Biology, University of Copenhagen (Denmark)

A Multi-disciplinary Study. Solution of the Structure and Reaction Mechanism of Phospholipase D from *Streptomyces sp.* Strain PMF

Phospholipids are major components of all living cells. They are synthesised and broken down by a diverse family of enzymes known as phospholipases. These are subdivided into classes A-D depending on where they attack the phospholipid molecule. Many of the products are used as signalling molecules, which enable cells to react to internal and external stimuli. As part of a long term structural study of phospholipases the structure of the 56 Kda Phospholipase D from *Streptomyces sp.* strain PMF (PLD_{PMF}) has been solved at the ESRF [1]. Diffraction data to 1.4 Å resolution for the enzyme and several potential heavy atom derivatives were collected on **BM1** (the Swiss Norwegian Beamline). None of the derivatives proved to be suitable to solve the structure but the presence of a single highly occupied tungstate ion was detected in one of them. This enabled a 4-wavelength MAD experiment on **BM14** which rapidly lead to solution of the structure at 1.9 Å including an almost complete amino acid sequence. After solvent flattening, histogram matching and phase extension, the structure was refined to convergence using SHELXL with the 1.4 Å **BM1** data [2].

A ribbon representation of PLD_{PMF} is shown in Figure 18. The protein backbone goes from N to C in this figure and is

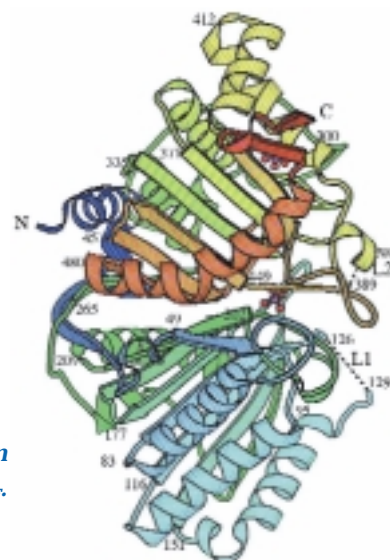


Fig. 18: Ribbon representation of PLD_{PMF} .

coloured through the rainbow so that one can see that it is folded into two topologically similar regions, so-called “domains”, which are related by a two-fold rotation axis. The active site of the enzyme, occupied by a phosphate group in the figure, lies on this axis with a histidine, an asparagine and a lysine residue from each domain. The sequence pattern for these residues in the two domains is, in both cases HXKX₄DX₉N.

This is the first structure of a phospholipase D. However it provides structural data for an extensive family of proteins with quite diverse biochemical activity. The “PLD-family” was identified by Ponting et al. [3] by searching protein sequence data bases for characteristic strings of amino acids. One of these strings was the HXKX₄DX₉N pattern which we have now found to occur twice in the active site of PLD_{PMF}. The PLD family also includes a 16 KDa endonuclease, nuc, from *Salmonella typhimurium*. Although this enzyme is much smaller than PLD_{PMF} and only contains a single copy of this sequence string, a recent crystal structure [4] has shown that nuc actually forms a dimer with an active site very similar to that in PLD.

As a consequence of the way the structure was determined it was found that one of the amino acids in the active site lies in two different orientations depending on whether enzyme activity is blocked by e.g. phosphate or tungstate or is available for catalysis. This led to a series of experiments on **ID14-4**, where crystals were soaked with a soluble phospholipid for different times before freezing and data collection. This has given a complete and detailed picture of the sequence of events, which occur when PLD_{PMF} breaks down its substrate into a so-called phosphatidic acid and choline [5]. In one of these experiments the chemical reaction was trapped in a so-called transition state. The experiments also caused some surprise since it appears that the enzyme is also able to hydrolyse its own phosphatidic acid product further, but that in doing so probably deactivates itself.

References

- [1] I. Leiros, E. Hough, P. D'Arrigo, G. Carrea, G. Pedrocchi-Fantoni, F. Secundo, S. Servi, *Acta Cryst. D*, **56**, 466-468 (2000).
- [2] I. Leiros, F. Secundo, C. Zambonelli, S. Servi, E. Hough, *Structure with Folding & Design*, **8**, 655-667 (2000).
- [3] C.P. Ponting, I.D. Kerr, *Protein Sci*, **5**, 914-922 (1996).
- [4] J.A. Stuckey, J.E. Dixon, *Nature Struct. Biol.*, **6**, 278-284 (1999).
- [5] I. Leiros, S. McSweeney, E. Hough, To be published.

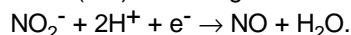
Authors

- E. Hough (a), S. McSweeney (b), I. Leiros (a).
 (a) University of Tromsø (Norway)
 (b) EMBL – Grenoble Outstation (France)

Macromolecular Crystallography Employing Cryo-trapping of Intermediates

Seeing an Enzyme at Work: Conformational Changes Occurring Upon Nitrite Reduction

Nitrite reductase (NiR) is a key enzyme of the denitrification pathway. It catalyses the reduction of nitrite (NO₂⁻) to nitric oxide (NO) according to the reaction:



NiR controls the rate of the production of toxic nitric oxide, and regulates its release into the atmosphere. Due to environmental issues, it is crucial to understand the reaction mechanism of such enzymes. Nitrite reductase from the pathogenic *Pseudomonas aeruginosa*, a soluble 120 kD homodimer, has been studied. The three-dimensional crystallographic structure of the fully oxidised enzyme was solved by molecular replacement from data collected on beamline **ID9** [1]. The data were reduced with a new integration package allowing the deconvolution of spatially overlapped diffraction spots, and improving the evaluation of weak spots [2].

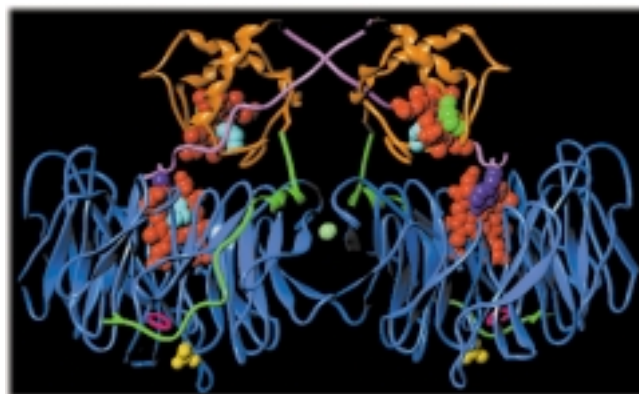


Fig. 19: Ribbon representation of the secondary structure of the C α tracing of nitrite reductase from *Pseudomonas aeruginosa*. The c and d1 hemes are represented in red, the c-domain in orange, the d1-domain in blue and the c-d1 linker in green.

As can be seen in **Figure 19**, each monomer carries a c-domain displaying a classical c-type cytochrome fold and containing a c-heme, and a d₁-domain displaying an eight bladed β -propeller structure and containing a non-covalently bound d₁-heme. The c-heme is first reduced in vivo by cytochrome C₅₅₁, and the electron is slowly transferred to the d₁-heme, where the nitrite substrate is reduced. Crystallographic data from the fully reduced enzyme have revealed significant structural modifications relative to the fully oxidised enzyme, an unusual feature in the field of redox enzymes [3]. These modifications appear

to be crucial for making the Fe of the d_1 heme accessible to the substrate. In order to understand the cascade of events that trigger catalysis, a correlation of the redox-state of the enzyme with its conformational changes was attempted. A mixed valence state was produced, in which the c-heme is reduced and the d_1 -heme still oxidised. The experiment was carried out in the following way: starting from the fully oxidised enzyme, ascorbate was rapidly diffused in the crystal, which was then freeze quenched after well-chosen delays. Absorption spectra were recorded for each time-delay on the micro-spectrophotometer (Figure 20). This enabled a crystal of the mixed-valence state to be isolated. This crystal was then exposed to X-rays on ID14. No significant structural modifications relative to the fully oxidised enzyme were observed. Therefore, it was concluded that it was the reduction of the d_1 -heme that was at the origin of the structural changes observed for the fully reduced enzyme.

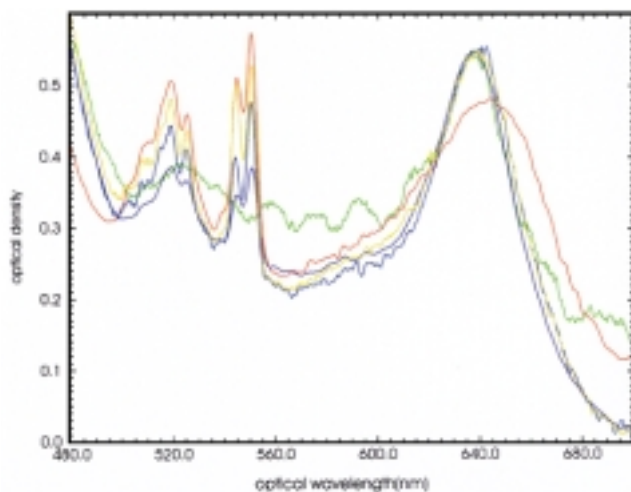


Fig. 20: Optical micro-spectrophotometer spectra of cryo-cooled (100K) nitrite-reductase crystals. Features at 500-560 nm are characteristic of the c-heme, whereas features at 620-670 nm are characteristic of the d_1 -heme. The green spectrum corresponds to the c-ox/ d_1 -ox state, the yellow spectrum corresponds to the c-red/ d_1 -ox state, and the red spectrum corresponds to the c-red/ d_1 -red state.

This result can be interpreted in the following way: as long as the d_1 -heme is oxidised, the enzyme needs to prevent binding of the substrate because this would result in a catalytically incompetent complex [1]. It is only once the d_1 -heme has been reduced that nitrite is allowed to bind. Therefore the structural changes that occur in the fully reduced enzyme, and that relax steric hindrance around the Fe of the d_1 heme, must take place after reduction of the latter.

References

- [1] N. Nurizzo, M.C. Silvestrini, M. Mathieu, F. Cutruzzola, D. Bourgeois, V. Fülöp, J. Hajdu, M. Brunori, M. Tegoni, C. Cambillau, *Structure*, **5**, 1157-1171 (1997).
- [2] D. Bourgeois, *Acta Cryst. D.*, **D55**, 1733-1741 (1999).
- [3] N. Nurizzo, F. Cutruzzola, M. Arese, D. Bourgeois, M. Brunori, C. Cambillau, M. Tegoni, *J. Biol. Chem.*, **274-21**, 14997-15004 (1999).

Principal Publication and Authors

N. Nurizzo (a), F. Cutruzzola (b), M. Arese (b), D. Bourgeois (c), M. Brunori (b), C. Cambillau (a), M. Tegoni (a), *J. Biol. Chem.*, **274-21**, 14997-15004 (1999).

(a) CNRS, AFMB Laboratoire, Marseille (France)

(b) La Sapienza University, Rome (Italy)

(c) IBS/ESRF

The Medical Beamline - ID17

Bronchography Studies in Rabbits Using Xenon K-edge Imaging

Radiography of lungs was one of the first applications of X-rays in medicine. With conventional radiography it is not possible to see the airways whereas with computed tomography (CT), the images may reveal morphological abnormalities. This has made CT the principal method for preoperative staging of lung cancer. For imaging the airways in studies of lung function, shorter acquisition times as well as better spatial resolution and contrast are needed.

K-edge subtraction (KES) radiography and CT by synchrotron radiation, using stable Xe gas as the contrast agent, have addressed most of the problems of lung imaging by X-rays. The method is an extension of the ID17 coronary angiography CT programs [1], where KES is used with iodine or gadolinium as contrast agents. K-edge subtraction allows quantitative measurements of indicator (Xe) concentrations, whereas traditional CT or MRI do not. Imaging of the airways of the lungs by KES using Xe gas has been demonstrated earlier [2]. The present work aims at functional imaging of rabbit lungs in vivo as the first stage in the program development.

The goal is to see the morphological details of the bronchial tree and filling of alveoli during the breathing cycle with Xe in the airways. The distribution of Xe is observed in a series

of KES images taken using two X-ray energies bracketing the Xe K-edge at 34.56 keV. The animal moves vertically through the 0.7 mm high fan beams, and an 80 x 120 mm image is acquired line by line with 1.3 ms sampling time of the dual-array Ge detector. The imaging sequence requires computer control of the breathing cycle and administration of the gas mixture. At the same time, physiological parameters such as heart rate, CO₂ level in the lungs, and tracheal pressure are monitored.

Anaesthetised rabbits were imaged in both the radiography and CT modes. The animals were imaged in the vertical position, fixed on a rotation stage on the angiography/CT chair. The inspiration phase could either be a mixture of air and oxygen or oxygen and xenon. Images were obtained during various sequences of inspiration, rest and expiration. In these initial experiments, the imaging was not gated by the breathing or cardiac cycle.

When the alveoli were filling, the view of the bronchial tree became obstructed in the radiographs. This will generally be true for radiographs. However, a high-resolution CT image of the 2-dimensional cross section of the animal can be obtained by tomographic reconstruction. In the present case the animal is rotated about an axis perpendicular to the plane defined by the beam. Typically, the full rotation takes 1 to 2 seconds, and about 1000 projections are acquired during the rotation with 1 ms sampling time. The distribution of Xe is reconstructed from the difference of the sinograms corresponding to the two energies.

Figure 21 demonstrates that, with correct timing, the entire bronchial tree may be imaged by radiographic projection.

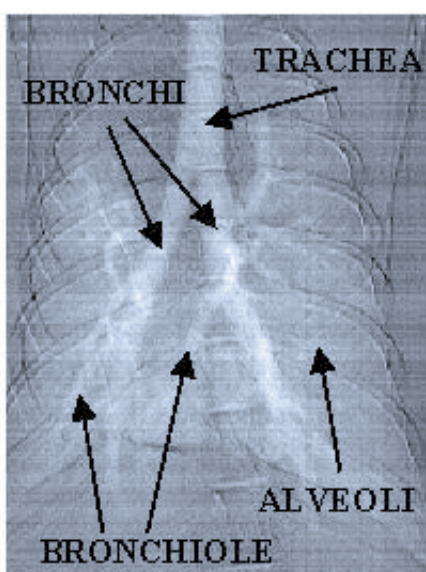


Fig. 21: *In vivo* digital subtraction image of rabbit lungs showing the distribution of the contrast agent of stable Xe in the bronchial tree.

The first bifurcation of the bronchial tree, as well as smaller bronchioles, is clearly seen along with the initial filling of alveoli. When the alveoli are filled, the details of lung structure are seen only in CT images. An example is shown in Figure 22. It corresponds to a transverse section in the upper part of the rabbit lungs. Absolute concentration of Xe can be calculated from the images, which is important for lung function studies.

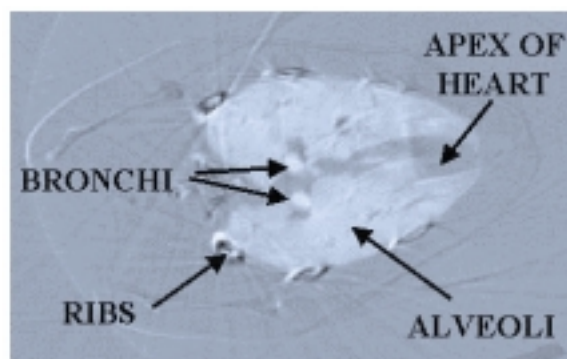


Fig. 22: *CT image of the distribution of Xe in a transversal section of rabbit lungs.*

The work was done in close collaboration between the ESRF staff, and teams working at the Medical Faculty of the Grenoble University and at the Central Hospital and the Department of Physics of the University of Helsinki.

References

- [1] H. Elleaume, A.M. Charvet, P. Berkvens, G. Berruyer, T. Brochard, Y. Dabin, M. C. Dominguez, A. Draperi, S. Fiedler, G. Goujon, G. Le Duc, M. Mattenet, C. Nemoz, M. Perez, M. Renier, C. Schulze, P. Spanne, P. Suortti, W. Thomlinson, F. Esteve, B. Bertrand, J.F. Le Bas, Nucl. Instr. and Meth., **A 428**, 513 (1999).
- [2] J. Giacomini, H. Gordon, R. O'Neil, A. VanKessel, B. Cason, D. Chapman, W. Lavender, N. Gmür, R. Menk, W. Thomlinson, Z. Zhong, E. Rubenstein, Nucl. Instr. Meth., **A 406**, 473 (1998).

Authors

G. Le Duc (a), S. Bayat (b), F. Grimbert (b), S. Fiedler (a), C. Nemoz (a), W. Thomlinson (a), L. Porra (c), P. Suortti (c), C-G. Standertskjöld-Nordenstam (c), A.R.A. Sovijärvi (c).
 (a) ESRF
 (b) University of Grenoble (France)
 (c) University of Helsinki (Finland)

Cerebral Blood Volume Measurements in Bolus Method with Synchrotron Radiation Computed Tomography

X-ray Computed Tomography (CT) and Magnetic Resonance Imaging (MRI) coupled to the injection of contrast agents are now common tools for imaging of the human body. Other techniques such as Ultra Sound imaging and Nuclear Medicine are also widely used despite a lower spatial resolution. Nowadays, efforts are aimed at extending the usefulness of these techniques beyond anatomic mapping to obtain functional information. Assessment of this information, i.e. physio-pathological parameters, is a key issue for the prediction of the evolution of a given pathology and for guidance in therapeutic choices. In this context, the Synchrotron Radiation Computed Tomography (SRCT) technique available on **ID17** appears as a complementary approach to MRI and CT to obtain quantitative information about physio-pathology. In particular, the technique is based on the subtraction of two images taken above the K edge of a particular contrast agent such as iodine (33.169 keV) or gadolinium (50.239 keV) before and after the injection of the contrast agent. The logarithmic subtraction of these two measurements leads to a precise quantification of the contrast agent in the tissue, i.e. to a fingerprint of the physio-pathology [1,2].

Brain circulation parameters have been widely studied to improve the understanding of various pathological states such as ischemia and tumour development. It is a well-known feature that vasculature is highly involved in the tumour growth mechanism. The purpose of these new experiments was to design a protocol enabling the measurement of two parameters derivable from the vascular function; the cerebral blood volume (CBV) and the cerebral blood flow (CBF). An anaesthetised rat bearing a C6 glioma was installed on a rotating stereotactic frame (1 turn in 2 sec) allowing computerised tomography attenuation profiles to be acquired continuously over a 34 second period. Each pixel of the CT images corresponds to a 0.043 mm³ cube of brain tissue. After a delay of two turns, a bolus of iodine based contrast agent was infused using a remote controlled injector (0.1 ml of a 350 mg/ml iodine solution). The image obtained before the bolus infusion was subtracted from the following images to obtain CT maps of the absolute iodine concentration with an initial temporal resolution equal to 2 sec. Nevertheless, reconstruction of images starting each 0.5 sec. led to an over-sampling of the iodine concentration curves. These curves provided the evolution of the absolute contrast agent concentration inside the rat brain. The observed curves were fitted with gamma functions. When choosing any arterial input, the CBV percentage in any given voxel of the

slice is equal to the ratio of the time integral of the fitted concentration curves (voxel observed / arterial input) [3], see [Figure 23](#). Deriving the cerebral flow is theoretically possible provided the two following conditions are verified; reproducibility and linearity in terms of the vascular response to the bolus infusion (work in progress).

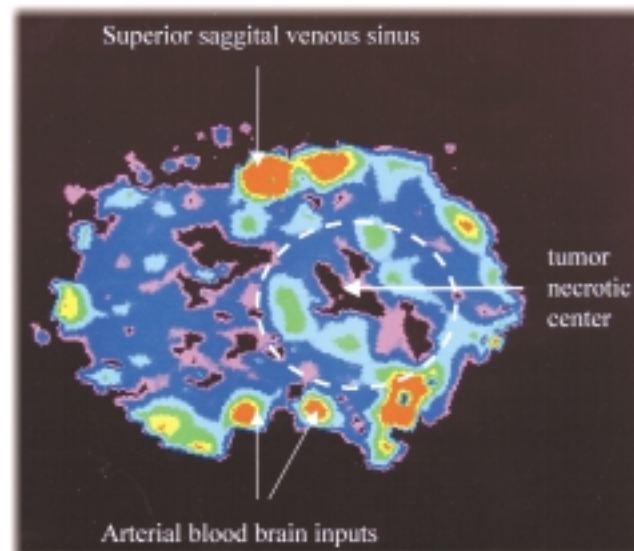


Fig. 23: Cerebral blood volume of a rat brain bearing a C6 glioma (axial orientation) obtained after a bolus infusion of 0.1 ml iodine based contrast agent (350 mg/ml). Slice thickness 0.35 mm, pixel size 0.35 x 0.35 mm², slice level 9 mm above the line between the external auditive meatus. Colour table from red to black (100%, 0% respectively). High vascular density is visible surrounding the necrotic centre of the tumour.

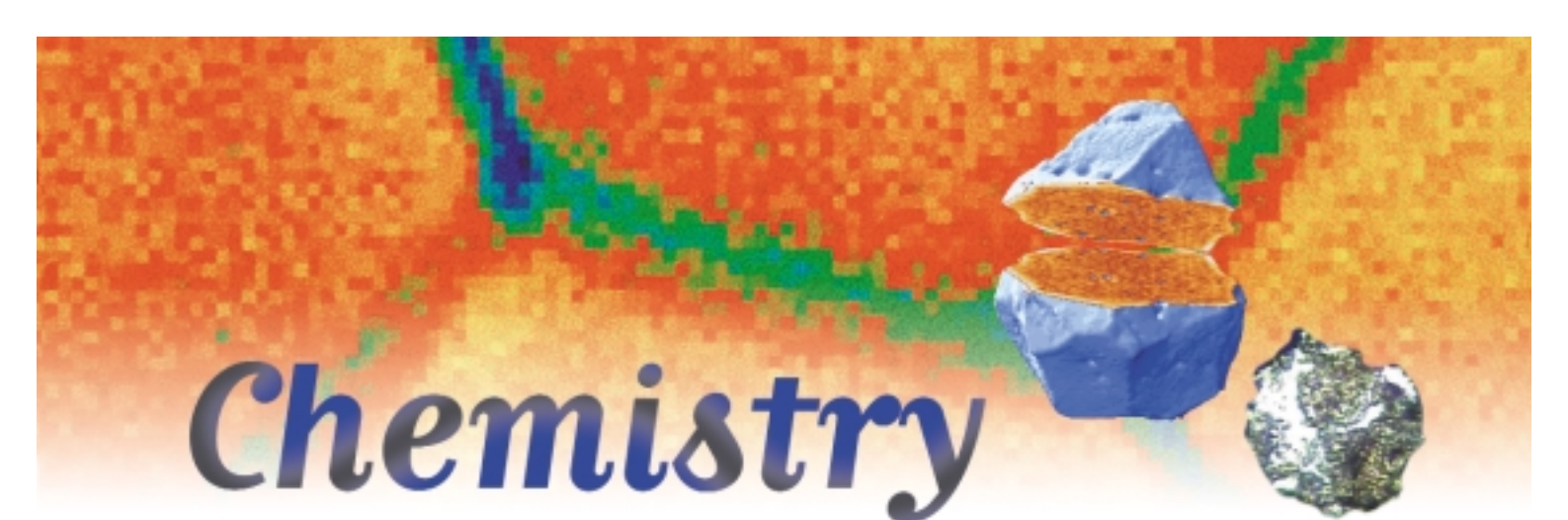
These studies will contribute towards the design of tools to observe vasculature changes in brain tumours.

References

- [1] H. Elleaume, A.M. Charvet, G. Le Duc, F. Estève, B. Bertrand, S. Corde, R. Farion, J.L. Lefaix, J.J. Leplat, P. Berkvens, G. Berruyer, T. Brochard, Y. Dabin, A. Draperi, S. Fiedler, C. Nemoz, M. Perez, M. Renier, P. Suortti, W. Thomlinson, J.F. Le Bas, *Cell. Mol. Biol.*, (2000) in press.
- [2] G. Le Duc, A.M. Charvet, H. Elleaume, F. Estève, S. Corde, S. Fiedler, A. Collomb, J.F. Le Bas, *European Radiology*, (2000) in press.
- [3] N.A. Lassen, W. Perl, *Tracers Kinetics Methods in Medical Physiology*, Raven Press, New York, (1979).

Authors

J.F. Adam, H. Elleaume, G. Le Duc, S. Corde, A-M. Charvet, J.F. Le Bas, F. Estève.
Equipe d'accueil "Rayonnement Synchrotron et Recherche Médicale", Unité IRM, CHU Grenoble (France).



Chemistry

Introduction

Chemists have often been considered as the “Cinderellas” of the synchrotron radiation user community, but it is now quite clear that not only are they coming to the “ball”, they also stay on long after midnight to pursue exciting and innovative science - without any adverse effects! The community is beginning to realise the full potential of synchrotron radiation and the pressure on beam time and support facilities continues to increase.

The Highlights selected for this section illustrate the wide range of opportunities that exists in the various fields of Chemistry. The first involves powder diffraction which was, until a few years ago, a technique considered mundane and restricted in application, for example, to the identification of compounds using a fingerprint technique. However, with the advent of high resolution powder patterns produced using synchrotron radiation (and neutrons), and the development of new refinement methods, powder diffraction is being increasingly used as an *ab initio* method of structure analysis. Applications of the technique are described to solve the structures of important catalysts and drug related molecules. The second opportunity concentrates on using microbeams to examine very small samples or small portions of a larger sample. The application of the μ X-ray Absorption Tomography and μ -XANES (X-ray Absorption Near Edge Spectroscopy) techniques, to characterise fuel particles released during a nuclear accident, is described. Finally, opportunities are described for studying photosensitive molecules with a picosecond time resolution. It is to be expected that time-resolved studies, on very short timescales and on longer timescales up to a millisecond, will play an increasing role in the field of Chemistry.

A number of Highlights demonstrate, once again, the wide range of applications and versatility of the XAFS (X-ray Absorption Fine Structure) spectroscopic technique. The following highlights then describe an application of high pressure techniques and a diffraction study of the deposition of fullerenes onto a gold (110) surface, and amply illustrate the varied range of applications of synchrotron radiation in Chemistry.

High-Throughput Crystal Structure Solution from Powder Diffraction Data

Routine organic crystal structure determination from powder diffraction data alone is an important goal for both the chemical industry and chemists in general. Recent developments in global optimisation methods, coupled with innovative processing of powder diffraction data, have made this goal realisable in an increasing number of cases. The global optimisation methods rely upon one having an isolated molecular description of the compound under study. Once the unit cell and space group have been determined, trial crystal structures can be postulated and optimised using a technique such as simulated annealing to give the best agreement between the measured and calculated diffraction data.

With organic compounds, it is often the case that the chemist is interested mainly in the packing and conformation of the molecule under study. In these circumstances, it is normally sufficient to solve the crystal structure to limited (perhaps 1.5 - 2.0 Å) resolution. In contrast to direct methods, global optimisation methods have little problem coping with this relatively low resolution, as prior information in the form of known molecular connectivity has already been imposed. With this low resolution comes the possibility of rapid data collection and thus the possibility of high-throughput powder diffraction structure solution.

In a set of powder diffraction experiments performed over a period of 9 shifts on beamline **BM16**, data for structure solution and refinement were collected from a series of organic and organometallic compounds. Data were typically collected to ca. 1.1 Å using an optimised count time scheme in which only about 3 hours of data were collected per sample. Where appropriate, the samples were also cooled to around 130 K using a Cryostream in order to improve the diffracted intensities at higher angles. By processing each data set whilst the next sample was being mounted and collected, six crystal structures were solved during the duration of the experiment; specifically, the anti-ulcer drug famotidine (forms A and B), the anti-convulsant remacemide (and its nitrate and acetate salts), and a palladium organometallic catalyst (Figure 24). Famotidine is an excellent example of a high-value pharmaceutical compound that exhibits polymorphism; whilst the form A structure was known from a single crystal study, the crystal structure of Form B was unknown. None of the remacemide structures were known, the salt forms being typical of ones evaluated in the early stages of drug development by way of improving aqueous solubility and

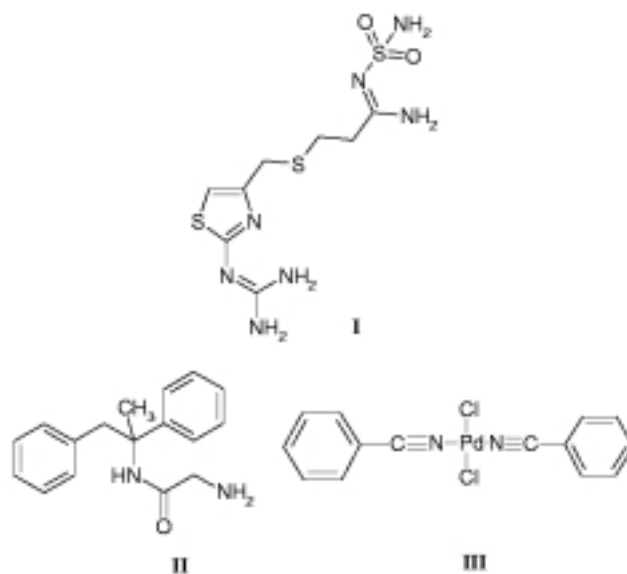


Fig. 24: The chemical structures of (I) famotidine, (II) remacemide and (III) the palladium organometallic compound.

dissolution. The actual structure solutions were obtained using data to typically ca. 1.5 Å resolution, with subsequent constrained Rietveld refinements carried out on the full range of collected data. Taking due account of the count time scheme, the important conclusion is that each structure was solved from less than one hour of diffraction data. Five more samples were successfully indexed and their structures are currently being analysed.

By matching data collection and analysis strategies to the capabilities of the powder diffractometer on BM16, the expectations of what can be achieved in terms of crystal structure solution from powder diffraction data during a period of synchrotron beam time have been redefined. Whilst powder diffraction cannot, as yet, be considered to be as straightforward as single-crystal diffraction for structure solution purposes, it need no longer be considered a method of last resort.

Principal Publications and Authors

K. Shankland (a), W.I.F. David (a), T. Csoka (a), Z. Krist, **212**, 550-552 (1997).

W.I.F. David, K. Shankland and N. Shankland (b), *Chem. Commun.*, **931** (1998).

(a) ISIS Facility, Rutherford Appleton Laboratory (UK)

(b) Department of Pharmaceutical Sciences, University of Strathclyde (UK)

μ -X-ray Absorption Tomography and μ -XANES for Characterisation of Fuel Particles

During the Chernobyl accident about 6-8 tonnes of uranium fuel were released and fuel particles were identified up to 2000 km from the site (e.g. Norway). During the initial explosion mechanical destruction of fuel occurred and fuel particles were deposited to the West of the reactor. During the subsequent reactor core fire, however, fuel particles were also deposited to the North. To assess the long term consequences, information on source and release dependent characteristics of the particles is needed. Thus, microscopic X-ray techniques such as μ -X-ray absorption tomography, μ -X-ray absorption near edge spectroscopy (μ -XANES) and μ -X-ray diffraction (μ -XRD) have been employed at beamline ID22. A combination of these techniques enables the determination of the uranium distribution, crystallographic structure and oxidation states, characteristics essential for understanding weathering and subsequent mobilisation of associated radionuclides.

Computed μ -tomography data collection and reconstruction techniques have provided 3-D images of uranium within individual particles, characterised by gamma spectrometry and SEM [1]. During rotation, images were recorded at 17 keV with a high resolution, cooled CCD-based X-ray detector. Due to the high coherence of the beam, image contrast is improved compared to pure absorption as the phase contrast caused by the phase shift of the plane incoming wave at edges or interfaces invokes a different increment of the refractive index.

Tomographic reconstruction (Figure 25a) and computerised slicing (Figure 25b) of the 3-D image demonstrated inhomogeneous distribution of U within the particles. Channels and cavities are probably caused by formation of volatile fission products during reactor operations.

Differences in U-oxidation states are manifested by shifts in pre-edge and bound-state edge features in μ -XANES spectra due to an increase in the binding energy of the core electron levels. Well-defined standards: U-metal (oxidation state 0), UO_2 (+4), U_3O_8 (i.e. $\text{UO}_2 \cdot 2\text{UO}_3$), and UO_2Ac_2 (+6) were used for calibration. Metallic U and UO_2Ac_2 served as the oxidation state scale endpoints. The μ -XANES spectra were obtained at 0.8 eV increments over a 160 eV energy range extending from about 40 eV below and 120 eV above the U L_{III} absorption edge at 17.163 keV. The μ -XANES spectra of the standards (Figure 26a) reflected a shift of the inflection point energy (central location of edge positions) with oxidation state, a near-linear relationship, having a slope of about 1 eV/oxidation state unit (Figure 26b).

μ -XANES spectra of particles collected at the Chernobyl North region were close to the standard U_3O_8 spectra. The inflection point energies corresponded to oxidation state 5.0 ± 0.5 (Figure 26b), in agreement with $\text{U}_2\text{O}_5/\text{U}_3\text{O}_8$. Using line scan XANES, particles released during the reactor fire were characterised by UO_2 cores surrounded by $\text{U}_2\text{O}_5/\text{U}_3\text{O}_8$ layers (Figure 26c). Surprisingly, μ -XANES spectra of West particles (Figure 26b) occurred as an intermediate between metallic U and UO_2 with inflection point energies corresponding to the oxidation state 2.5 ± 0.5 . This finding is both novel and surprising. Using line scan XANES, particles released during the initial explosion were

characterised by a UO_2 core surrounded by a layer of reduced U, probably due to interactions with graphite from the damaged moderator. Although the presence of UC_2 and UO was indicated by μ -XRD, further analysis is needed to establish the phases. Although UO_2 fuel is the common source, particle characteristics such as oxidation states depend on the release scenario (explosion or fire). The differences in oxidation states of uranium in fuel particles explain

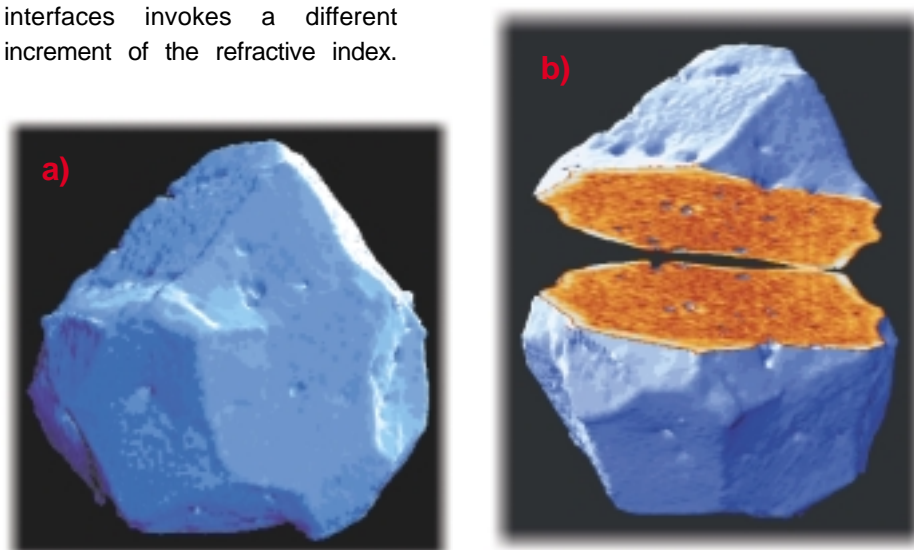


Fig. 25: a) μ -XAS-tomography of a U fuel particle collected from Chernobyl soil, mounted on a glass capillary. The image shows a 3-D rendering of 500 tomographic slices of the particle. Each projection image consisted of 1024×1024 pixels and required 10 seconds exposure time. b) By opening a computerised data block, the inner structure cavities and channels reflect the formation of volatile fission products during reactor operations.

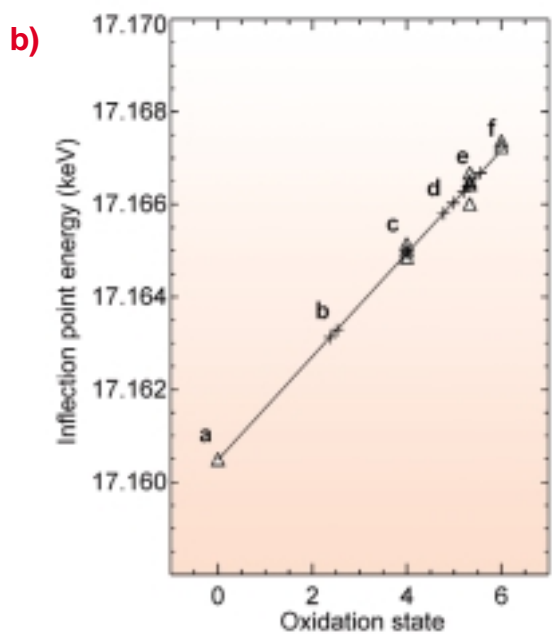
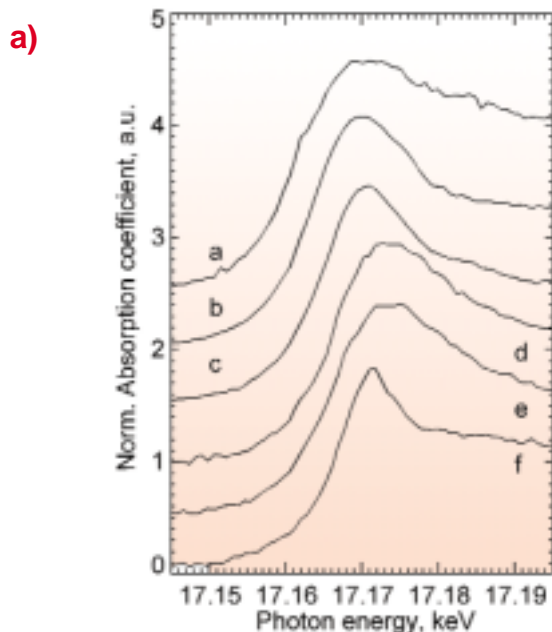


Fig. 26: Oxidation states of U.

a) μ -XANES analysis of U-standards and Chernobyl particles (a: metallic U, b: Chernobyl West particle, c: UO_2 , d: Chernobyl North, e: U_3O_8 , f: UO_2Ac_2).

b) Inflection point energy versus oxidation states of uranium in the analysed particles. The inflection point energies of the Chernobyl West particles show the oxidation state $+2.5 \pm 0.5$, while for particles collected to the North of the reactor the oxidation state was $+5 \pm 0.5$.

c) XANES line scan of Chernobyl West particle having reduced core and oxidised surface layer.

well the observed differences in weathering kinetics, mobility and soil-to-vegetation transfer coefficients of particle associated radionuclides West and North of the reactor.

Reference

[1] B. Salbu, T. Krekling, D.H. Oughton, *Analyst*, **123**, 843-849, 1998.

Authors

B. Salbu (a), K. Janssens (b), T. Krekling (a), A. Simionovici (c), M. Drakopoulos (c), C. Raven (c), I. Snigireva (c), A. Snigirev (c), O.C. Lind (a), D.H. Oughton (a), F. Adams (b), V.A. Kashparov (d).

(a) Department of Chemistry and Biotechnology, Agricultural University of Norway, Aas (Norway)

(b) Department of Chemistry, University of Antwerp (Belgium)

(c) ESRF

(d) Ukrainian Institute of Agricultural Radiology, Kiev (Ukraine)

Picosecond Structures of Photosensitive Molecules Using Pulsed Synchrotron Radiation

For many years chemists (and biologists) have dreamt about recording the atomic positions of reacting molecules in real time in order to understand the formation of new molecules. Indeed the 1999 Nobel Prize in Chemistry was awarded to Ahmed Zewail from Caltech, who used femtosecond optical spectroscopy to study the formation (and breakage) of chemical bonds in gas molecules. These studies have shown that bond formation happens in 10 to 100 fs, a factor of 1000 faster than the duration of the X-ray pulse from a synchrotron. In these experiments, a molecular beam is excited by a femtosecond pulse and the

reaction products are probed by a delayed probe pulse derived from the pump beam. Once the reaction products are formed, they usually proceed to the final state through a sequence of intermediates. The lifetimes of these intermediates can vary from 1 ps to 1 ms.

On beamline **ID9** a pump & probe setup has been built which uses single pulses of X-rays combined with optical pulses from a femtosecond laser. It is a very flexible system which has enabled picosecond intermediates to be studied using Laue diffraction, oscillation diffractometry, powder diffraction and diffuse scattering techniques. Despite the synchrotron pulses being 1000 times longer than the laser pulses used by Zewail, X-rays are attractive since they probe interatomic distances directly. Moreover in those cases where the reacting species can be held in a crystal, diffraction techniques make it possible to record three-dimensional movies of atomic motion of all the atoms in the unit cell.

Recently the ID9 team has studied electron transfer reactions in chemical systems. Powder samples of organic compounds comprising linked donor- and acceptors units (PyDMA, DMABN) have been studied and the difference maps between the excited and non-excited states have shown the presence of large-amplitude motions on the picosecond timescale. Specifically, the angle between the planar donor and acceptor units in PyDMA and DMABA rotates 8 degrees in less than 200 ps. These systems relax back into the ground state after 3 - 4 ns, which makes it possible to repeat and accumulate the data stroboscopically.

The trans to cis isomerisation of the stilbene molecule has also been studied. This system is best characterised as a molecular hinge which rotates upon the absorption of a photon. The molecule consists of two benzene rings which are linked via an ethylene double bond, see **Figure 27**. In the planar ground state 1, the two benzene rings are positioned on the same side of the double bond. The system is excited by a 150 fs pulse, which brings the ethylene bond into an anti-bonding state 2. The molecule responds by rotating one of the benzene rings 90 degrees in 3 ps. The new orthogonal state 3, decays then in 20 to 120 ps into either the original trans state 1 or to the cis state 4. The time it takes to decay is a function of the specific stilbene derivative and the friction from the surrounding solvent. Note that the benzene rings are rotated 20 degrees in the cis state 4. In these experiment the stilbene molecule was dissolved in methanol and exposed to the laser/X-ray pump & probe beam. In practice a UV pulse initiates the reaction and a delayed X-ray pulse is used to record the diffuse scattering from the dilute sample. The pump and probe sequence is repeated at 900 Hz and the data accumulated on a CCD camera. The experiment is finally

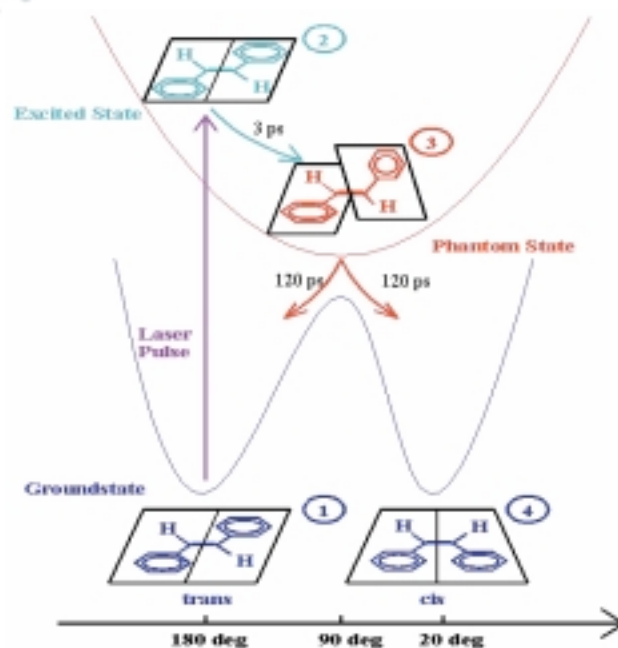


Fig. 27: The structure of the stilbene molecule during its photocycle. The potential energy curve as a function of rotation angle is also shown.

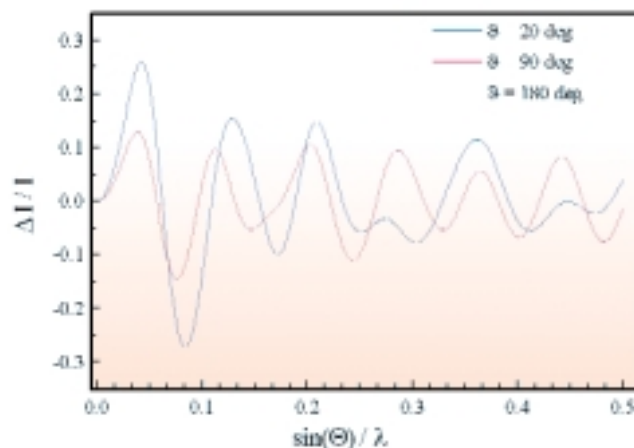


Fig. 28: Calculated change in the diffuse scattering in going to the ghost state at 90 degrees and the trans-conformation at 20 degrees. The excitation level is set to 30%. The calculations agreed qualitatively with the experiments.

repeated at several time points between -1 ns to $+1$ ns. The measurements have shown that it is possible to isolate the weak stilbene signal (ca 1%) and that the difference patterns are in qualitative agreements with expectations from laser spectroscopy. **Figure 28** shows the calculated change in the diffuse intensity between the trans, cis and orthogonal states.

Authors

S. Techert, F. Schotte, M. Wulff.
ESRF

X-ray Absorption Spectroscopy

Catalysis

In situ Time-resolved EXAFS of Surface Organometallic Sites

Heterogeneous catalysts are frequently used in the chemical industry and form the bedrock of environmental clean-up processes. The ease of separation of the solid phase catalyst from the gaseous or liquid reagents and products is the key advantage of these materials. However, such catalysts generally consist of a dispersion of metal particles supported on a disordered oxide surface with a high area. This combination of disorder and site dispersion obscures the fundamental chemistry of catalyst formation and operation.

EXAFS is one of a few techniques which can provide direct structural information on such materials under reaction conditions. The development of Energy Dispersive EXAFS on **ID24** provides a way of acquiring analysable EXAFS data on sub-second timescales even on dilute materials (ca 3% metal) within a tubular reactor. The Laue monochromator allows high resolution spectra to be obtained over a substantial k range for the Rh K-edge. By combining in situ EXAFS with diffuse reflectance FTIR data, it has been shown that the complex $[\text{Rh}_2\text{Cl}_2(\text{CO})_4]$ reacts cleanly with high area (100 m²/g) alumina to form the surface site $[\text{Rh}(\text{CO})_2\text{Cl}(\text{O-Al})]$; multiple scattering analysis

of the EXAFS data confirms the presence of the two linear carbonyl groups on each rhodium. The selectivity of this surface reaction provides the opportunity of describing the reactivity of the surface organometallic centre at a molecular level.

The optics on ID24 with the Laue monochromator yield a focal spot of less than 0.1 mm in size, and this was focussed on a quartz tube micro-reactor fitted with gas mass-flow controllers and on-line multiple ion monitoring by a quadrupole mass spectrometer. This has been used to follow the process of metal particle formation under reactive and inert gases. Under hydrogen and a temperature ramp (5°/min), a rapid transformation into small metal particles was apparent at 330 K. Sintering of these clusters occurs at above 373 K, eventually leading at 673 K to large fcc particles with high local order. For the first time the formation and sintering of metal particles from mononuclear rhodium centres has been observed and found to be more rapid than normally thought.

Since rhodium is one of the components in the automotive exhaust catalyst, the reaction of $[\text{Rh}(\text{CO})_2\text{Cl}(\text{O-Al})]$ with NO is of some interest. On a hydroxylated surface of Al₂O₃ there is a rapid reaction at room temperature to form a mononitrosyl species. A stack plot of the Rh K-edge EDE spectra obtained during this reaction is shown in **Figure 29**. Concomitantly, the mass spectral data shows that CO evolution is rapid and the flow of NO achieves its limiting value once the evolution of CO is complete. Again, multiple scattering EXAFS analysis was required, this showing a surface co-ordination centre of $[\text{Rh}(\text{NO})\text{Cl}(\text{O-Al})_2]$. The Rh-N-O angle of ca 120° indicates a $\text{Rh}-(\text{NO})^-$ formulation. The second mass-time plot shows that the NO can be displaced by CO, albeit more slowly than the forward reaction. The in situ EDE data shows that the $[\text{Rh}(\text{CO})_2\text{Cl}(\text{O-Al})]$ centres are reformed. Hence, the molecular chemistry of such surface organometallic centres can be followed in real time.

Authors

D.G. Burnaby (a), A.J. Dent (b), J. Evans (a), T. Neisius (c), M.A. Newton (a).
 (a) University of Southampton (UK)
 (b) Daresbury Laboratory (UK)
 (c) ESRF

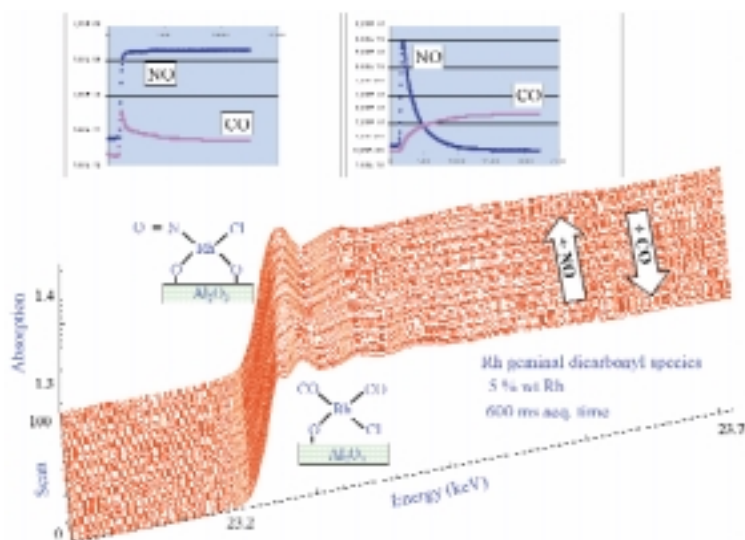


Fig. 29: Stack plot of the Rh K-edge EDE spectra obtained during the reaction of $[\text{Rh}(\text{CO})_2\text{Cl}(\text{O-Al})]$ with NO, with the mass spectral data in the insets.

Solutions

X-ray Absorption Spectroscopy Investigations of Metal-ammonia Solutions

Alkali metals dissolve freely in liquid ammonia, to yield conducting solutions - intensely blue and salt-like when dilute; bronze-gold and truly metallic when concentrated. In the transitional range between non-metallic and metallic, cooling the sample gives rise to a striking liquid-liquid separation of the two phases. Because of these novel electronic and thermodynamic properties, the solutions have been the subject of intense research effort, ever since their discovery by Sir Humphry Davy, in 1808 [1].

Recent research into metal-ammonia solutions has focussed on the transition from localised to itinerant electronic states, and the concomitant liquid-liquid phase separation. In fact, a number of electronic states have been proposed; isolated polarons, spin-paired bipolarons, excitonic atoms, metal anions, and delocalised electrons [1]. To determine which, if any, of these species are present at the various levels of dilution requires high-resolution structural studies of the solutions. In this context, X-ray absorption spectroscopy is an extremely powerful probe, since it can provide ion-centred local information, over the full range of concentrations. Rb-NH₃ solutions have been studied on **BM29** using the EXAFS technique to measure the fine structure above the Rb K-absorption edge, at photon energies of around 15.2 keV.

The Rb-NH₃ solutions were made in situ by condensing a known volume of anhydrous ammonia directly onto pre-weighed rubidium metal. The sample temperature was maintained close to the point at which phase separation was proposed, namely 206K at a concentration of 4 mole per cent metal [2]. By using an X-ray camera, we are able to observe directly the dissolution of the Rb into NH₃. The "live" X-ray images of our samples also provided the first direct evidence for liquid-liquid phase separation in Rb-NH₃, and enabled a view of the liquid-liquid interface itself.

A typical photograph of the equilibrated liquid-liquid interface is shown in **Figure 30**. Note that the concentrated bronze-gold phase is less dense than the dilute phase due to the volume occupied by the delocalised electrons. For this reason, bubbles of ammonia vapour form at the liquid-liquid interface, and are seen escaping from the dilute blue region. However, these bubbles do not break the meniscus of the gold phase.

In addition to providing the first image of this very unusual liquid-liquid interface, the data also show directly that phase

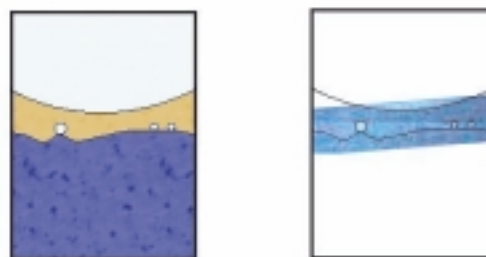


Fig. 30: Liquid-liquid interface as observed using the X-ray camera. This figure denotes a snapshot of the phase separation in dilute (blue) and concentrated (gold) phases solutions. For clarity, the coloured schematic (left) highlights the two phase region observed in the photograph opposite. The upper meniscus, liquid-liquid interface, and ammonia bubbles forming at the interface are shown. The width of the sample container is 1 cm.

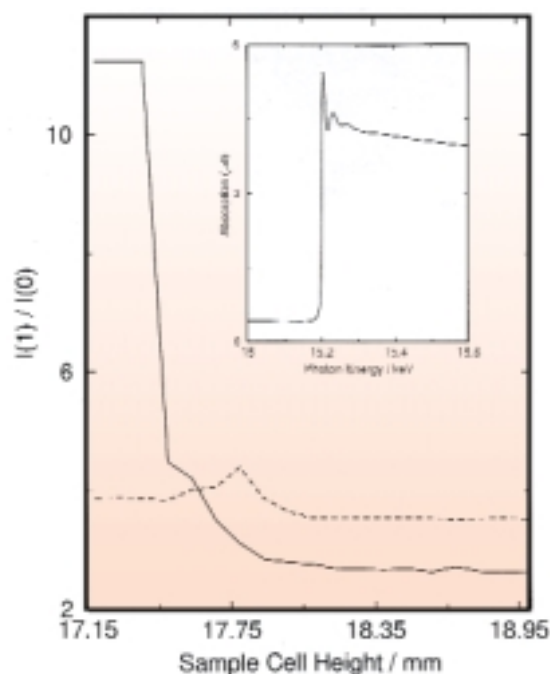


Fig. 31: The ratio of the transmitted to incident intensity through the two phase solution, shown in **Figure 30**, as a function of the height of the sample container relative to the X-ray beam. Data are presented for photon energies of 15.3 keV (above the Rb K- absorption edge; solid curve) and 15.1 keV (below the Rb K- absorption edge; broken curve). The inset shows the Rb-K edge absorption jump at 15.2 keV, and EXAFS signal, for the dilute phase.

separation does indeed occur in the Rb-NH₃ system [2,3]. This is confirmed by the data presented in **Figure 31**, in which the ratio of the transmitted to incident beam intensity, $I(1)/I(0)$, is plotted as a function of sample cell height. By moving the sample cell ~ 2 mm (from 17.15 to 18.95 mm) through the fixed energy X-ray beam, the change from a

metallic to a non-metallic liquid is identified by the change in the sample absorption on crossing the interface.

Within homogenous solutions, the EXAFS signal provides details of the Rb-centred structure. A well-defined solvation shell around Rb⁺ is observed, but with evidence of an increased cation-ammonia radius in the dilute phase. This is consistent with a weak tendency for solvated (localised) electrons to associate with a cation.

The aim of future work will be to obtain a better understanding of the microscopic structure and electronic species of the metallic and nonmetallic solutions, thereby allowing the mechanism(s) for the metal, non-metal transition to be elucidated.

References

- [1] P.P. Edwards, *Adv. Inorg. Chem.*, **25**, 135 (1982).
 [2] G. Lepoutre, J-P. Lelieur, "Properties of concentrated metal-ammonia solutions" in *Metal Ammonia Solutions*, J.J. Lagowski and M.J. Sienko eds., Butterworths, London, 272 (1970).
 [3] A.C. Sharp, R.L. Davies, J.A. Vanderhoff, E.W. LeMaster and J.C. Thompson, *Phys. Rev.*, **A 4**, 414 (1971).
 J.V. Acrivos, K. Hathaway, A. Robertson, A. Thompson and M.P. Klein, *J. Phys. Chem.*, **84**, 1206 (1980).

Authors

J.C. Wasse (a), S. Hayama (a), N.T. Skipper (a), D. Morrison (b), D.T. Bowron (c).
 (a) Dept. of Physics, University College London (UK)
 (b) Dept. of Chemistry, University College London (UK)
 (c) ESRF

Dilute Samples

Structural and Chemical Information at 1 ppm Levels

Generally for the EXAFS technique, if the absorber concentration is very low (< 100 ppm), its contribution to the total absorption of the sample becomes negligible. Simply monitoring the photon flux before and after the sample is not sufficient to provide information on the chemical environment of the absorber. An indirect method involving the measurement of the fluorescence from the absorber is required. Under these circumstances, the absorber contribution to the total absorption is proportional to the ratio of the absorber fluorescence and the incoming flux. This approach combines the sensitivity of X-ray fluorescence with the accurate short range structural and chemical information provided by X-ray absorption spectroscopy (XAS).

K-edge EXAFS measurements of transition elements at 25 ppm absorber concentration can be performed at several synchrotron radiation sources by using energy-dispersive solid-state fluorescence detectors. However, in order to obtain good statistics, acquisition times of 1 day or more are normally necessary. Beamline ID26 has already shown that with the flux and stability of third generation sources, appropriate detectors, and by using filters, energy resolution is not so important at that concentration level. Moreover the measurements can be performed with a timescale ranging from seconds to a couple of hours [1].

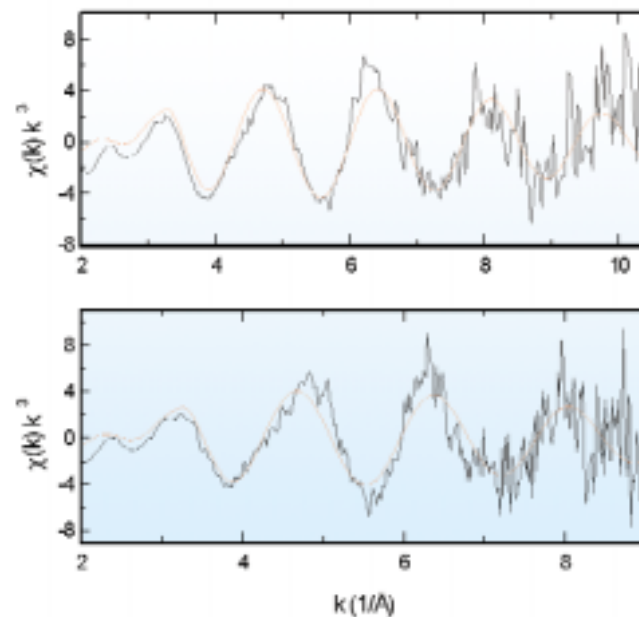


Fig. 32: Cu K-edge k^3 weighted EXAFS of 4.4 ppm Cu in 0.7 M NaHS solution at 9.5 pH (top) and of 1.2 ppm Cu in a 0.5 M NaHS solution at 7.4 pH (bottom).

Nevertheless, the ultimate detection limits can only be achieved by using energy-dispersive detectors. With a 12-element Silicon Drift Detector [2] and appropriate filters (6 absorption lengths of Ni), concentrations as low as 4.4 and 1.2 ppm of Cu (i.e. 69 and 19 μM) in hydrosulfide solutions have been measured at ID26. These concentrations were determined by inductively coupled plasma mass spectrometry (ICP-MS). Figure 32 reproduces the EXAFS data at both concentrations. The 4.4 ppm data set was acquired in about 12 hours elapsed time while the 1.2 ppm data set was acquired in about 8 hours elapsed time. With this remarkable performance ID26 is opening new possibilities in environmental and analytical sciences.

References

- [1] V.A. Solé, C. Gauthier, J. Goulon, F. Natali. *J. Synchrotron Rad.*, **6**, 174-175 (1999).
 [2] E. Moguiline, C. Gauthier, G. Goujon, J. Goulon, M.O.

Lampert, P. Dressler, R. Henck. J. Phys. IV France, 7, 339-340 (1997).

Principal Publication and Authors

J.F.W. Mosselmans (a), R.A.D. Patrick (b), J.M. Charnock (a,b) and V.A. Solé (c), Mineralogical Magazine, 63, 769-772 (1999).

(a) CCLRC Daresbury Laboratory (UK)

(b) Department of Earth Sciences, University of Manchester (UK)

(c) ESRF

XANES

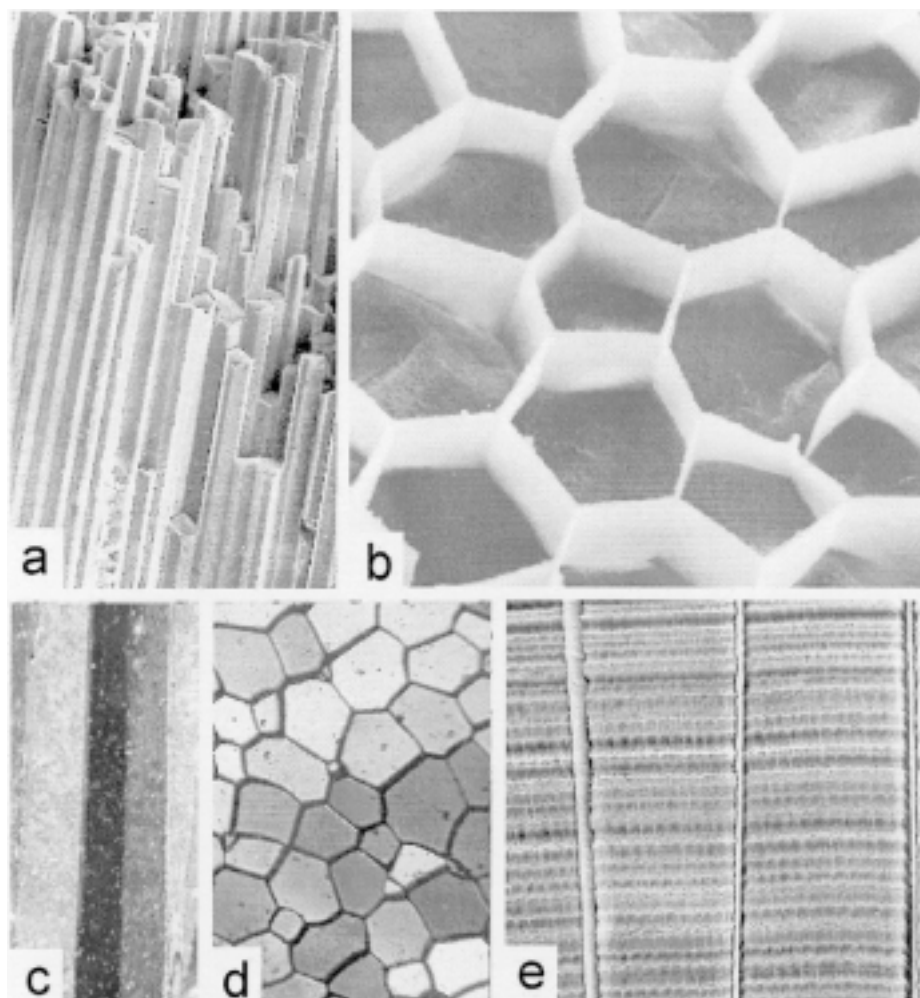
Mapping of Sulphur in Calcareous Mollusc Shells

Among biologically produced minerals, Ca-carbonate prismatic units of Mollusc shells epitomise the paradox of biocrystals. The long-standing recognition of their biologically controlled sizes and shapes has raised questions about the sequence of “molecular tectonic” events [1] that lead to formation of crystalline objects so

visibly growing apart from crystallographic rules. The modelling of biomineral growth, controlled from the nanometre to the millimetre scale, requires the understanding of the roles of the mineral and organic matrices and their interaction [2]. However, little information on the organic matrix is available, in particular no correlation has yet been established between its high sulphur content and the mineralising process. Sulphur can be found in both proteins and glucids, the two major organic compounds that compose organic matrices responsible for calcification in carbonate producing organisms [3]. Therefore, studying the chemical state of sulphur may be used as an indicator of the relationship between the mineralising matrices and the mineral ions.

A study was carried out on calcitic units that built the external layer of a Mollusc shell, the Pelecypod species *Pinna nobilis*, rather common in the Mediterranean Sea. These units appear as linear prisms, closely and very regularly packed side-by-side, of 50 to 75 micrometers in transverse sections and up to 3-4 millimetre in length (Figure 33). The prisms of *Pinna* offer remarkable advantages for the investigation of the organisation of biocrystals. They are the largest units that globally exhibit a single crystal like organisation, although they are typical

Fig. 33: (a) The studied mollusc shell appears as linear prisms, closely and very regularly packed side-by-side. (b) The upper level compartment, the organic template that surrounds mineral prisms, can easily be made visible after acidic etching. (c,d,e) Microscopic observation of thin sections (polarised light) allows the monocrystalline appearance of prisms to become evident.



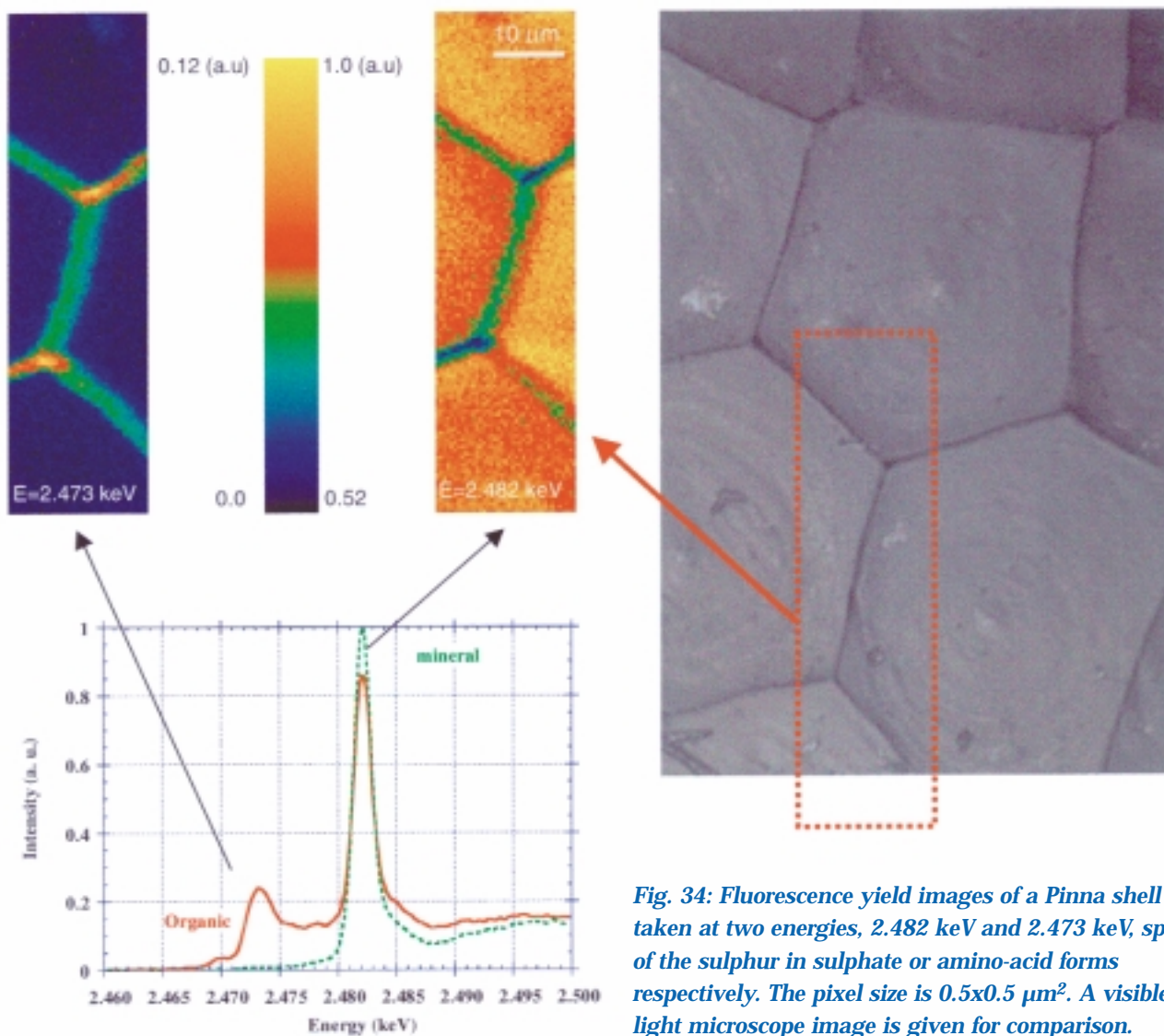


Fig. 34: Fluorescence yield images of a Pinna shell taken at two energies, 2.482 keV and 2.473 keV, specific of the sulphur in sulphate or amino-acid forms respectively. The pixel size is $0.5 \times 0.5 \mu\text{m}^2$. A visible light microscope image is given for comparison.

polyclinic structures. Chemically, they are characterised by the highest sulphur content ever observed, about 0.3 to 0.4%, a chemical feature that could be related to its exceptional crystallographic coherence. The experiment was carried out on **ID21** using the scanning X-ray microscope in fluorescence mode at the sulphur K-edge. The microscope used a Fresnel zone-plate as a focussing lens and delivered a microbeam of $0.25 \times 0.25 \mu\text{m}^2$. Sulphur speciation analysis was performed in both intra- and inter-prismatic unit matrices. Mapping of these composites at two energies revealed for the first time the existence of at least two different sulphur compounds in the matrices of *Pinna nobilis* (Figure 34). The spectra measured in the organic and mineral phases were compared with XANES spectra of pure standard products (cystin, cystein and chondroitin sulphate). These preliminary results indicate clearly the absence – or the very low concentration – of sulphidic crosslinks, the predominance of sulphate in the intra-prismatic matrix and the high concentration of “amino-acid” type sulphur in the

inter-prismatic matrix, in particular at the nodes of the hexagonal mesh of the matrix. Further analysis must be performed to clarify the exact role of the various sulphur compounds in this organic-inorganic interface, which drives the bio-mineralisation process.

References

- [1] S. Mann, *Nature*, **365**, 499 (1993).
- [2] S. Weiner, L. Addadi, *J. Mater. Chem.*, **7**(5), 689, (1997).
- [3] Y. Dauphin, J.P. Cuif, *Annales des Sciences Naturelles*, **2**, 73, (1999).

Authors

Y. Dauphin (a), M. Salomé (b), J. Susini (b), J. Doucet (c), J.P. Cuif (a).

(a) Geology-Paleontology Laboratory, CNRS, University Paris XI (France)

(b) ESRF

(c) LURE, University Paris XI (France)

Plutonium.

XAFS Measurements of Plutonium Hydrates

The first XAFS measurements of aqueous solutions containing Pu-242 were an important milestone for **BM20** (ROBL CRG beamline). Such measurements contribute toward a better understanding of the behaviour of actinide elements in the environment. The goal of these first measurements was twofold. Firstly, we wanted to demonstrate that all requirements were met for the preparation and transportation of plutonium solutions from the home institution in Germany to the ESRF and for the XAFS measurement of these samples at BM20. This should encourage others to do similar experiments with radioactive samples. Secondly, the hydrate is the simplest chemical form of plutonium in aqueous solution. The knowledge of the structural parameters of the hydration sphere is important for the interpretation of EXAFS results on complicated aqueous plutonium complexes or sorbates where the water molecules are partly or fully replaced by other ligands. In general, the number of hydrating water molecules depends on such factors as ionic radius and charge and ion concentration.

The Pu(VI) hydrate was prepared by dissolution of highly purified PuO₂ (Pu-242) and electrochemical oxidation. Part of this solution was reduced to Pu(III) in an electrochemical cell. The Pu(III) and Pu(VI) hydrates were in perchloric and nitric media (1 M acidic solutions), respectively. The final concentration of Pu was 0.05 mol/L. The Pu oxidation states were confirmed by UV/Vis spectroscopy. About 4.7 mL of solution (7.5 MBq) was filled and sealed in polyethylene cuvettes. The samples were shipped by special transportation from Forschungszentrum Rossendorf in Dresden, Germany to the ESRF. Forty-eight hours after their preparation, the Pu solutions were positioned for the XAFS measurements inside the glove box of the radiochemistry hutch at ROBL (see photograph). ROBL is the only experimental station at the ESRF and one of few stations worldwide that is dedicated to XAFS studies on solid and liquid radioactive samples with a maximal activity of 185 MBq. According to the safety requirements for a radiochemistry laboratory, the glove box is complemented by a safety system with separate ventilation, air filtering and air monitoring systems [1]. The Pu L_{III}-edge (18057 eV) XANES and EXAFS spectra were measured at room temperature in transmission mode using the Si(111) double-crystal monochromator and two Pt coated mirrors for rejection of higher harmonics.

As one can see from **Figure 35**, the L_{III} absorption edge of Pu(VI) is shifted by 4 eV toward higher energy as compared to that of Pu(III). The distinct XANES features of these two

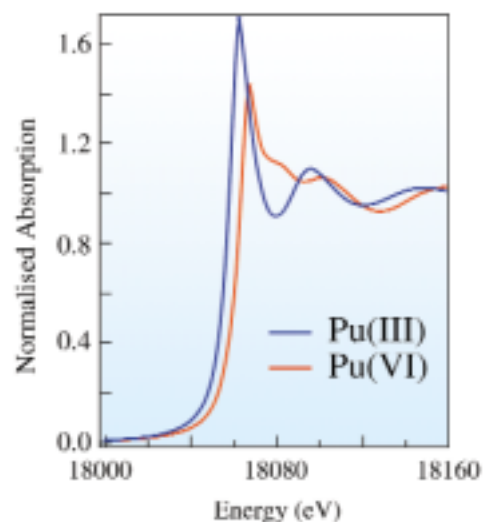


Fig. 35: Pu L_{III}-edge XANES spectra Pu(III) and Pu(VI) hydrates.

Pu hydrates have been modelled by a relativistic multiple-scattering calculation [2]. The different electronic and molecular structures of Pu(III) and Pu(VI) hydrates are also

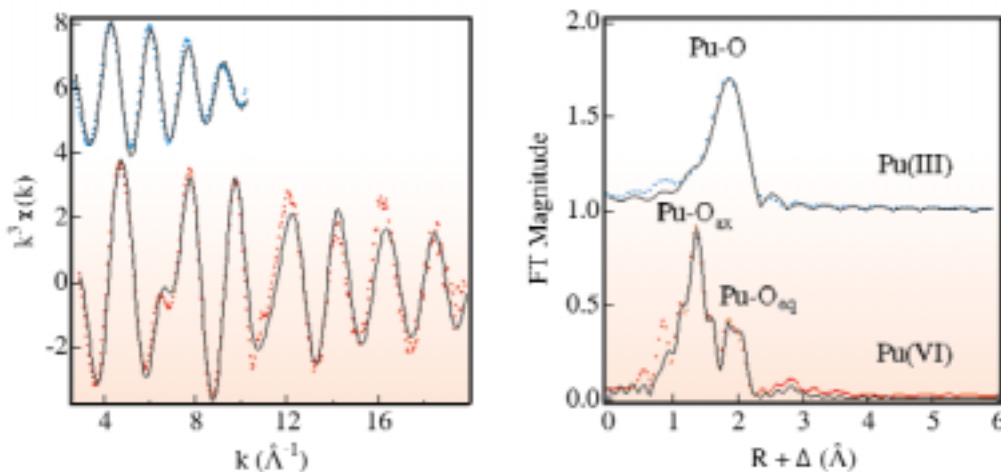


Fig. 36: Pu L_{III} -edge k^3 -weighted EXAFS spectra and their corresponding Fourier transforms of Pu(III) and Pu(VI) hydrates. Dots – experiment; solid line – fit.

reflected in the EXAFS shown in **Figure 36**. The coordination sphere of Pu(III) hydrate can be written as $\text{Pu}(\text{H}_2\text{O})_8^{3+}$ with an average Pu-O bond distance of 2.48 Å. The Fourier transform corresponding to the EXAFS of Pu(VI) hydrate shows two coordination shells. The Pu(VI) forms a plutonyl ion $\text{PuO}_2(\text{H}_2\text{O})_{4-5}^{2+}$. The axial and equatorial Pu-O bond distances are 1.74 and 2.42 Å, respectively. The structural parameters of Pu(VI) hydrate are nearly identical to those of U(VI) and Np(VI) hydrates, which were measured recently at BM20 [3]. Studies of other Pu oxidation states are in preparation.

References

- [1] W. Matz et al., *J. Synchrotron Rad.*, **6**, 1076 (1999).
 [2] A.L. Ankudinov et al., *Phys. Rev. B.*, **57**, 7518 (1998).
 [3] T. Reich et al., *Radiochim. Acta* (accepted for publication).

Authors

T. Reich, G. Geipel, H. Funke, C. Hennig, A. Rossberg, G. Bernhard. Forschungszentrum Rossendorf, Institute of Radiochemistry, Dresden (Germany)

Thin Films

EXAFS Determination of the Local Environment of Column III and V Elements in Amorphous Germanium Thin Films

Hydrogenated amorphous semiconductors are a class of materials with increasing applications in the photo-electronic industry. Among them, the hydrogenated amorphous germanium (a-Ge:H) is especially interesting, due to its narrow gap, for the production of infrared

sensitive devices. Most of the potential advantages, however, rely on the ability of controlling the electronic properties of the active semi-conducting layer by chemical doping. Such processes in an amorphous semiconductor are much less well understood than for the crystalline material due to the lack of atomic periodicity. To shed more light on this subject, careful preparation and characterisation of intrinsic and doped hydrogenated amorphous semiconductors is being undertaken by using various techniques, among which EXAFS plays a dominant role for its local order sensitivity.

Single doped hydrogenated amorphous germanium thin films were prepared with high dilutions extents ranging from $1.5 \cdot 10^{18}$ up to $4.5 \cdot 10^{20} \text{ cm}^{-3}$. The average thickness of the films was 3 μm with a number of doping atoms exposed to the X-ray beam (4 mm x 1.5 mm) of the order of $3 \cdot 10^{13}$ to $8 \cdot 10^{15}$. The K-edge of the doping elements (Ga, In, Sb) has been measured in fluorescence mode at **BM8** (GILDA CRG beamline): typical EXAFS signals are reported in **Figure 37**. Interesting results were obtained for the coordination number (N) and Debye-Waller (DW) factor. A general behaviour of N as a function of impurity concentration was found for all the dopant species, as shown in **Figure 38** (solid symbols). In general, the rising of concentration results in a lower coordination of the dopant atom. At the lowest concentrations, for Ga and In a four-fold coordination is apparent, while for Sb a slightly smaller value has been obtained. Values close to 2 were found for all the impurity atoms at the highest concentrations. The abrupt decrease in coordination doesn't follow the modified "8-N Mott's rule" model proposed by Street [1], which was achieved for P and B impurities in a-Si:H. In addition, only 1% of four-fold coordinated sites was found electrically active. Moreover, the comparison between conductivity and N shows only a partial agreement, which suggests that the conduction mechanism cannot be completely related to the substitutional doping.

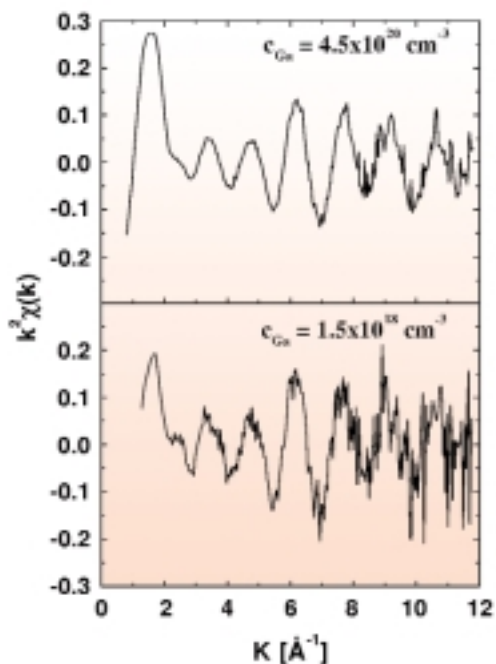


Fig. 37: k^2 -weighted spectra of two typical samples (Ga-doped a-Ge:H).

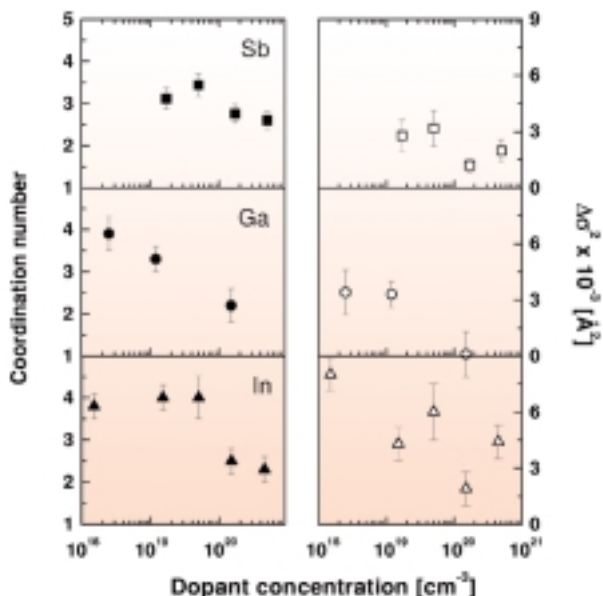


Fig. 38: Coordination number N (solid symbols), relative Debye-Waller factor (open symbols) for Ga, In, and Sb in a-Ge:H thin films.

For an estimation of the disorder induced by the doping process, the ratio method, based on the cumulant expansion, was used. By this procedure, it is possible to estimate the variation, with respect to a reference model, of the second cumulant, which is related to the overall

disorder of the sample under investigation. The outcome of previous investigations showed that hydrogen can reduce the effect of the doping-induced network stress by completing dangling bonds [2]. Surprisingly, the adding of chemical impurities reduces the disorder even more, as can be seen in Figure 38 (open symbols).

On the basis of these results, a new model has been proposed to explain the doping properties of group III metals in a-Ge:H. The proposed mechanism is not only related to the fraction of four-fold coordinated doping atoms, but it considers the effect on the coordination and electrical conductivity of the compressive stress induced by the atomic and ionic size differences between the germanium atom and the four-fold coordinated impurity. To verify the validity of these assumptions, further EXAFS measurements on heavier (Tl and Bi) and lighter (Al and P) acceptors and donors are planned in the near future.

References

- [1] R.A. Street, *Phys. Rev. Letters*, **49**, 1187 (1982).
- [2] G. Dalba, P. Fornasini, R. Grisenti, F. Rocca, I. Chambouleyron, C.F.O. Graeff, *J. Phys.: Condens. Matter*, **9**, 5875 (1997).

Principal Publications and Authors

G. Dalba (a), P. Fornasini (a), R. Grisenti (a), F. Rocca (b), D. Comedi (c), I. Chambouleyron (c), *Appl. Phys. Lett.*, **74**, 281 (1999).

I. Chambouleyron (c), D. Comedi (c), G. Dalba (a), P. Fornasini (a), R. Grisenti (a), F. Rocca (b), submitted to *Phys. Rev. Lett.*, (1999).

(a) Dipartimento di Fisica and INFM, Università di Trento (Italy)

(b) CeFSA - Centro CNR-ITC di Fisica degli Stati Aggregati, Trento (Italy)

(c) Instituto de Fisica Gleb Wataghin, Universidade Estadual de Campinas-UNICAMP, Campinas (Brasil)

High Pressure Studies: Superhard Polymeric Carbon Dioxide

The synthesis of polymeric carbon dioxide has long been of interest to many chemists and materials scientists. Very recently, the polymeric phase of carbon dioxide (called CO₂-V) at high pressures and temperatures was discovered [1]. This new material can be quenched to ambient temperature above 1 GPa. The vibration spectrum of CO₂-V is similar to that of SiO₂ polymorphs, indicating that it is an extended covalent solid with carbon-oxygen

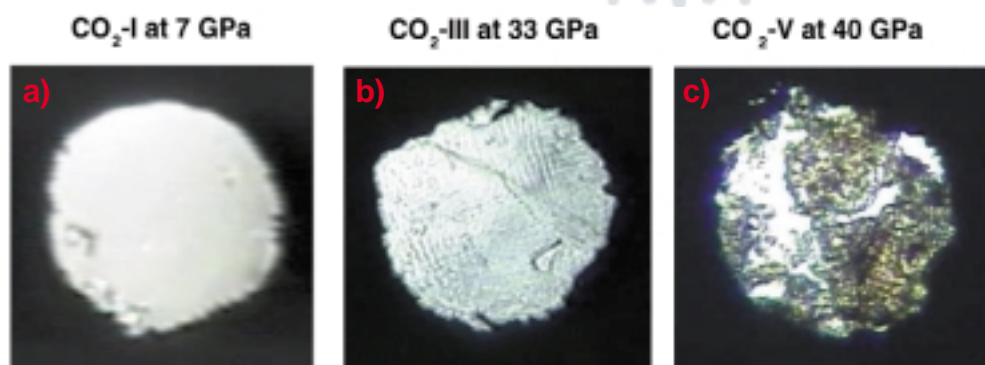


Fig. 39: Crystal phases of carbon dioxide:
(a) CO_2 -I,
(b) CO_2 -III, and
(c) polymeric CO_2 -V.

single bonds. It also exhibits a very interesting optical behaviour, generating the second harmonic of Nd:YLF laser at a wavelength of 527 nm with a conversion efficiency near 0.1%.

The determination of crystal structure of CO_2 -V has, however, been a challenge due to (i) the incomplete transformation resulting in a mixture phase of CO_2 -III and V, (ii) relatively low-Z materials, (iii) complex, low symmetry crystal structure, and (iv) a highly strained lattice with strongly preferred orientation. Despite these difficulties, the characterisation of the crystal structures of various CO_2 phases has been possible, including the polymeric phase by using an intense 10 μm -size focused monochromatic synchrotron X-ray beam and a fast scanning image-plate detector at ID30 at the ESRF [2].

Carbon dioxide crystallises to an optically isotropic cubic Pa3 structure, CO_2 -I at 1.5 GPa and ambient temperature (Figure 39a). Above 11 GPa, CO_2 -I transforms to the orthorhombic Cmc21 phase, CO_2 -III, which exists in a wide range of pressures above 70 GPa. The large quadrupole moment of linear CO_2 molecule is considered to stabilise both CO_2 -I and III at least at relatively low pressures. However, above 30 GPa, CO_2 -III develops a very characteristic texture indicative of a highly strained lattice (Figure 39b). It also shows an abnormally large pressure gradient exceeding 20% of the maximum pressure of the sample within 100 μm . These observations clearly indicate that CO_2 -III has high material strength at these pressures, which is rather unusual for a molecular crystal. In fact, it has been found that the bulk modulus of CO_2 -III is unusually high at 87 GPa, comparable to that of elemental silicon.

Above 35 GPa and 1800 K, highly strained CO_2 -III transforms into a new phase CO_2 -V that can be quenched at ambient temperature (Figure 39c). It clearly shows that the texture in the transformed area is distinct from that in a non-transformed area. In this study, the crystal structure of CO_2 -V has been found to be orthorhombic ($P2_12_12_1$), analogous to SiO_2 tridymite (a distorted high temperature

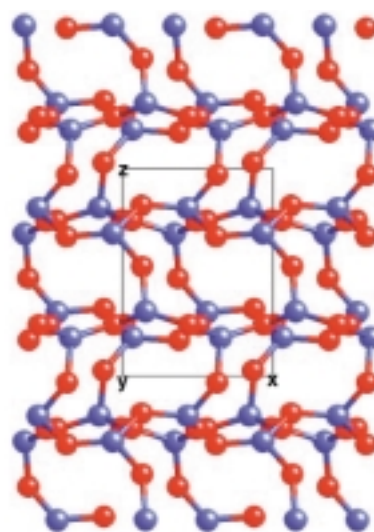


Fig. 40: An "ideal" crystal structure of CO_2 -V in $P2_12_12_1$ with 8 molecules per unit cells.

phase of β -quartz). Each carbon atom is bonded to four oxygen atoms at a carbon-oxygen distance of 1.36 \AA at 40 GPa and an O-C-O angle of 110° . These CO_4 tetrahedral units share their corner oxygen atoms to form a layered structure in the ab-plane; whereas, the apices of the tetrahedra are connected through oxygen atoms along the c-axis (Figure 40). This interconnected layer structure of tetrahedra results in a C-O-C angle of 130° , substantially smaller than those of SiO_2 tridymites 174 - 180° or of quartz 145° . Such rigidity in the C-O-C angles may reflect the fact that oxygen atoms in CO_2 -V are more tightly bound than in SiO_2 and result in a higher covalence and bulk modulus for CO_2 -V than for any of the SiO_2 polymorphs. In fact, we found that the bulk modulus of CO_2 -V is about 362 GPa, substantially higher than SiO_2 -quartz (37 GPa) and even stishovite (310 GPa). It is nearly the same value with cubic-BN (369 GPa) and thus could be a good candidate for a superhard polymer.

References

[1]. V. Iota, C. Yoo, H. Cynn, *Science*, **283**, 1510 (1999).

[2]. C.S. Yoo, H. Cynn, F. Gygi, G. Galli, M. Nicol, D. Häusermann, S. Carlson, C. Mailhot, *Phys. Rev. Lett.*, in print (1999).

Authors

C.S. Yoo (a), H. Cynn (a), F. Gygi (a), G. Galli (a), V. Iota (a), M. Nicol (b), S. Carlson (c), D. Häusermann (c), C. Mailhot (a).

(a) Lawrence Livermore National Laboratory, Livermore (USA)

(b) High Pressure Science Center at the University of Nevada (USA)

(c) ESRF

Study of $C_{60}/Au(110)$ $p(6 \times 5)$ Reconstruction from In-plane X-ray Diffraction Data

In recent years, much attention has been paid to the study of thin films of C_{60} , generally named fullerene, deposited on different substrates. C_{60} molecules interact via Van der Waals forces, forming a bulk fcc crystal structure at room temperature. Recent studies have also shown that the bond character of C_{60} with different substrates may vary widely from Van der Waals to strong ionic. As the electronic properties of C_{60} , including superconductivity, are strictly related to their charge state, the understanding of early film growth stages on different surfaces has both scientific and technological importance. The quantitative structural investigation of well ordered C_{60} monolayers (MLs) can enlighten the interaction mechanism of the fullerene molecules with the environment. Ordered C_{60} MLs can be grown on various surfaces and the charge state strongly depends on the type of substrate. In general, a C_{60} single layer deposited on an uncorrugated substrate shows a tendency to be hexagonal close packed.

The Au(110) surface exhibits the (1x2) missing row reconstruction: one out of every two close packed atomic rows along the [1 -1 0] direction is missing. As a consequence it is a very anisotropic surface. C_{60} interacts with it via ionic bonding as indicated by electron spectroscopy studies. The strong electronic interaction is associated with a strong structural re-ordering as indicated by STM [1]. In that work, evidence was shown of an hexagonal close packed and corrugated C_{60} layer resulting in a (6x5) surface periodicity.

In order to obtain further information on the atomic arrangement of the $C_{60}/Au(110)$ interface, X-ray diffraction

experiments were performed on the (6x5) $C_{60}/Au(110)$ system. The measurements were carried out at ID3 (Surface Diffraction Beamline). A total of 300 in-plane fractional order reflections were measured which reduced to 130 symmetrically independent ones.

The application of standard procedures routinely employed in Surface Crystallography to solve the structural details of the $C_{60}/Au(110)$ $p(6 \times 5)$ surface reconstruction proved to be useless due to the complexity of the structure. Instead 'direct methods' were used to attempt to solve the problem. The phases of the largest structure factors which are necessary for computing the projected δ -map (map of the atomic distortions in the unit cell), were determined by maximising the 'direct methods' δ sum function [2,3]. In a preliminary low resolution study a hexagonal packing model as well as (1 x 2) and (1 x 3) symmetry of the surface rows compatible with the model obtained by STM were shown [4].

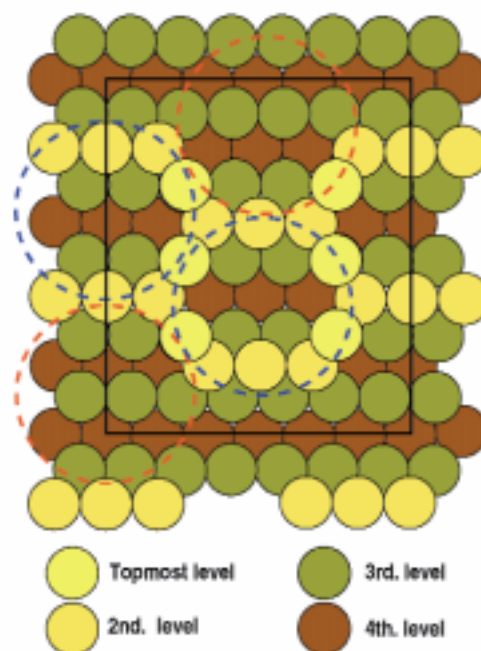


Fig. 41: Top view projection of the Au(110)- $p(6 \times 5)$ surface reconstruction. The relative heights of the Au atoms are indicated by different colours (darker colours represent deeper atoms). The dashed circles are the projections of the fullerene molecules which are ordered in a hexagonal close packed arrangement. By looking at the substrate atoms underneath the central fullerene molecule, one may observe that a total of seven Au atoms have been displaced from their original positions in the substrate (the topmost four atoms plus 3 atoms in the second level) in order to form a cavity to accommodate the fullerene. This indicates an interaction between the fullerenes and the Au surface which is much stronger than through van der Waals forces alone.

Although the analysis of the data is still not complete, good agreement was achieved with the experiments using the model depicted in **Figure 41**. The surprising result is that the interaction of the fullerene molecules with the substrate is so strong that several Au atoms are displaced from their original configurations in order to form a sort of calyx-shaped arrangement to better accommodate the fullerene balls indicated in the figure as dashed circles.

References

- [1] S. Modesti, S. Cerasari, P. Rudolf, *Phys. Rev. Lett.*, **71**, 2469 (1993).
- [2] C.A.M. Carvalho, H. Hashizume, A.W. Stevenson, I.K. Robinson, *Physica (Utrecht)*, **B221**, 469 (1996).
- [3] X. Torrelles, J. Rius, F. Boscherini, S. Heun, B.H.

Mueller, S. Ferrer, J. Alvarez, C. Miravittles, *Phys. Rev. B* **57**, **R4281**, (1998).

[4] X. Torrelles, J. Rius, M. Pedio, R. Felici, P. Rudolf, J. Alvarez, S. Ferrer, C. Miravittles, *Phys. Stat. Sol.*, **215**, 773 (1999).

Authors

M. Pedio (a), R. Felici (b), X. Torrelles (c), P. Rudolf (d), M. Capozzi (a), J. Rius (c), S. Ferrer (e).

(a) ISM-CNR, Area Science Park Trieste (Italy)

(b) INFN-OGG, c/o ESRF

(c) I.C.M.A.B. (CSIC), Barcelona (Spain)

(d) L.I.S.E. Facultes Universitaires Notre Dame de la Paix, Namur (Belgium)

(e) ESRF





Surfaces and interfaces

Introduction

The physics and chemistry of an interface between two media differs considerably from that in bulk materials due to differences in dimensionality and atomic arrangement. Of particular interest are the studies on catalysis and artificially-structured components for new technologies, which are giving this field additional importance. This was recognised many years ago and has led to a booming field of research which has now reached a steady state.

The use of brilliant, well-collimated beams at the ESRF has opened new possibilities. Surface physics is studied at two specially devoted beamlines, ID3 and ID32. Whereas phenomena occurring at interfaces are dealt with at many other beamlines. They are in part presented in other chapters since their results may be better understood in the context of applied research, materials or others.

Here we highlight only a few examples. A real breakthrough was achieved by the inauguration of a sample cell which permits the investigation of surface structures by high-energy X-ray diffraction. The energy was chosen in such a way that the X-rays can penetrate a thick Be wall which allows the vessel to be both evacuated to ultra high vacuum and later pressurised to several atmospheres. The researchers involved in this project call it "bridging the pressure gap". Indeed, in the past, the interaction between gases and surfaces has been studied mainly under reduced pressures, whereas, most catalytic processes occur at atmospheric or higher pressures. Hence, structural characterisation can now be performed under conditions which better reflect those found in real processes.

Grazing-incidence diffraction can be used to study monolayers and other small structures grown or deposited on a surface. In this section, its use is represented by the investigation of the structure of films of organic molecules grown on single-crystal surfaces. Additionally, the recent technique of grazing-incidence small-angle scattering is described and its use demonstrated by the study of the three-dimensional growth of metallic nano-particles deposited on a surface.

Another type of investigation of great importance is the analysis of the interaction of dot-like structures with a substrate. An example of inter-diffusion is presented, for germanium deposited on silicon, studied using X-ray absorption spectroscopy.

Although not represented, there is also a large class of investigations where the distortion of the underlying lattice can be unravelled. Such research gives important input for an understanding of the issue of self organisation at surfaces.

The Adsorption of CO on Pt(111) Near Atmospheric Pressures

One of the major goals of modern Surface Science has been the understanding of the surface chemical bond and its role in chemical reactions in heterogeneous catalysis, which have major economic and technological importance. Since the early days, the chemisorption of gas molecules such as CO, O₂, H₂... on transition metals has been studied extensively and the structure of several hundreds of chemisorption systems has been determined with a variety of techniques. Practically all the structural studies have been done under Ultra-High-Vacuum or High Vacuum environments. As catalytic reactions are performed at atmospheric pressures, the question of the “pressure gap” has been open for many years: are the UHV structures the ones that actually exist in the surfaces of the catalysts under real reaction conditions? To try to answer this question, experiments involving the transfer of a crystal from a catalytic reactor to a UHV environment have been performed extensively after the initial success by Somorjai et al. in the late seventies.

There is little doubt that in situ techniques can best reveal the surface structure at industrially important pressures and temperatures. These techniques have to be optical techniques (photons in the incoming and scattered beams) since the mean free paths of electrons or ions are too small at atmospheric pressures. Third generation X-ray synchrotron sources may provide the adequate probing beams to tackle the above question thanks to the intense X-ray beams available.

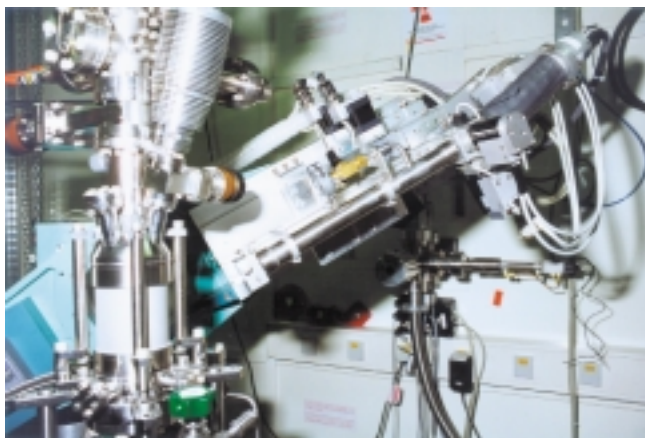


Fig. 42: Photograph of the chamber mounted on the diffractometer. The rigid rods around the Be window can be removed during data collection.

With this idea in mind, an UHV/HP (Ultra-High-Vacuum/High Pressure) chamber has been designed to perform grazing X-ray diffraction experiments on single crystal surfaces (Figure 42) on the beamline ID3 [1]. The

sample surfaces can be prepared in UHV with the traditional recipes of Surface Science (ion etching, annealing etc.) and they can be pressurised to several bars in order to study the surface structures of the adsorbed gases and the possible modifications of the substrates induced by the gases. The chamber is mounted in a high-precision diffractometer to perform diffraction experiments with large scattering angles allowing the exploration of extended regions of reciprocal space. The rocking scan in Figure 43 is effectively the scattering from the topmost atomic layer of the Pt(111) surface under 0.33 bar CO. The peak sharpness and intensity show that the surface can be well prepared in UHV and then characterised at elevated pressure despite the beam passing twice through the 2-mm beryllium window.

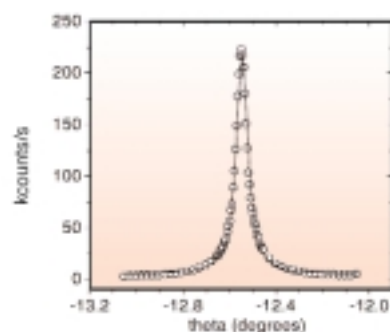


Fig. 43: Rocking scan around the surface normal from a Pt(111) crystal face at the minimum of a crystal truncation rod. The crystal was at room temperature and at an ambient pressure of 0.33 bar of CO. The peak counting rate is 222 kcoun/s over a background measured at the long tails of the scan of 2.5 kcoun/s. The full width at half maximum of 0.057° is indicative of the large (~200 nm) surface terraces.

The adsorption of CO on Pt(111) has been studied extensively in the past under UHV conditions [2]. The adsorption is non-dissociative. At low temperatures, several ordered structures have been reported which disorder via order-disorder phase transitions upon reaching room temperature. The maximum coverages for the different structures range from 0.5 to 0.7 monolayers.

The description of our main experimental result follows. A Pt(111) surface having terraces of several thousand Angstroms was prepared in UHV ($p = 10^{-9}$ mbar). Then, with the sample at room temperature, CO was admitted into the chamber up to a pressure of 100 mbar, the crystal temperature was increased to 330°C for several minutes and then it was cooled down to room temperature.

The above CO-temperature experiment resulted in a very large decrease of the integrated intensity of the Pt crystal truncation rods. The intensity decreased by a factor of

about 10 while the width of the Pt reflections was unaffected. A $\sqrt{7} \times \sqrt{7}$ R 19.1 degrees structure was formed on the surface. 82 in-plane reflections were measured which were reduced to 30 non-equivalent reflections after taking into account the symmetry and the domains. Also, six rods and three crystal truncation rods were collected.

Although the structural analysis is still being done and no model has been proposed so far, several comments are appropriate. To our knowledge, the above structure has never been observed before, in vacuum experiments. However, it has been observed in an electrochemical environment, with STM measurements on an electrochemical cell consisting of a Pt(111) electrode and CO gas bubbling in an acidic solution [3]. A simple model of the structure (to be confirmed) gives a coverage of 0.57 layers which is relatively high. The formation of the $\sqrt{7}$ structure has both a temperature and pressure requirement. The threshold of pressure has not yet been determined with precision but we have evidence that at least a few mbar of pressure are required. The temperature required is of about 250°C or more depending of the duration. It is also interesting to note, that the $\sqrt{7}$ structure is different from the high coverage structures predicted theoretically with Monte Carlo calculations [4].

In summary, by exposing Pt(111) to 0.1 atm of CO we have obtained and measured a new ordered structure which may be relevant to the understanding of the surface of a real catalysts under standard operating conditions.

References

- [1] P. Bernard et al., Rev. Sci. Instruments, **70**,1478 (1999).
- [2] G. Ertl et al., Surf. Sci., **64**, 393 (1977).
- [3] I. Villegas et al., J. Chem. Phys., **101**, 1648 (1994).
- [4] B.N. Persson et al., J. Chem. Phys., **92**, 5034 (1990).

Authors

K. Peters, P. Steadman, H. Isern, J. Alvarez, O. Robach, P. Bernard, S. Ferrer.
ESRF

Highly Oriented Films of Aromatic Molecules for Applications in Molecular Electronics

We have studied the structure and epitaxial properties of films of the aromatic molecules p-sexiphenyl and POPOP grown on atomically well-ordered KCl(001) substrates.

These electroluminescent molecules have potential applications in optoelectronic devices such as organic light-emitting diodes.

Samples of p-sexiphenyl and POPOP on KCl(001) were grown at Kobe University by vapour deposition in vacuum. Figure 44 shows a fluorescence micrograph of a POPOP film. The film consists of needle-like crystallites which show clearly a preferential orientation. Structure and epitaxial properties of these samples were characterised on the ID10B 2+2 diffractometer using grazing-incidence diffraction. Grazing-incidence geometry proved to be crucial for the study of these films, in order to limit radiation damage.

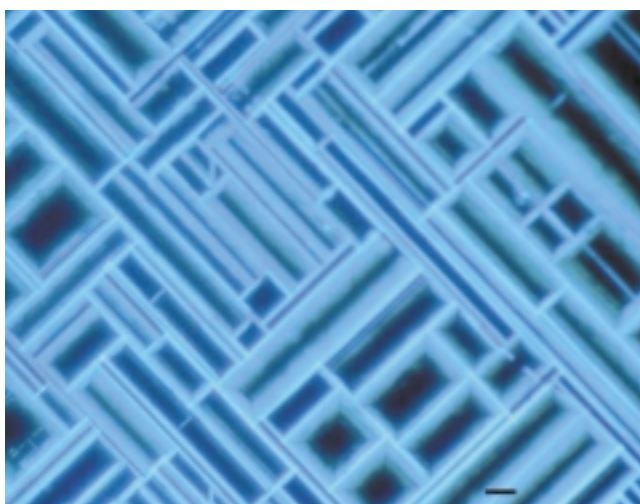


Fig. 44: Fluorescence micrograph of a POPOP film vapor-deposited onto a KCl(001) substrate. Needle-like crystallites with preferential orientations are clearly to be seen. The black bar in the lower right corner corresponds to 10 μm .

Figure 45a shows an in-plane scan along the [110] high-symmetry direction of the KCl substrate. Three peaks labelled A^* , $2A^*$ and B^{*1} according to their in-plane scattering vectors can be identified as due to the POPOP film. $2A^*$ occurs at twice the q-value of A^* , whereas B^{*1} is not related to the other two reflections. At these in-plane positions, rod scans along the surface normal were performed, as shown in Figure 45b. The rod scans at A^* and $2A^*$ display split peaks with the splitting for $2A^*$ increasing to twice the value at A^* . The splitting of the A^* reflections indicates an oblique crystal lattice. The two components are due to crystallites rotated by 180°. The B^{*1} rod features single peaks and can be identified as $2b^*$, where b^* is the reciprocal lattice vector along the special direction of the monoclinic bulk structure. The B^{*1} rod can be identified as due to POPOP crystallites rotated by 90° with respect to the crystallites giving rise to the A^* reflections.

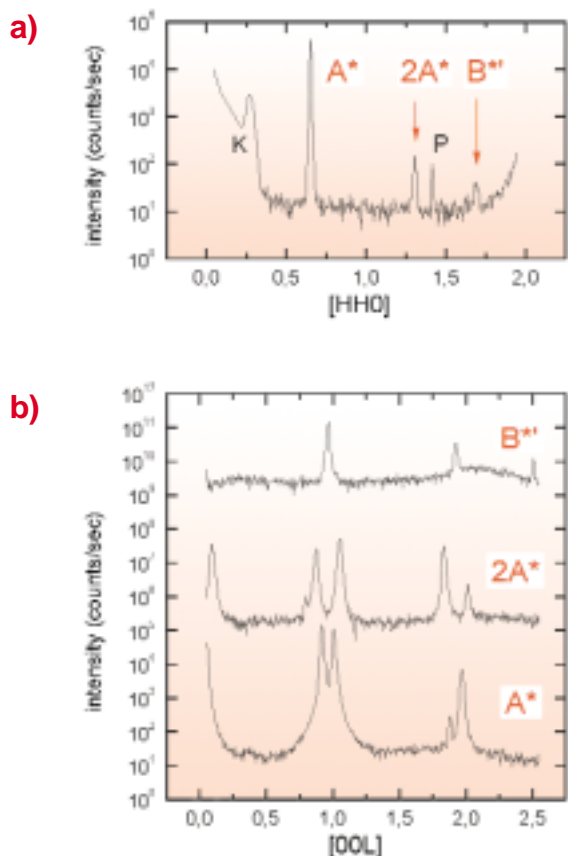


Fig. 45: Grazing-incidence diffraction from a POPOP film grown on KCl(001). (a) shows an in-plane scan along the [110] azimuth of the substrate. Reflections due to the film are marked by their in-plane scattering vectors as A^* , $2A^*$, and B^{**} , whereas K denote scattering from a Kapton window and P a powder ring of the substrate. (b) displays rod scans taken at the three in-plane scattering vectors found in the scan shown above.

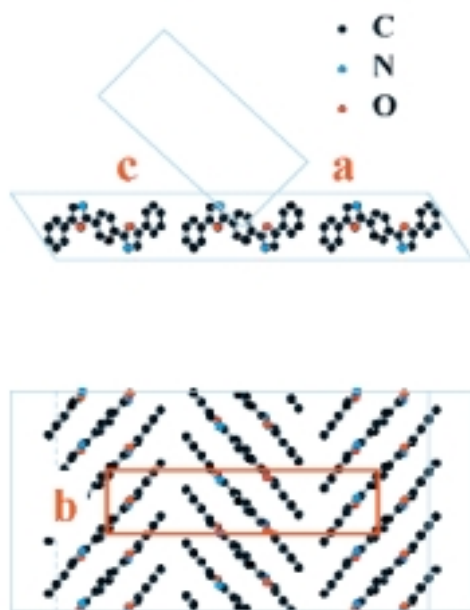


Fig. 46: Side view and top view of a POPOP layer grown on KCl(001). Films grow with the POPOP bulk structure in (102) orientation. The (102) plane contains POPOP molecules with their long axes in the plane forming a herringbone arrangement. Shown are the bulk lattice vectors a , b , c and the surface projected unit cell (red). The crystallographic b axis of the monoclinic bulk lattice is lined up with the [110] direction of the KCl(001) substrate to within 0.7 deg. The good epitaxial alignment indicates that the film structure persists all the way to the interface with the substrate.

From the spacing of the reflections along the rods we found that the POPOP crystallites grow with the (102) plane parallel to the surface and in fact all observed POPOP reflections could be indexed according to the bulk structure. The (102) planes consist of layers of molecules with the long molecular axes in the plane forming a herringbone arrangement (Figure 46). These layers are oriented parallel to the substrate with the crystallographic b axis parallel to the [110] direction of the substrate to within 0.7°. The good epitaxial alignment indicates that the film structure persists all the way to the interface with the substrate. In future studies we want to investigate the structure and growth mode of the first few layers.

Authors

D-M. Smilgies (a), N. Boudet (a), B. Struth (a), Y. Yamada (b), H. Yanagi (b).

(a) ESRF

(b) Faculty of Engineering, Kobe University (Japan)

The Morphology of Growing Nanoparticules by Grazing-Incidence Small-Angle X-ray Scattering

Determining the morphology of islands during their growth on a substrate is a very important task in the control of the fabrication of nano-objects. We have developed the recent technique of Grazing-Incidence Small-Angle X-ray scattering (GISAXS) to analyse the morphology of growing particles in situ, in ultra high vacuum (UHV), and in real time, starting from the very beginning of the growth. We have chosen metal/oxide systems which are known to grow in three dimensions, and for which the use of imaging techniques is difficult, because the AFM tip often moves the

metal clusters, and because STM can not be used on an insulating substrate. The growth of Pt, Pd and Ag on MgO(001) surfaces was investigated at different temperatures.

A fully-dedicated experimental setup has been built on the **ID32** beamline without a window before the sample, thus avoiding any background scattering. The beam was defined by two pairs of motorised slits working in the secondary vacuum. A hollow diode measuring the scattering by the beam-defining slits was used as a monitor, followed by a fast (1 ms of closure time) beam shutter. A 1-metre long differential pumping pipe was installed between this beam-defining line, with a pressure of 5×10^{-8} mbar, and the UHV chamber (base pressure 10^{-10} mbar) mounted on a six circle diffractometer. The UHV chamber was hooked to the entrance line by a CF38 bellow, allowing for a small rotation of the chamber around the vertical axis, used to define the angle of incidence of the X-ray beam with respect to the vertical sample surface. A 0.8 metre-long cone was connected to an exit pipe through a CF38 bellow, and ended by a 100 mm diameter beryllium window placed just in front of a 16-bit X-ray CCD detector. The cone and the detector were hooked to the goniometer detector arm, thus allowing precise vertical and horizontal alignment of the camera. A motorised tantalum beam-stop with a T-shape was introduced between the exit Be window and the 2-D detector.

Figure 47 shows a typical GISAXS pattern obtained on a 18 Å-thick Ag deposit. The lateral extension of the scattering yields the average lateral dimension of the islands; the perpendicular extension, and in particular the location of the second-order scattering peak yields the average height; while the location of the interference peaks parallel to the surface yields the average separation between the islands.

Figure 48 shows the evolution of the GISAXS during room-temperature growth of Ag on MgO(001), from 0.5 Å up to 50 Å equivalent thickness. As growth proceeds, all the scattering become more and more concentrated toward the origin of the reciprocal space, which corresponds to a continuous increase of all dimensions in real space. A detailed analysis shows that the growth proceed via nucleation, growth and coalescence at the same time, and finally percolation of the islands.

The pictures are quantitatively very precise, thus enabling the deduction of the average lateral size, height and separation between islands, and even the width of the distributions of these parameters. As an example, **Figure 49** shows a cut of the scattered intensity perpendicular to the surface, together with a fit without and with a distribution of islands heights. Clearly, the minima can only be reproduced by introduction of a finite distribution.

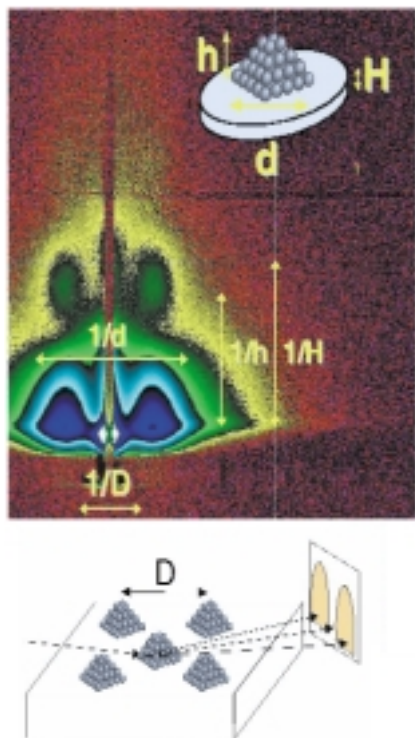
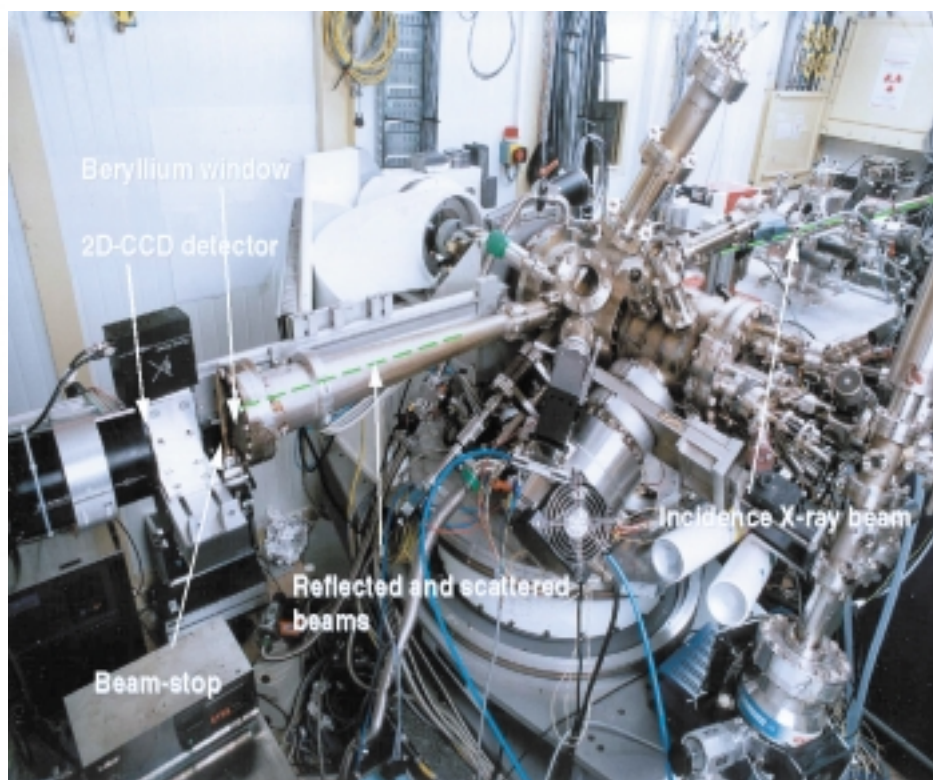


Fig. 47: Principle of GISAXS and experimental pattern.



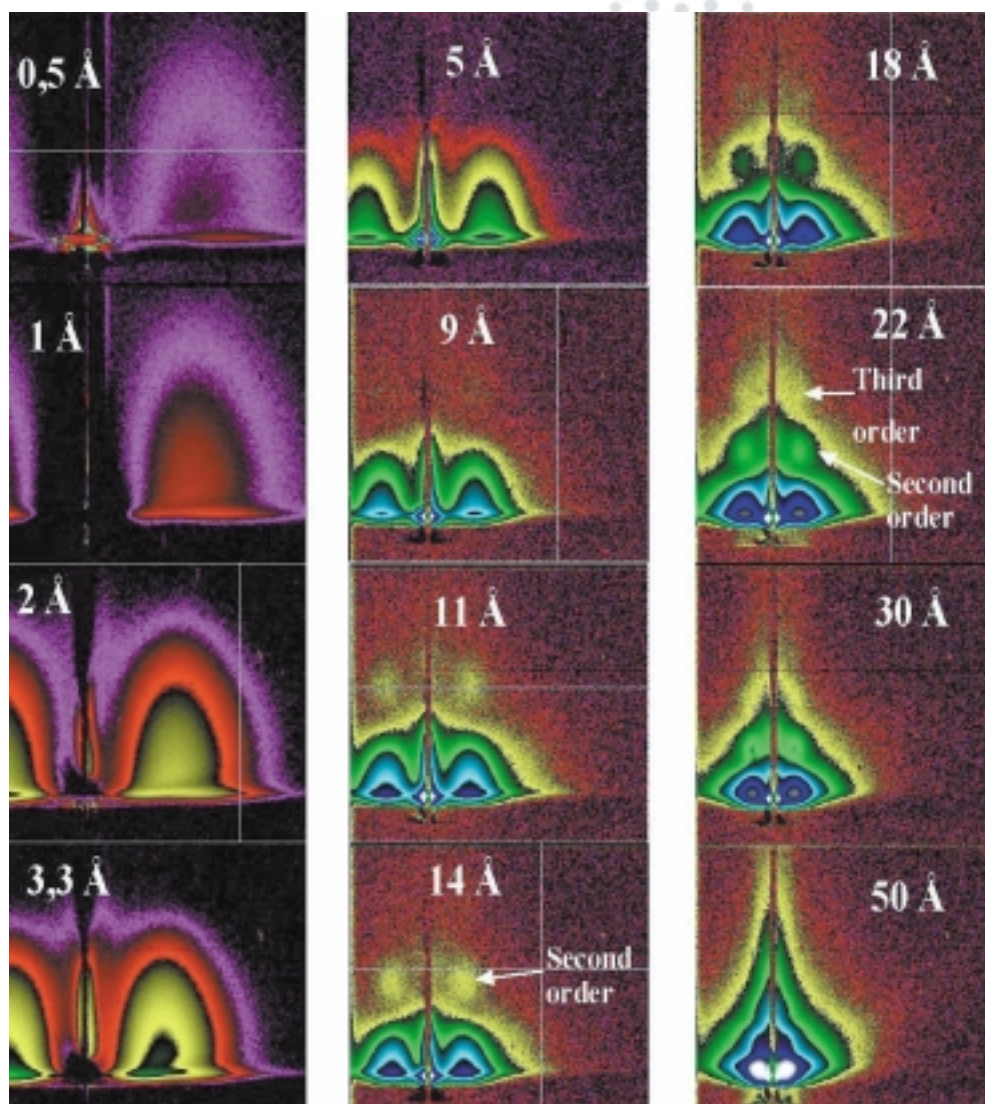


Fig. 48: Evolution of the GISAXS pattern during room-temperature growth of Ag on MgO(001).

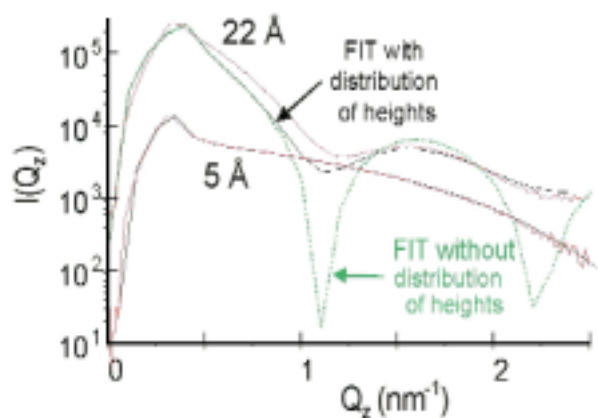


Fig. 49: Example of quantitative analysis of out-of-plane data.

Authors

G. Renaud (a), M. Noblet (a), A. Barbier (a), C. Revenant (a), O. Ulrich (a), Y. Borensztein (b), R. Lazzari (c), J. Jupille (c), C. Henry (d).
 (a) CEA-Grenoble (France)

(b) Laboratoire d'Optique des Solides, Université P. et M. Curie, Paris (France)
 (c) Laboratoire CNRS, Saint-Gobain (France)
 (d) CRMC2, Marseille (France)

Atomic Intermixing in Ge Quantum Dots

Semiconductors, structures and devices of reduced dimensionality have attracted much interest during the last few years; in particular for group IV semiconductors. This is due to the improvement of the electron-hole recombination efficiency by quantum confinement effects, and to the possibility of developing Si-based optoelectronics.

It is known that the growth of Ge on Si is of the Stranski-Krastanow type: a 2-D wetting layer initially forms, followed

by the appearance of 3-D islands. The degree and type of strain in these islands is currently under investigation although a clear picture of the mechanisms of strain relaxation is not yet available. In particular, there have been some recent indications that intermixing between substrate and epilayer may be significant, but no clear evidence has been provided. In [Figure 50](#) we show AFM images [1] of individual Ge dots contained in our samples: in (a) the morphology is typical of a relaxed structure (dome) while in (b) a single dislocation can be observed attached to a pyramid.

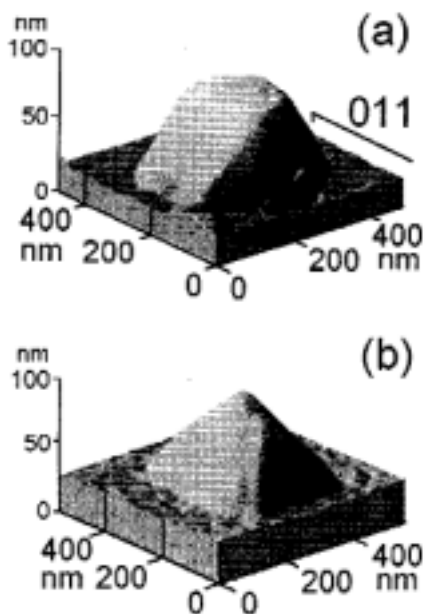


Fig. 50: AFM images [1] of single Ge dots on Si(001).

X-ray absorption spectroscopy (XAFS) in the fluorescence mode is able to provide a local structural characterisation of semiconductor nanostructures. Ge K-edge XAFS obtained in our experiment clearly demonstrate that substantial intermixing takes place for Ge dots deposited on Si substrates. In [Figure 51](#) we show selected XAFS spectra along with standards of pure bulk Ge and of a Ge impurity in Si; the spectra of all samples deviate significantly from those of Ge, especially at low k , where a positive oscillation typical of a Si environment can be observed. An essential tool to obtain this new result has been the advanced instrumentation available at **BM8** (the GILDA beamline), in particular the multi-element solid state detector, fast digital electronics and specially designed LNT sample holder.

For Ge/Si(001) deposited by CVD at 600°C, with equivalent thicknesses ranging between 5 and 40 nm, we find that Ge is always surrounded by 1 Si atom and 3 Ge atoms. In this thickness range, AFM shows a transition from pyramidal to

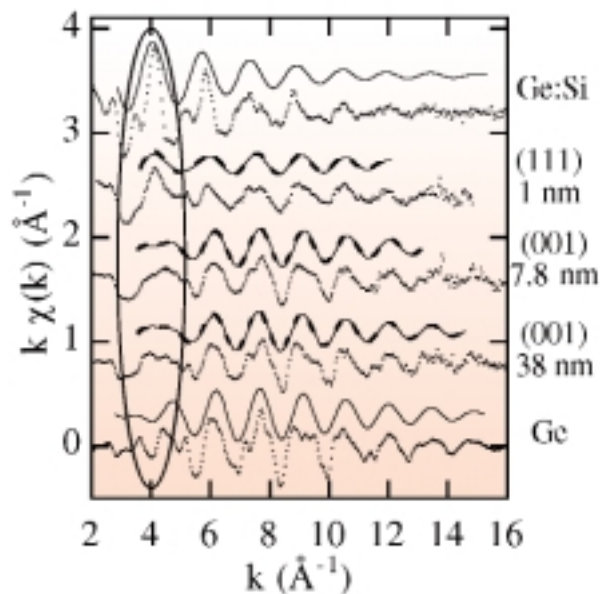


Fig. 51: Selected XAFS spectra. The ellipse highlights the spectral region where the signature of Si nearest neighbours to Ge is most evident.

dome-shaped dots. For Ge/Si(111) deposited by MBE at 500°C, we probe thicknesses of 1 and 1.7 nm; the thinner sample consists essentially of the 2-D wetting layer. For all Ge/Si(111) samples we find increased intermixing, with equal Ge-Si and Ge-Ge coordination numbers of 2. The common conclusion which can be drawn from the data is that considerable diffusion of Si into the Ge dots takes place – even at the relatively low growth temperatures employed.

The basic physics underlying these findings is that alloying can reduce the strain energy. In particular, a linear increase in the Si concentration in the Ge dots is expected to reduce quadratically the strain energy. Strain-enhanced diffusion of Si is thus thermodynamically favoured. Our study suggests that interdiffusion must be considered as one of the energy-reduction mechanisms for quantum dots, along with, for example, the formation of dislocations.

Reference

[1] G. Capellini, L. DiGaspare, F. Evangelisti, and E. Palange, *Appl. Phys. Lett.*, **70**, 493 (1997).

Principal Publication and Authors

F. Boscherini (a), G. Capellini (b), L. DiGaspare (b), N. Motta (c), F. Rosei (c), S. Mobilio (a), *Appl. Phys. Lett.*, **76**, 682 (2000).

(a) Frascati Nat. Lab. and University of Bologna (Italy)

(b) University of Roma Tre (Italy)

(c) University of Roma Tor Vergata (Italy)



Electronic states and Lattice dynamics

Introduction

With the advent of third generation synchrotron radiation sources several techniques have been developed or brought to maturity which allow the characterisation of electronic properties and dynamic properties of lattices using X-rays.

One of the foremost examples is inelastic X-ray scattering with, at present, a resolution of about 1 meV at 20 keV incident energy on beamlines ID16 and ID28. This technique complements the high energy resolution of inelastic neutron scattering with high resolution and universal accessibility to all regions in momentum space. It is particularly suited to the study of elementary excitations for liquids, the example presented here concerns the relaxation processes which occur within water.

Photoemission experiments with circular polarisation from the unique station ID12B allow a complete characterisation of electronic bands in terms of binding energy and spin state as exemplified by the research on Zhang-Rice singlets in high-temperature superconductors.

One of the most noteworthy and heavily discussed subjects of the last year was the observation of orbital ordering in vanadium oxide, studied at ID20. Here a simultaneous exploitation of several properties of a third generation source occurred. Scattering in resonance was combined with polarisation analysis and polar scans of the lattice planes. The experiment required a small beam and utmost stability. This single experiment has initiated a fruitful theoretical discussion centred around the interpretation of the observed effect. Furthermore, the fact that such experiments are possible has incited a large number of follow-up investigations.

The other highlights chosen for this chapter further demonstrate how a variety of techniques can be used to furnish valuable information about the energy levels and electronic transitions that exist in a diverse selection of materials such as quasicrystals, organometallic complexes, metal oxides and organic donor-acceptor complexes.

Experimental Determination of the Structural Relaxation in Liquid Water

The investigation of large wavevector excitations in liquid water has shown the existence of a positive dispersion in the velocity of sound. This dispersion has been inferred in the pioneering computational [1] and experimental [2] studies of the dynamic structure factor, $S(Q,E)$, and has been recently assessed by Inelastic X-ray Scattering (IXS) [3]. Using IXS, the transition of the longitudinal sound velocity from the adiabatic value, $c_0 \approx 1500$ m/s, to a value more than twice larger, $c_\infty \approx 3200$ m/s, was studied at $T = 5^\circ\text{C}$. This sound velocity dispersion is qualitatively similar to that observed in glass-forming liquids. There, the transition between the two dynamic regimes is determined by the coupling of the propagating density fluctuations with the dynamics of the structural rearrangements of the particles in the liquid. The complex dynamics of such a rearrangement can be described by a relaxation process with a characteristic time, τ . The transition takes place when the condition $\Omega\tau \approx 1$ is fulfilled. In glass-forming liquids τ has a very steep temperature dependence; its typical values are in the nanosecond range close to the melting point and dramatically increases near the calorimetric glass transition temperature T_g . This relaxation process (α -process) has a cooperative nature and the density fluctuations are influenced differently in the two opposite frequency limits: the system has a solid like elastic behaviour for $\omega\tau \gg 1$, and a viscous one for $\omega\tau \ll 1$. One could speculate that also in liquid water the physical mechanism responsible for the dispersion of the sound velocity is an α -relaxation process.

The experimental characterisation of the α -process is typically obtained by the determination of the dispersion of the sound velocity as a function of T and at a constant Q transfer value. At the inflection point "t" of such an "S"-shaped curve the condition $\Omega_t(Q,T)\tau(T) \approx 1$, with $\Omega(Q,T) = c_{\text{app}}(Q,T) Q$, is fulfilled. In glass forming liquids, this condition is met by Brillouin Light Scattering (BLS) measurements close to melting, and by Ultrasonic (US) methods close to T_g . Indeed, the typical frequencies allowed by these two techniques are such that $\Omega(Q,T)\tau(T) \approx 1$ is met for values of τ in the 100 ps (BLS) and 1 μs (US) ranges. In the case of water, as a consequence of the small value of τ close to melting, the BLS cannot access the relevant excitations energy region. The complete determination of the "S"-shaped curve as a function of either T or Q requires, however, the use of IXS [3].

This scenario has motivated an experiment on the

ultra-high energy resolution inelastic X-ray scattering spectrometer of ID16 on the temperature dependence of the transition from normal to fast sound in liquid water in the $T = 260\text{-}570$ K and $Q = 1\text{-}12$ nm^{-1} regions. In order to emphasise the thermal effects, and to minimise the modification of the hydrogen bond dynamics due to large variations of the excluded volume, the density was kept in the range $\rho = 0.94\text{-}1.07$ g/cm^3 . This was obtained adjusting the pressure in the 0-2 kbar range. The existence of a relaxation process is demonstrated by Figure 52 which shows that the transition between the two sound regimes takes place at increasing Q values with increasing temperatures. The associated time-scale extends into the sub-picosecond region with increasing temperature.

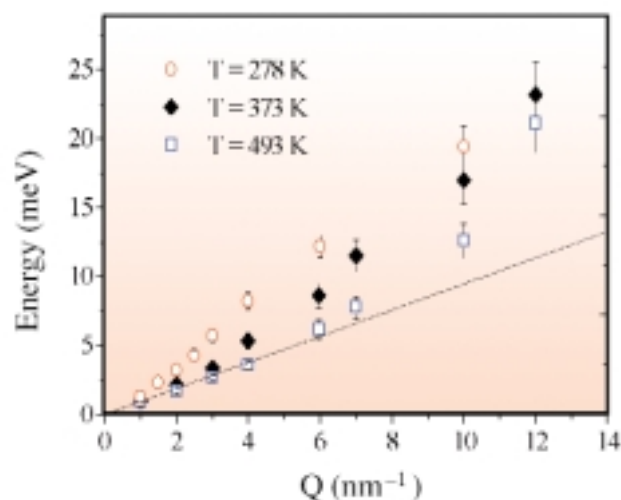


Fig. 52: Dispersion relation of the energy position parameter $h\Omega$ as a function of Q at the indicated temperatures. The $h\Omega$ parameter has been obtained fitting the inelastic part of the IXS data to a damped harmonic oscillator model. The excitation values have been scaled by the factor $c_0(278\text{ K}) / c_0(T)$, with $c_0(T)$ obtained from the equation-of-state. This has been done to emphasise in the same plot the departure of the dispersion relation from the $c_0(T)$ law, shown by the solid line, which is valid in the $Q \rightarrow 0$ limit. This figure demonstrates that, in the dispersion relations, the transition from c_0 to c_∞ takes place at increasing Q values with increasing temperatures.

The analogy with the glass-formers phenomenology, implies that the fast relaxation process studied in this work can be identified with an α -process. The derived values of τ are consistent with previous estimations: they roughly follow an Arrhenius behaviour with an activation energy comparable to the hydrogen bond energy. This suggests that, in water, the α -process is associated with the rearrangement (making and breaking) of molecular structures kept together by the hydrogen bond.

The IXS data were analysed both with an empirical model and with a visco-elastic model, and in each case it was possible to determine the detailed T and Q dependence of the relaxation time, τ .

References

- [1] Rahman and Stillinger, *Phys. Rev.*, **A 10**, 368 (1974).
- [2] J. Teixeira, M.C. Bellisent-Funel, S.H. Chen, B. Doznez, *Phys. Rev. Lett.*, **54**, 2681 (1985).
- [3] F. Sette et al., *Phys. Rev. Lett.*, **75**, 850 (1995); *Phys. Rev. Lett.*, **L77**, 83 (1996).

Principal Publications and Authors

A. Cunsolo (a), G. Ruocco (b), F. Sette (a), C. Masciovecchio (a), A. Mermet (a), G. Monaco (b), M. Sampoli (a), R. Verbeni (a), *Phys. Rev. Lett.*, **82**, 775 (1999).

G. Monaco, A. Cunsolo, G. Ruocco, F. Sette, *Phys. Rev.*, **E 60**, 5505 (1999).

(a) ESRF

(b) Università di L'Aquila and Istituto Nazionale di Fisica della Materia (Italy)

(c) Università di Firenze and Istituto Nazionale di Fisica della Materia (Italy)

Direct Observation of the Zhang-Rice Singlets in High-Temperature Superconductors

More than a decade has passed since the discovery of high temperature (HTc) superconductors. However, despite an intense research effort the mechanism responsible for these phenomena is still not fully understood. In order to test the basic assumptions of HTc superconductivity theories, it is important to have experimental evidence for the electronic structure of these materials. In many mainstream theories, like the single band Hubbard model and the $t - J$ model, the relevant states in the $(\text{CuO}_2)_2^-$ planes are of local singlet spin character (two holes with antiparallel spins, $S = 0$). In the single-band $t - J$ model these states are often referred to as Zhang-Rice singlets [1]. Singlet states are contrary to what would normally be expected from Hund's first rule (i.e. triplet states, two holes with parallel spins, $S = 1$). Calculations have also shown that the photoemission spectrum can be directly related to the ground state electronic structure of the doped material. Consequently, one would like to measure the spin-resolved single-particle excitation spectrum to derive the energies of the different spin-dependent electronic states close to the Fermi level. The observation of the singlet states would

provide strong support for the existence of the Zhang-Rice singlets in HTc cuprates [1].

Recently the feasibility of this type of study was demonstrated for CuO [2]. The experiment is based on spin-polarised resonant photoemission measurements made using circularly polarised X-rays. In these new experiments we have studied optimally doped ($T_c = 91$ K) $\text{Bi}_2\text{Sr}_2\text{CaCu}_2\text{O}_{8+\delta}$ samples. The experiments were carried out on the helical undulator based beamline **ID12B** and the spectra were recorded using an electron analyser coupled to a spin polarimeter. The resonant photoemission measurements were achieved by tuning the photon energy to the peak of the Cu $2p_{3/2}$ (L_3) photoabsorption white line ($h\nu = 931.5$ eV).

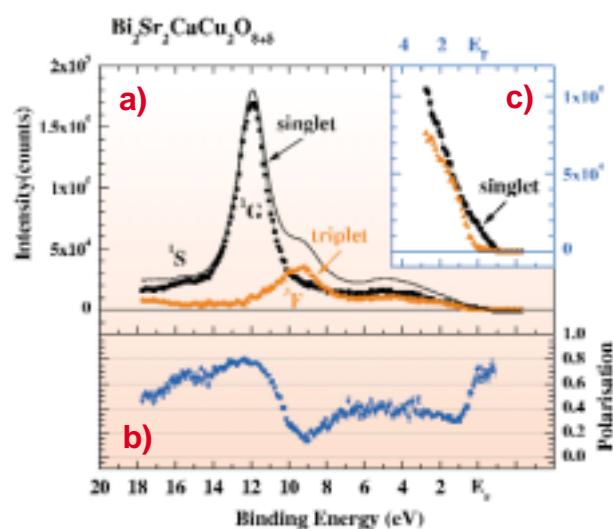


Fig. 53: a) The solid line gives the spin-integrated circularly polarised resonant photoemission spectrum. The photon energy is set at the Cu L_3 absorption peak ($h\nu = 931.5$ eV). The spectrum is separated into its singlet (■) and triplet (▲) components as explained in the text. b) The spin polarisation curve (●) corresponding to the spectra in Figure 53a. c) The Fermi level region taken with good statistics and separated into singlet (■) and triplet (▲) components.

In Figure 53a we show the spin integrated resonant photoemission spectra (full line) and in Figure 53b we show the spin polarisation given by the spin difference (using both helicities) normalised to the spin integrated spectrum. The spectrum results principally from Cu $3d^8$ final states and the peak at ~ 12 eV binding energy can be assigned to an atomic like 1G state. This is completely analogous to the previous work on CuO [2]. The spin polarisation of this peak is $\sim 80\%$. This value is consistent with an analysis of the selection rules which give for a $3d^9$ ion, neglecting the small

3d spin-orbit interaction, $5/6$ (83.3%) for pure singlet states and $-1/3 * 5/6$ (-27.8%) for triplet states. The strong dip in the polarisation at ~ 9 eV binding energy indicates a significant triplet contribution to the spectra at this energy. Assuming these model values for the polarisation of singlet and triplet states, we can separate the spectra into the two contributions. These are shown by the symbols in Figure 53a.

We are principally interested in the electronic states close to the Fermi level. Although the intensity is extremely low, it is clear that the spin polarisation increases dramatically around the Fermi level (see Figure 53b). This is the first evidence that the states close to the Fermi level are mostly of singlet character. In Figure 53c we show the region close to the Fermi level taken with good statistical quality. The spectrum is separated into its singlet and triplet components. It is quite clear that the intensity closest to the Fermi level and over more than 1 eV is dominated by singlet states. Consequently, we can conclude that for the $\text{Bi}_2\text{Sr}_2\text{CaCu}_2\text{O}_{8+\delta}$ superconductor that the first ionisation state is of nearly pure singlet character. This provides compelling evidence for the existence and stability of the Zhang-Rice singlets in HTc cuprates [1].

References

- [1] F.C. Zhang, T.M. Rice, *Phys. Rev.*, **B 37**, 3759 (1988).
 [2] L.H. Tjeng, B. Sinkovic, N.B. Brookes, J.B. Goedkoop, R. Hesper, E. Pellegrin, F.M.F. de Groot, S. Altieri, S.L. Hulbert, E. Shekel, G.A. Sawatzky, *Phys. Rev. Lett.*, **78**, 1126 (1997).

Authors

N.B. Brookes (a), G. Ghiringhelli (a), O. Tjernberg (a), L.H. Tjeng (b), T. Mizokawa (b), T.W. Li (c), A.A. Menovsky (c).
 (a) ESRF
 (b) Solid State Physics Laboratory, Materials Science Centre, University of Groningen, (The Netherlands)
 (c) Van der Waals-Zeeman Laboratory, University of Amsterdam (The Netherlands)

Direct Observation of Orbital Ordering by Resonant Scattering Technique

The influence of orbital ordering on the electric and magnetic properties of strongly correlated 3d transition metal systems has attracted significant theoretical and experimental interest since the early 1960s. However it is

only in the last few years, after the discovery of colossal magnetoresistance in perovskite-type manganites, that the physical phenomena related to charge, spin and orbital degrees of freedom have been recognised as a central issue in a broad range of materials, such that it has become one of the most popular topics in hard condensed matter physics. An important step forward in this field is represented by the very recent observation that resonant X-ray scattering can provide an accurate and direct experimental method to observe the long-range order for orbital occupancy. The orbital degeneracy is commonly lifted by the crystal field or by Jahn-Teller distortion. In both cases the orbital order can be deduced from the crystal structure, which is easily observable with standard scattering techniques. However, there are systems like V_2O_3 where orbital order is not accompanied by any cooperative Jahn-Teller phenomenon. In these cases, and if magnetism is involved, one can infer the existence and structure of orbital order only from the knowledge of the magnetic structure, which strongly depends on the occupied orbitals. Twenty years ago Castellani et al. [1] proposed an orbitally-ordered structure compatible with the observed magnetic structure determined by neutron diffraction (Figure 54). Taking into account both the spin and orbital degrees of freedom, this model can justify the breaking of trigonal symmetry in the honeycomb plane, in which the pseudo-spin associated with the orbital occupancy have the same sign as the in-plane exchange coupling, whereas it is the opposite between the vanadium sites along the hexagonal axis.

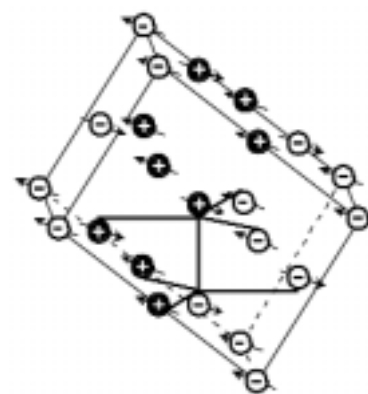


Fig. 54: Antiferromagnetic (arrows) and orbital (black and white circles) structures of V_2O_3 in the monoclinic crystallographic cell. The sign + and - indicates the linear combination of 3d electronic wavefunctions and the arrows the magnetic moment directions.

The experiments were carried out at **ID20** (magnetic scattering beamline) on a Cr-doped V_2O_3 single crystal. The orbital Bragg peaks appear below the Néel temperature ($T_N = 180$ K) at positions in reciprocal space

which are forbidden for antiferromagnetic and charge reflections, and can be observed only by tuning the incident photon energy at the pre-edge of Vanadium K-photoabsorption. This resonance involves transitions from 1s core level to 3d electronic states via weak quadrupolar transitions. Crucial to these studies was the observation of a peculiar dependence of the diffracted intensity from the azimuthal rotation angle around the orbital reflection (Figure 55). Moreover, the analysis of the complex azimuthal dependence of scattered polarised photons provides information on the spatial symmetries of ordered orbitals.

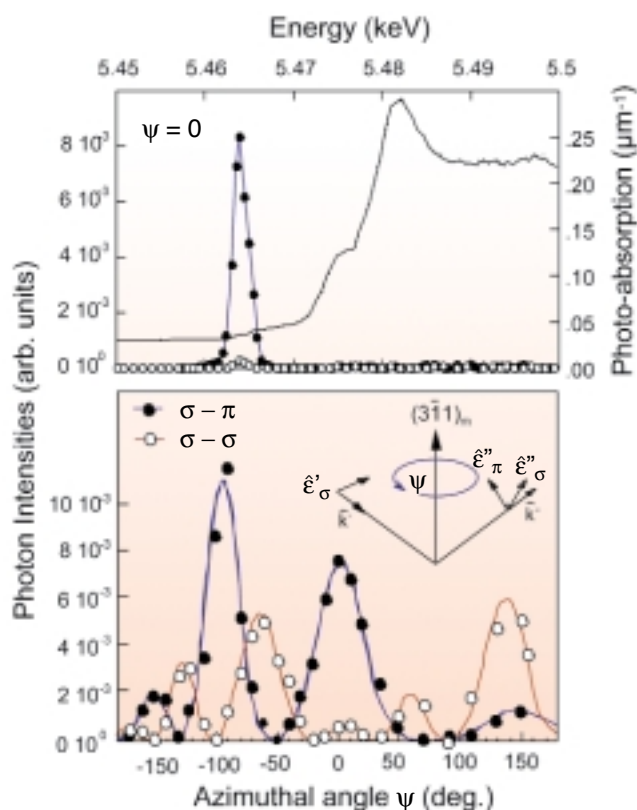


Fig. 55: Energy dependence of orbital reflection $(3,-1,1)_m$ (upper panel) and the relative azimuthal dependence (lower panel) in the two polarisation channel $\sigma-\pi$ (closed circles) and $\sigma-\sigma$ (open circles). The sharp resonance appears at the threshold of Vanadium K-photoabsorption edge ($E = 5.465$ keV) in both polarisation channels and corresponds to the quadrupolar transitions from 1s to 3d electronic states.

These observations confirm the interplay between the orbital and magnetic order in V_2O_3 and illustrate a new experimental method to extract information on the electronic orbital occupancy in solids.

References

[1] C. Castellani, C.R. Natoli, J. Ranninger, *Phys. Rev. B*, **18**, 4945 (1978).

[2] L. Paolasini, C. Vettier, F. De Bergevin, F. Yakhou, D. Mannix, A. Stunault, W. Neubeck, M. Altarelli, M. Fabrizio, P.A. Metcalf, J.M. Honig, *Phys. Rev. Lett.*, **82**, 4719 (1999).

Authors

L. Paolasini (a), C. Vettier (a, b), F. De Bergevin (c), F. Yakhou (a), W. Neubeck (a), A. Sollier (a), D. Mannix (a), A. Stunault (a), M. Fabrizio (d), M. Altarelli (e), P.A. Metcalf (f), J.M. Honig (f).

(a) ESRF

(b) Present address: ILL, Grenoble (France)

(c) Laboratoire de Cristallographie, CNRS, Grenoble (France)

(d) International School for Advanced Studies, SISSA, and International Center for Theoretical Physics, ICTP, Trieste (Italy)

(e) Sincrotrone Elettra, Trieste (Italy)

(f) Department of Chemistry, Purdue University (USA)

Coherent X-ray Diffraction and Phasons Fluctuations in Quasicrystals

Quasicrystals are ordered materials which lack translational invariance. As for other incommensurate structures, the lack of periodicity leads to new long wavelength modes called phasons. At the microscopic level, this corresponds to the possibility for an atom to occupy two nearby positions having almost an equivalent local environment. Correlations between these microscopic rearrangements lead either to Bragg peak broadening or to diffuse scattering.

Both effects have been observed in the most perfect quasicrystals currently available, the icosahedral AlPdMn phase. The long wavelength phasons fluctuations give rise to a characteristic intensity distribution of the diffuse scattering around the Bragg reflections, which has been observed by neutron and X-ray diffraction. The observed distribution of the diffuse scattering can be reproduced using the elasticity theory of quasicrystals, and considering only two phason elastic constants. A temperature study of the diffuse scattering showed that it is related to pretransitional phasons fluctuations.

Unlike displacive modulated structures, but similarly to composite incommensurate structures, phason modes are not collective propagative modes in icosahedral quasicrystals, but are diffusive modes. A mode with a given

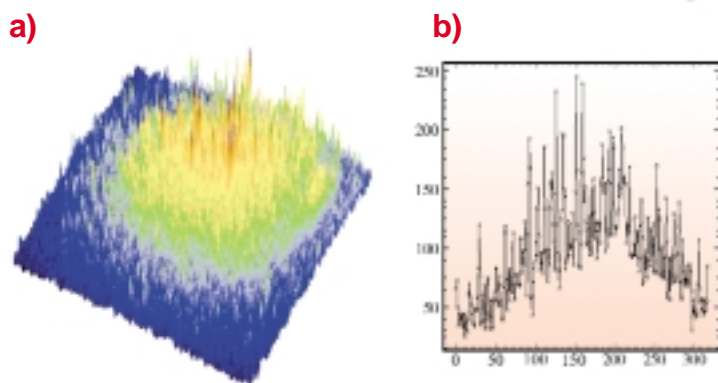


Fig. 56: (a) 2-D image of the speckle pattern taken in the diffuse tails of a Bragg reflection (b) slice through Figure 56a. Intensity fluctuations are much larger than the counting statistics.

Figure 56 shows a speckle pattern recorded in 1 h at room temperature, at a distance $q = 0.025 \text{ \AA}^{-1}$ away from a strong Bragg reflection. The slice through the 2-D intensity distribution, shows intensity fluctuations, much larger than the Poisson statistics, as expected for a speckle pattern. The sample was then slowly heated up to 550°C . At this temperature the first time dependence in the speckle pattern has been observed. Figure 57 shows the time correlation function retrieved from the measured data. As expected the phason fluctuations show an exponential time decay, with a time scale of the order of 400 s, for a phason wavelength equal to 250 \AA . These results are very promising and open the route for a complete study (as a function of q and T) of the dynamics of phasons fluctuations in quasicrystals.

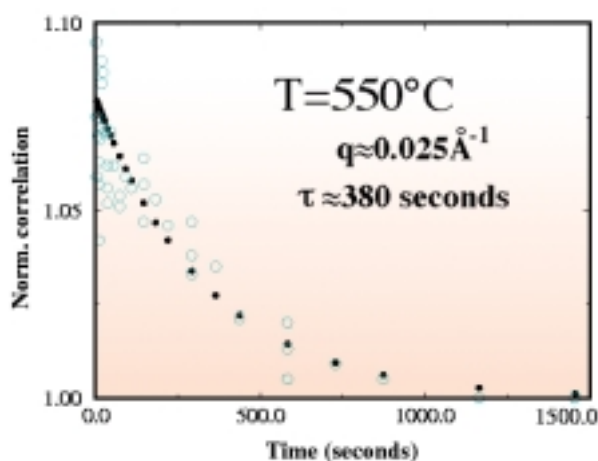


Fig. 57: Time correlation of the speckle pattern at 550°C .

wave-vector q , is expected to follow an exponential time decay, with a q^{-2} dependence of the characteristic time decay. The time scale for such fluctuations has not yet been measured, but is supposed to be in the accessible range for coherent X-ray photon spectroscopy, i.e. of the order of minutes. Since the diffuse scattering is directly related to phason fluctuations, a measure of the time dependence of the speckle pattern in the diffuse scattering will give the time relaxation directly.

The coherent X-ray beam was produced by focussing optics located on beamline **ID20**. The incoming energy of the beam (7.6 keV) was selected by a double Si (111) crystal, with sagittal bending. A $10 \mu\text{m}$ diameter pinhole close to the sample provided a coherent beam. A Princeton Instrument Direct Illumination CCD chip was used as a 2-D photon counter using a droplet algorithm and was located 1.8 m away from the sample. With this setting, a $\beta = 40\%$ coherence was achieved with a flux equal to $7 \cdot 10^8$ photon/sec at the sample position (200 mA beam current).

Authors

A. Létoublon (a) , F. Yakhou (b), F. Livet (a), F. Bley (a), M. de Boissieu (a), R. Caudron (c), C. Vettier (b).
 (a) LTPCM UMR CNRS 5614, St Martin d’Heres (France)
 (b) ESRF
 (c) ONERA – LEM, Chatillon (France)

Mode Selective Studies of Lattice Dynamics in Macromolecules

Lattice dynamics of macromolecules is complicated due to the large amount of existing vibrational modes. In contrast to the easily accessible structural information, there is still a poor knowledge on macromolecular dynamics because of the limited experimental access. For instance, coherent inelastic neutron scattering cannot handle dispersion relations of thousands of vibrational modes. On the other hand, incoherent inelastic neutron scattering gives a featureless distribution of density of phonon states (DOS), which does not allow any further analysis of vibrational modes. As a result, the information on lattice dynamics of macromolecules today is better accessible via theoretical simulations than through the experimental studies.

Addressing the problem, we have demonstrated a possibility of mode selective analysis of lattice dynamics in large macromolecules using nuclear inelastic absorption. The method is isotope selective, thus it is sensitive only to the vibrational modes involving the atoms of the resonant

Mössbauer isotope. Other advantages of the technique are precise averaging over phonon momentum space, high count rate, and access to small samples.

At beamline **ID18**, we have measured the partial density of phonon states of iron atoms in $[^{57}\text{Fe}(\text{bpp}_2)][\text{BF}_4]_2$ macromolecular polycrystalline powder, where the ligand bpp is 2,6-bis(pyrazol-3-yl)pyridine ($\text{C}_{11}\text{H}_9\text{N}_5$). **Figure 58** shows a central part of the molecule. The unit cell of the molecular crystal has eight molecules and contains 488 atoms. Consequently there are 1464 vibrational modes, which makes problems in the application of conventional inelastic techniques.

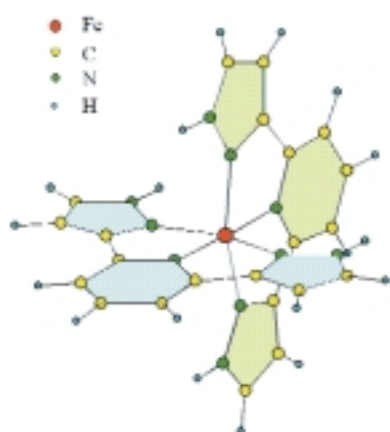


Fig. 58:
Structure of the $[\text{Fe}(\text{bpp}_2)][\text{BF}_4]_2$ macromolecule. Two bpp ligand units are marked with blue and green planes, respectively. Two tetrafluoroborate groups have been omitted for simplicity.

The macromolecule belongs to a class of iron (II) complexes, which exhibit a thermally driven high-spin \Leftrightarrow low-spin ($^5\text{T}_{2g} \Leftrightarrow ^1\text{A}_{1g}$) transition. For this particular molecule it occurs at 179 K. We have measured the energy spectra of nuclear inelastic absorption in $[^{57}\text{Fe}(\text{bpp}_2)][\text{BF}_4]_2$ with an energy resolution of 0.65 meV at two temperatures, 9 K and 295 K, which correspond to the low-spin and high-spin states, respectively. The obtained iron-partial density of phonon states is shown in **Figure 59**. For both states the DOS has a continuous energy distribution at lower energy and several well-localised optical modes at higher energy. According to their energies, the latter may be assigned to the Fe-N bond stretching.

Initial parabolic growth of the density of states at low energy gives a mean sound velocity of about 2.6 km/s. This indicates that the acoustic part of the DOS is limited to 4...5 meV. The density of states in this energy region is identical for both spin states (Figure 59). Thus our results show that the spin crossover does not change the intermolecular dynamics of the system. In contrast to acoustic modes, the optical modes of intramolecular dynamics have completely different frequencies (Figure

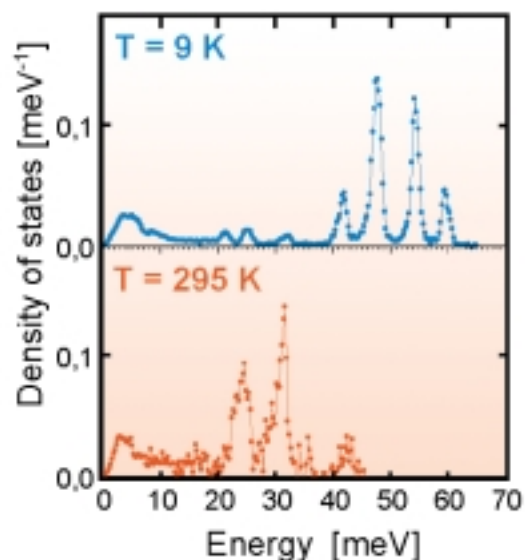


Fig 59: *Iron-partial density of phonon states in low-spin and high-spin states of the $[\text{Fe}(\text{bpp}_2)][\text{BF}_4]_2$ macromolecule, measured at 9 K and room temperature, respectively. Energy resolution is 0.65 meV. Solid lines are to guide the eye.*

59). In the low-spin state they spread up to 62 meV, whereas in the high-spin state, within statistical accuracy, there are no modes above 46 meV. Further processing of the experimental data allowed determination of the mean-square displacement, mean kinetic energy and mean force constant separately for each optical mode. Besides that, the partial contribution to entropy and specific heat from the iron atoms was calculated.

This example demonstrates a potential of nuclear inelastic absorption to provide accurate mode-selective information on lattice vibrations in complicated macromolecules. In the present experiment the measuring time was about 20 hours for each spectrum. The statistical accuracy of the results may be traced via the “scattering” of the experimental points. It is excellent for low temperature, though somewhat worse for room temperature data, where a significant contribution of the multiphonon absorption has been subtracted from the raw experimental spectrum. The characteristic energy of the Fe-N bond stretching in the low-spin state was determined with 0.4% accuracy. These experimental data show a possibility of new insight into the dynamics of large macromolecules and provide a solid basis to examine the corresponding theoretical simulations.

Authors

A. Chumakov (a), R. Ruffer (a), O. Leupold (a, b), H. Grünsteudel (a), A. Barla (a), T. Asthalter (a, c).
(a) ESRF
(b) Hamburg University (Germany)
(c) Munich Technical University (Germany)

Two-Dimensional Charge Stripes in $\text{La}_{5/3}\text{Sr}_{1/3}\text{NiO}_4$

Strontium-doped La_2NiO_4 (LSN) is isostructural with the high- T_c cuprates, $\text{La}_{2-x}\text{Sr}_x\text{CuO}_4$ (LSC) and $\text{La}_{2-x}\text{Ba}_x\text{CuO}_4$ (LBC). With substitution of 15% Sr, LSC shows a superconducting transition at $T_{SC} = 35$ K, but LSN remains insulating at doping levels up to 70%. The substitutions of La with Sr provide hole carriers, and the doped holes tend to order in a stripe-like structure acting as domain walls within the NiO_2 planes. The interplay between this ordered state and the spins of Ni dominates the transport behaviour at low temperatures. Despite the demonstrations of charge ordering and spin ordering in related colossal magnetoresistance manganites by neutron scattering, X-ray scattering has the merits of superior spatial resolution and direct probing of the charge density modulation.

Using high-resolution synchrotron X-ray diffraction on **BM28** (the UK - CRG XMaS beamline), we have demonstrated the existence of quenched disordered charge stripes in a single crystal of $\text{La}_{5/3}\text{Sr}_{1/3}\text{NiO}_4$ at low temperatures. In accord with the neutron scattering studies, satellite reflections were observed at low temperatures at positions of $(h \pm 2\epsilon, 0, l)$, $\epsilon \approx 1/3$, $h = \text{even}$ and $l = \text{odd}$.

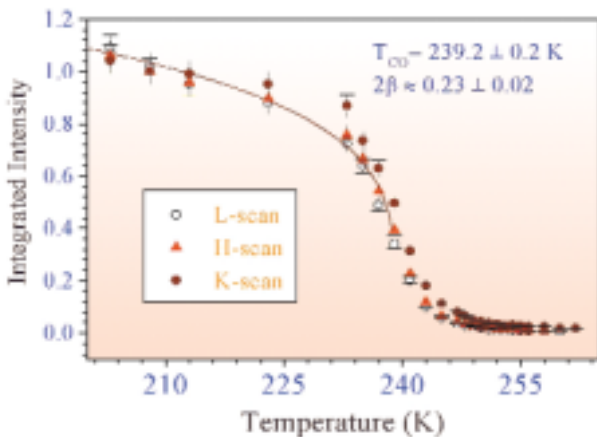


Fig. 60: Temperature dependence of the integrated intensities of the charge stripe satellite (4.66 0 5) along all three principle directions in reciprocal space.

The solid line is the best fit to a power law

$$I(t) \propto \left(\frac{T_{CO} - T}{T_{CO}}\right)^{2\beta}.$$

Figure 60 shows a plot of the integrated intensity, along each of the reciprocal space directions, of the charge ordering peak (4.66 0 5) versus temperature. Clearly, the data can be fitted to a power law $I(t) \approx \left(\frac{T_{CO} - T}{T_{CO}}\right)^{2\beta}$, with

$2\beta \approx 0.23 \pm 0.02$, and $T_{CO} \approx 239.2 \pm 0.2$ K, and shows the transition to be second order in nature. The measured exponent of 2β clearly demonstrates that below T_{CO} the charge stripes in $\text{La}_{5/3}\text{Sr}_{1/3}\text{NiO}_4$ are in the 2-D universality class.

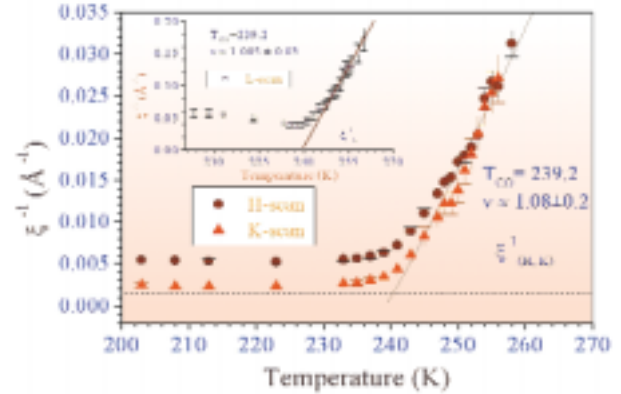


Fig. 61: The evolution of the inverse correlation lengths of the charge stripe satellite (4.66 0 5) along the H, and K directions. The data can be fitted to a power law

$$\xi(t)^{-1} \propto \left(\frac{T - T_{CO}}{T_{CO}}\right)^\nu.$$

The inset shows the evolution and the best fit along the L direction.

In Figure 61, we display the evolution of the correlation lengths with temperature. Above the transition temperature $T_{CO} \approx 240$ K, only very weak scattering is observed at the expected positions in reciprocal space. It is caused by critical scattering, owing to dynamic spatial fluctuations into the charge stripe phase. We believe this to be the first observation of charge stripe critical fluctuations existing above T_{CO} . The size of these clusters varies with temperature and shows a marked divergence close to T_{CO} . Fitting the data in Figure 61 to a power law for the inverse correlation length, $\xi(t)^{-1} \approx \left(\frac{T - T_{CO}}{T_{CO}}\right)^\nu$, allows the extraction

of ν for the exponent of the correlation length of charge ordering. The fitting gave the value of $\nu = 1.08 \pm 0.2$, in excellent agreement with the predicted value of $\nu = 1$ expected for a 2-dimensional system.

In conclusion, we have shown that 2-dimensional disordered charge stripes are formed below T_{CO} in a single crystal of $\text{La}_{5/3}\text{Sr}_{1/3}\text{NiO}_4$. The correlation length of these charge stripes does not increase as the temperature is lowered significantly below T_{CO} , indicating that the length scale of the disorder is quenched at low temperatures. We have obtained quantitative measurements of the correlation lengths and critical exponents that demonstrate this reduced dimensionality. In addition we have, for the first time, observed critical fluctuations above T_{CO} and up to

$T_{CO} + 20$ K which also demonstrate that within these fluctuations the stripes are still two-dimensional. The doping with Sr provides extra holes to form the striped structure in the NiO planes, and it is likely that the stripes are disordered by the strain energy resulting from the mismatch of the radius of cations of La ($r_A = 1.26$ Å) and Sr ($r_A = 1.31$ Å).

Principal Publication and Authors

C-H. Du (a), M.E. Ghazi (a), Y. Su (a), I. Pape (a), P.D. Hatton (a), S.D. Brown (b,c), S-W. Cheong (d,e), *Phys. Rev. Lett.*, **84**(17), 3911-3914 (2000).

(a) Department of Physics, University of Durham (UK)

(b) ESRF

(c) Department of Physics, University of Liverpool (UK)

(d) Department of Physics and Astronomy, Rutgers University, New Jersey (USA)

(e) Bell Laboratories, Lucent Technologies, New Jersey (USA)

Charge Ordering and Forbidden Reflections in Magnetite

Mixed valence transition metal oxides exhibit many interesting properties such as superconductivity, colossal magnetoresistance and metal insulator phase transitions. Generally, the description of the electronic state of these compounds is made on the basis of the ionic model and it implies the spatial or temporal charge localisation on the transition metal atoms.

Magnetite was the first material in which a charge ordering transition was proposed to explain the metal insulator phase transition which occurs at 125 K [1]. The classical mechanism to describe this transition states that the distribution of octahedral Fe^{3+} and Fe^{2+} ions changes from dynamical disorder to long range order by lowering the temperature. Nevertheless, this point has not yet been demonstrated.

We report the observation of the d-glide plane 002 and 006 forbidden reflections, below and above the Verwey transition (125 K), by means of X-ray resonant scattering at the iron K-edge [2]. Experiments were performed at beamline **BM2** (D2AM French CRG). The energy dependence of the intensity of the 002 and 006 reflections, with the X-ray beam polarisation along the [110] direction, at 20 K and at room temperature is shown in **Figure 62** together with the fluorescence spectrum. As it can be observed, the energy dependence of the scattered intensity is the same for both temperatures. No detectable intensity

below the absorption edge was observed. Three main features can be distinguished on the spectra as a function of the energy [3]: a) a resonance at the pre-peak energy of the fluorescence spectrum corresponding to a virtual excitation and de-excitation through dipolar-quadrupolar channels at the tetrahedral iron atom b) a strong resonance at the 1s-4p energy transition, due to the anisotropy of the dipolar scattering factor of octahedral iron atoms at the trigonal ($-3m$) site. iii) the extended part above the edge that has the same origin as the main resonance and shows

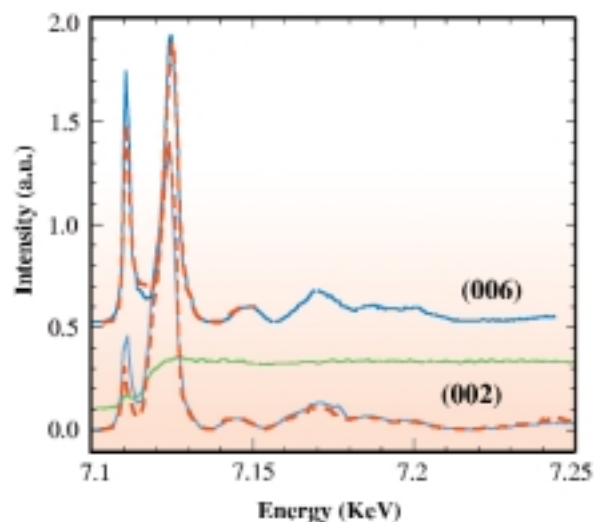


Fig. 62: Intensity versus photon energy of 002 and 006 forbidden reflections with the incident light polarisation vector parallel to the [110] crystallographic direction. The spectra have been recorded at 20 K (- - -) and room temperature (—). The fluorescence spectrum is also shown. The fluorescence background was subtracted but the spectra are not corrected for self-absorption.

an oscillatory behaviour as a function of the energy. The oscillatory signal is a sum of cosine terms whose frequencies are proportional to the differences in distance of the coordination shells. This is the first time that anisotropy of the atomic scattering factor in the extended part is reported and a coherent explanation of its origin is discussed. The dependence of the integrated reflection intensity, at 7124 eV, as a function of the azimuthal angle ϕ , is shown in **Figures 63a** and **63b** for the two reflections. The theoretical azimuthal dependence (solid lines) is sketched as total, $[(\sigma - \sigma) + (\sigma - \pi)]$ and $(\sigma - \sigma)$ channel, intensities. The analysis of the experimental data show that the anomalous scattering factor is anisotropic but identical for all the octahedral iron atoms at room temperature and remains unaltered across the Verwey transition. As a matter of fact, it is well established that the main difference of the

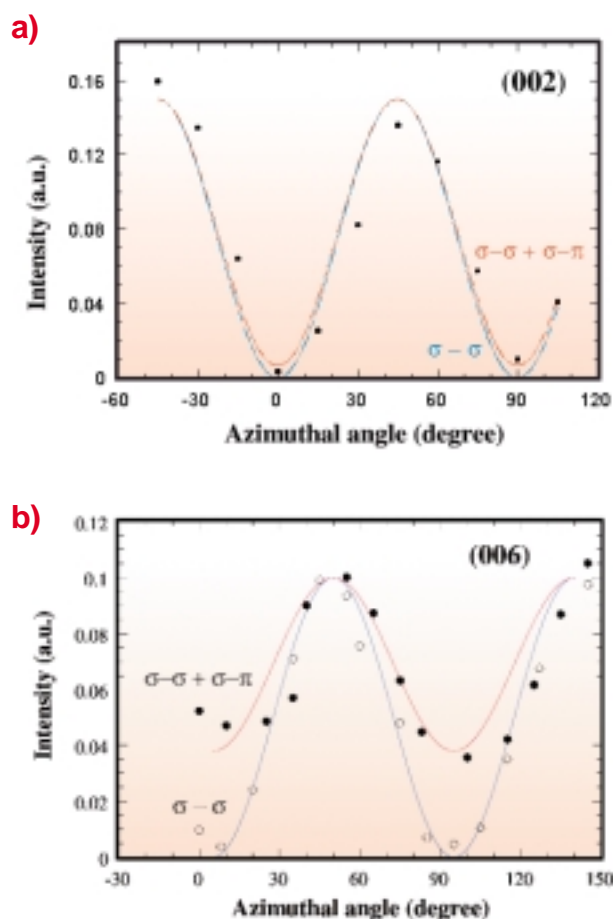


Fig. 63: Dependence of the integrated reflection intensity, at 7124 eV, as a function of the azimuthal angle ϕ , for the two reflections 002 and 006. The theoretical azimuthal dependence (solid lines) is also shown for the $[(\sigma - \sigma) + (\sigma - \pi)]$ and $(\sigma - \sigma)$ channels and compared with the experimental intensities measured without (●) and with (○) analyser (MgO (222)).

anomalous scattering factors between different oxidation states is given by the chemical shift (edge splitting). In the case of Fe^{3+} and Fe^{2+} , the chemical shift is between 3 and 5 eV, appreciably larger than the calculated splitting due to the anisotropy (1 eV), so charge fluctuation at room temperature with a time duration longer than the interaction time for the virtual process involved (10^{-16} sec), would destroy the structural coherence for diffraction. The identical behaviour (energy and azimuthal dependence) for both, low and room temperature phases, discard a charge localisation in a periodic arrangement. As a general conclusion we can say that octahedral iron atoms in magnetite can not be described as pure ionic Fe^{3+} or Fe^{2+} ions, neither spatially or temporally. As a consequence, the metal-insulator transition is likely produced by

crystallographic distortion rather than by charge localisation.

References

- [1] E.J.W. Verwey, *Nature*, **144**, 327 (1939).
- [2] D.H. Templeton, L.K. Templeton, *Acta Cryst.* **A36**, 237 (1980).
- [3] J. Garcia, G. Subias, M.G. Proietti, H. Renevier, Y. Joly, J.L. Hodeau, J. Blasco, M.C. Sanchez, J.F. Berar, *Phys. Rev. Lett.*, in press.

Authors

- J. Garcia (a), G. Subias (a), M.G. Proietti (a), J. Blasco (a), H. Renevier (b), J.L. Hodeau (b), Y. Joly (b).
 (a) Instituto de Ciencia de Materiales de Aragón, Consejo Superior de Investigaciones Científicas y Universidad de Zaragoza (Spain)
 (b) Laboratoire de Crystallographie, CNRS, Grenoble (France)

Neutral-Ionic Layered Ordering and Condensed Charge-Transfer Exciton-Strings in DMTTF-CA

One of the most fascinating features of some organic materials is the possibility to tune between different ground states. This situation especially occurs in some quasi-one-dimensional charge-transfer (CT) complexes with a mixed-stack architecture, where the alternation of electron donor (D) and electron acceptor (A) molecules gives rise to chain multistability between a regular neutral (N) state $\dots\text{D}^{\circ}\text{A}^{\circ}\text{D}^{\circ}\text{A}^{\circ}\text{D}^{\circ}\text{A}^{\circ}\dots$ and two degenerate dimerised ionic (I) states $\dots(\text{D}^+\text{A}^-)(\text{D}^+\text{A}^-)(\text{D}^+\text{A}^-)\dots$ and $\dots\text{D}^+(\text{A}^-\text{D}^+)(\text{A}^-\text{D}^+)(\text{A}^-\text{D}^+)\dots$. At finite temperature the thermal excitation of boundaries between "phases" destroys any long range order and the isolated chain becomes intrinsically inhomogeneous with the condensation of structurally relaxed CT exciton-strings. Inter-chain coupling in the crystal can drive phase transitions [1], and thus the so-called N-I transition may be induced by temperature, pressure and also light. Crystalline interchain organisations may lead to different ordering schemes, such as the interesting possibility for this transition to occur in stages ("staging") due to frustrated interstack Coulomb interactions, when, between certain planes, each D (or A) has other D (or A) nearest neighbours [2]. It has been theoretically predicted that N layers may be inserted between I layers to reduce the Coulomb repulsion,

so that multiple periodic long range ordering may occur in the ground state within an infinite stepped sequence of first order transitions (Devil's staircase). It is of fundamental interest to obtain some experimental evidences of such complex charge ordering phenomena due to long range Coulomb and electron-lattice interactions.

We have performed high resolution X-ray scattering measurements on **BM2** (the D2AM CRG beamline) on the 2,6-dimethyltetrahydrofulvalene- p-chloranil (DMTTF-CA) which appears from spectroscopic measurements as a good candidate. We have observed below $T_c = 65.5$ K, and in a direction perpendicular to the stack axis, the emergence of superstructure Bragg peaks characteristic of a cell-doubling. This constitutes the first direct structural evidence of periodic ordering of neutral and ionic planes. The structural analysis has shown that simultaneously to the neutral-ionic layer ordering, theoretically expected, an antiparallel dimerisation ordering takes place, leading to an unconventional "ferrielectric" structure (Figure 64).

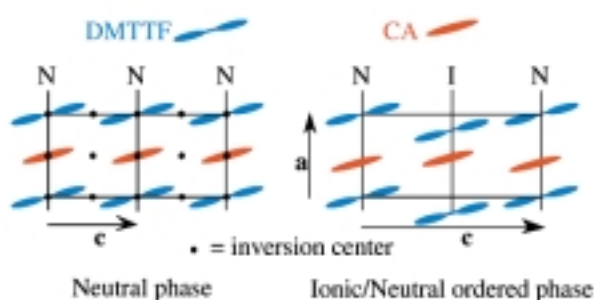


Fig. 64: Schematic drawing of the Neutral-Ionic layer ordering and of the ferrielectric arrangement by crossing the transition in DMTTF-CA.

An important physical feature of the observed phenomenon is the interplay between the staging ordering and the CT exciton-string condensation. Thus, instead of a multistep behaviour, only one cell-doubling occurs related to the largest plateau of the Devil's staircase with a continuous evolution of the order parameter, as evidenced by the temperature evolution of superstructure peak intensity. Above T_c , diffuse quasi-planes perpendicular to the stacking axis are clearly observed (Figure 65). This is a direct signature of the quasi-one dimensional nature of these compounds and gives the first direct estimation of the size of condensed-relaxed CT exciton-strings (more than 100 Å). These non-linear excitations are at the heart of the unusual physical properties of these systems, in particular of the photo-induced phase transformations due to cooperative electron transfer, which has begun to be studied by ultrafast time-resolved crystallography on ID9 beamline.

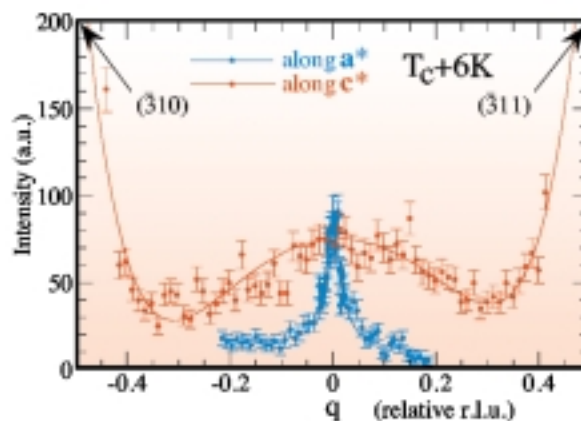


Fig. 65: Scans at $T_c + 6$ K around $(\bar{3} 1 0.5)$ showing diffuse (b^*, c^*) planes (BM2, $\lambda = 1.04$ Å). The diffuse scattering along b^* , similar to the one plotted along c^* , is not shown here for clarity. The lines are guides for the eye.

References

- [1] M.H. Lemée-Cailleau, M. Le Cointe, H. Cailleau, T. Luty, F. Moussa, J. Roos, D. Brinkmann, B. Toudic, C. Ayache, N. Karl, Phys. Rev. Lett., **79**, 1690-1693 (1997).
- [2] J. Hubbard, J.B. Torrance, Phys. Rev. Lett, **47**, 1750-1754 (1981) and R. Bruinsma, P. Bak, J.B. Torrance, Phys. Rev. B, **27**, 456-466 (1983).

Principal Publication and Authors

- E. Collet (a), M. Buron-Le Cointe (a), M.H. Lemée-Cailleau (a), H. Cailleau (a), M. Meven (b), S. Mattauch (b), G. Heger (b), J.F. Béarar (c), N. Karl (d), Phys. Rev. Lett, submitted.
- (a) Université Rennes 1, GMCM, UMR-CNRS 6626, Rennes (France)
 (b) RWTH, Institut für Kristallographie, Aachen (Germany)
 (c) ESRF and CNRS, Grenoble (France)
 (d) Universität Stuttgart, Physikalisches Institut (Germany).



Introduction

We present here the results obtained in the study of the magnetic properties of solids. The use of X-rays is today a very well established technique, which is highly complementary to those involving neutrons.

The examples described here have been obtained on 9 different beamlines and concern six different techniques (Compton scattering, nuclear scattering, magnetic scattering, dichroism, emission spectroscopy, powder diffraction). Quite often the experiments are done near an absorption edge, giving direct information on the element and the electron shell.

Until recently, resonant magnetic scattering was mostly used to study elements that have a magnetic moment. The results described below on the uranium compounds show that very interesting information can be obtained at the anion K edge, specially if combined with dichroism measurements. The size of the signal observed in the dichroism experiment is astonishing: 250 times larger than the amplitude at the iron K edge in pure ferromagnetic iron! In the magnetic scattering experiment the signal is also very strong and, from polarisation analysis, seems to correspond to a dipole transition. However it is obvious that the signal does not arise from a simple magnetic dipole located at the non-magnetic element because it would have been seen easily by neutrons. The effect is more subtle – probably involving a hybridisation of anion p orbitals and uranium 5f magnetic states.

Since the discovery in 1988 of the giant magnetoresistance in magnetic multilayers, a lot of experiments have been performed by various techniques to study the

magnetic properties of systems with reduced dimensionality (thin films, clusters, dots, etc.). This is due to the fact that the magnetic properties of a material can be modified by changing the structural parameters. This is nicely illustrated below by the study of one-dimensional nanostructures and by the use of nuclear scattering to observe, for the first time, rotation of the Fe moments in 10 successive Fe layers sandwiched between fcc-Co(100) layers.

Giant Induced Polarisation Effects of Non-Magnetic Elements in Uranium Compounds

When the photon energy is tuned near an absorption edge in either scattering or absorption experiments, a considerable change occurs in the cross section. Most importantly an intermediate excited state is formed, which corresponds to the promotion of a core electron into electronic states above the Fermi level. This process is then followed by the decay of the intermediate into the original state with photon re-emission. As pointed out some ten years ago [1,2], there is a special interest when the electron shells involved in the excited state are spin polarised. The resulting theories and experiments have given rise to two new fields of synchrotron magnetic studies, X-ray magnetic circular dichroism (XMCD) and resonant X-ray magnetic scattering (RXMS). XMCD is sensitive to only the imaginary part of the anomalous scattering amplitude, while RXMS measures the modulus squared of the total scattering amplitude including both the real and imaginary parts of the anomalous scattering. Both techniques have the special advantage that they are element and electron shell specific. In the case of XMCD, sum rules [3], which are based on atomic models, are available for extracting the spin and orbital contributions to the magnetic moments. Of course, practitioners of these two spectroscopic methods have focused almost without exception on elements that have appreciable magnetic moments. However, a series of recent experiments at the ESRF using both dichroism and scattering techniques have been performed at the anion K edge of various uranium compounds. The size of the resonant signal has been a considerable surprise.

Dichroism experiments were performed at beamline ID12A on ferromagnetic uranium sulphide. This material orders below $T_c = 174$ K with a saturation magnetic moment of $1.7 \mu_B$. The measurements were performed at 160 K in an applied external magnetic field of 2 Tesla, using total fluorescence detection mode. The differential XMCD spectrum is obtained by flipping the helicity of the X-rays at each point of the energy scan using the recently installed ElectroMagnet/Permanent magnet Hybrid Undulator [4]. The dichroic signal obtained at the sulphur K-edge is much larger than expected and can be easily seen by simply comparing the XANES spectra recorded for both circular polarisations shown in Figure 66. To check that the experimental results are free from any eventual artifacts, the same spectra were recorded for the opposite direction of the external magnetic field. If one corrects the experimental XMCD spectrum for the circular polarisation rate of the monochromatic beam and for the sample

magnetisation (which is only 15% in this energy range), the amplitude of the signal at the sulphur K-edge is about 25%. This effect is 250 times bigger than the signal at the iron K-edge in pure ferromagnetic iron and also much greater than found at the K edge of sulphur in EuS [5].

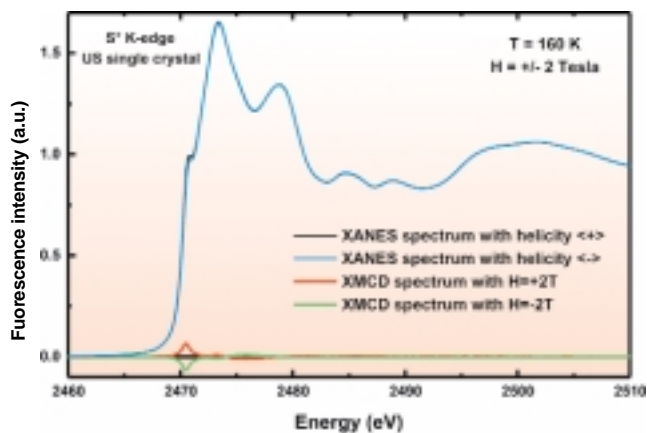


Fig. 66: X-ray magnetic circular dichroism intensity and XANES spectra at the sulphur K edge in ferromagnetic uranium sulphide. XMCD data are presented as measured.

Scattering experiments were first performed on single crystals of antiferromagnetic UGa_3 at the ID20 magnetic scattering beamline. This material orders below $T_N = 67$ K with a moment of $0.6 \mu_B$ on the uranium site and with a magnetic propagation vector of $(1/2, 1/2, 1/2)$. The photon energy was tuned to the K edge of gallium (10.37 keV) at a temperature of 10 K. A very large (by a factor of ~ 1000) enhancement of the small non-resonant magnetic scattering intensity was observed. This is demonstrated by plotting the integrated intensity as a function of incident photon energy in Figure 67a (solid points). The energy width is ~ 4 eV, essentially the expected core-hole lifetime of the intermediate state. Also shown in Figure 67a is the fluorescence spectrum measured in the same experiment (dashed line). The position of the peak in energy strongly suggests that the resonance is dipolar in nature, i.e. involves the 4p electron states of Ga. The signal is present only in the $\sigma \rightarrow \pi$ channel with σ incident polarisation from the synchrotron, again consistent with a dipole transition. Figure 67b shows the intensity as a function of position in reciprocal space. The signal has a periodicity identical to that of the uranium magnetic structure, is long range in real space, and disappears by T_N . Similar effects were subsequently observed in UAs when photons were tuned to the K edge of arsenic. In these experiments intensities of up to 80,000 cts/sec in full polarisation mode were observed on ID20. Such enhancements of the non-resonant scattering signal are much greater than found on other K edges, even those of the magnetic 3d elements.

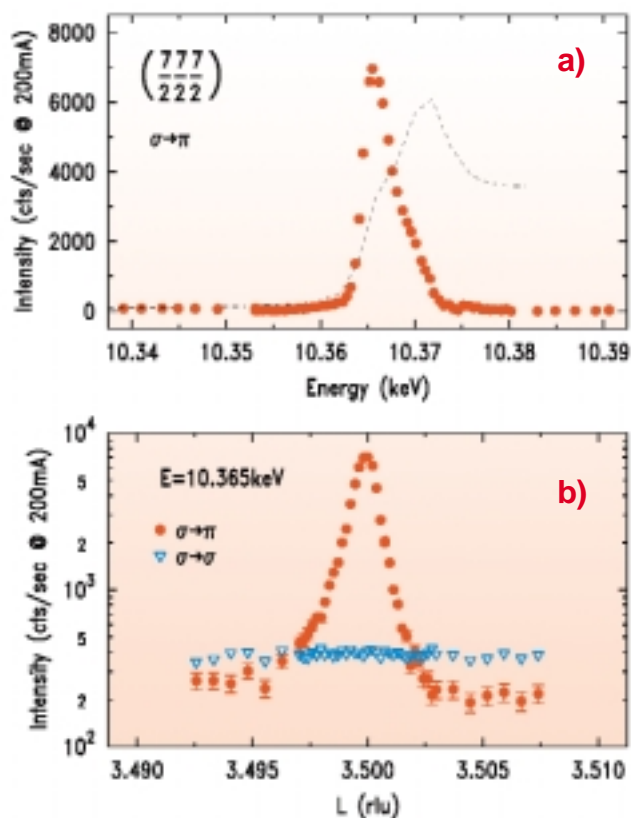


Fig. 67: Resonant X-ray magnetic scattering intensity associated with Gallium K edge in the antiferromagnet UGa_3 . a) Data points are integrated intensity as a function of incident photon energy. The dashed curve superposed is the fluorescence. The tabulated value of the Ga K edge is 10.37 keV, the data were taken at a temperature of 10 K. b) Intensity at a photon energy of 10.365 keV for the antiferromagnetic Bragg reflection as a function of the longitudinal wavevector $[7/2^7/2^7/2]$, where these are coordinates in reciprocal space. The peaks occur at exactly the same positions as those from the uranium moments, and their narrow width (in q -space) indicates long-range real-space correlations. The higher background in the $\sigma \rightarrow \sigma$ channel arises from the specular charge truncation rod.

In all experiments reported here, the signal does not arise from a simple magnetic dipole situated at the non-magnetic element – its size would have to be so large that it would have been seen easily by neutron scattering. The effect is undoubtedly more subtle than that, perhaps involving the hybridisation of the anion p orbitals with the uranium 5f magnetic states. Theory continues to address the underlying physics, but the experiments open new perspectives using resonant effects, which will certainly be the subject of future efforts.

References

- [1] D. Gibbs et al., Phys. Rev. Lett., **61**, 1241 (1988); J.P. Hannon et al., Phys. Rev. Lett., **61**, 1245 (1988).
- [2] G. Schütz et al., Phys. Rev. Lett., **58**, 737 (1987).
- [3] P. Carra, M. Altarelli, Phys. Rev. Lett., **64**, 1286 (1990).
- [4] A. Rogalev et al., Proc. SPIE, **4774**, 275 (1999).
- [5] A. Rogalev et al., J. Phys. Cond. Matter, **11**, 1115 (1999).

Authors

RXMS: D. Mannix (a,b), L. Paolasini (b), N. Bernhoeft (c), A. Stunault (b), C. Vettier (b,d), D. Kaczorowski (e), G.H. Lander (a); XMCD: A. Rogalev (b), J. Goulon (b), J.P. Sanchez (c), N. Kernavanois (c).

(a) ITU, Karlsruhe (Germany)

(b) ESRF

(c) CEA-Grenoble (France)

(d) ILL, Grenoble (France)

(e) Polish Academy of Sciences, Wroclaw (Poland)

The Magnetism of One-Dimensional Nanostructures Studied by Magnetic Circular Dichroism: Fe on Cu(111)

The constant demand for higher storage density in the magnetic device industry explains the recent and dramatic increase of interest in nanostructures. In order to produce nanoparticles with high magnetisation and stable properties the basic physics of these particles needs to be understood. As a model system, we have chosen the epitaxial growth of iron on a Cu(111) substrate. Depositing iron on a copper single crystal allows iron to be stabilised at room temperature in its fcc phase (γ -Fe). For bulk Fe this phase only appears at temperatures (>1186 K) above the Curie temperature. Moreover, the magnetic structure of the γ -Fe strongly depends on its lattice constant. In general theory predicts for γ -Fe an increasing magnetic moment, as well as ferromagnetic coupling, with increasing lattice parameter [1]. Since the Cu substrate has a lattice parameter slightly bigger than γ -Fe at equilibrium, we can expect γ -Fe to have a higher moment for pseudomorphic growth.

To obtain nanostructures we take advantage of the step decoration effect of Fe grown on vicinal Cu(111). This surface is characterised by monoatomic steps and regular 10 nm wide terraces. As Fe atoms are deposited they tend to nucleate along the steps thus forming 1-D Fe stripes [2]. Going from a few percent of a monolayer (ML) to 4 ML, we cover the whole thickness range of interest for the γ -Fe. In particular below the 0.8 ML thickness range, the Fe forms

essentially elongated clusters of low extension (less than 3000 atoms per cluster) and from 0.8 ML to ~1.5 ML the Fe forms 1-D stripes with increasing width, until 2-dimensional percolation occurs. Thus we expect a dependence of the magnetic properties both on size (growth of nanoparticles) and on structure (high sensitivity of γ -Fe magnetic properties to small structural changes).

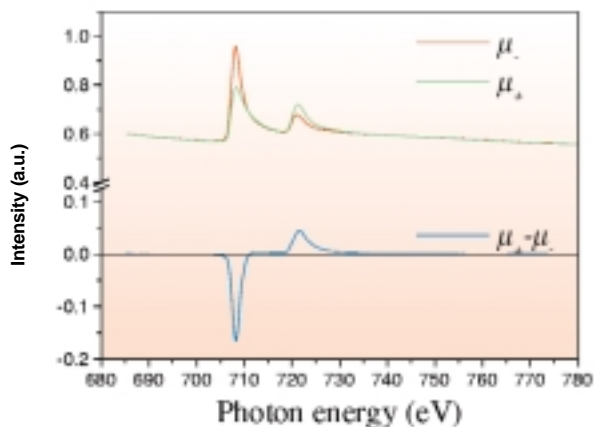


Fig. 68: Typical XMCD spectra for a coverage of 0.13 ML of Fe/Cu(111)-vic (total electron yield mode). μ_+ and μ_- correspond respectively to the geometry where the magnetic field has the same or opposite direction as the circular polarised light. This measurement has been made at normal incidence ($\gamma = 0^\circ$), $T = 20$ K and $H = \pm 4$ T.

The magnetic characterisation was done at the beamline **ID12B** using X-ray magnetic circular dichroism (XMCD) at the Fe $L_{2,3}$ absorption edges. An example for 0.13 ML of Fe/Cu(111) can be seen in **Figure 68**. The dichroic signal, i.e. the difference between two absorption spectra taken with opposite circular polarisation, allows a quantitative determination of the magnetic moment using magneto-optic sum rules.

In **Figure 69** we plot the magnetic spin (m_{spin}) and orbital (m_{orb}) moments per hole in the 3d band, as deduced from our XMCD measurements. Several observations can be made: The increase of the magnetic moment above ~2 ML is due to the start of the fcc to bcc phase transition. The bcc phase with larger magnetic moments dominates at 4 ML where we obtain the values for bulk bcc Fe. The clear increase of the orbital moment at low coverage is due to size effects, as it is well known that a more atomic-like structure, like at a surface or in a cluster, leads to an enhancement of the orbital moment. However, the most striking result is the observation of two low-spin phases, LS1 and LS2 (**Figure 69**), above and below 0.8 ML thickness that corresponds to the coalescence of the clusters into 1-D stripes. The presence of these two

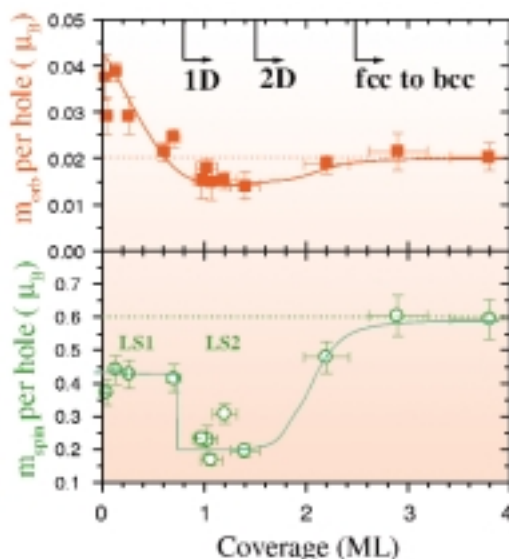


Fig. 69: Orbital (a) and spin magnetic moment (b) per hole as a function of the coverage. The solid lines are only to guide the eyes. The dashed lines correspond to the values for the magnetic moments commonly accepted for bulk bcc Fe. The arrows on the top scale at 0.8 ML, 1.5 ML and 2.5 ML correspond to the approximate coverages where the Fe starts to coalesce into a 1-D wire, reach the 2-D percolation and undergoes the fcc to bcc phase transformation, respectively.

magnetic phases is tentatively ascribed to a structural relaxation: the Fe clusters, purely pseudomorphic at low coverage ($a_{\text{Fe}} = a_{\text{Cu}} = 3.61$ Å), undergo a strain relaxation to their stable value ($a_{\text{Fe}} = 3.59$ Å) once they coalesce and form a larger structure. This decrease in the volume could explain the decrease in m_{spin} for the LS2 phase.

In conclusion, this type of study can lead to a basic understanding of the effect of size and structural changes caused by reducing the size of magnetic nanoparticles.

References

[1] V. L. Moruzzi, P.M. Marcus, J. Kübler, Phys. Rev. B, **39**, 6957 (1989).
 [2] J. Shen, M. Klaua, P. Ohresser, H. Jenniches, J. Barthel, Ch.V. Mohan, J. Kirschner, Phys. Rev. B, **56**, 11134 (1997).

Authors

P. Ohresser (a), G. Ghiringhelli (a), O. Tjernberg (a), M. Finazzi (b), N.B. Brookes (a).
 (a) ESRF
 (b) TASC-INFN, Elettra Synchrotron Light Source, Trieste (Italy)

Magnetism: From Monolayers to Multilayers

The properties of surfaces and interfaces have drawn considerable interest in recent years. Phenomena such as giant magneto-resistance, interlayer coupling, and interface anisotropy are current topics of discussion. Nuclear resonance scattering makes a handy experimental tool which is capable of contributing to the field on an atomistic scale. The scattering process proceeds via nuclear resonances lying in the hard X-ray regime, with a very high cross-section and remarkable optical activity. This high cross-section opens the possibility of studying monolayer systems even when they are buried. Additionally, due to selection rules and optical activity, the technique is very sensitive for the determination of internal fields (hyperfine fields), their magnitudes and directions. Depending on the chosen geometry of the wave vector \mathbf{k} , the polarisation ε of the X-rays, and the external and internal magnetic fields, contributions of different transitions such as $\Delta m = \pm 1$ and $\Delta m = 0$ might give very pronounced and different spectra. Being a time resolved technique, it benefits from the excellent time structure of synchrotron radiation and an outstanding signal-to-noise ratio. Each type of magnetism (ferro-, ferri-, antiferro-, para-, dia-magnetism), either static or dynamic, can be studied.

The following examples were studied at ID18 utilising the ^{57}Fe resonance at 14.4 keV. The beamline offers the corresponding sample environment: a 6-8 circle diffractometer and cryo-magnet systems mounted on circles for grazing incidence scattering experiments.

Non-collinear Magnetism in fcc-Fe/Co (100) Films

A fundamental issue in solid state physics is the relation between atomic geometry and magnetism. Being at the borderline between antiferromagnetically and ferromagnetically-ordered transition metals Fe is an exemplary case for the influence of structural effects on the magnetic properties. It is well known that the magnetic structure of Fe can be altered by modifying the structural parameters. In particular, while metallic Fe is a simple ferromagnet in its normal bcc structure, it is theoretically expected to be ordered antiferromagnetically in the fcc structure for a certain range of lattice parameters.

We investigated the magnetic structure of thin, 2-10 atomic layers (ML), epitaxial fcc-Fe films sandwiched between fcc-Co(100) layers on a Cu(100) single crystal substrate at room temperature. Two different kinds of samples were grown: (i) a fcc- ^{57}Fe film with a wedge of 2-10 ML (wedge

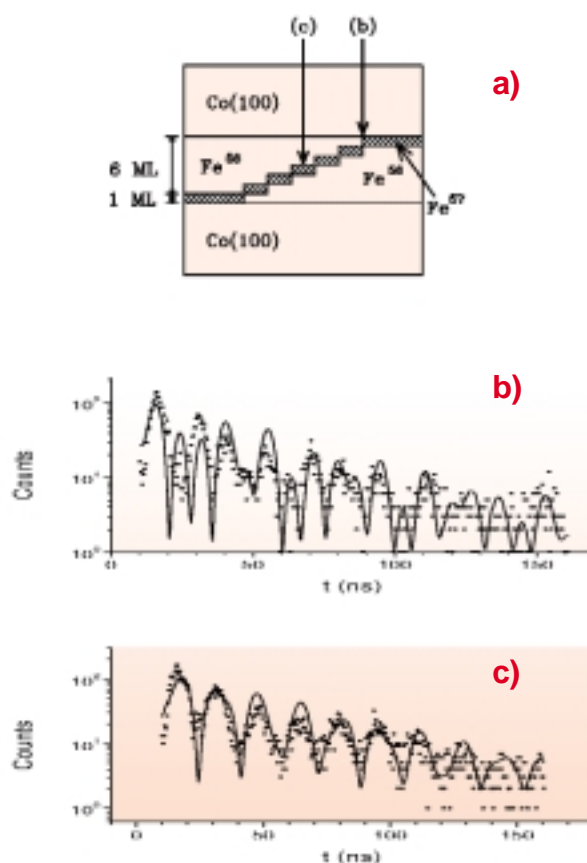


Fig. 70: (a) Scheme of the sample with a uniform fcc-Fe film with a thickness of 7 ML. A single ^{57}Fe monolayer is inserted at various positions within the ^{56}Fe film. Layer-resolved spectra have been measured by scanning the beam transversely over the sample. Time spectrum of nuclear specular reflection from the ^{57}Fe layer at the interface (b) and from the ^{57}Fe layer in the centre of the Fe film (c), respectively.

slope 1 ML/mm), and (ii) a 7 ML Fe film with a single ^{57}Fe monolayer at various positions within the ^{56}Fe film (see Figure 70a).

By scanning the X-ray beam over the wedge, one measures the quantum beat pattern in the time spectrum of nuclear specular reflection originating from different thicknesses and different depths of the sample, respectively. The interference pattern demonstrates that the Fe films are magnetically ordered at room temperature for all thicknesses. This implies an enhanced ordering temperature with respect to the Néel temperature and the surface Curie temperature reported for fcc-Fe films on Cu(100).

Further analysis of sample (i) gave an unexpected magnetic structure which could not be explained by any simple pattern. However, the analysis of the quantum beat spectrum from sample (ii) (Figure 70 (b,c)) gave a clear result of the magnetic structure at different depths. The hyperfine field vector at the interface lies close to the

film plane, whereas it points at an angle of more than 60° from the film plane in inner atomic layers. These results also permit an explanation of the magnetic structure of sample (i).

The results provide evidence for an unexpected non-collinear magnetic structure at the interface formed by these two materials, where the orientation of the Fe moments coherently rotates in successive atomic layers. This appears to be the first established case of non-collinear magnetism among all ultrathin films of itinerant magnetic systems.

Anti-ferromagnetic Coupling and Spin Fluctuations in Thin Fe₃O₄ Films

Thin epitaxial layers of Fe₃O₄ on MgO(100) show a number of surprising features in their magnetic behaviour. It is difficult to reach magnetic saturation, which is related to the fact that the magnetic moments point out of the plane in zero field. Ultrathin layers ($d \leq 5$ nm) lose their magnetisation completely at room temperature because of spin fluctuations. It has been argued that these phenomena are caused by the presence of antiphase boundaries between structural domains that are bound to form in the

Fe₃O₄ layer because its lattice constant is twice that of the MgO substrate.

A 15 nm thick ⁵⁷Fe₃O₄ layer was investigated at 280 K in magnetic fields up to 5 T, using a grazing incidence geometry. Some representative spectra are displayed on the left of Figure 71. The spectra can be fitted with the two components known from bulk Fe₃O₄. The A-site (tetrahedral) Fe³⁺ ions have a positive hyperfine field whereas the B-site (octahedral) Fe ions, which have an average charge of +2.5, have the field in the opposite direction. In a field of 5 T only the $\Delta m = \pm 1$ transitions contribute to the spectrum, in agreement with the fact that the spins are aligned in the magnetic field, which was oriented in the plane of the sample and perpendicular to the photon beam.

However, in lower magnetic fields the $\Delta m = 0$ transitions are also present, showing that not all magnetic moments are aligned along the magnetic field. It is possible to describe this behaviour quantitatively by the following model. Across an antiphase boundary (APB), spins at B-sites are strongly coupled antiferromagnetically. To minimise their magnetic energy, they turn perpendicular to the magnetic field while staying in the plane of the APB. Because the field is in the plane of the layer, these spins must turn perpendicular to

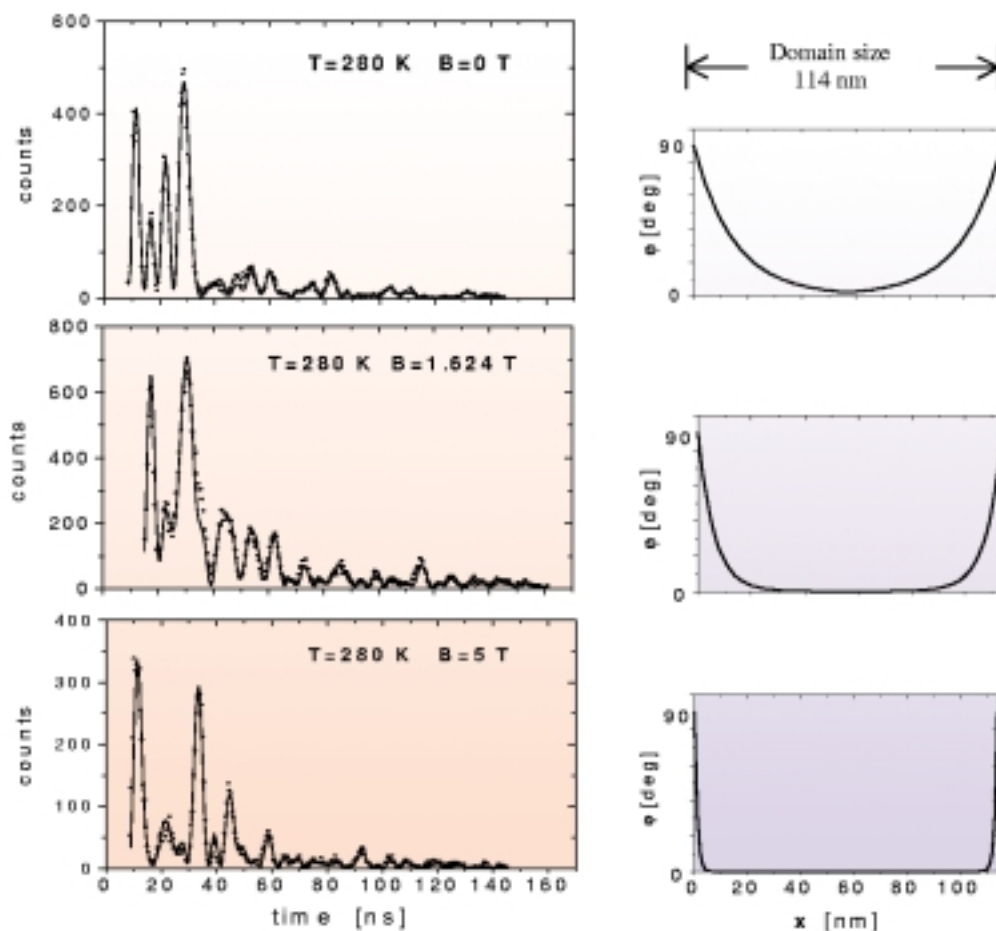


Fig. 71: Left panels: Time spectrum of nuclear specular reflection from a thin Fe₃O₄ layer in various magnetic fields. Right panels: corresponding orientation of the magnetic moments within a structural domain. ϕ is the angle between the spin orientation and the magnetic field which lies in the sample plane. The measurement is only sensitive to the magnitude of ϕ .

the sample plane. The orientation of neighbouring spins is governed by the competition between the exchange interaction, which tries to keep the spins (anti) parallel and the magnetic field (external field plus shape anisotropy field), which tries to align them in the sample plane. The only adjustable parameter in this model is the average distance between the APB's.

Fits to the spectra using this model are shown in the same figure. The panels on the right show the corresponding spin profile, i.e. the orientation of the spins as a function of their distance to the APB. The resulting average size of the structural domains, 114 nm, is in reasonable agreement with estimations from electron microscope pictures.

Bulk Spin Transition in a Magnetic Superlattice

Metallic multilayers built from ferromagnetic layers separated by non-magnetic spacer layers often show antiferromagnetic (AF) interlayer coupling, a well-known example being the Fe/Cr system. Besides their interlayer interaction J , the layer magnetisations \mathbf{M} experience the magneto-crystalline anisotropy A . Of particular interest as a model system are Fe/Cr superlattices of an even number of magnetic layers with external magnetic field \mathbf{H}_{ext} in the magnetocrystalline easy axis of Fe. In case of a fourfold anisotropic symmetry and with the provision that \mathbf{M} of each Fe layer is confined to the sample plane, for $H_{\text{ext}} = 0$ one has two, mutually perpendicular, initial directions of equal energy of the magnetisation axis. In nonzero external fields one of the anisotropy-stabilised configurations becomes energetically unfavourable and, at a certain critical external field depending on the J/A ratio, it moves to a more favourable state. This is an example of the bulk spin flop (BSF) transition, a well-known phenomenon in atomic antiferromagnets. Nevertheless, the first evidence of a BSF transition in a multilayer is new and the change of the direction of the layer magnetisation during a BSF transition in multilayers has not yet been directly observed.

BSF was experimentally studied on a MgO(001) / $[^{57}\text{Fe}(25\text{\AA})/\text{Cr}(14\text{\AA})]_{20}$ superlattice at 294 K. The magneto-optical Kerr effect was indicative of AF coupling with a saturation field of about 1 T and of BSF at a field about 25 mT. The epitaxial relationship on MgO(001) substrate is MgO(001)[110]/Fe(001)[100], therefore the magnetisation of the individual Fe layers points parallel or anti-parallel to either of the Fe[010] or Fe[100] axes in the film plane (cf. the blue double arrows in inset 1 of Figure 72).

First the sample was saturated in plane in one of the easy directions (inset 2) then the external field was decreased to zero (inset 3), and then the sample was turned in plane by

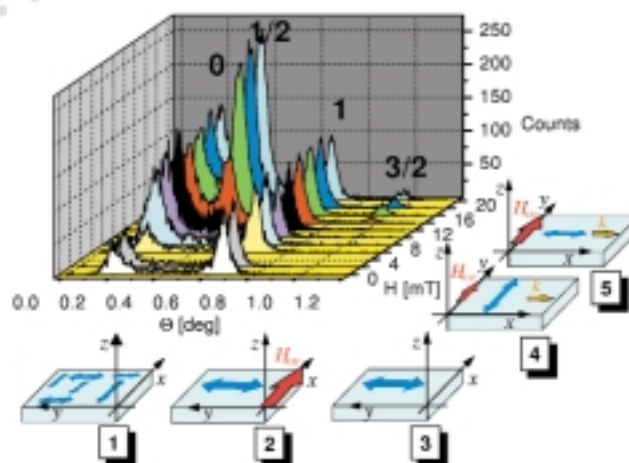


Fig. 72: Time integral nuclear reflection curves taken on a MgO(001)/ $[^{57}\text{Fe}(25\text{\AA})/\text{Cr}(14\text{\AA})]_{20}$ superlattice in increasing magnetic field. The appearance of the antiferromagnetic reflections shows the rotation of the layer magnetisations at the bulk spin flop transition. The system of co-ordinates is fixed to the superlattice.

90° and time integral angular scans were recorded as a function of increasing external magnetic fields (insets 4 and 5) at a grazing angle between 0° and 1° . The scattering plane was vertical and the wave-vector \mathbf{k} was perpendicular to the in-plane magnetic field. Under such conditions, no AF superreflections can be observed in the time integral scans if \mathbf{M} is perpendicular to \mathbf{k} but they will appear if \mathbf{M} is parallel to \mathbf{k} . The spectra in Figure 72 are a series of time integral scans taken in increasing magnetic fields up to 25 mT. The appearance of the 1/2 and 3/2 order AF reflections from 14 mT on is a direct evidence of the 90° rotation of the Fe layer magnetisations, i.e. of the BSF process. The peaks 0 and 1 are the total reflection peak and the first order structural Bragg reflection, the latter being used for arbitrary normalisation of the spectra. This state is preserved after the magnetic field is removed because of the fourfold symmetry of the anisotropy.

Principal Publications and Authors

C. Carbone (a), A. Dallmeyer (a), M.C. Malagoli (a), K. Maiti (a), J. Wingbermühle (a), W. Eberhardt (a), D.L. Nagy (b), L.H. Bottyán (b), L. Deák (b), E. Szilágyi (b), R. Rüffer (c), O. Leupold (c), to be published.

(a) Institut für Festkörperforschung des Forschungszentrums Jülich (Germany)

(b) KFKI Research Institute for Particle and Nuclear Physics Budapest (Hungary)

(c) ESRF

L. Kaley (a), T. Hibma (a), F.C. Voogt (a), L. Niesen (a), R. Rüffer (b), O. Leupold (b), to be published.

(a) Nuclear Solid State Physics, Materials Science Centre,

Groningen (The Netherlands)
(b) ESRF

L. Bottyán (a), J. Dekoster (b), L. Deák (a), B. Degroote (b),
E. Kunnen (c), C. L'abbé (b), G. Langouche (b), O. Leupold
(d), M. Major (a), J. Meersschant (b), D.L. Nagy (a),
R. Rüffer (d), to be published.

(a) KFKI Research Institute for Particle and Nuclear
Physics Budapest (Hungary)

(b) IKS KU Leuven (Belgium),

(c) VSM KU Leuven (Belgium)

(d) ESRF

High Pressure X-ray Absorption Studies of Magnetism

Magnetovolumic effects are essential in many applications of bulk magnetic materials produced in high quantities and with widespread use. Magnetostrictive properties yield actuators which can be micrometric in size, as in medical applications: valves or motors can be produced with the best force/weight ratio and the unique advantage of use without connecting leads. More recently, the study of element-selective magnetovolumic properties has been triggered from the worldwide interest in nanoparticles grown by epitaxy on surfaces. Due to the epitaxial constraint, a significant reduction in atomic volume occurs when compared with the bulk material.

The volume occupied by a magnetic atom drives its microscopic properties, magnetisation and anisotropy, through its hybridisation with its neighbours. Element selective X-ray Magnetic Circular Dichroism carried out under pressure is a direct way to evaluate the magnetism induced on a specific non-magnetic element (5d) due to the hybridisation with a magnetic (3d) element in an alloy. XMCD is an orbital moment-sensitive probe, and due to the spin-orbit interaction it is also sensitive to spin. Therefore it is able to probe the strength of the spin hybridisation as it varies with pressure, i.e. with interatomic distance.

Thanks to the excellent focusing properties of its energy dispersive spectrometer, and to the availability of a Quarter Wave Plate to tune the helicity of the incoming photons, ID24 can undertake such lines of research. However, such experiments impose severe constraints on beam stability, since a very small signal (the XMCD signal in the hard X-ray range is of the order of 10^{-3}) has to be measured on samples in Diamond Anvil Cells. The increased stability of the beam resulting from the recent installation of the local feedback has finally made possible such experiments on ID24.

The Pt₃Cr alloy is a good candidate for the investigation of volume-dependent magnetism. Recent works [1,2] report on the very unusual magnetism of Pt 5d bands in this alloy: the L₃ and L₂ XMCD signals have the same sign, meaning that the dominant contribution to the magnetic signal is due to the orbital moment.

Figure 73 illustrates the variation with pressure of the Pt L₂ and L₃ edge XMCD signal in a Pt₃Cr alloy. The initial decrease in the signal reflects the attenuation of the Pt 5d moment, due either to the decrease in the Cr 3d moment or to a change of the magnetic order.

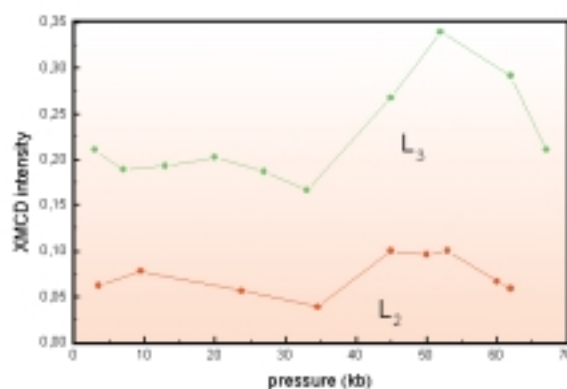


Fig. 73: Integral of Pt L₃ and L₂ XMCD signals on Pt₃Cr as a function of pressure.

The rapid enhancement of both L₂ and L₃ signals at around 35 kb reflects the increase of Pt 5d band magnetic moment. This is induced by the increasing hybridisation between the 3d Cr band and the 5d Pt band with increasing pressure.

The remarkable result of the present study is the constant branching ratio (L₃/L₂) along the pressure domain. This means that there is no variation of the orbital/spin magnetic moment ratio of Pt between 0 and 50 kb which is rather surprising for two reasons. First, because the magnetic moment (here largely given by the orbital moment) is known to be strongly influenced by crystallographic order. Second, because this ratio remains surprisingly insensitive to the reduction of the interatomic distance, which is about 0.7% in this pressure range.

References

- [1] W. Grange et al., J. Synchr. Rad., **6**, 679-681 (1999).
- [2] H. Maruyama et al., J. Magnetism and Magnetic Materials, **43**, 140-144 (1995).

Authors

F. Baudalet (a), J.P. Itié (a), A. Polian (a), J.P. Kappler (b),
A. Fontaine (c), S. Pizzini (c), S. Pascarelli (d), T. Neisius
(d), F. Natali (d), S. Diaz Moreno (d).
(a) PMC Jussieu, Paris (France)

- (b) IPCMS, Strasbourg (France)
 (c) Lab. Louis Néel, Grenoble (France)
 (d) ESRF

Magnetism and Structure: the Fe α - ϵ Phase Transition Monitored by X-ray Emission Spectroscopy

Iron, and specifically iron under extreme conditions of high pressure and temperature, is an element of great importance for its geophysical and practical implications. At room temperature and with increasing pressure, iron shows a phase transition from a bcc (α) phase to a hcp (ϵ) phase at a pressure of 130 Kbar. This transition is found to take place in a ~ 30 Kbar pressure interval. Beside the structural phase transition, one finds also an important change in the magnetic properties of the iron atom: namely iron which is ferro-magnetic in the α -phase becomes non-magnetic in the ϵ -phase. The magnetic properties of iron under pressure and their interplay with the structural phase transitions have been the subject of various theoretical studies.

The investigation of the properties of condensed matter under extreme thermodynamic conditions has received a great impulse since the recent development of very high pressure techniques based on the use of diamond anvil cells (DAC). Using a DAC, it is now possible to bring samples to pressures in the Mbar range. The DAC-based methods have been very successful also when used in combination with intense and small size synchrotron radiation-based X-ray beams, especially those produced at third generation X-ray sources. This has allowed the study of iron's magnetism under high pressure using the ^{57}Fe Mossbauer resonance.

The recent development of high energy resolution X-ray emission spectroscopy (XES) provides an alternative method to Mossbauer to probe the local magnetic properties of atoms. The XES spectra show a series of features which reflect the energies of the different electronic configurations of the excited atom. In particular, we consider an excited atom which has valence electrons with unpaired spins giving rise to a magnetic moment. Here, the exchange interactions between these magnetic electrons and the core electrons in the orbital where the photon emission process has left a core hole are responsible for the appearance of multiplet families in the emission spectrum with a dominant spin character. The energy separation of these families, and therefore the possibility to

observe them easily, is related to the strength of this interaction, which is maximum when the hole is in an orbital with the same principal quantum number, n , of the magnetic electrons. In the case of iron, this situation is obtained for the K_{β} fluorescence line, where the final state hole is in the 3p orbital and the magnetic electrons are in the 3d orbitals.

An experiment was carried out at the inelastic X-ray scattering undulator beamline ID16, aiming to investigate by XES the magnetism in pure Fe under high pressure. The Fe K_{β} line has been measured across the α - ϵ phase transition, taking place around $P_0 = 130$ Kbar. The disappearance at the phase transition pressure of the satellite peak at the low emission energy side of the Fe K_{β} line indicates the collapse of the magnetisation in ϵ -Fe, confirming the earlier Mossbauer studies. This transition takes place at the same pressure of the structural phase transition, and its width is found as sharp as that of both previous structural and magnetic studies. This observation, reported in Figure 74, demonstrates that the XES method can be used successfully to monitor the magnetic properties of materials as a function of thermodynamic variables as temperature and pressure. Therefore it is an alternative and complementary method to Mossbauer spectroscopy, particularly useful for all those atoms without

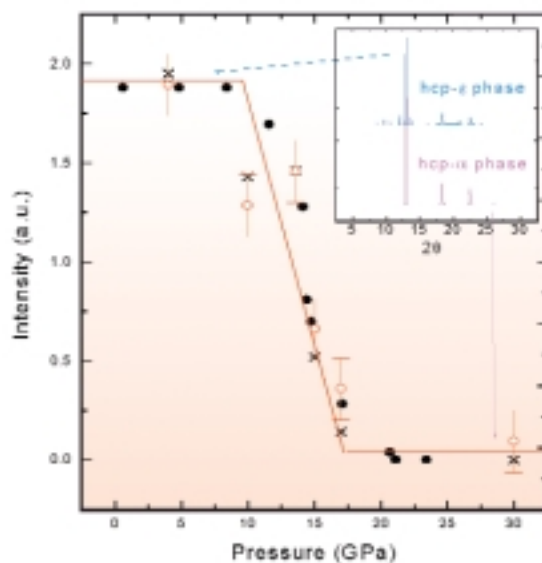


Fig. 74: Integrated intensity of the satellite of the Fe K_{β} line (open circles) compared to the α -phase fraction determined by Mossbauer spectroscopy (Taylor et al., 1991) (solid circles) upon pressure increase. The later curve has been scaled to the low-pressure XES satellite intensity. The solid line is a guide to the eyes. The intensity of the XES satellite was calculated from the difference spectra obtained by subtracting the 230 Kbar spectrum from each scan. The plateau at low (high) pressure corresponds to the magnetic (non-magnetic) phase. The diffraction pattern measured in both phases, shown in the inset, confirms the structural change.

easily accessible isotopes. This new approach is now being exploited to study the magnetism under high pressure of Invar alloys and other magnetic systems.

Principal Publication and Authors

J.P. Rueff, M. Krisch, Y.Q. Cai, A. Kaprolat, M. Hanfland, M. Lorenzen, C. Masciovecchio, R. Verbeni, F. Sette. Accepted for publication in *Physical Review B*, Rapid communications. ESRF

Spin Moments in the Reentrant Ferromagnet SmMn_2Ge_2

The magnetic behaviour of the RMn_2Ge_2 sub-series (R = rare earth) of naturally layered ternary compounds depends critically on the Mn next-neighbour distance. For values greater than 2.87 Å ferromagnetism is observed, whereas below this antiferromagnetic ordering is favoured. Within this sub-series, SmMn_2Ge_2 is a unique case because the Mn-Mn planar distance is approximately equal to this critical value, and numerous magnetisation measurements have shown a complex temperature dependence of the magnetic ordering in the compound. SmMn_2Ge_2 has three magnetically ordered phases. At 345 K (above which the compound is paramagnetic), the material becomes ferromagnetic. Below 155 K, antiferromagnetic ordering occurs, and remains for temperatures down to 105 K, then the compound becomes ferromagnetic once more, i.e., it exhibits re-entrant ferromagnetism. The ordering is strongly anisotropic: in the high temperature ferromagnetic phase, the easy axis lies along the [001] (c-axis) direction, whereas in the low temperature ferromagnetic phase it lies along the [110] (basal plane) direction. As a naturally-layered material, the properties of SmMn_2Ge_2 provide an important complement to studies of artificial multilayer materials, and therefore a full understanding of its magnetisation is essential.

Magnetic Compton scattering, which is uniquely sensitive to the spin component of magnetisation, was used to study the spin density distribution in SmMn_2Ge_2 . The basal plane magnetic Compton profile (MCP) for SmMn_2Ge_2 was measured on the high energy X-ray beamline **ID15A**, with an incident beam energy of 296 keV, and at temperatures of 40 K and 230 K. The MCP measured at 40 K is shown in **Figure 75**, together with model profiles for Sm 4f and Mn 3d electrons based on relativistic Hartree Fock free atom wavefunctions, which have been fitted to the data for the momentum range $p_z > 2$ a.u. The profiles for Mn 3d and Sm 4f electrons are significantly different, the latter being 50%

broader, and therefore fitting at high momenta can be used to separate the moments. This difference in the characteristic widths of the Compton lines can be thought of as simply arising from the fact that the Sm 4f electrons are more tightly bound than the Mn 3d electrons. The position space and momentum space wavefunctions constitute a Fourier pair and thus this difference manifests itself in higher momentum components for the 4f against the 3d electrons: a result which is also evident from simple consideration of the uncertainty principle.

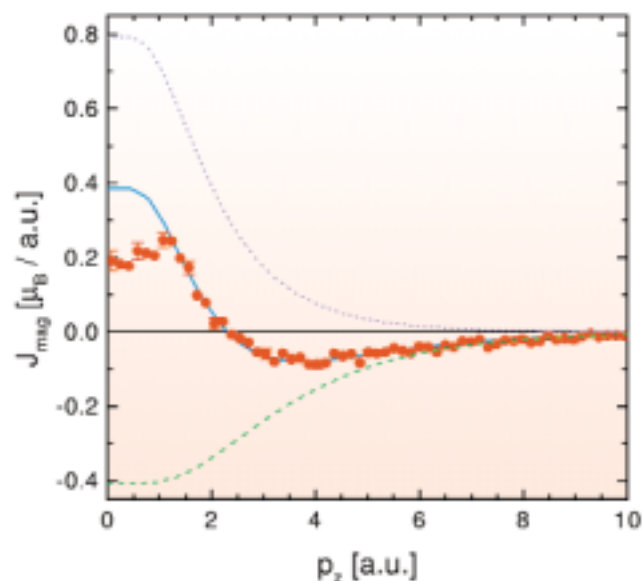


Fig. 75: The experimental magnetic Compton profile of SmMn_2Ge_2 (solid circles) at $T = 40$ K. The fit was performed for $p_z > 2$ a.u., using RHF predictions for the Mn 3d (dotted line) and Sm 4f moment (dashed line), convoluted with a Gaussian with FWHM = 0.44 a.u. to represent the experimental resolution. The resultant curve is presented as a blue line.

The results presented in Figure 75 clearly show that there is a large negative 4f spin moment, opposed to the positive Mn 3d moment. For 4f electrons, deviations from the atomic behaviour are small. The area under the fitted 4f curve therefore gives a reliable estimate of the Sm spin moment which we deduce to be $3.2 \pm 0.5 \mu\text{B}$. The total spin moment, calculated simply by integrating the MCP, is zero. Therefore the spin moment associated with the Mn 3d electrons together with the delocalised electrons, also amounts to the same value, $3.2 \mu\text{B}$, but with an antiparallel alignment. The fitted Mn 3d profile (dotted line in Figure 75) is inappropriate at $p_z < 2$ a.u. because the 3d electrons are sensitive to the solid state environment, and their contribution will differ from free atom behaviour. In addition there are likely to be small delocalised low momentum contributions from both Mn (4sp-like) and Sm (5d- and 6sp-like). From these results, we may simply interpret that there is a Sm 4f spin

moment of $3.2 \mu\text{B}$, which is aligned antiparallel to the Mn 3d, and total magnetisations. Since the total spin moment is zero, in order to account for the macroscopic ferromagnetic moment of $4.1 \mu\text{B}$, measured by SQUID magnetometry, there must be an orbital moment of this size. This orbital moment is aligned with the total magnetisation, i.e. parallel to the Mn spin direction. The total Sm moment is therefore $0.9 \pm 0.5 \mu\text{B}$ and is aligned parallel to the bulk magnetisation direction. These results show clearly that, despite the small size of the total Sm magnetisation as measured by neutrons, the spin and orbital contributions are both large, and the magnetic Compton scattering experiment provides a unique method to access this information. The magnetic Compton profile measured at $T = 230 \text{ K}$ and presented in Figure 76, shows a clear difference in shape. The Sm 4f moment is very much reduced, but the high momentum region is not purely Mn 3d-like. In order to fit to these data, there must still be a small Sm 4f moment antiparallel to the Mn moment. As far as the authors are aware, this is the first time the high temperature Sm moment has been observed conclusively in this material.

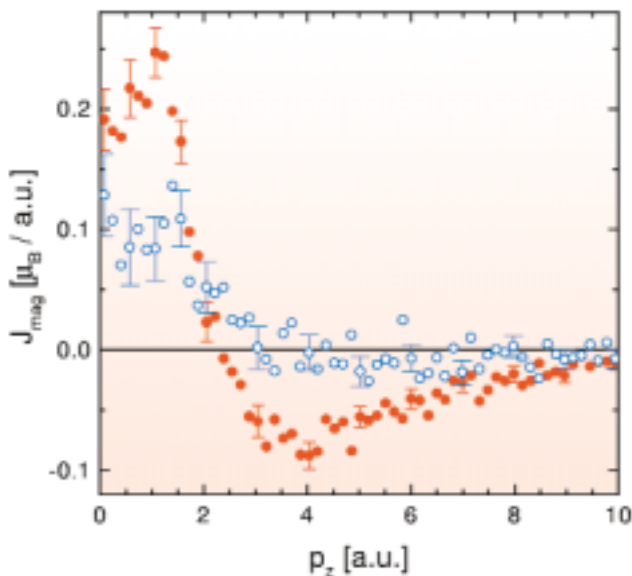


Fig. 76: The experimental magnetic Compton profiles of SmMn_2Ge_2 , at $T = 40 \text{ K}$ (solid circles) and $T = 230 \text{ K}$ (open circles). At 230 K the MCP is still negative at high momenta, and this means that although the Sm 4f moment is considerably reduced, it is still non-zero.

Authors

J.E. McCarthy (a), J.A. Duffy (b), C. Detlefs (a), M.J. Cooper (b), P. Canfield (c).
 (a) ESRF
 (b) University of Warwick (UK)
 (c) Ames Laboratory, Iowa State University (USA)

Double Magneto-Elastic Phase Transition in ErFe_4Ge_2

The compound ErFe_4Ge_2 undergoes on cooling a first-order transition from a paramagnetic to a magnetically-ordered state at $T_N = 44 \text{ K}$. The high-resolution powder X-ray diffraction patterns collected at **BM16** revealed a double symmetry breaking at the magnetic transition (Figure 77). The X-ray data enabled us to distinguish between the structural and the magnetic satellite peaks present in the neutron-diffraction patterns below T_N [1]. The satellites display a highly complex peak topology, and were very difficult to interpret. The interdependence of the structural and magnetic transitions is now unveiled.

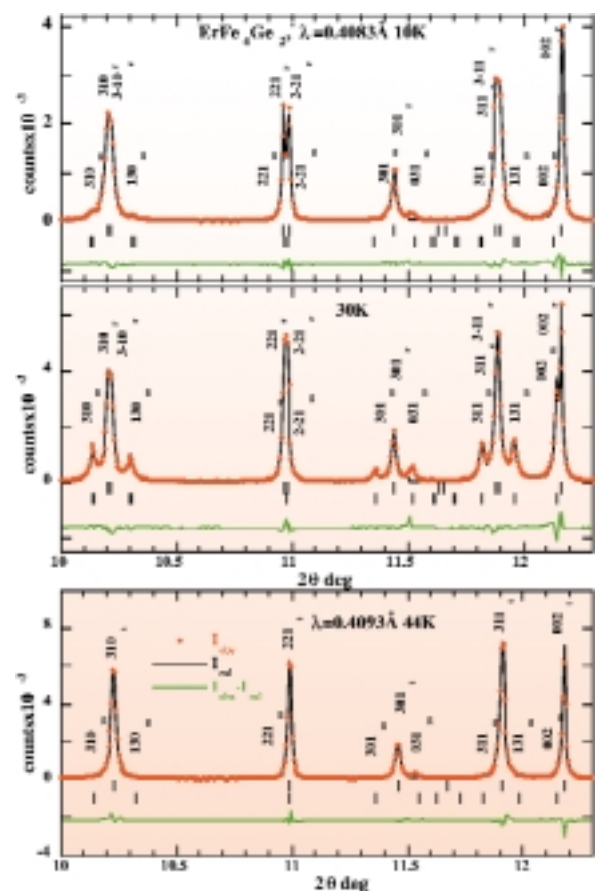


Fig. 77: Portions of refined powder X-ray diffraction patterns showing the splitting of $hhl_t \rightarrow \{hhl_r, hhl_l\}$ reflections ($Cmmm$ phase, P -cell: $a_r = b_r, \gamma \neq 90^\circ$ and the decoration of the $hkl_t \rightarrow \{hkl_m, hkl_l\}$ reflections ($Pnmm$ phase, $a_m \neq b_m$) at: (bottom) 44 K , paramagnetic tetragonal phase (99%) hkl_t ; (middle) 30 K , intermediate-temperature magnetically-ordered region with highest content (31%) of $Pnmm$ hkl_m ; and (top) 10 K , low-temperature region with the highest content (95%) of the orthorhombic $Cmmm$ phase hkl_r with maximum hhl_t splitting (upper hkl markers).

The powder-diffraction measurements show that the high temperature paramagnetic phase (space group $P4_2/mnm$) disproportionates at $T_N = 44$ K into two symmetrically distinct phases with orthorhombic symmetry. The respective space groups are $Cmmm$ and $Pnmm$. Both phases coexist in the intermediate temperature range (20 K $< T < T_N$) in proportions varying with temperature (Figure 78). The $Pnmm$ phase reaches its highest concentration of $\sim 31\%$ near 30 K. Below 20 K, the $Cmmm$ phase dominates, up to 95%.

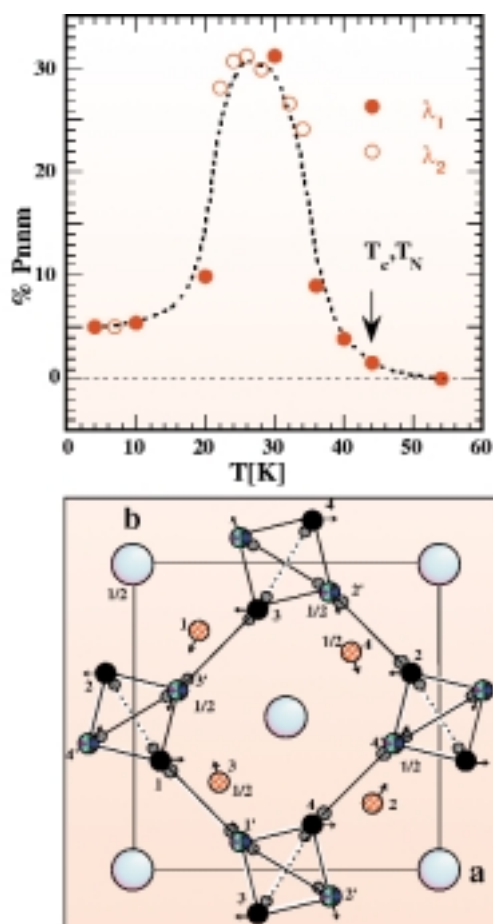


Fig. 78: (Top) The variation of the percentage of the minority orthorhombic $Pnmm$ phase with temperature. Full and empty symbols correspond to data sets collected with a slightly different λ . (Bottom) The displacive $P4_2/mnm \rightarrow Pnmm$ mechanism in the (001) plane in $ErFe_4Ge_2$. The arrows indicate the displacement field of the two Fe orbits (distorted tetrahedron). Atoms 1-4 (orbit 1) have only a $\pm\Delta x$ component. Atoms: 1'-4' (orbit 2) have a predominant $\pm\Delta y$ component.

This is the first time such a phenomenon has been observed. We suggest that it originates from competing magneto-elastic mechanisms, involving the Er crystal field anisotropy, the Er-Er, Er-Fe and the Fe-Fe exchange interactions and their coupling with the lattice strains.

The transition is accompanied by strong microstrain effects, which lead to a noticeable (hkl) dependence of the line broadening. The shear strain accompanying the $P4_2/mnm \rightarrow Cmmm$ transition was attributed to the magneto-elastic coupling between the Er-Er dominant interaction and the lattice strains [1]. The observed $a_c/b_o \neq 1$ deformation (referring to the $\sqrt{2}a_t, \sqrt{2}a_t, c_t$ cell) is due to the fact that the Er-Er exchange interaction is negative along b_o and positive along a_o . The $P4_2/mnm \rightarrow Pnmm$ transition is most probably driven by the tensile strain resulting from the Fe displacement field (Figure 78). Given that the shortest Fe-Fe distances are in the strongly deformed tetrahedron, the antiferromagnetic Fe-Fe interaction probably plays a dominant role in this transition as a result of geometric frustration. We assume that below T_N the Er-Er and Fe-Fe interactions are of comparable strength but involve different order parameters, leading to the double symmetry breaking as a consequence of the coupling between the magnetic order parameter and the lattice strains.

Reference

[1] P. Schobinger-Papamantellos, J. Rodríguez-Carvajal, G. André, C.H. de Groot, K.H.J. Buschow, J. Magn. Magn. Mat., **191**, 261 (1999).

Principal Publication and Authors

P. Schobinger-Papamantellos (a), J. Rodríguez-Carvajal (b), K.H.J. Buschow (c), E. Dooryhee (d), A.N. Fitch (d), J. Magn. Magn. Mat., **210**, 121-137 (2000).
 (a) Lab. für Kristallographie, ETHZ Zürich (Switzerland)
 (b) Lab. Leon Brillouin, (CEA - CNRS) Saclay (France)
 (c) Van der Waals-Zeeman Institute, University of Amsterdam, (The Netherlands)
 (d) ESRF

4f and 5d Magnetism in Samarium

Resonant X-ray magnetic scattering (RXMS) is based on the enhancement of the - otherwise weak - magnetic scattering cross section when the photon energy is tuned to an absorption edge. The resonant process is interpreted in terms of an electric multipolar transition between a core level and the vacant states of a polarised electronic shell. At the $L_{2,3}$ edges of rare earths, the transitions can be dipolar ($2p-5d-2p$), and the resonance will carry information on the polarisation of the 5d band, or quadrupolar ($2p-4f-2p$), reflecting the polarisation of the 4f shell. Our detailed spectroscopic study of the resonance at the L_3 edge of samarium in a single crystal epitaxial film shows how the exploitation of the resonant process can lead to a deeper

understanding of long range magnetic order in samarium. Using RXMS, we could measure quantities representative of the 4f and 5d polarisation independently, which is an important complement to neutron scattering.

The experiments were carried out at beamline **BM28** (XMaS, UK CRG) on a samarium 5000 Å epitaxial film, grown by Molecular Beam Epitaxy (MBE) in the Laboratoire de Physique des Matériaux, University of Nancy, France. The energy dependence of the magnetic intensities shows three resonances, one below and two above the absorption

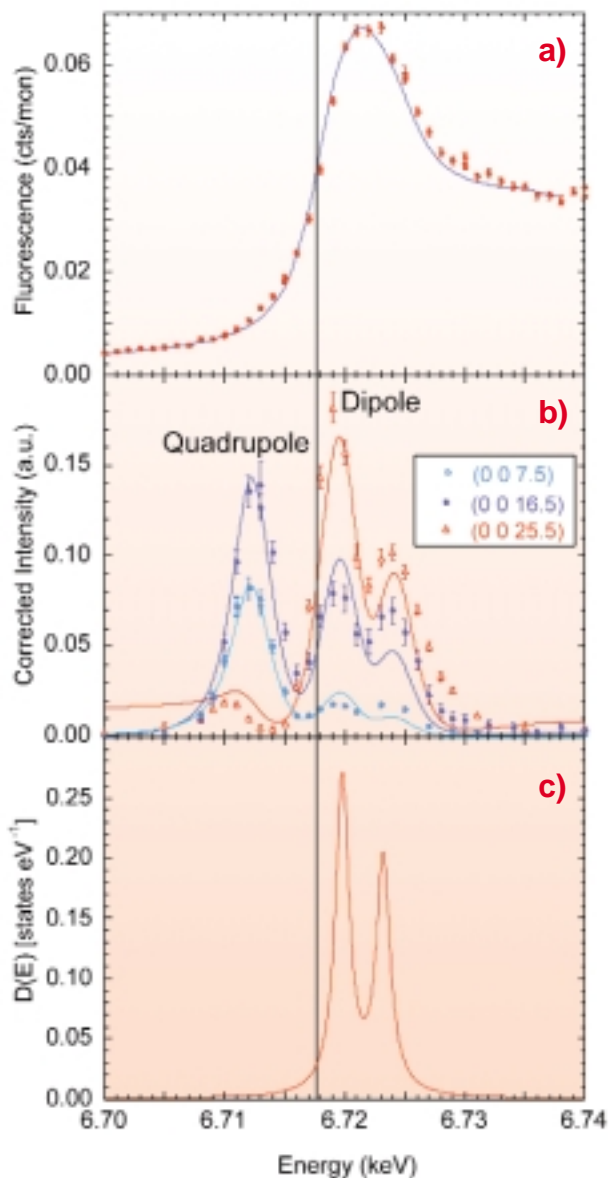


Fig. 79: Energy dependence of the fluorescence (a) and the resonance at three different magnetic reflections (b) at the L_3 edge of samarium. Dipolar and quadrupolar resonances depend on the wave-vector transfer in a different way. The vertical line shows the position of the absorption edge. The solid lines in (a) and (b) are the result of a calculation using the model density of states (c).

edge (Figure 79b) [1]. The study of the dependence of the resonant intensities with the wave vector transfer shows that the resonance observed below the L_3 edge is quadrupolar in origin, probing 4f magnetism, and can be fully interpreted using atomic considerations. The energy dependence of the dipolar resonance at and above the L_3 absorption edge shows two maxima and can be interpreted in the framework of a model density of 5d states $D(E)$ (Figure 79c). The same $D(E)$ accounts for both the white line in the fluorescence (solid line in Figure 79a) and for the energy line shape of the resonance (Figure 79b). A similar experiment has been conducted on a bulk samarium single crystal [2], also on BM28. The energy dependence also shows a single quadrupolar and a double dipolar resonances.

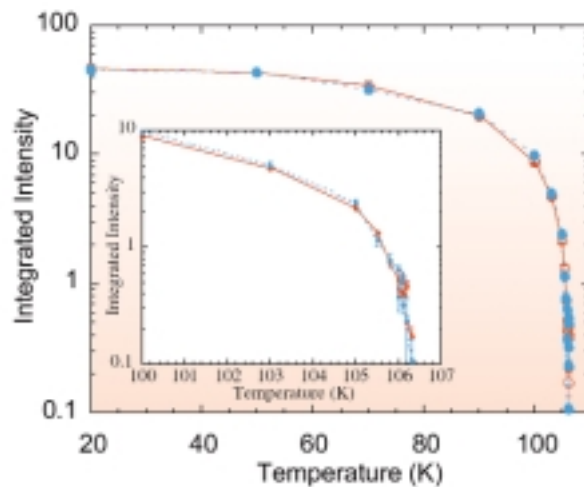


Fig. 80: Temperature dependence of the (0 0 16.5) magnetic reflection at the dipolar and quadrupolar resonances, taken at 6.719 keV (full circles) and 7.712 keV (open circles) respectively. The dipolar intensities have been multiplied by 2.4 for easier comparison.

The temperature dependence of the magnetic intensity has been studied at two energies, 6.712 keV and 6.719 keV, chosen as representative of the polarisation of the 4f and 5d electrons respectively (Figure 80). The dipolar and quadrupolar resonances follow the same temperature dependence, which implies that the 4f and 5d electrons are polarised in the same ratio, even very close to T_N , substantiating the RKKY model for long range magnetic order in rare earths.

References

[1] A. Stunault, C. Vettier, N. Bernhoeft, F. de Bergevin, C. Dufour, K. Dumesnil, SPIE Proceedings, **3773**, 295-303 (1999).
 [2] A.D.F. Herring, W.G. Stirling, N. Burton, M.M.R. Costa, A. Stunault, to be published.

Authors

A. Stunault (a,b), N. Bernhoeft (c), K. Dumesnil(d),

C. Dufour (d), C. Vettier (e).

(a) ESRF

(b) Department of Physics, University of Liverpool (UK)

(c) CENG, Grenoble (France)

(d) Laboratoire de Physique des Matériaux, Université Henri Poincaré-Nancy 1, Vandoeuvre les Nancy, (France)

(e) ILL, Grenoble (France)

X-ray Natural Circular Dichroism

In recent years, near-edge dichroism in crystals, i.e. the dependence of X-ray absorption on crystal and/or magnetic orientations with respect to the polarisation of the photon, has been thoroughly investigated at synchrotron radiation sources. The phenomenon occurs when the X-ray energy approaches the value required to excite an inner-shell electron to an empty orbital of its atom's valence shell. Particular attention has been given to magnetic circular X-ray dichroism, namely the difference in absorption between right- and left-circularly polarised photons in a system with a net magnetisation. Various authors have demonstrated the effect, which requires the breaking of time-reversal symmetry and the presence of a spin-orbit interaction. Electric-dipole (E_1) and, in some cases, electric-quadrupole (E_2) transitions accounts for the inner-shell excitations.

Much theoretical effort has gone towards the identification of the crystalline microscopic properties revealed by the observed spectra. Atomic theory has provided a number of results including a set of sum rules, which relate integrated dichroic intensities to the ground-state expectation values of effective one-electron operators. These operators coincide with the spin and orbital contributions to the magnetic moment, in the case of magnetic circular X-ray dichroism, thus providing experimentalists with a simple interpretative paradigm.

More recently a novel phenomenon, termed X-ray natural circular dichroism (XNCD), was observed in an organic non-centrosymmetric single crystal and in a stereogenic organometallic complex. The effect stems from the interference between E_1 and E_2 transitions, thus requiring the breaking of space inversion. These experiments were performed at the ESRF by Goulon et al. [1,2]. Building on previous work of Natoli et al. [3], the ESRF theory group has carried out a theoretical investigation of this new experimental work and found an XNCD sum rule, relating the integrated spectra to the ground-state expectation value of an orbital pseudodeviator [4], namely a rank-two tensor which is even under time reversal and odd under space

inversion. The theoretical analysis turned out to be particularly challenging, as it demanded the use of an extended symmetry group to account for interference effects. The extended symmetry was identified with a de Sitter group, $O(3,2)$, a non-compact version of $O(5)$, the rotation group in five dimensions. The theory also provides a microscopic expression for the long-sought vector term in gyrotropy. This term has recently been observed by Goulon and Rogalev through the detection of E_1 - E_2 linear X-ray dichroism in V_2O_3 . In the $O(3,2)$ framework an exhaustive picture of one-electron effects accessible to X-ray dichroism is obtained. Four cases are distinguished:

1. Time-odd electronic properties in centrosymmetric crystals. They are detected by X-ray magnetic circular dichroism. For E_1 transitions, the familiar orbital sum rule (L_z) is recovered.
2. Time-even electronic properties in centrosymmetric crystals. They are detected by X-ray linear dichroism. For E_1 transitions, the quadrupolar orbital sum rule is obtained.
3. Time-even electronic properties in non-centrosymmetric crystals. They are detected by X-ray circular dichroism. For E_1 - E_2 interference, the orbital-pseudodeviator sum rule is obtained. (If ferromagnetism is present, pure electric multipole transitions will also contribute yielding time-odd orbital tensors, usually detected by X-ray magnetic circular dichroism. These terms vanish when the magnetisation direction is perpendicular to the photon wave vector.)
4. Time-odd electronic properties in non-centrosymmetric crystals. They are detected by X-ray linear dichroism. For E_1 - E_2 interference, the gyrotropic vector term and other electronic properties will be observed. (In the case of a magnetic crystal, pure electric transitions will also contribute yielding time-even effects. These terms can be distinguished by full angular-dependence analysis.)

From the foregoing theoretical considerations it is clear that interference dichroism, by probing intrinsic hybridisation moments, appears as a novel powerful experimental technique for investigating electronic properties of centro- and non-centrosymmetric crystals.

References

- [1] J. Goulon, C. Goulon-Ginet, A. Rogalev, V. Gotte, C. Malgrange, C. Brouder, C.R. Natoli, *J. Chem. Phys.*, **108**, 6394 (1998).
- [2] L. Alagna, T. Prosperi, S. Turchini, J. Goulon, A. Rogalev, C. Goulon-Ginet, C. R. Natoli, R.D. Peacock, B. Stewart, *Phys. Rev. Lett.*, **80**, 4799 (1998).
- [3] C.R. Natoli, C. Brouder, P. Sanctavit, J. Goulon, C. Goulon-Ginet, A. Rogalev, *Eur. Phys. J.*, **B 4**, 1 (1998).
- [4] P. Carra and R. Benoist, unpublished.

Author

P. Carra.
ESRF



High pressure

Introduction

The investigation of matter under extreme conditions is one of the natural strongholds of a third-generation synchrotron radiation source. High-pressure research benefits from the large number of photons in spots of $10\ \mu\text{m}$ size or less. The highest pressures, in the 300 GPa region, can thus be attained using diamond anvil cells. This is one of the branches which is followed intensely at beamlines ID9 and ID30. High pressures are combined with laser heating, which again profits from the small size of the samples. While a first experimental setup involving laser heating was operated successfully in collaboration with competent users, the ESRF is now setting up a much more powerful facility.

The other branch of high pressure research makes use of the Paris-Edinburgh cell which allows us to exert a pressure of up to 2 MPa on several mm^3 of material. In these cells, the synthesis of materials can be investigated in real time, such as the formation of hard B, N, C compounds, the crystallisation of fullerenes, and the molten forms of iron under pressure. The latter research is of great geophysical relevance.

This year the ESRF has acquired a new large-volume Paris-Edinburgh cell which will be used primarily on BM29. This cell is both compact and light (25 kg), which facilitates its transfer and installation at several other beamlines. Thus, among others, it can be used for EXAFS, nuclear scattering and inelastic scattering experiments.

Investigating Electron-Electron Correlation in Sodium: Compton Scattering Under High Pressure

Understanding how electrons interact in a real solid is one of the important issues in solid-state physics. These electron-electron correlation phenomena and the consequences in the physical properties are studied in many systems, ranging from simple metals to complex compounds. The approach presented here is to investigate a rather simple model system, the free electron gas, where the experiment allows direct access to a theoretical model parameter: the free electron density. According to many-body calculations in such a system the electron-electron correlation only depends on the average intra-electron distance. In many cases the free electron theory serves for metals as a first order approximation and, with suitable corrections, it can be applied to more complex solid state systems.

Compton scattering (inelastic X-ray scattering at high momentum transfer) directly probes the electron ground state properties of matter. The behaviour of the electron density in a free electron system when external parameters are changed can be evaluated from the value of the Fermi momentum as derived from experimental Compton profiles. In earlier studies mainly alkali metals like Li, Na, K, Rb and Cs with different electron densities were investigated to evaluate the importance of electron-electron correlation. However, in the majority of these experiments, solid state effects modify the free electron behaviour and in general it is difficult to separate these two contributions. Therefore in the experiment presented here, the electron density was dynamically changed via the external pressure applied to the same sample. This type of experiment became feasible only recently thanks to the availability of sufficient photon flux of high energy X-rays and thanks to the development in high-pressure techniques.

The first pressure dependent Compton scattering data from sodium, which are almost free from contamination by the pressure cell, have been measured at the high-energy beamline ID15B. A solid state detector, and the recently developed large-volume cell of ID30 were used. Compton profiles under various pressures have been collected up to 4.2 GPa and the relative differences are shown in Figure 81. The experimental data clearly reflect the pressure induced increase in the electron density: the momentum density becomes broader and the Fermi momentum larger. The pressure dependence of the Fermi momentum also reveals the corresponding change of the electron-electron correlation: a simple free electron theory is not adequate while a proper RPA calculation including

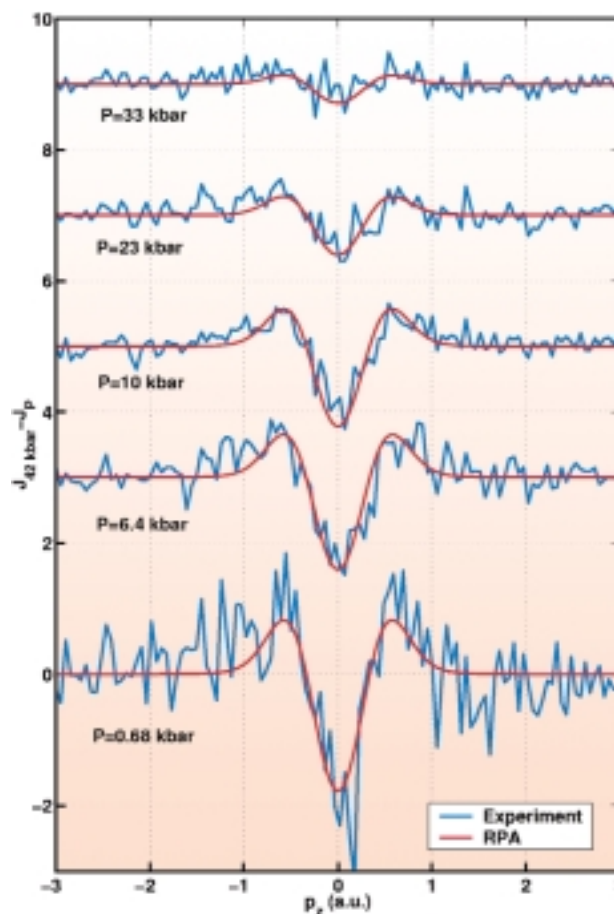


Fig. 81: Difference between Na Compton profiles at different pressures

correlation effects agrees quite well with the data. A more detailed analysis to compare different theoretical correlation models is in progress.

The success of the work presented will also open up new possibilities for materials science as a possible use of high-pressure Compton scattering is to study phase transitions which are related to electronic topological transitions.

Authors

K. Hämäläinen (a), S. Huotari (a), J. Laukkanen (a), A. Soininen (a), S. Manninen (a), C.-C. Kao (b), T. Buslaps (c), M. Mezouar (c).

(a) University of Helsinki (Finland)

(b) NSLS (USA)

(c) ESRF

Complex Crystal Structures of Heavy Alkali Metals at High Pressures

The heavy alkali metals exhibit a rich variety of high-pressure phase transitions. The pressure-driven electronic $s \rightarrow d$ transition is believed to be the driving force for destabilising the common high-symmetry crystal structures adopted near ambient conditions (bcc and fcc) with respect to lower-coordination structures. In particular at intermediate densities, both Rb and Cs adopt a body centred tetragonal structure, where the atoms are only eightfold coordinated. Solving the crystal structures of several other high-pressure modifications of the alkalis has remained a long-standing problem. Hereafter, we briefly summarise results of recent high-pressure structural studies of Rb. [1] Based on angle-dispersive synchrotron powder X-ray diffraction diagrams measured at the ESRF, we have solved the structure of Rb-IV which is found to be surprisingly complex.

Diffraction experiments were carried out at the beamline ID9 using diamond anvil pressure cells. The X-ray diffraction patterns were recorded at 300 K using a wavelength near 0.45 Å and an image plate detection system. Both the good angular resolution and the high sensitivity of the experimental setup at ID9 were essential for solving the crystal structures.

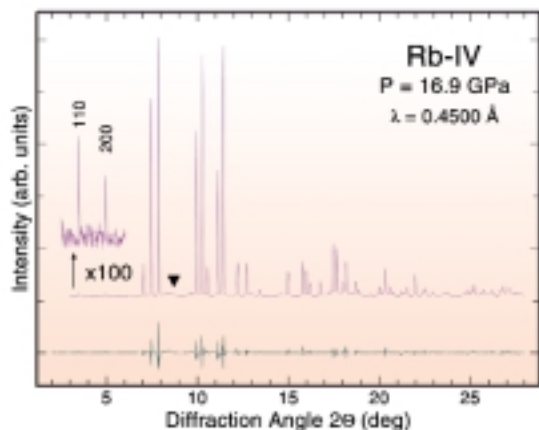


Fig. 82: X-ray diffraction diagram of the phase Rb-IV at 16.9 GPa. The lower curve represents the difference between measured data and refined profile.

Figure 82 shows the integrated diffraction pattern of the phase Rb-IV at a pressure of 16.9 GPa. The pattern can be indexed on the basis of a cubic cell with $a_c \approx 10.35$ Å. However, weak peak splittings observed at higher pressures indicate that the symmetry of the Rb-IV structure is in fact tetragonal. Solutions of the crystal structure were

performed in the centrosymmetric space group $I4/mcm$. Application of direct methods reveals that one set of Rb atoms occupies the Wyckoff positions 16k ($x,y,0$; $x \approx 0.79$, $y \approx 0.08$). The resulting arrangement of Rb1 atoms (see Figure 83) consists of columns of face-sharing square antiprisms interconnected by short Rb1-Rb1 contacts (red lines in Figure 83). The closest separation between Rb1 atoms (3.04 Å at 16.9 GPa) corresponds to twice the ionic radius of Rb^+ (1.52 Å).

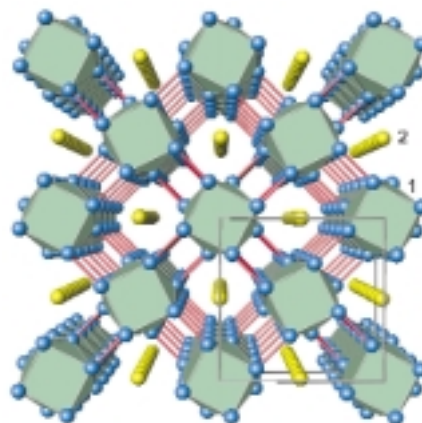


Fig. 83: The tetragonal structure of Rb-IV viewed along the c -axis. Rb1 atoms form a framework structure, which hosts linear chains of Rb2 atoms. Note that the chain sites indicated in this figure have an average occupancy factor of less than 0.5 (see text).

The Rb1 framework hosts chains of a second set of Rb atoms as evidenced by electron density maxima in the difference Fourier map (see Figure 84). Maxima occur at the 8g ($0.5,0,z$) site. Thus, the Fourier map in combination with the maximum possible number of 20 atoms per unit cell – as inferred from atomic volumes of neighbouring phases – suggest an average Rb2 arrangement with statistical occupation of 8g sites and an occupation factor of 0.5. However, for this atomic arrangement, within the chains the average interatomic distance would drop to 2.6 Å, which is 15% smaller than the ionic radius of Rb and therefore difficult to accept.

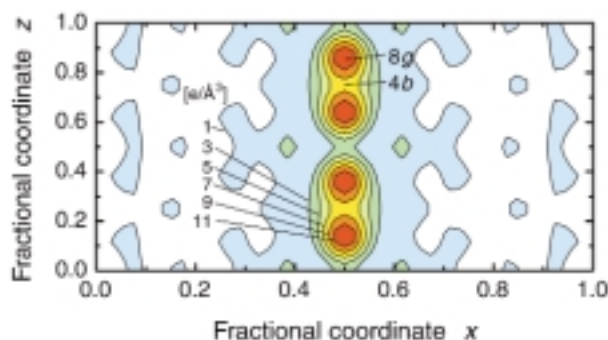


Fig. 84: Difference Fourier map of Rb-IV for a (010) plane. The x and z coordinates refer to the a - and c -axes of the tetragonal unit cell, respectively.

We therefore conclude that the number of Rb2 atoms in chain sites is less than four per unit cell. A refinement, in which occupation factors of sites along the chains are treated as free parameters, converges to occupation numbers corresponding to an average chain atom separation of about 2.97 Å. We have not observed any supercell reflections which would indicate a commensurate ordering of the chain atoms with respect to the framework of Rb1 atoms. However, some diffraction patterns of Rb-IV show an extra reflection corresponding to a d-value of about 3.0 Å (marked by a triangle in Figure 82). If interpreted as a reflection arising from the intra-chain ordering, the absence of other additional reflections would indicate that chains are not correlated with respect to each other.

There is a quite surprising resemblance of the Rb-IV structure to the metal atom sublattice of the W_5Si_3 -type structure. Furthermore, it has been pointed out earlier by Nesper and v. Schnering, that the Cs-IV-type structure, also adopted by the phase Rb-V, corresponds to the metal sublattice in the $ThSi_2$ -type structure. This leads to a more general concept, namely that at intermediate densities the alkali metals adopt crystal structures, which represent cation sublattices of binary intermetallics.

The results for Rb-IV demonstrate that the pressure-driven breakdown of the nearly-free electron character of a simple metal induces a phase transition to a rather complex structure. The present work partly closes the gap in our knowledge about the phase transition sequence in heavy alkali metals during the early stages of the $s \rightarrow d$ transition. Furthermore, structure solutions for Rb-VI [2], Cs-V [3] and Cs-VI [4] are important steps for an understanding of the structural evolution of heavy alkali metals, when they are fully turned into monovalent d-transition metals by the application of pressure.

References

- [1] U. Schwarz, A. Grzechnik, K. Syassen, I. Loa, M. Hanfland, *Phys. Rev. Lett.*, **83**, 4085 (1999).
 [2] U. Schwarz, K. Syassen, A. Grzechnik, M. Hanfland, *Solid State Commun.*, **112**, 319 (1999).
 [3] U. Schwarz, K. Takemura, M. Hanfland, K. Syassen, *Phys. Rev. Lett.*, **81**, 2711 (1998).
 [4] K. Takemura, N.E. Christensen, D.L. Novikov, K. Syassen, U. Schwarz, M. Hanfland, *Phys. Rev. B*, submitted.

Authors

U. Schwarz (a,b), K. Syassen (a), M. Hanfland (c), A. Grzechnik (a), I. Loa (a), K. Takemura (d).
 (a) MPI für Festkörperforschung, Stuttgart (Germany)
 (b) MPI für Chemische Physik fester Stoffe, Dresden (Germany)
 (c) ESRF
 (d) NIRIM, Tsukuba (Japan)

Study of the Properties of Iron under Conditions Existing at the Earth's Core

Successful interpretation of available geophysical data requires both experimental and theoretical information on the elasticity of solids under the physical conditions of the Earth's interior where there are pressures up to 360 GPa and temperatures over several thousand degrees. Since iron is considered as the major component in the Earth's core, elastic properties of iron at high pressures and temperatures are very important for modelling its composition and dynamics. We have determined the thermal equation of state (EOS) and the Debye-Waller temperature factors and calculated aggregate sound velocities and Grüneisen parameter of ϵ -iron for the first time using a new approach which is based on Rietveld refinement at high pressures and temperatures. We used new in situ X-ray diffraction data on ϵ -iron at static pressures up to 300 GPa and temperatures to 1200 K, and showed that the inner core compressional (V_p) and shear (V_s) sound velocities could match properties of pure iron without any contributions from low-velocity components.

The experiments were performed on beamline **ID30**. In our experiments, powder diffraction data were collected with a fine incident X-ray beam of approximately rectangular shape ($8 \times 9 \mu\text{m}^2$) of 0.3738 Å wavelength on the FastScan imaging plate. The collected images were integrated in order to obtain a conventional diffraction spectrum.

We heated the samples externally in a Mao-Bell type diamond anvil cell (Figure 85). The external electrical

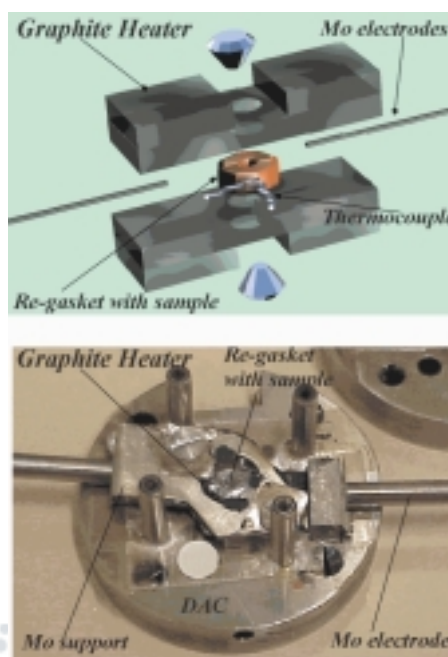


Fig. 85: Schematic diagram of a graphite heater (top) and the graphite heater mounted in the diamond anvil cell (bottom).

heating assemblage employs flexible graphite foils and makes it possible to reach temperatures over 1400 K at multimegabar pressure range. A procedure of high temperature (800 K) synthesis of the ϵ -Fe from a submicrometre iron powder was developed, this allowed us to overcome problems associated with a preferred orientation, stresses and recrystallisation, and to collect reliable diffraction data to over 300 GPa. In total, 188 data points were collected over the pressure range of 18 to 305 GPa at temperatures between 300 to 1300 K to determine the EOS of the ϵ -iron. As a result, a thermal expansion of the ϵ -Fe was measured for the first time in the static compression experiments at conditions close to those at the Earth's Inner-Outer Core boundary (Figure 86). Our results generally support earlier shock wave data [1], except for the fact that the difference in density of ϵ -Fe and Preliminary Reference Earth Model (PREM) [2] (Dziewonski and Anderson, 1981) density at the inner core conditions is 2 to 4 times less than the earlier estimate and is just 2.5 - 5%.

Accurate Rietveld refinement and temperature dependence of intensities of different reflections of ϵ -iron at various pressures give enough information for determination of the Debye-Waller temperature factors as a function of P and T. Using the theory of lattice dynamics and experimental data on the density, bulk modulus and Debye-Waller parameters, we have found aggregate sound velocities and the acoustic Grüneisen parameter of ϵ -Fe at pressures up to 300 GPa and temperatures over 1200 K (Figure 86). For the first time it was demonstrated that shear sound velocities of ϵ -Fe at the Earth's Inner Core conditions are reasonably close to the PREM values (Figure 86).

References

- [1] J.M. Brown, R.G. McQueen, *J. Geophys. Res.*, **91**, 7485-7494 (1986).
- [2] A.M. Dziewonski, D.L. Anderson, *Phys. Earth Planet. Inter.*, **25**, 297-356 (1981).

Principal Publication and Authors

L.S. Dubrovinsky, S.K. Saxena, F. Tutti, S. Rekhi, D. Le Beller, T. Le Bihan, *Phys. Rev. Lett.*, **84**, 1720-1723 (2000).
Institute of Earth Sciences, Uppsala University (Sweden).

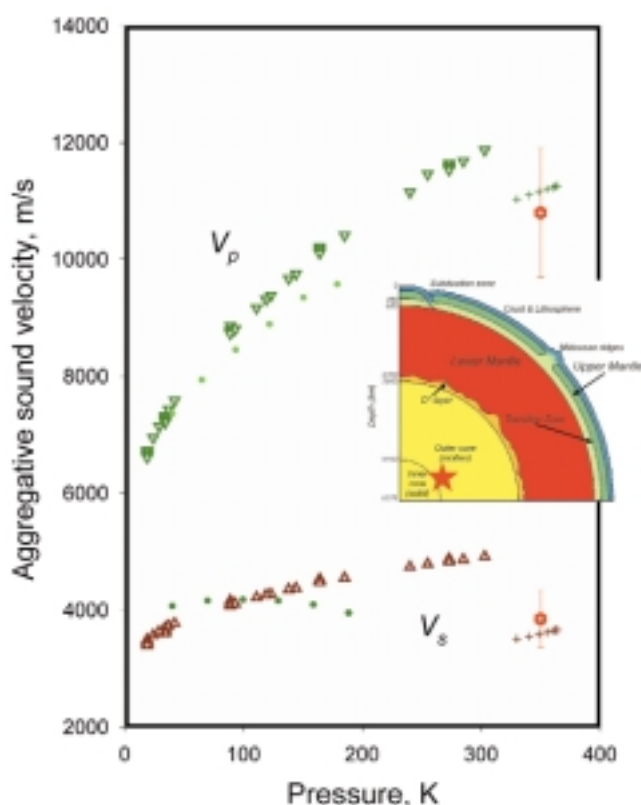


Fig. 86: Comparison of the present results (triangles) with shock-waves studies [1] (dotted lines), and with seismic observations (PREM) [2] in the inner core (crosses). Estimation of sound velocities for the inner core conditions (350 GPa and 6000 K) is shown by red hexagons. Thermoelastic properties and aggregate sound velocities of iron were studied up to conditions which correspond to the depth in the Earth interior marked by the red star in inset.

Zintl Polyanions Under Extreme Conditions: the KTe System Probed by X-ray Absorption Spectroscopy

In a semiconducting compound with a rather small electronic band gap, one would expect a great interplay between atomic disordering and electronic properties. For example, the increase in the disordering is reflected in a higher scattering probability of the mobile electrons and consequently in a decrease in the conductivity. This process competes with an increasing overlap of the non-bonding orbitals, and hence the formation of conduction paths, through which the carriers can move freely [1]. Evidence of this competitive behaviour can be observed in all of the elemental semiconductors, which upon melting undergo an electronic transition towards a (semi-)metallic state.

Zintl compounds are semiconductors which possess a peculiar local atomic arrangement, and therefore it is particularly interesting to study the interplay between the electronic and structural degrees of freedom. One can produce Zintl phases by alloying alkali metals (AM) with post-transition metals (PTM). Due to the high difference in the electronegativities of the components ($\Delta\chi^*$), the equiatomic mixture forms compounds in which the PTM

atoms cluster in polyanionic units, surrounded by the AM cations. The occurrence of the polyanions in such alloys is necessarily accompanied by the formation of covalent bonds, from which the origin of the semiconducting behaviour can be traced. Several neutron diffraction (ND) studies have been performed in the last decades on the melting of this class of semiconductors [2]. These show a persistence of the negatively charged units in the liquid state (at least up to the dissociation temperature), together with the absence of any obvious increase in the conductivity.

To investigate this ability of the alkali metals to prevent extensive electronic orbital overlap, we performed an X-ray absorption spectroscopy (XAS) measurement at beamline **BM29**. This experiment simultaneously probed the local atomic arrangement and the electronic state of a particular Zintl compound (KTe) under high temperature and high pressure (300-1000 K, 0.1-5 GPa), to understand if any electronic transition can be driven by applying an external force.

These extreme conditions were applied through a two-anvil large-volume press of the Paris-Edinburgh type. The experimental setup included the parallel detection of the diffraction pattern to monitor the sample condition and to check for the continued absence of chemical contaminants during the P-T cycles. To overcome the difficulties arising from the high corrosivity of the alkali metals and the extreme conditions, we have developed a technique by which it is possible to protect the sample from oxygen and moisture, but still allows for the performance of proper XAS experiments.

With this experimental setup we have collected for the first time XAS spectra at several temperatures and pressures of

solid and liquid KTe (see [Figure 87](#)). We have confirmed the ND results of Fortner [3] who observed a high degree of structural ordering in the liquid at ambient pressure. Our data clearly indicate the existence of Te dimers in the molten state up to 3 GPa. In addition, our measurements show a clear shift of the Te K-edge of approx 1.5 eV, upon melting at the constant pressure of 3 GPa (see [Figure 88](#)). An analogous behaviour, even at ambient pressure, is well known to occur in elemental semiconductors, such as Ge or Te [4], where the structural disordering due to the liquid state results in an increased overlap of the orbitals. We postulate that this observation is consistent with the filling of the covalent band gap at the Fermi level, and supports our initial hypothesis as to the role of pressure in this and related systems.

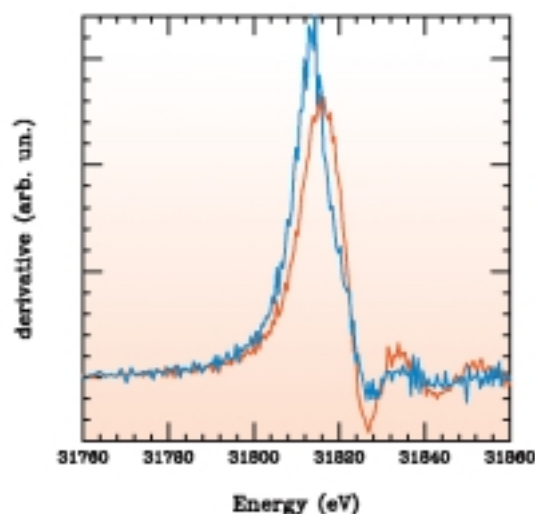


Fig. 88: Energy derivative $\partial\alpha(E)/\partial E$ of the absorption of solid (red line) and liquid (blue line) KTe at 3 GPa. The shift of the maximum of the derivative upon melting is due to the metallisation of the compound.

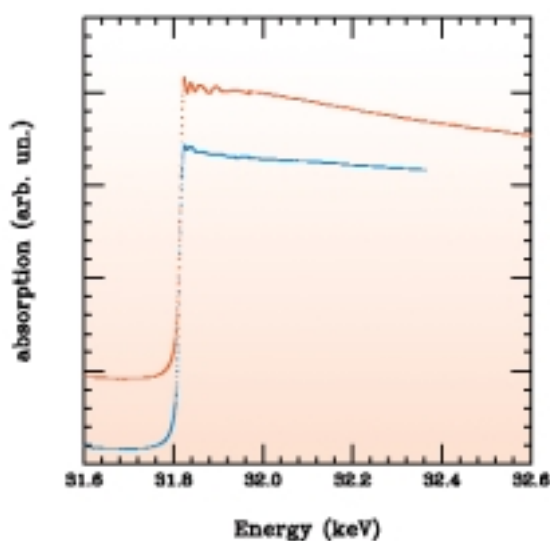


Fig. 87: XAS spectra at the Te K-edge in the solid (room temperature, red line) and in the liquid (730 K, blue line) state of KTe at 3 GPa.

References

- [1] J.E. Enderby, A.C. Barnes, Rep. Prog. Phys., **53**, 85 (1990).
- [2] See the review in: W. van der Lugt, J. Phys.: Condens. Matter, **8**, 6115 (1996).
- [3] J. Fortner et al., Phys. Rev. Lett., **69**, 1415 (1992).
- [4] S. De Panfilis, A. Filipponi, Europhys. Lett., **37**, 397 (1997).

Authors

- S. De Panfilis (a), M. Borowski (a), C. Meneghini (b), M. Minicucci (c), L. Comez (c), T. Neisius (a), A. Polian (d), J.-P. Itié (d).
- (a) ESRF
- (b) LNF-INFN, Frascati (Italy)
- (c) Dip. di Matematica e Fisica, Università di Camerino (Italy)
- (d) Lab. Physique des Milieux Condensés, Université P. et M. Curie, Paris (France)



Materials

Introduction

Materials research in its different aspects is the ultimate goal of 90% of all the investigations with synchrotron radiation at the ESRF. Contributions on this topic are therefore found in almost all of the chapters. In this one, we present examples on the structural aspect of matter which fit neither into the section on Applied or Industrial research nor anywhere else. They are representative of the great variety of activities which take place at the ESRF.

The highlights selected this year concern biopolymers, metals, and aqueous suspensions. The first one reports how the fibrous structure of wood has been investigated using fibre diffraction. The precision of this technique permitted a determination of both the location and the orientation of fibres in the cross-section of a cell. Then two highlights concern metals and alloys; one describes how imaging techniques combined with a specially built furnace have been used to study the microstructures within an alloy under conditions of a thermal gradient. The other shows how high energy X-rays permitted a study of grain growth within the bulk material during the annealing of aluminium.

The last two highlights are representative of the field of soft condensed matter and they concentrate on the dynamics of aqueous suspensions. In the first, charge-stabilised colloidal silica was studied using X-ray photon correlation spectroscopy; in the second, aqueous suspensions of vanadium pentoxide ribbons were subjected to shear conditions in a Couette cell and studied using small-angle X-ray scattering.

Imaging of the Helical Arrangement of Cellulose Fibrils in Wood Cells

The function of complex biological materials such as wood or bones is related to their hierarchical structure. The local variation of the nanostructure can be non-destructively investigated by microbeam scanning diffractometry [1, 2]. Experiments performed on ID13 combine reciprocal space resolution on the unit cell level with the resolution of a light microscope provided by micrometre-sized scanning-steps. This method has been applied to the study of the orientation of cellulose fibrils in a single wood cell wall [3]. On the nanometric scale, the wood cell wall is a fibre composite consisting of an amorphous matrix and crystalline cellulose microfibrils. In the dominating S2 layer, the cellulose microfibrils are tilted with respect to the longitudinal cell (MFA: microfibril angle) and are helically wound around the cell wall (Figure 89). While standard X-ray diffraction techniques are capable of determining an average tilt angle, information on the helical superstructure has been principally derived from optical techniques. In view of the importance of this superstructure for the mechanical properties of wood it was of interest to verify whether scanning X-ray diffractometry also provides this information.

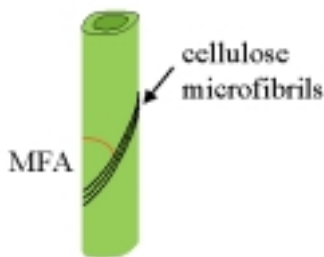
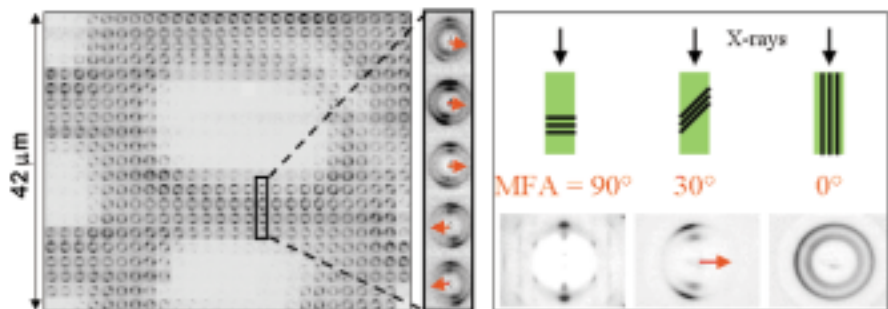


Fig. 89: Schematic design of single tracheid wood cell. The cellulose microfibrils are wound helically around the cell wall in the S2 layer.

Experiments were performed on a cross section (thickness 10 μm) of *Picea abies* (Norwegian spruce) tracheid cells, with the X-ray beam parallel to the cell walls. The result of a complete scan of a 52 x 42 μm^2 area is shown in Figure 90.

Fig. 90: Mesh scan of a single *Picea abies* wood cell on a 2x2 μm^2 grid. A single line of patterns has been enlarged. A red arrow symbolises the orientation of the microfibrils relative to the cell wall.

The determination of this orientation, as defined by the MFA, is shown schematically on the right. A perfect powder pattern is observed when the microfibrils (black lines) are parallel to the incoming X-ray beam (MFA = 0°) while a fibre diffraction pattern is observed when they are at right angles (MFA = 90°). The distortion allows a determination of the MFA.



Individual diffraction patterns recorded by a CCD detector are limited to the range of the 110/200 reflections. The outline of the wood cells can be obtained immediately. As shown in Figure 90, the orientation of the microfibrils relative to the X-ray beam modifies the diffraction pattern in a characteristic way. An arrow here symbolises the orientation. The patterns can be perfectly simulated by assuming a sharply defined MFA-angle of about 23° [3]. The overall projection of the fibril orientation is shown schematically in Figure 91. The arrows form a flow pattern around the wood cell and there is a clear line of cell walls belonging to neighbouring cells. The flow pattern is an exact representation of the projection of the helical superstructure (Figure 89) on a plane and proves the presence of a right-handed Z helix in spruce wood.

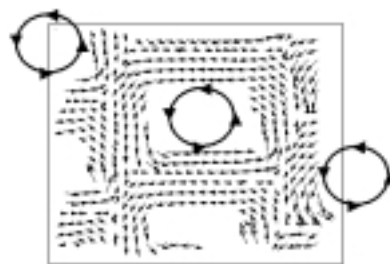


Fig. 91: Map of local cellulose fibril orientation in single wood cell. Following the arrows readily yields the trace of the fibrils around the cell wall.

References

- [1] P. Fratzl et al., J. Appl. Cryst., **30**, 765-769 (1997).
- [2] C. Riekel et al., Macromolecules, **30**(4), 1033-1037 (1997).
- [3] H. Lichtenegger et al., J. Appl. Cryst., **32**, 1127-1133 (1999).

Authors

H. Lichtenegger (a), M. Müller (b), O. Paris (a), C. Riekel (b), P. Fratzl (a).

(a) Erich Schmid Institute of Materials Science, Austrian Academy of Sciences and Metal Physics Institute, University of Leoben (Austria)

(b) ESRF

Dendritic Growth in PbSn Alloys

A solid-liquid interface propagating under non-equilibrium conditions can appear as a spatiotemporal macroscopic structure. In solidified alloys, dendritic microstructures resulting from such growth processes are common. The main driving forces for dendritic growth are thermal and chemical diffusion, combining to determine the morphology and velocity field of the phase front. Unfortunately, an analytical solution to the problem is unavailable, even in the case of a single one-way diffusion process, due to the form of the kinetic and thermodynamic boundary conditions. These would have to account for a crystallographically induced surface-tension anisotropy resulting in a non-linear integral representation for the recasted diffusion equation. Numerical simulations have been compared with experimental observations on optically transparent model systems to extract physical information on the growth mechanism [1]. The transparent systems give information on the interface dynamics from phase contrast light microscopy, but do not in general include optically opaque alloying elements to reveal phase specific information on segregation. The validity of diffusion postulates is difficult to judge when extracted from simulations where thermal and chemical diffusion are both present and experimentally indistinguishable. Further complications arise from the interaction (through diffusion) between interfacial features, locally dependent upon factors like convective currents, etc. It would be a significant improvement if experiments were devised that could provide simultaneous information on segregation, dynamics and phasefront morphology.

Direct beam X-ray imaging of dendritic growth in real alloys turns out to be a promising method. Binary alloys of PbSn have been studied during solidification at beamline **ID22** using a specially designed furnace to control the growth process and a high-resolution fast-readout FRELON [2] camera. Details on experiment and equipment are given elsewhere [3].

Figure 92 shows equiaxed dendritic growth in a Sn-52wtPb alloy. Once above a critical size Pb nuclei develop morphological instabilities; features, with crystallographic growth directions corresponding to the highest expansion rate wrt. atomic attachment are energetically favourable (in fcc Pb the six $\{100\}$ directions). The diffusion process is mainly thermal, although Sn diffusion builds up with the increasing interfacial size. Pb crystals can survive at temperatures higher than that of the liquidus at this composition, resulting in a thermal supercooling in the liquid. As the liquid temperature falls below the liquidus slope, nucleation occurs ahead of the growing dendrites.

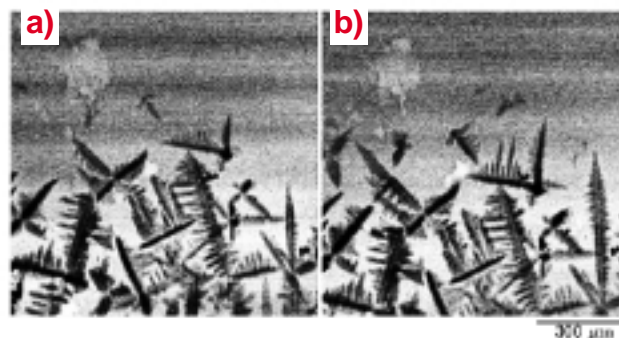


Fig. 92: Equiaxed dendritic growth of Pb crystals in an Sn-52wt%Pb alloy. Thermal gradient, $(\partial T/\partial z)_{global} \sim 29.5$ K/mm, sample translation $v_{||z} = -9.6$ $\mu\text{m/s}$, 1.0 s exposure. Positive z points vertically upwards. Sample-detector distance 75 cm. (a) t_0 , (b) 3 frames later, $t_0 + 4.5$ s.

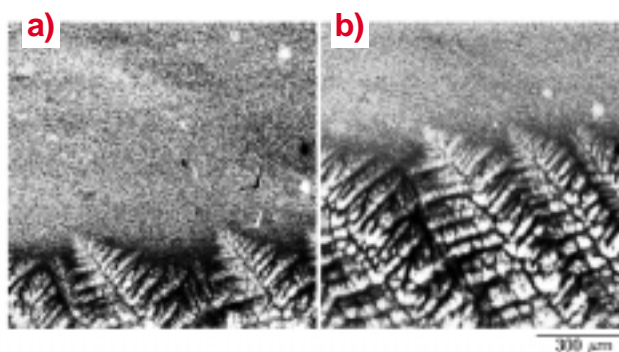


Fig. 93: Columnar dendritic growth of Sn crystals in an Sn-10wt%Pb alloy. Thermal gradient, $(\partial T/\partial z)_{global} \sim 19$ K/mm, sample translation $v_{||z} = -9.6$ $\mu\text{m/s}$, 1.0 s exposure. Positive z points vertically upwards. Sample-detector distance 10 cm. (a) t_0 , (b) 10 frames later, $t_0 + 15$ s.

Figure 93 shows directional dendritic growth for an alloy composition Sn-10%wtPb. The parallel primary β -Sn dendrites originate from the same nuclei. Initially the diffusion process is thermal, but chemical diffusion becomes dominant as excess Pb builds up in the liquid surrounding the pure β -Sn solid. When interfacial features come close, growth directions most parallel to the thermal gradient survive and develop secondary and then tertiary branches, the latter growing parallel to the primary stalk. Pb trapped in between dendrites solidifies in an eutectic microstructure. The substantial Pb concentration building up ahead of the progressing interface gives rise to a constitutional type of supercooling.

The difference in absorption of Sn and Pb resulted in clearly visible segregation in both liquid and solid phases. Collected images have not been compared with simulations due to inadequate spatial and temporal resolution. More

transparent alloys combined with the fast readout abilities (~50 ms) of the FRELON should be sufficient to extract quantitative physics regarding diffusion fields from comparison of experiment with numerical simulations.

References

- [1] A. Karma, W.-J. Rappel, *Phys. Rev. Lett.*, **77**, 4050 (1996).
 [2] J.-C. Labiche, J. Segura-Puchades, D. van Brusel, J.P. Moy, *ESRF Newsletter*, **25**, 41 (1996).

Publication

- [3] R.H. Mathiesen (a), L. Arnberg (b), F. Mo (a), T. Weitkamp (c), A. Snigirev (c), *Phys. Rev. Lett.*, **83**, 5062 (1999).
 (a) Dept. of Physics, NTNU (Norway)
 (b) Dept. of Mat. Techn., NTNU, (Norway)
 (c) ESRF

Kinetics of Individual Grains During Recrystallisation

Recrystallisation is a thermally activated process during which the energy stored in a plastically deformed metal or alloy is reduced [1]. Recrystallisation is generally separated into two distinct processes: nucleation and growth, which may occur consecutively or simultaneously. During nucleation, almost defect-free nuclei form in the deformed microstructure. During growth, these nuclei grow by grain boundary migration until they impinge upon each other. Following impingement the grains may continue to grow at much reduced velocities by curvature driven growth (secondary recrystallisation).

A plethora of models exists to simulate recrystallisation ranging from purely geometrical numerical models to fundamental analytical models. A common characteristic of the models is that they focus is on the average behaviour of the nuclei. Hence, one or more of the following assumptions are generally applied: randomly distributed nucleation sites, instantaneous or constant nucleation rates, and a growth rate identical for all the nuclei. The main reason for these assumptions is the lack of experimental data for the behaviour of the individual nuclei.

Here we present the first result of an X-ray diffraction technique for in situ studies of the nucleation and growth of individual grains during recrystallisation of metals (Figure 94). The experiment was performed using the 3DXRD microscope at beamline ID11 [2,3]. Using high energy X-rays (50-100 keV) from a synchrotron source

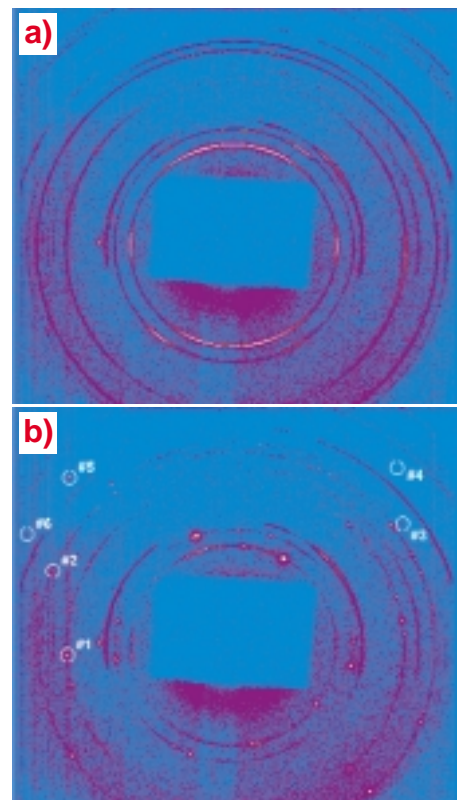


Fig. 94: Diffraction patterns measured by the position sensitive detector during annealing at 270°C. **a)** At $t = 0$ min (start of annealing). **b):** At $t = 162$ min, where the recrystallisation is 96% completed. The 6 grains analysed are marked by circles.

ensures the observation of true bulk behaviour. A suitable intrinsic gauge volume is defined by focusing the incoming beam and by performing ray tracing on the diffracted beams, using a two-dimensional detector. By this procedure, the orientation and volume of several hundred nuclei can be determined simultaneously during annealing. The first results relate to 90% cold-rolled 99.5% pure aluminium of type AA1050. As seen in Figure 95 the threshold for observation of the nuclei is in this case a radius of 1 micrometre. In contrast to model assumptions the variations in nucleation time and growth velocity are substantial. Note also the slow increase in integrated intensity indicative of an incubation process taking place prior to the onset of the grain growth (for example, grain #4 and #6 in Figure 95a).

In short, a general-purpose technique for bulk studies of recrystallisation is presented. It allows in situ studies of the nucleation and growth of individual nuclei. The setup used here for aluminium applies to all other metals and alloys, as penetration depths of 1 mm are universally obtainable with hard X-rays. The specific results obtained for AA1050 type Al include qualitative new information. Contrary to what is generally believed, incubation periods are observed and the curvature driven growth can be sufficiently fast for small

grains to disappear abruptly (for example, grain #4 in Figure 95b).

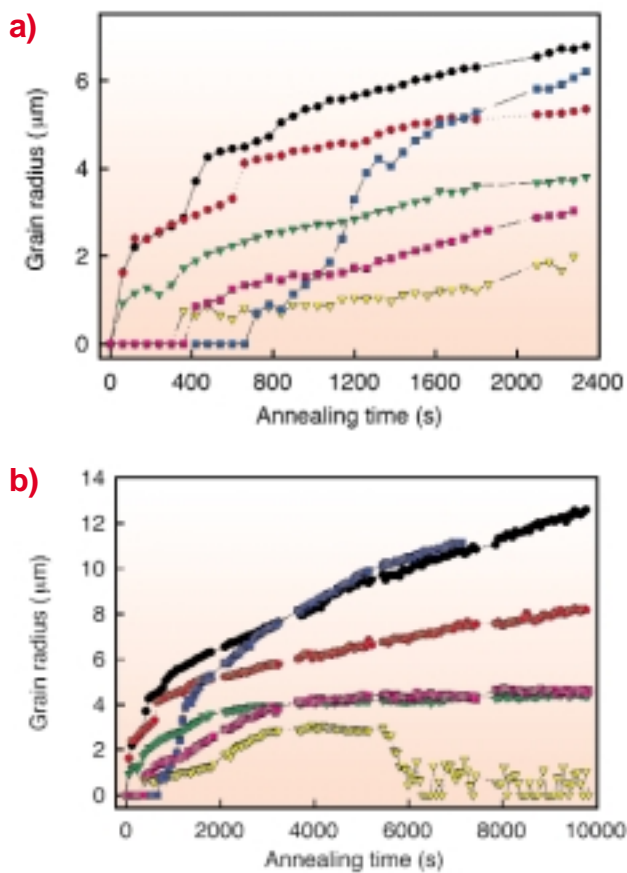


Fig. 95: Derived grain radius of the 6 analysed grains: Grain #1, Grain #2, Grain #3, Grain #4, Grain #5 and Grain #6. a) in the early stage of recrystallisation; b) for the entire annealing period - notice the abrupt disappearance of grain #4. At the end of the annealing period the sample was 96% recrystallised.

References

- [1] Proc. of ReX'99: The Fourth International Conference on Recrystallisation and Related Phenomena, Ed: T. Sakai, H.G. Suzuki.
 [2] H.F. Poulsen, S. Garbe, T. Lorentzen, D. Juul Jensen, F.W. Poulsen, N.H. Andersen, T. Frello, R. Feidenhans'l, H. Graafsma. *J. Synchrotron Rad.*, **4**, 147-154 (1997).
 [3] U.Lienert, H.F. Poulsen, Å. Kvik. Proceedings of the 40th conference of the American Institute of Aeronautics and Astronautics on Structures, Structural Dynamics and Materials, St. Louis (USA), April 1999.

Principal Publication and Authors

E.M. Lauridsen (a), D.J. Jensen (a), U.Lienert (b), H.F. Poulsen (a), *Scripta Mater.*, accepted for publication.
 (a) Materials Research Department, Risø National Laboratory, Roskilde (Denmark)
 (b) ESRF

Dynamics of Charge-Stabilised Colloidal Silica Suspensions Probed by Correlation Spectroscopy with Coherent X-rays

Dynamic Light Scattering (DLS) with visible coherent light is a well established technique used to investigate the static and dynamic properties of colloidal suspensions. It is however subject to two main limitations. One is the occurrence of multiple scattering in opaque systems (e.g. concentrated colloidal suspensions) which considerably complicates the interpretation of the experiments. The other is that using visible light prevents the dynamics to be traced on length scales smaller than about 2000 Å. Both limitations can be surmounted by X-ray photon correlation spectroscopy (XPCS) with the coherent X-ray beam available from beamline **ID10A**. We have used XPCS to measure the short time diffusion coefficient $D(Q)$ of charge-stabilised colloidal silica in concentrated suspensions up to their solidification point [1]. The free particle diffusion coefficient D_0 was determined by DLS and XPCS in dilute samples. The static structure factor $S(Q)$ was measured by small-angle X-ray scattering (SAXS). **Figure 96** shows $S(QR)$ and the normalised inverse diffusion coefficient $D_0/D(QR)$ as a function of QR for a suspension containing 15 vol% of colloidal particles with radius $R = 555$ Å. Multiple scattering of visible light in dense suspensions can be suppressed by carefully matching the refractive indices of the solvent and the particles leading to identical DLS and XPCS spectra [2]. DLS data taken under such conditions are shown for comparison in Figure 96 (closed squares) illustrating also the limitation of DLS to the low Q regime. The static structure factor shows a pronounced peak that deviates in both position and

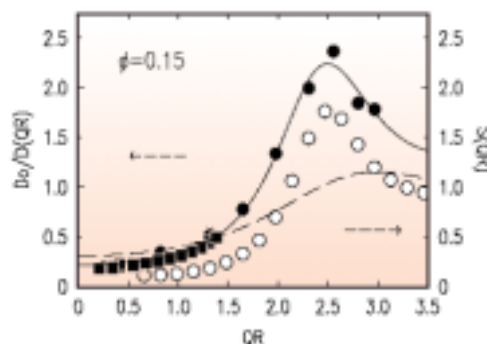


Fig. 96: Static structure factor $S(QR)$ for a suspension of colloidal silica with volume fraction $\Phi = 0.15$ (open symbols). The dashed line represents the calculated hard-sphere structure factor. Normalised inverse diffusion coefficient $D_0/D(QR)$ taken by XPCS (closed circles) and DLS (closed squares).

amplitude from the calculated structure factor for a suspension of hard spheres (dashed line): it thus underlines the charge-stabilised character of the system. The normalised inverse diffusion coefficient $Do/D(QR)$ peaks at $QR = 2.5$ corresponding to a minimum in the diffusion coefficient. This slowing-down occurs at the maximum of the static structure factor $S(QR)$, showing that the most likely density fluctuations decay the slowest. It is apparent from Figure 96 that $Do/D(QR)$ mimics the behaviour of $S(QR)$ but is not identical. This indicates that indirect, hydrodynamic interactions are relevant for the system. These interactions can be quantified by extracting the hydrodynamic function $H(QR) = S(QR) / (Do/D(QR))$ from the data. These functions, shown for three different volume concentrations in Figure 97, are asymmetric and skewed towards the high Q side, indicating that the long-wavelength modes are damped more strongly than the short-wavelength ones. Furthermore, $H(QR) < 1$ and decreases with increasing volume concentration. This is expected if hydrodynamic interactions act as additional “friction” that further slows down the dynamics. This is typically observed in sterically stabilised (hard-sphere) colloidal suspensions but is in contradiction to theory and previous DLS work in moderately concentrated (≤ 10 vol%), highly-charged colloidal silica suspensions, where speed-up effects ($H(QR) > 1$) were reported. The results also illustrate that the hydrodynamic interactions in colloidal suspensions can be determined over the relevant wave-vector range, and are free from any modelling of the static or dynamic properties thanks to the availability of coherent X-ray beams.

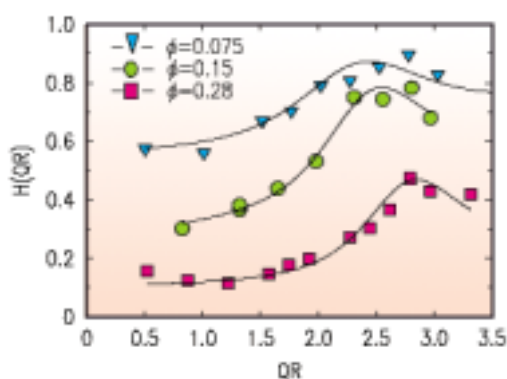


Fig. 97: Hydrodynamic functions $H(QR)$ for charge-stabilised colloidal silica for three different concentrations ($\Phi = 0.075, 0.15$ and 0.28).

The solid lines are guides to the eye.

Principal Publications and Authors

[1] G. Grübel (a), D.L. Abernathy (a), D.O. Riese (b), W.L. Vos (b), G.H. Wegdam (b), *J. Appl. Cryst.*, **33**, 424 (2000).

[2] D.O. Riese (b), W.L. Vos (b), G.H. Wegdam (b),

F.J. Poelwijk (b), D.L. Abernathy (a), G. Grübel (a), *Phys. Rev. E*, **61**, 1676 (2000).

(a) ESRF

(b) Van der Waals-Zeeman Institute, University of Amsterdam (The Netherlands)

Aqueous Suspensions of Vanadium Pentoxide Ribbons: SAXS Experiments at Equilibrium and Under Shear

Aqueous suspensions of vanadium pentoxide (V_2O_5) ribbons can be considered as a model system for a lyotropic nematic liquid crystal. Electron microscopy on dried samples shows that these mineral particles are roughly 1 nm thick, 10 nm wide and a few hundred nm long. Such sizes can be probed directly on aqueous suspensions using small-angle X-ray scattering (SAXS) techniques, which gives additional information about the nature of the interactions stabilising the system.

The polymorphism of these suspensions is essentially determined by their volume fraction ϕ [1]. Dilute suspensions are isotropic whereas more concentrated ones are nematic. This first order transition (at $\phi \sim 0.5\%$) is well described by the Onsager theory of uniaxial nematic ordering which is based on excluded volume interactions.

In the dilute isotropic phase, the analysis of the scattered intensity at very small scattering vectors (form factor analysis) allowed us to determine the width (25 nm), the persistence length (100-200 nm), and the chemical stability of the ribbons depending on pH and concentration [2]. In the nematic phase, investigations on single domains were carried out at scattering angles lower than that at which a correlation peak is observed. A small and very well collimated synchrotron beam is necessary to probe very small single domains and to observe their small angle scattering (Figure 98). In principle, for a nematic phase, this “central” scattering pattern is expected to be anisotropic. However, this has rarely been observed so far because the particles or molecules are usually small (as in thermotropic liquid crystals) so that the scattering anisotropy is too small. In contrast, Figure 98 clearly shows the SAXS anisotropy of these V_2O_5 suspensions. Besides, a careful analysis of the scattering along the nematic director direction provided an estimate of the contour (or overall) length of the ribbons (800 - 1000 nm) [2].

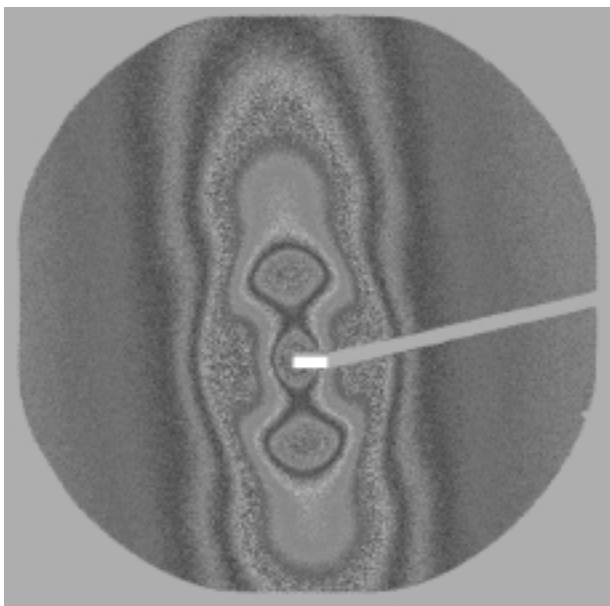


Fig. 98: Iso-contours of the scattered intensity by a fluid nematic single domain ($\phi = 0.8\%$). Note the elliptical anisotropic contour lines of the SAXS at the centre of this scattering pattern.

At larger volume fraction ($\phi > 1.5\%$), the system exhibits a transition from a sol to a weak physical gel which is still nematic. At low volume fraction ($\phi < 4\%$), the swelling of this gel is 2-dimensional (expected for a common uniaxial nematic phase) whereas, strangely enough, it is 1-dimensional at higher volume fraction ($\phi > 4\%$). One way to prove the biaxiality suggested by such a behaviour is to study a single domain of the nematic phase, i.e. to macroscopically orient the sample. Unfortunately, the gel properties of the phase prevent its alignment by an electric or a magnetic field. Nevertheless, shearing these suspensions in a Couette cell was found to be an elegant and efficient means of achieving biaxial orientation. SAXS experiments under shear were performed on **ID2** on two nematic gel samples of volume fractions $\phi = 2\%$ and 5% . Two orthogonal configurations were defined by sending the X-ray beam either radially through the shear cell or tangentially (**Figure 99**). Combining the information obtained in these two configurations allowed us to analyse the symmetry of the scattering (**Figure 100**) and to prove the biaxial character of the more concentrated nematic phase [3]. Moreover, the thermodynamic and flow properties of this biaxial nematic phase are well described by recent theoretical models.

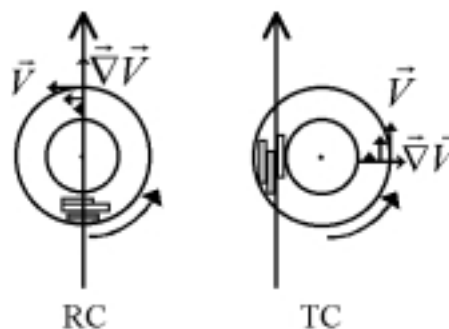


Fig. 99: Top views of the Couette cell in the radial (RC) and tangential (TC) configurations.

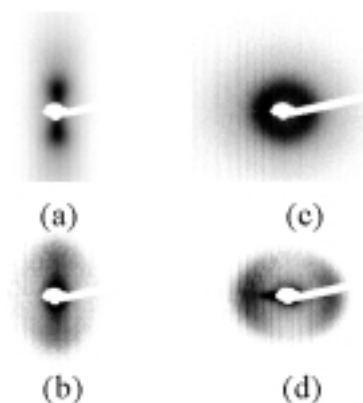


Fig. 100: Scattering patterns obtained - with the 2% sample: a) in the RC b) in the TC - with the 5% sample: c) in the RC d) in the TC

References

- [1] a) P. Davidson, C. Bourgaux, L. Schouffet, P. Sergot, C. Williams, J. Livage, *J. de Physique II*, **5**, 1577 (1995). b) X. Comminhes, P. Davidson, C. Bourgaux, J. Livage, *Adv. Mat.*, **9**, 900 (1997).
- [2] O. Pelletier, C. Bourgaux, O. Diat, P. Davidson, J. Livage, submitted to *Eur. Phys. J. B*.
- [3] O. Pelletier, C. Bourgaux, O. Diat, P. Davidson, J. Livage, *Eur. Phys. J. B*, Dec 1999, in press.

Authors

O. Pelletier (a), C. Bourgaux (b), O. Diat (c), P. Davidson (a), J. Livage (d).

(a) Lab. de physique des Solides, Université de Paris Sud, Orsay (France)

(b) LURE, Université de Paris Sud, Orsay (France)

(c) ESRF, and presently DRFMC/SI3M, CEA Grenoble (France)

(d) Lab. de Chimie de la Matière Condensée, Univ. Pierre et Marie Curie, Paris (France)

Applied and industrial research

Introduction

The year 1999 was marked by a change in the ESRF's policy for applied and industrial activities. Instead of trying to initiate industrial collaboration concerning all the domains and techniques as in previous years, a special effort was focussed on half a dozen industry-related projects. This effort was supported by the hiring of an engineer and a scientist whose activities are not only directed towards data collection but also to processing and analysing the data for the industrialists. This initiative permitted the opening of a more comprehensive analytical service.

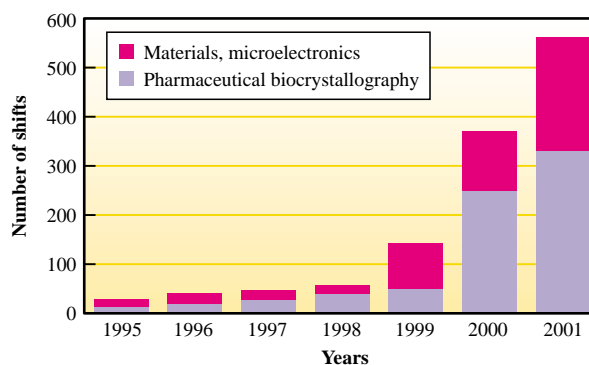
Protein crystallography data collection is still the main industrial proprietary activity at the ESRF, and it represents about half of the overall beam time purchased by companies (see [graph](#)). The systematic scheduling of measurement slots (on BM14 and ID14 beamlines) for industrialists now facilitates rapid access. In the near future, the program for automated data collection, presently being launched in collaboration with the EMBL, will permit a decrease in the dead-time between two sessions of data collection on different samples. As a consequence, it should allow us to meet the need for greater rapidity due to the increasing demand for protein structures issuing from pharmaceutical companies and the genome project.

Microelectronics is the second major domain and advances in this area have been encouraged by the construction of beamline ID27 specifically designed for surface micro-contamination analysis on silicon wafers by total X-ray reflection fluorescence. The beamline was completed during 1999, as part of the MEDEA program, and it should receive industrial customers from July 2000 onwards. ESRF beamlines are also used for many other types of measurements related to microelectronics has illustrated here by two examples on the structure of molten silicon and the interface structure between two silicon wafers.

Demand for the technique of microtomographic reconstruction has increased significantly, due to technical improvements both in data collection and image processing, and, more importantly, to the launching of a complete service. Companies can now submit their samples by post and the full analysis is rapidly carried out by an engineer of the ID19 staff specially assigned to this task. Two typical illustrations, on polymer foam and metal alloys, are given in this section.

A similar type of service for strain-stress analysis of metallic pieces will perhaps be offered to companies in the near future. The new diffractometer from the Risø Institute is now operational on ID11 and the high energy beams available on ID15 permit the analysis of bulk samples. This is illustrated by the contribution on residual stress.

Proprietary shifts at the ESRF



The growing interest in powder diffraction is due to the high quality of the patterns, to the ability to follow processes in real-time – cf. the contribution on intermetallic-ceramic synthesis – and even to the application in situ of extreme pressures and temperatures – cf. the contribution on the crystallisation of cubic boron nitride –. A new service for pharmaceutical drug characterisation using the high resolution powder data on ID11 and BM16 should start at the end of the year 2000.

Our industrial collaborators also take advantage of many other techniques, including absorption spectroscopy and micro-analysis. Here the former has been used for the

characterisation of a metallic catalyst and the latter has been used in the project of microdiffraction on human hair.

This new policy probably accounts for the doubling of the quantity of beam time that was purchased during 1999 by companies with respect to 1998. It has now reached 1.5% of the allocated beam time, but this value is still much smaller than the percentage of applied research that is carried out through the free-of-charge peer-reviewed access (about 20% to 25%). It is worth mentioning that the applied activity has been acknowledged officially at the ESRF, with the creation of the review committee section “Materials Engineering and Environmental Matters”.

Structure of Molten Silicon

To produce large-size, defect-free single crystals for the next generation of ultra-large scaled integrated circuit devices, a better understanding of the crystallisation process from the melt is required. In particular, the atomic-scale structure of the melt is of interest in a wide temperature range, including the equilibrium and the undercooled state. Therefore, X-ray diffraction (XRD) experiments were performed at the ESRF to determine the structure of molten silicon. In order to access the undercooled regime and to provide high-purity conditions, the containerless electromagnetic levitation technique was employed. This technique uses an rf-electrical current which is sent through a conical coil to produce lift and heat in a small drop (approx. 5 mm in diameter) as shown in [Figure 101](#). It is possible to levitate solid Si electromagnetically by preheating the sample; as molten Si is conducting [1]. So far, only one X-ray diffraction experiment on aerodynamically levitated Si has been performed [2].

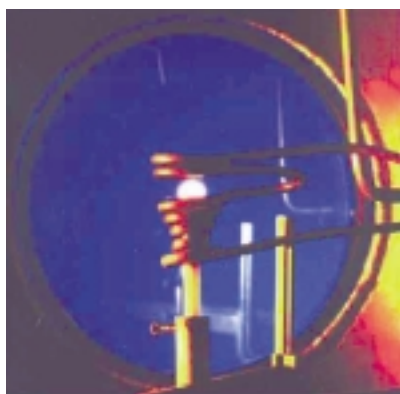


Fig. 101: Copper coil consisting of two counterwound sections. The conical shape of the lower section creates a gradient in the magnetic field which in turn produces lift. The magnetic field of the upper section prevents the sample from being ejected. The coil is housed by a UHV vacuum chamber. The bright spot between the upper and lower windings is the levitated liquid sample.

The experiments were carried out at beamline **ID9**, where an intense white X-ray beam is available for energy dispersive measurements. With the X-ray detector positioned at a fixed angle the structure factor $S(Q)$ can be measured as a function of temperature. Temperature is measured by non-contact pyrometry and is controlled either by adjusting the heater power of the rf-generator, or by convectively cooling the sample with a gas stream of high-purity helium. With this setup it was possible to scan a temperature range from 1150°C to 1650°C, including a maximum undercooling of $\Delta T = 290^\circ\text{C}$.

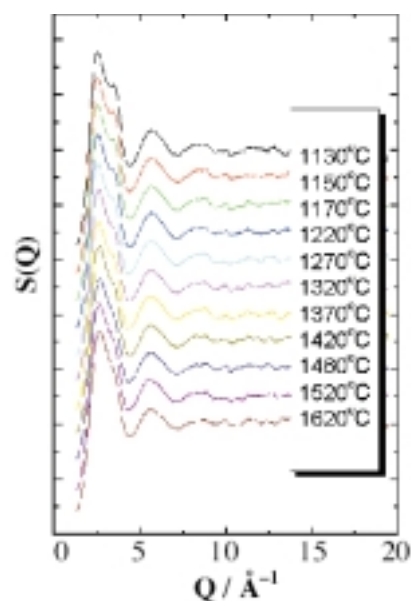


Fig. 102: Scattering intensity vs. momentum transfer for different temperatures. The spectra are shifted vertically for clarity. The appearance of a shoulder on the high- Q side of the first maximum is evident (see text)

$S(Q)$ yields information about the coordination around the Si atoms and helps to determine an improved empirical interatomic potential which can be used for molecular dynamics calculations. The spectra obtained are shown in [Figure 102](#). They clearly show the appearance of a shoulder on the high- Q side of the first maximum. This feature becomes more pronounced and develops into a maximum with increased undercooling. This maximum is characteristic for molten silicon, in contrast to normal metals. The spectra of liquid metals, like, e.g., Ni, do not show such a maximum in agreement with the generally accepted picture that the structure of molten metals corresponds to that of closely packed spheres. In contrast, the silicon melt has a different structure, reminiscent of its tetrahedrally bonded character in the solid state.

References

- [1] M. Langen, T. Hibiya, M. Eguchi, I. Egry, J. Crystal Growth, **186**, 550 (1998).
- [2] S. Ansell, S. Krishnan, J.F. Felten, D. Price, J. Phys., C10, L73 (1998).

Principal Publication and Authors

I. Egry (a), D. Holland-Moritz (a), T. Schenk (a), K.-R. Bauchspieß (a), S. Schneider (a), H. Kimura (b), M. Watanabe (b), K. Izumi (b), T. Hibiya (b), M. Hanfland (c), to be published.

(a) Institut für Raumsimulation, DLR, Köln (Germany)

(b) Fundamental Research Labs, NEC Corporation, Tsukuba (Japan)

(c) ESRF

The Interface Structure of Bonded Silicon Wafers

Where two crystalline solids meet and bond together the atoms or molecules will form an interface structure, the most general example being grain boundaries in polycrystalline materials. For such boundaries between identical materials the misorientation between the two crystals determines the interface structure. We can distinguish between rotational misfit, twist, and bending misfit, tilt. Usually the boundaries have both tilt and twist misfit and are buried deeply inside solids and therefore difficult to study. However, semiconductor wafers can be bonded together with predetermined orientations and with ideal covalent bonds [1]. Using this technique combined with the intense X-ray beams at moderately high energy (23 keV) available at the ESRF, it has been possible to take detailed measurements of the atomic structure of the interface of bonded silicon crystals as a function of both twist and tilt angles.

Apart from being an ideal model system for grain boundaries, the interface of bonded silicon wafers are also of interest for potential applications of practical value. Determined by the chosen twist and/or tilt orientations, periodic elastic modulations are induced in the region around the interface and this can give rise to novel electronic and optical properties. Further, by a special technique, a wafer may be thinned down to the extent that the elastic modulation from a bonded interface may reach through the entire wafer to the external surface thus inducing a modulated surface structure with a periodicity given by the twist and/or tilt misfit.

The silicon wafers are bonded as follows: Standard 350 μm thick wafers are dipped in HF acid removing the native oxide layer and resulting in hydrogen terminated surfaces.

In a clean room the wafers are contacted and finally they are annealed above 1000°C to achieve covalent bonding at the interface [2].

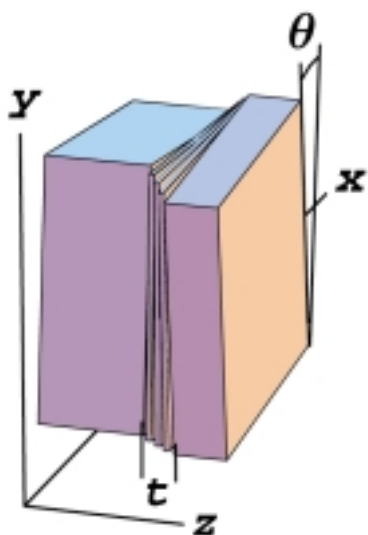


Fig. 103: Bonded crystals with twist angle θ have an interface with thickness t with modulated deformation.

Figure 103 shows a pair of bonded crystals with twist angle θ and with thickness t of the modulated interface. Measurements at the ESRF, performed at beamline ID32, have shown that the thickness t of the modulated interface varies from a few \AA to several hundreds \AA , and the functional form of the elastic modulation can be quite accurately determined. In Figure 104 the left panel shows the reciprocal lattice, parallel to the interface of the bonded crystals turned by the angle θ from each other. The circles show the (h, k) -coordinates of bulk Bragg points of the two crystals whereas the crosses correspondingly show where the diffraction signal from the modulated elastic deformation may be observed. By measuring the scattering intensity at many of these cross-positions both harmonic and anharmonic terms of the deformation-waves are determined. The line shape of the decay of the elastic deformation away from the interface is measured in diffraction scans perpendicular to the interface.

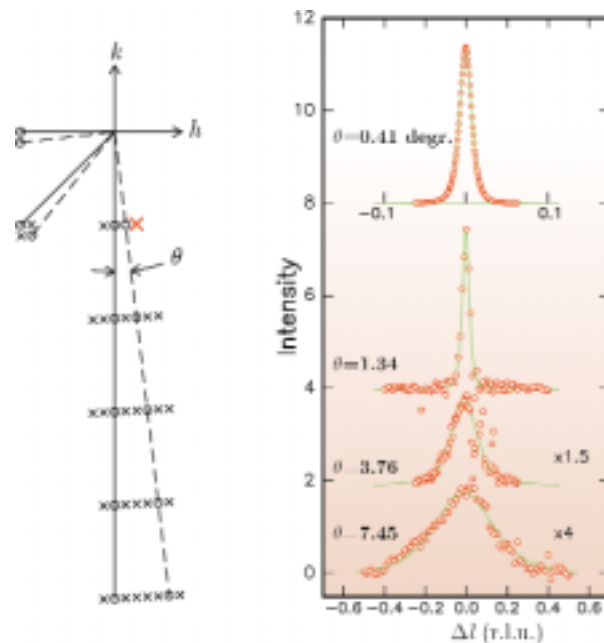


Fig. 104: The diffraction signal, red points, from the interface deformation field in X-ray scans perpendicular to the interface of bonded silicon wafers with twist angles θ . The left panel shows for both crystals the reciprocal lattice plane parallel to the interface and the red cross is the in-plane coordinate of the scans to the right.

The width (fwhm) of such diffraction profiles varies dramatically with the twist angle θ as shown in Figure 105. This width can be translated into the thickness t of the interface, also given in the figure. By line shape analysis, the decay function of the harmonic component of the elastic

In situ Deformation of Open-Cell Flexible Foams Using 3-D Computed Microtomography

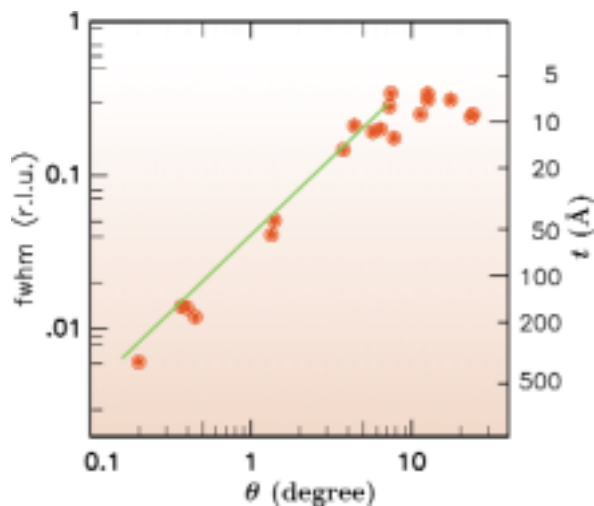


Fig. 105: The width of the strained interface layer t as deduced from the width, $fwhm$, of the scans in Figure 104, for bonded silicon wafers with twist angles θ . The line shows calculated data using a simple dislocation model with no fitted parameters.

deformation is proven to be exponential and the interface thickness t is determined as the double exponential decay length.

The experimental results are in good agreement with an idealised model for the interface, where all the deformations are described by a lattice of dislocations located in the interface. In Figure 105 the full line is calculated using this model. For twist angles θ smaller than 8 degrees the thickness is inversely proportional to θ and this holds at least down to the smallest angles studied, $\theta = 0.2$ degree. For $\theta > 8$ degrees t becomes a few atomic layers independent of θ .

References

- [1] M. Nielsen, R. Feidenhans'l, P.B. Howes, F. Grey, K. Rasmussen, J. Vedde, *Surf. Sci. Lett.*, **442**, 989 (1999).
- [2] S. Weichel, F. Grey, K. Rasmussen, M. Nielsen, R. Feidenhans'l, P.B. Howes, J. Vedde, *Appl Phys. Lett.*, **76**, 70 (2000).

Authors

M. Nielsen (a), R. Feidenhans'l (a), P.B. Howes (a, b), S. Weichel (c), F. Grey (c), M. Poulsen (c), J. Vedde (d).
 (a) Risø National Laboratory, Roskilde (Denmark)
 (b) Now at University of Leicester (UK)
 (c) Mikroelektronik Centret, Technical University of Denmark (Denmark)
 (d) TOPSIL Semiconductor Materials A/S, Frederikssund (Denmark)

Open-cell flexible foams are industrially important materials with widespread use in household furniture and car seating. The cushioning application of these materials depends critically on how they deform under a compressive load.

Using 3-D X-ray computed microtomography on the ID19 beamline it has been possible to study in fine detail the exact mechanisms by which open-cell flexible foams deform in compression. The characterisation of the deformation process at the microscopic length scale in 3-D, in the bulk, represents a key step towards a better understanding of the relationship between the structure of foams and their mechanical properties.

In order to observe the deformation mechanisms in these relatively low-density materials two criteria need to be satisfied. Firstly, a spatial resolution better than 10 micrometres is required to clearly resolve the fine struts making up the foam structure. Secondly, it is preferable to perform "local tomography" on a small region inside a larger sample so that edge effects during the compression are minimised. The actual experiment involved compressing a 2 cm-diameter cylinder of foam in a custom-built compression rig mounted onto the rotation stage of the tomography setup. The imaged volume was a 7 mm x 7 mm x 7 mm cube in the centre of the foam cylinder. Tomographic scans were taken at successively increasing levels of compressive strain. A standard filtered back-projection algorithm was used to reconstruct the volume from the local projection data. By setting one edge of the imaged volume coincident with the stationary plunger, it has been possible to correlate the structure seen at one level of compression with the structure observed at each other level of compression.

Figure 106 shows 3-D reconstructions of the sample at three different strain levels. The face of the stationary plunger can be seen at the bottom of each image. The 3-D renditions represent volumes of 7 mm x 7 mm x 1.4 mm.

A comparison of the struts around the cells marked C and D between Figure 106a and Figure 106b shows clearly that the initial phase of the compression occurs by a process in which struts bend. This early deformation is accompanied by a roughly linear elastic response. By comparing Figure 106b and Figure 106c it can be seen that a whole band of the structure comprising cells labelled A to E actually collapses. A plateau in the stress/strain curve accompanies this second mode of deformation.

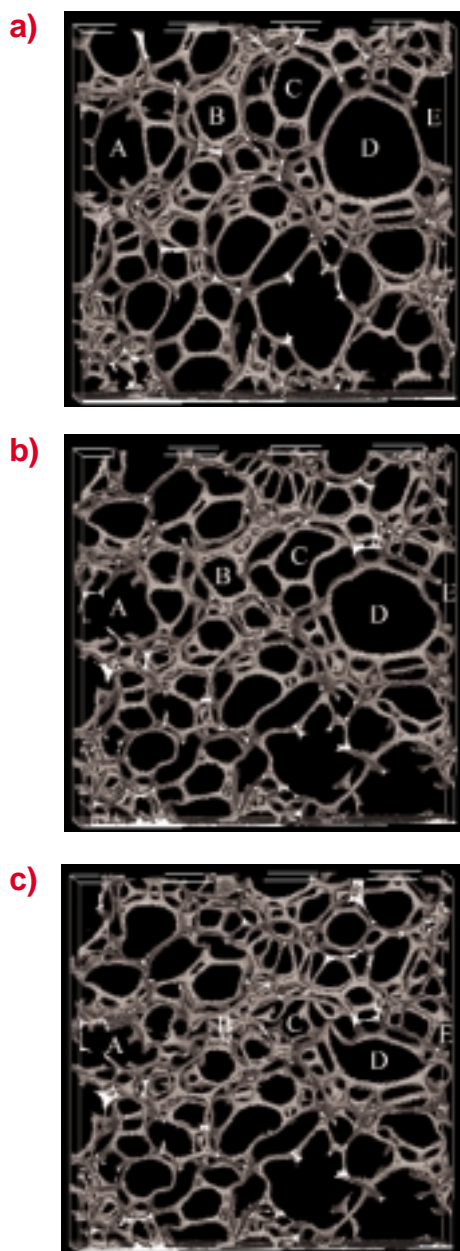


Fig. 106: Reconstruction of an open-cell flexible polyurethane foam at several levels of compressive strain
 a) 0% applied strain, b) 10% applied strain, c) 23% applied strain.

Authors

A.H. Windle (a), J. Elliott (a), R.J. Oldman (b), J.R. Hobdell (c), G. Eeckhaut (c), J. Baruchel (d), S. Bouchet (d,e), W. Ludwig (d), P. Cloetens (d), E. Boller (d).
 (a) Department of Materials Science and Metallurgy, Cambridge University (UK)
 (b) ICI Chemicals and Polymers Ltd., Runcorn (UK)
 (c) Huntsman Corporation, Everberg (Belgium)
 (d) ESRF
 (e) CMM, ENS des Mines de Paris (France)

Microtomographic Observation of Grain Boundary Wetting in Al Alloys

The penetration of liquid metals into the grain boundaries of polycrystalline solid metals may in some cases lead to the formation of micrometre-thick liquid phase layers and thereby to severe degradation of the mechanical properties of the solid metal. The underlying mechanisms of this grain boundary penetration and wetting process are still poorly understood and depend on the specific metal couple under investigation.

Synchrotron radiation X-ray microradiography and microtomography have been used on **ID19** to investigate the penetration of liquid gallium into the grain boundaries of aluminium - a system known for very high penetration rates. Due to the large difference in absorption, sub-micrometre thick Ga layers in the bulk of millimetre-sized Al samples can be detected. **Figure 107** shows a reconstructed cut through an Al sample which has been exposed to liquid Ga. A comparison of the tomographic reconstruction before and after the penetration revealed that the individual grains have moved with respect to each other by several micrometres - in other words, the liquid phase has replaced the grain boundaries and separates the grains [1].

Comparison of the tomographic data with electron backscattering diffraction mappings recorded on the surface of the same sample indicates that the wetting and the thickness of the liquid phase layer depend on the relative grain misorientation. A more detailed analysis is foreseen, taking advantage of the complete 3-D grain

Although these processes have been understood for some time, this experiment allows them to be visualised in the bulk in unprecedented detail and will allow further clarification of the mechanisms of foam deformation.

Software applications have been developed at the ESRF to extract the locations of the nodes in the reconstructed foam volumes and also to determine the connectivity of the structures. The data will be used to construct finite element models and a comparison of the simulated deformation and the actual observed deformation will be performed. The advantage of using the modelling approach in tandem with the experimental characterisation is that insight into the actual stresses inside the foam may be deduced from the calculations.

orientation information provided by the tracking technique recently developed at ID11.

In situ radiographic observation turned out to be a promising tool for the characterisation of the kinetics of the propagating liquid metal films. The optimised setup at ID19 takes advantage of the 4 channel parallel read-out capability of the FRELON camera and allows the recording of sequences of up to 400 high resolution images (spatial resolution $1\ \mu\text{m}$) with frame-rates of up to 15 images per second. Measurements on well-defined grain boundaries (bicrystals) should allow the investigation of the influence of various parameters like temperature and liquid metal composition.

In addition the microtomographic observation of Ga decorated grain boundaries might be used as a unique technique for three-dimensional visualisation and analysis of polycrystalline aluminium samples: shape and size of the individual grains are readily obtained from the segmented volume data. Figure 108 shows a 3-D rendition of a small part of the same polycrystalline sample presented in Figure 107. An application of this technique is shown in Figure 109: the propagation of cracks with respect to grain boundaries can be studied within the bulk of the sample [2].

Principal Publications and Authors

[1] W. Ludwig (a), D. Bellet (b), J. Mater. Sci. Eng., in press.
 [2] W. Ludwig (a), J-Y. Buffière (c), S. Savelli (c), S. Bouchet (a,d), D. Bellet (b), to be published.

- a) ESRF
- b) Laboratoire GPM2, ENSPG, INPG, Grenoble (France)
- c) Laboratoire GEMPPM, INSA, Lyon (France)
- d) CMM, Ecole Nationale Supérieure des Mines de Paris (France)

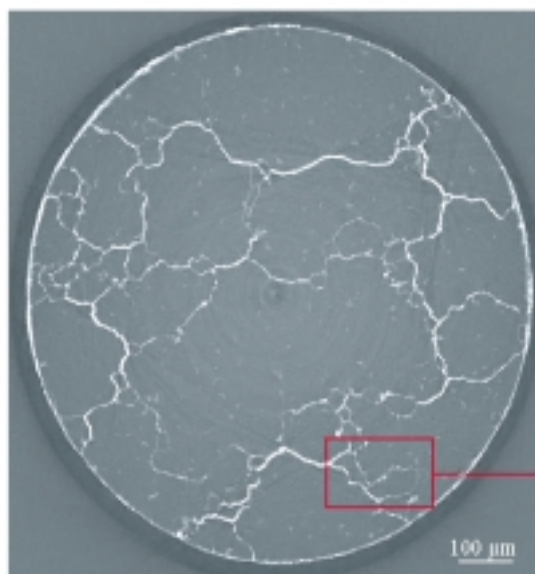


Fig. 107: Reconstructed tomographic slice (pixel size: $1\ \mu\text{m}$) through a cylindrical Al sample which has been exposed to liquid Ga for 4h at 320 K: the wetting of the grain boundaries by liquid Ga can be observed; the magnified image shows the varying thickness of the Ga layer.

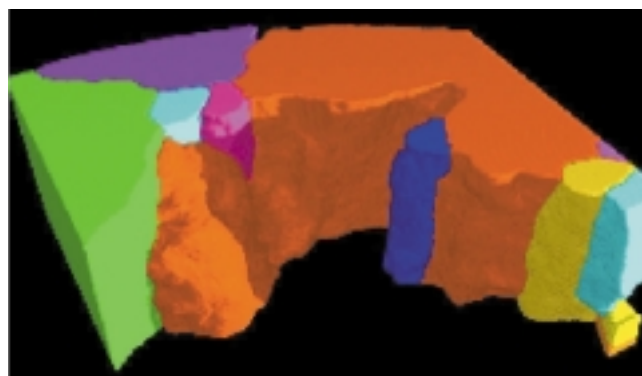
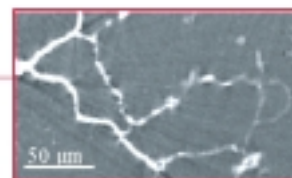
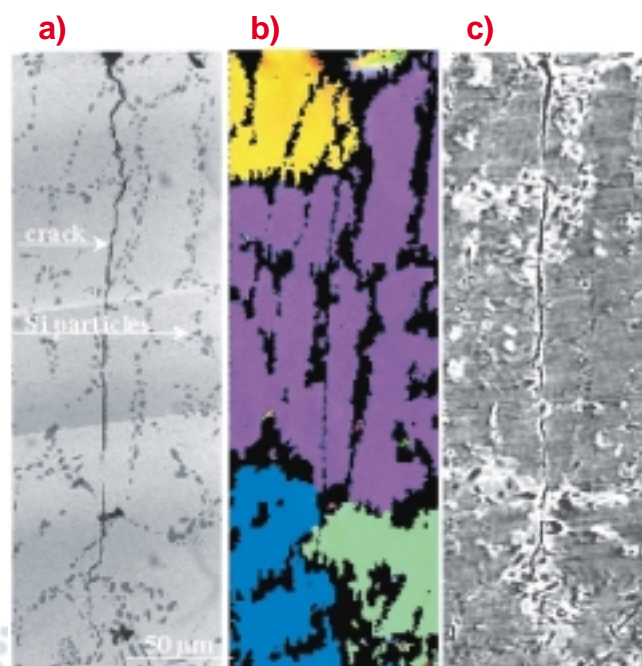


Fig. 108: 3-D rendition of a small sub-volume of the polycrystalline Al sample shown in Figure 107. Due to the extrusion process, the grains are elongated along the vertical axis. The grain in the centre of the image has been set to transparent.

Fig. 109: Same zone on the surface of a pre-fatigued Al-Si sample observed with three different techniques: a) optical micrograph, b) grain orientation mapping (EBSD): different colours correspond to different crystalline orientations, c) tomographic reconstruction after infiltration of Ga: cracks, Si particles and grain boundaries (enhanced absorption due to Ga) are easily distinguished. Note that a) & b) are restricted to the sample surface whereas the tomographic dataset contains information throughout the whole volume.



White High Energy Synchrotron Radiation:

A New Tool for Non-Destructive Texture and Residual Stress Analyses in the Bulk of Samples and Components

The properties of components and semi-finished products depend not only on geometrical dimensions but also strongly on the material properties such as the microstructure and the texture as well as on the residual stress state. The microstructure, the texture and the residual stress distribution are particularly inhomogeneous throughout the component in the case of local high thermal or mechanical loading such as in welding processes and in conversion processes. Thus, often very small gauge volumes are necessary in order to find local extrema e.g. of the texture and the residual stresses.

A non-destructive quantitative texture and residual stress analysis can be performed using diffraction methods. The easiest accessible radiation is conventional characteristic X-radiation (e.g. $E_{CuK\alpha1} = 6.9$ keV, $E_{CrK\alpha1} = 5.4$ keV), which has a penetration depth of some ten μm and therefore is only suitable for the determination of the residual stresses in near surface layers. Neutron diffraction can provide information at significantly higher depths of several 10 mm's in components, but for intensity reasons the local resolution of neutron residual stress analysis is in the order of a gauge volume size of approximately 1 mm^3 .

Using high energy synchrotron radiation (Energy range up to 300 keV), for instance in light-weight materials such as Al-alloys, penetration depths comparable to neutrons are achievable while significantly smaller gauge volumes – potentially as small as $60\ \mu\text{m} \times 60\ \mu\text{m} \times 0.6\text{ mm}$ – can be realised thanks to the high intensity and parallelism of the beam. Thus, white high energy synchrotron radiation at the



Fig. 110: Initial state (front) and extrudates after full forward extrusion (back).

ESRF was employed for strain and stress analyses on a variety of materials and problems [1].

The use of white high energy synchrotron radiation enables a simultaneous analysis of residual stresses, texture and phase composition with high local resolution in cold extruded steel rods (Figure 110) with a diameter as large as 15 mm. Figure 111 shows the spectra obtained during approximately 30 minutes each in the centre and near the surface of the cold extrudates. The spectra illustrate the decrease of strength of the $\langle 110 \rangle$ fibre texture towards the outer border of the extrudates [2]. The consequence of this

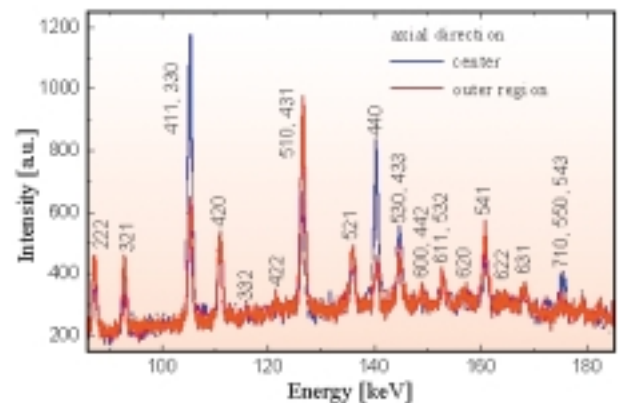


Fig. 111: Spectra in axial direction in the centre and nearer to the surface of an extruded steel sample.

texture inhomogeneity is an inhomogeneity of the mechanical properties present across the diameter of the sample. Subsequent residual stress analyses (Figure 112) revealed the residual stress state. The residual stress distribution and the quantitative values support the results of FEM calculations and enable an optimisation of the process parameters such as the extrusion ratio, die opening angle and the ejection method.

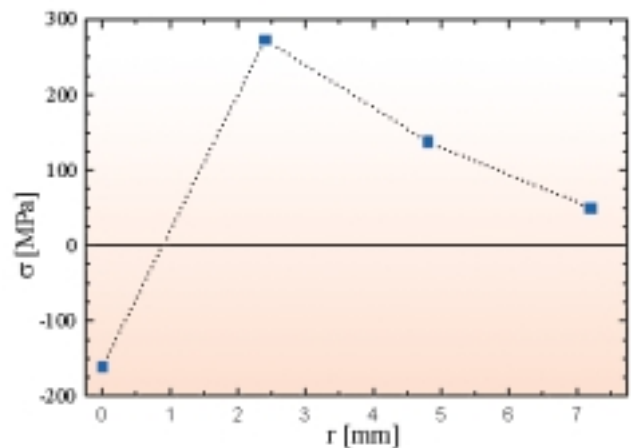


Fig. 112: Residual stress in hoop direction ($r = 0$: centre of the sample, $r = 7.5$: surface)

Further measurements performed on thermal barrier coatings, functionally graded Ni/ZrO₂ materials and ceramic matrix composites revealed that, using high energy synchrotron radiation, residual stress analyses with a local resolution of a hundred micrometres are possible.

Principal Publications and Authors

[1] W. Reimers (a), A. Pyzalla (a), M. Broda (a), G. Bruschi (a), D. Dantz (a), T. Schmackers (a), K.-D. Liss (b), T. Tschentscher (c), *J. Mat. Sci. Lett.*, **18**, 581-583 (1999).

[2] A. Pyzalla (a), W. Reimers (a), A. Royer (b), K.-D. Liss (b), *Proc. 20th Risoe International Symposium on Materials Science: Deformation-Induced Micro-structures: Analysis and Relation to Properties*, ed. J.B. Bilde-Sorensen et al., Risoe National Laboratory, Roskilde, Denmark, 453-458 (1999).

(a) Hahn-Meitner-Institut, Berlin (Germany)

(b) ESRF

(c) HASYLAB, Hamburg (Germany)

Time-Resolved Studies of Intermetallic-Ceramic Synthesis by Self-Propagating High-Temperature Synthesis

Self-Propagating High-Temperature Synthesis (SHS) is an alternative for producing a wide variety of light-weight intermetallic compounds, ceramics and composite materials. The method [1] is exothermic and after ignition the reaction proceeds as a reaction front travelling at speeds of 10-250 mm/s through a compacted powder sample with reaction front temperatures of up to several thousand degrees (Figure 113). The procedure is inexpensive and has large potential for industrial applications. Limited information is available on the actual mechanisms and products involved because of the high temperatures and the fast reactions.

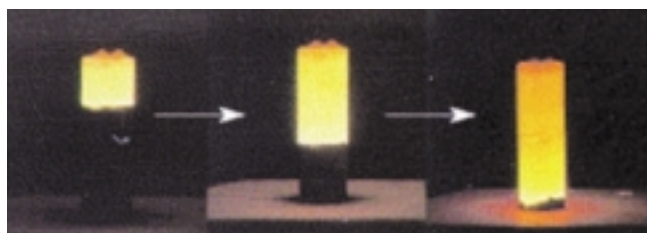


Fig. 113: High-temperature synthesis of intermetallic compounds.

Although pioneering work has been performed at second generation synchrotron X-ray sources [2], these early

studies were complicated by limited counting statistics and access only to the surface regions of the sample.

The Materials Science Beamline, ID11, has now been used to study the exothermic reactions of the systems Al-Ni, Al-Ni-C-Ti and Ti-C [3]. Circular pellets of equal amounts of Al, Ni, C and Ti were produced by compressing the powder mixtures using a steel die to about 45% of maximum density. The pellets were 20 mm in diameter and about 2 mm in thickness. The powder samples were ignited by passing a current through a tungsten wire attached to one side of the pellets. An X-ray beam of dimensions 0.2*0.2 mm at a wavelength of 0.295 Å produced by an in-vacuum undulator of 138 magnetic poles and a gap of 8 mm was centred on the middle portion of the sample. X-ray diffraction patterns were collected every 100 ms. 25 ms of exposure time and 75 ms of readout time from a 1024*1024 pixel FRELON CCD camera gave a sequence of diffraction patterns of the reaction as the reaction front passed the X-ray beam. The experimental setup is illustrated in Figure 114.

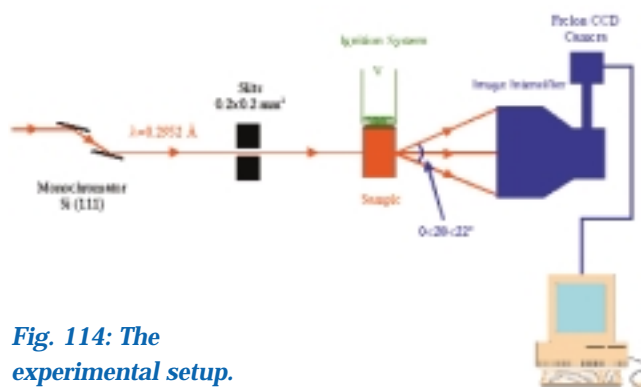


Fig. 114: The experimental setup.

A sequence of the changes of the patterns is illustrated in Figure 115. for the system Al-Ni-Ti-C. The start of the reaction involves the melting of the Al and the reaction proceeds through an intermediate ternary phase with the life-time of 400-500 msecs. The final products

Fig. 115: Powder diffraction patterns, recorded every 100 ms during the reaction.

aluminumnickelide and titaniumcarbide finally stabilises 4.3 secs after the onset of the reaction.

These studies firmly establishes synchrotron radiation experiments at the brilliant third generation sources as a new important tool for studies of a large class of solid-state reactions on a millisecond timescale. Other studies of potentially interesting industrial processes are under way.

References

- [1] Z.A. Munir, U. Anselmi-Tamburini, *Materials Science Report*, **3**, 277-365 (1989).
 [2] and references within: J.F. Javel, M. Dirand, J.J. Kuntz, F.Z. Nassik, J.C. Gachon, *J. of Alloys and Compounds*, **247**, 72-81 (1997).
 [3] C. Curfs, I.G. Cano, G.B. Vaughan, M.A. Rodriguez, X. Turrillas, *Int. J. of Self-Propagating High-Temperature Synthesis* (1999), in press.

Authors

- C. Curfs (a), Á. Kvick (a), G.V. Vaughan (a), I.G. Cano (b), M.A. Rodriguez (b), X. Turrillas (c).
 (a) ESRF
 (b) Instituto de Ceramica y Vidrio, Madrid (Spain)
 (c) Instituto Eduardo Torroja, Madrid (Spain)

In Situ X-ray Diffraction Studies of Crystallisation of Cubic Boron Nitride from BN Solutions in Supercritical Hydrazine at High Pressures and Temperatures

Cubic boron nitride (cBN) is the material used worldwide for the machining and polishing of ferrous metals due to its extreme hardness, which is second only to diamond. cBN is similar to diamond in both its structure and physical properties such as high strength, thermal conductivity, and atomic density, and it is even more resistant to chemical attack. Despite its promising physical properties, cBN is the least studied wide band gap semiconductor, because the only reliable methods of producing this phase involve high pressures (> 4 GPa) and high temperatures (> 1600 K). Recently it has been found that the threshold pressure of cBN formation can be drastically reduced when it crystallises from BN solutions in supercritical fluids (ammonia, hydrazine, etc.) [1]. The present work is the first attempt to study in situ regularities of cBN crystallisation in

the BN - N₂H₄ system at high pressures and temperatures employing X-ray diffraction with synchrotron radiation. The high-pressure experiments were carried out using a large-volume Paris-Edinburgh press. The diffraction measurements were performed in the energy-dispersive mode at beamline ID30.

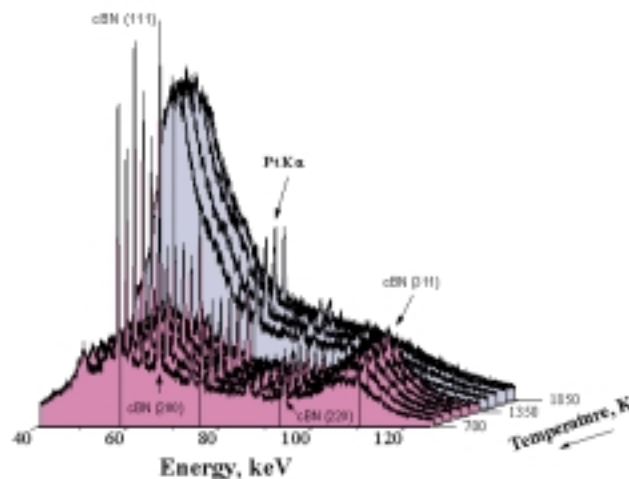


Fig. 116: Diffraction patterns of the BN-N₂H₄ system (81 mol.% BN) at 4.1 GPa.

Our findings have shown that at 4.1 GPa the cooling of the solution containing 81 mol.% BN from 1460 to 1400 K results in a spontaneous crystallisation of cubic boron nitride (Figure 116). The emergence of cBN lines is accompanied by a simultaneous change in the shape of the solution spectrum, in particular by appearance of a broad halo with the maximum at 107 keV ($d_{hkl} = 1.1 \text{ \AA}$). A similar change in the shape of the solution spectrum was also observed at 4 GPa and 1350 K in cooling the solution containing 33 mol.% BN. In this case, however, no formation of any crystalline phase was recorded even in cooling the solution down to room temperature.

A subsequent heating of the above BN-N₂H₄ mixtures up to 1600 K in all the cases gave rise to a recovery of the characteristic shape of the solution spectrum due to dissolution of solid phase(s).

The above experimental facts should be attributed to the existence of the $L = X + \text{cBN}$ eutectic reaction at $1400 \pm 15 \text{ K}$ and 4 GPa. This reaction results in the crystallisation of cBN and the formation of an unknown amorphous phase of the BN - N₂H₄ system (phase X). A hypothetical phase diagram of the BN-N₂H₄ system at 4 GPa is shown in Figure 117.

Thus, the spontaneous crystallisation of cubic boron nitride was observed for the first time at 4.1 GPa which is the lowest pressure of cBN formation without a catalyst. This result will probably lead to a new method of synthesising high-purity cubic boron nitride at relatively low pressures.

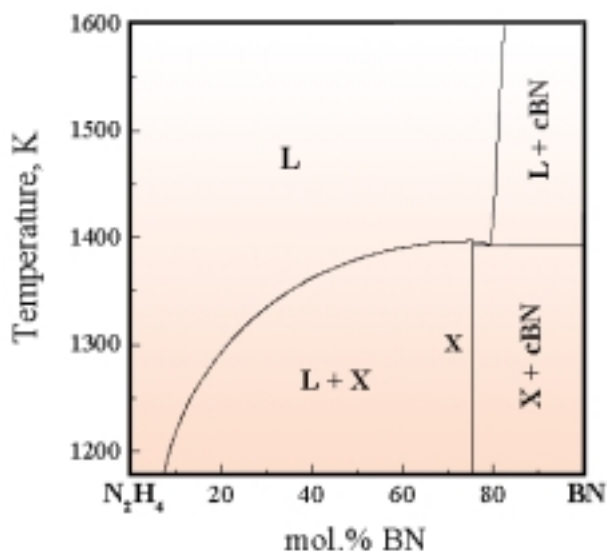


Fig. 117: A hypothetical phase diagram of the BN-N₂H₄ system at 4 GPa.

Reference

[1] V.L. Solozhenko, *Diamond & Relat. Mater.*, **4**, 1 (1994).

Authors

V.L. Solozhenko (a), Y. Le Godec (b), M. Mezouar (c), J.-M. Besson (b), G. Syfosse (b).

(a) Institute for Superhard Materials, National Academy of Sciences of Ukraine, Kiev (Ukraine)

(b) Physique des Milieux Condensés, Université P&M Curie, Paris (France)

(c) ESRF

Design of a Ni/Au Surface Alloy Catalyst for Steam Reforming

Bimetallic catalysts find increasing applications in the industry, e.g. in the petroleum industry for catalytic reforming of petroleum fractions and in the environmental sector for the removal of harmful exhaust gases from automobiles. Recent theoretical calculations and surface science experiments have contributed significantly to the understanding of bimetallic alloy systems [1]. The improved fundamental understanding was used to design a steam-reforming catalyst consisting of supported Ni particles with Au alloyed into the surface of the nickel. The chemical properties of the surface alloy could be tuned by varying the Au/Ni atomic ratio in the surface of the catalyst metal alloy particle. In this way it was possible, for the first time, to

prepare a bimetallic catalyst based on a fundamental knowledge of the structure, segregation, and reaction processes at a metal surface [2].

Au-Ni nano-particle catalysts were prepared and characterised by a combination of in situ transmission EXAFS in combination with on-line mass spectrometry (MS), transmission electron microscopy (TEM), X-ray powder diffraction and thermogravimetric analysis (TGA). The EXAFS measurements were performed at beamline **BM29**.

Figure 118 shows the Fourier back-transformed XAFS spectrum obtained from a reduced MgAl₂O₄ supported Ni catalyst (16.5 weight % Ni) modified with 0.3 weight % Au. Only if we allow that Au has Ni as nearest neighbours at Ni interatomic distances the data can be fitted properly. Because Au and Ni are immiscible in the bulk, this demonstrates that Au is alloyed into the Ni surface layer.

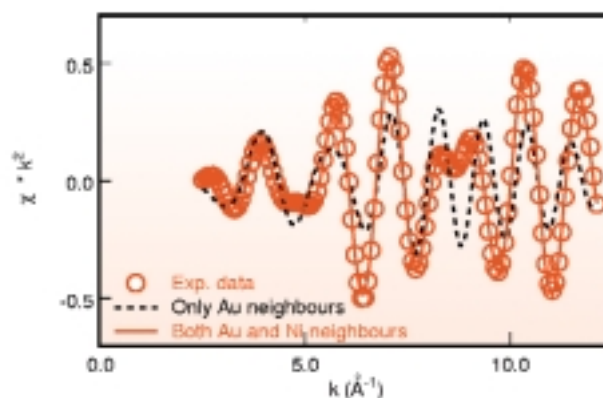


Fig. 118: k^2 -weighted EXAFS spectrum, $\chi(k)$, after extraction of the nearest-neighbour shell contribution at the Au L₃-edge of the Au/Ni MgAl₂O₄-supported catalyst. The circles represent experimental data. The dashed curve shows the best fit to the experimental spectrum with only Au amplitude and phase functions. The solid curve shows the best fit to the data with Au and Ni reference functions.

After reduction in pure hydrogen the catalysts were exposed to a diluted n-butane gas at 550°C and an on-line MS measured the steam-reforming activity of a Ni and a Ni/Au catalyst. In Figure 119 it can be seen that the pure Ni catalyst deactivates rapidly, whereas the conversion for the Ni/Au sample is almost constant. The deactivation of the Ni catalyst is typical for this type of catalyst under extreme steam-reforming conditions. It is associated with the formation of graphite, which can be observed by TEM and by the weight increase in a TGA setup. No weight increase was observed for the Au/Ni catalyst during steam reforming.

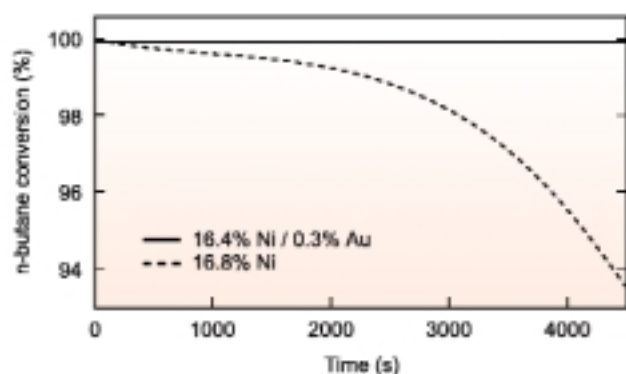


Fig. 119: Conversion of n-butane as a function of time during steam reforming in a 3% n-butane/ 7% hydrogen / 3% water in helium mixture at a space velocity of 1.2 hour⁻¹. The dashed curve shows the n-butane conversion for the Ni and the solid curve is for the supported Ni/Au catalyst.

In conclusion, the combination of a fundamental theoretical understanding of structure and reactivity and several experimental in situ techniques has resulted in the design of a new catalyst for the steam-reforming reaction.

References

- [1] L.P. Nielsen, F. Besenbacher, I. Stensgaard, E. Lægsgaard, C. Engdahl, P. Stoltze, K.W. Jacobsen, J.K. Nørskov, *Phys. Rev. Lett.*, **71**, 754 (1993).
 [2] F. Besenbacher, I. Chorkendorff, B.S. Clausen, B. Hammer, A.M. Molenbroek, J.K. Nørskov, I. Stensgaard, *Science*, **279**, 1913 (1998).

Authors

A.M. Molenbroek (a,b), J.K. Nørskov (a), B.S. Clausen (c).
 (a) Center for Atomic-scale Material Physics, Technical University of Denmark, Lyngby (Denmark)
 (b) Present address: Haldor Topsøe Research Laboratories, Lyngby (Denmark)
 (c) Haldor Topsøe Research Laboratories, Lyngby (Denmark)

Study of the Keratinisation Process in Human Hair Follicle by X-ray Microdiffraction

Hair grown in vitro is used by L'Oréal as a model for the study of the influence of nutrients or cosmetics on hair fibre production and the keratinisation process. In the field of

cosmetics, X-ray microdiffraction could be useful to evaluate and compare the efficacy of different cosmetic treatments particularly in the field of hair growth treatment and for the development of products for the prevention of hair loss.

Human hair fibre is made of keratin, a protein synthesised and progressively organised into filaments by the cortical cells of the keratogenous zone of the bulb. The hair fibre keratin contains two structures: α -keratin and amorphous keratin. In the α -structure, molecules of keratin are organised into tetramers (or protofilaments) and form hexagonal superstructures: the microfilaments. These structures give the typical X-ray SAXS and WAXS diffraction patterns which have been studied for many years using X-ray diffraction [1]. However, as yet, the corresponding molecular structure is not very clear [2] and the keratinisation process, during which keratin is formed and its structure becomes organised and stabilised, has not been completely elucidated.

The microfocus beamline, **ID13**, provides intense synchrotron radiation microbeams. A monochromatic ($\lambda=0.948$ Å) microbeam of 10 μm was selected. This makes it possible to obtain diffraction data for hair, from molecular to supramolecular structures, in less than 30 s exposure time. Synchrotron X-ray micro-diffraction studies along the bulb and the hair fibre allowed us to follow the keratinisation process and the progressive organisation of the keratin.

In vivo grown hairs were dissected out from scalp biopsies with their intact bulb. Some of them were grown in vitro in a nutritive solution for four days.

Scanning along the follicle (Figure 120) made it possible to follow the keratinisation process and the progressive organisation of the keratin:

- molecular organisation appears progressively in the bulb. Keratin is gradually organised from amorphous to α structure. The formation of α -helices is completed inside the bulb.
- supramolecular organisation appears only outside of the bulb. Filament structure is observed far from the bulb.
- The medium axis of α -helices tilts randomly around the main axis of the hair in the bulb: the organisation of the keratin is not stabilised. Changes in oscillation vanish when distance from the bulb increases, and disappear in the fibre.

Our microdiffraction experiments can be compared to experiments done by Mercer [3] with human plucked hairs, using a 100 μm collimated X-ray beam (copper anode filament) and an exposure time of 24 hours. The five zones, designated by Mercer from A to D, are described by diffraction patterns, birefringence, and thermal stability. The birefringence showed that the amount of oriented structures

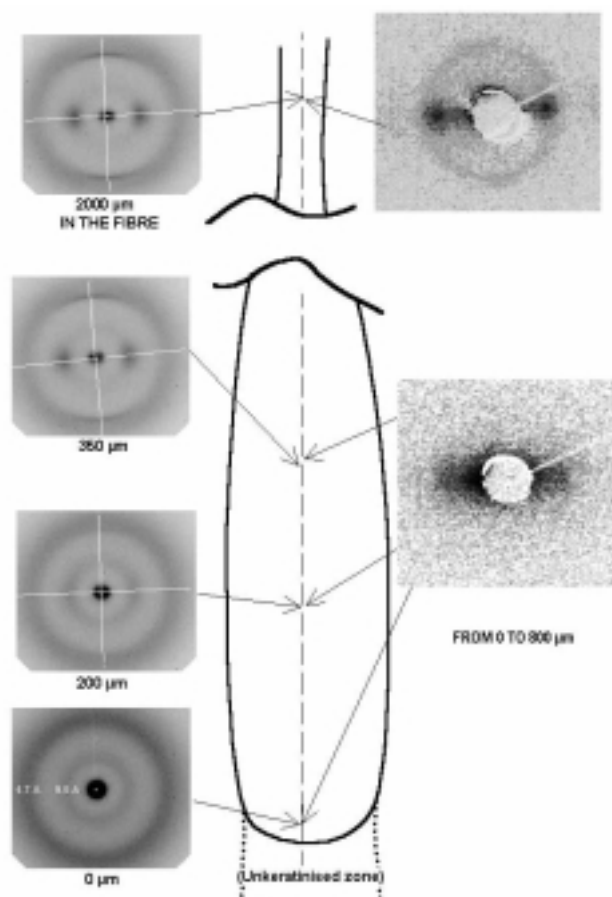


Fig. 120: WAXS (left) and SAXS (right) patterns observed along the follicle.

increases progressively between about 300 and 700 μm along the fibre. This corresponds with our observations with the WAXS patterns about the formation of the α -helices and the simultaneous formation of the dimers.

Our SAXS observations show that the supramolecular structure of microfibrils is achieved at over 1000 μm . This seems to correspond to the consolidation zone, as defined by Mercer in terms of thermostability of the keratin structure. However, Mercer proposed that the supramolecular structures could be explained by a progressive aggregation of smaller organised structures, and caused with less importance, by an extrusion-like phenomenon. SAXS observations made by microdiffraction indicate that supramolecular organisation exists early on in the time frame of the keratinisation process. However, the progressive evolution of the diffraction patterns to the fibre SAXS pattern could indicate that a phenomenon of densification occurs simultaneously to the keratinisation process.

Comparisons between structures observed for in vitro and in vivo grown hair, whether in the bulb or in the fibre, indicate there is no evidence of any structural difference.

Moreover, no variation in the transition in vivo/in vitro zone has been observed. In vitro and in vivo fibres exhibited the same structure, which is encouraging for in vitro growth technique development.

References

- [1] R.B. Corey, R.W.G. Wyckoff, *The Journal of Biological Chemistry*, **114**, 407-416 (1936).
- [2] B. Bussion, F. Briki, J. Doucet, *Journal of Structural Biology*, **125**, 1-10 (1999).
- [3] E.H. Mercer, In: *Keratin and Keratinisation – An Essay in Molecular Biology*, Pergamon Press New York (1961).

Principal Publication and Authors

- F. Balteneck (a), B.A. Bernard (b), J.-C. Garson (a), P. Engström (c), C. Riekel (d), F. Leroy (a), A. Franbourg (a), J. Doucet (e), *Cellular and Molecular Biology*, In press.
- (a) L'OREAL Recherche, Aulnay-sous-Bois (France)
 (b) L'OREAL Recherche, Clichy (France)
 (c) KCK, Chalmers University of Technology, Göteborg (Sweden)
 (d) ESRF
 (e) LURE, Université Paris Sud, Orsay (France)



Techniques and instrumentation

Introduction

The permanently evolving fields of microimaging and phase-contrast based imaging, time-dependent studies and the ever increasing X-ray power – mainly due to new in-vacuum insertion devices – give rise to ongoing improvements and create new challenges for beamline instrumentation.

In this chapter, the progress of two very recent imaging techniques, namely holotomography and atomic-resolution X-ray holography, is presented. The first method is based on the phase contrast that can be observed in coherent X-ray beams when the X-rays pass through samples composed of volumes with different refractive indices. The boundaries of these zones can be made visible with much higher sensitivity than when the traditional absorption contrast is used. This opens a wide range of important applications in areas such as medical imaging and materials science. The second technique again studies the local atomic environment by phase-shift effects, but on a much smaller scale, and similar to that of EXAFS experiments. Whereas the first method observes objects of sizes ranging from micrometres up to centimetres (X-ray beam size), the second concentrates on atomic arrangements within a few angstroms.

The other contributions selected for this chapter describe the tools, in particular the properties of the optical elements, that allow us to extend the capabilities of the instrumentation to better resolution and higher sensitivity, or simply to a better conservation of the unique properties of the ESRF X-ray beams. Two of them deal with improvements of optical elements for focusing: blazed Fresnel zone plates and curved multilayers with a gradient

in the layer thickness along the beam footprint. Both are diffractive optics as opposed to refractive and specular (mirror) optics, which are also used on ESRF beamlines. We thus have the possibility of choosing the element(s) that are best suited for a given application. Thanks to the development of blazed zone plates and perfectly-shaped and homogeneously-graded multilayers, sub-micrometre resolution can now be achieved with high efficiency. Hence, the term “microfocusing” could even be replaced by “nanofocusing”.

The performance of mirrors and multilayers, with respect to both coherence preservation and focusing, critically depends on the surface quality (microroughness and slope or shape errors). Here a big step forward has been achieved by ion-beam figuring which increases the surface quality by one order of magnitude. Furthermore, it is very important to keep the optical quality unchanged when the element is exposed to the very intense X-ray beam. The question of how much we can increase the source strength without substantial losses caused by the thermal deformation of the optics – generated by cooling – must be addressed. Significant progress has been made to understand the diffraction process in deformed crystals and to predict, with a high level of confidence, the performance of crystal optics by combining finite element analysis with diffraction theory.

Finally, a recent result of time-resolved applications of synchrotron radiation is presented. Here the multiple reflections of X-rays in a channel cut crystal were studied in backscattering geometry; the X-rays were “stored” in a kind of cavity for a few nanoseconds.

Holotomography Now Operational

Until the ESRF went into operation, it seemed preposterous to envisage imaging phase objects with X-rays except with the very demanding technique of X-ray interferometry. Phase objects affect the phase $\varphi(\mathbf{r})$ of the amplitude transmitted through a sample, with $E = E_0 e^{i\varphi(\mathbf{r})}$ right after the specimen if it is E_0 just before, leaving the intensity $I = |E|^2$ unchanged. Several groups discovered that, thanks to the spatial coherence of the beams from third-generation synchrotron radiation sources, phase objects do produce intensity contrast, provided the beam is allowed to propagate over a distance after the sample. Fresnel diffraction, i.e. interference between non-affected and diffracted components of the beam, then produces fringes at phase jumps (discontinuities in the optical path-length) or an in-line hologram depending on the specimen-detector distance D . Because the phase jumps could, in a first approximation, be handled by the usual algorithm for absorption tomography, qualitative tomography could be performed using phase images recorded at small D for many orientations of the specimen with respect to the beam. This is useful to detect density discontinuities, such as reinforcing particles in a metal-matrix composite [1]. However, the spatial resolution is then limited by the Fresnel fringe distribution and artefacts occur due to the ill-suited algorithm.

Holotomography is a new approach which has been implemented to extract the quantitative distribution of the phase (and attenuation) in two-dimensional projection images, and then to turn it into 3-D reconstructions [2]. It is based on images obtained at several values of D for each angular position of the sample, in analogy with a technique developed for electron microscopy. In holotomography, the resolution is much improved because the Fresnel fringes are unravelled, and limited by the detector to about $1 \mu\text{m}$. Reconstructed slices essentially show the mass density ρ because, when dispersion can be neglected, the refractive index decrement is proportional to the electron or mass density. The need for many images means long acquisition times. Because high monochromaticity is not needed in this approach, it is feasible to use multilayers instead of perfect-crystal monochromators. The total acquisition time is then reduced below 1 hour on the wiggler beamline ID19.

This technique was used to study the connectivity of an aluminium-silicon alloy in the semi-solid state: the sample was partially remelted at 585°C during 5 minutes and then rapidly quenched in water. Figure 121a is a tomographic slice recorded at $D = 7 \text{ mm}$, sensitive only to variations in absorption. It is impossible to distinguish the two phases. Some bright spots appear corresponding to iron-rich

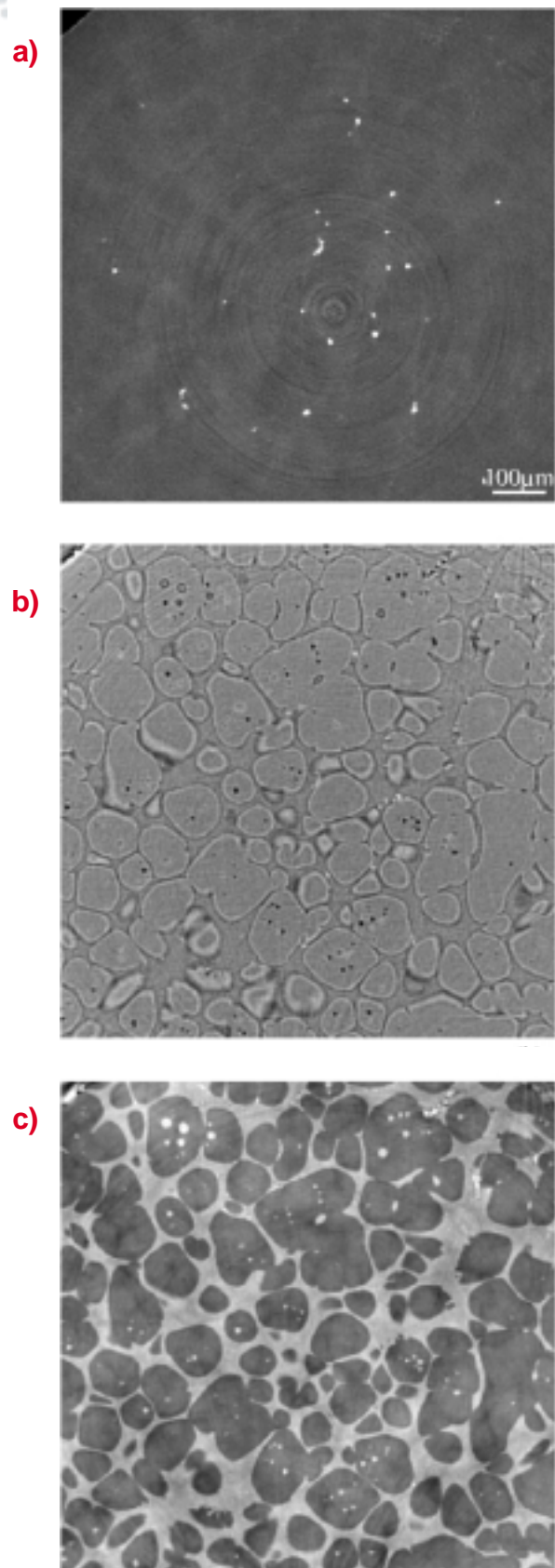


Fig. 121: Three tomographic slices of an aluminium-silicon alloy quenched from the semi-solid state, obtained (a) using absorption contrast, (b) using phase contrast and a single propagation distance, (c) using phase contrast and holotomography based on four distances.

inclusions. **Figure 121b** is a tomographic slice obtained for a single distance $D = 0.6$ m, revealing density jumps as dark/light fringes. Binarisation of such an image is extremely tedious. **Figure 121c** is a reconstructed map of the refractive index decrement, clearly showing the slightly different densities of two (metallurgical) phases ($\Delta\rho \approx 0.05$ g/cm³). The grey phase was the liquid in the semi-solid state and is aluminium-silicon eutectic. The dark phase was the solid in the semi-solid phase and it is essentially pure aluminium with substitutional silicon. The data set consisted of 4 times 800 images recorded at distances of 7, 200, 600 and 900 mm from the sample, using the FRELON camera. The beam was monochromatised to 18 keV by a Ru/B₄C multilayer.

This research demonstrates the holotomographic approach, which makes it possible to fully exploit the sensitivity of phase contrast imaging. It also shows that ID19 is now operational for holotomographic studies.

References

- [1] J-Y. Buffière, E. Maire, P. Cloetens, G. Lormand, R. Fougères, *Acta Mater.*, **47**, 1613-1625 (1999).
- [2] P. Cloetens, W. Ludwig, J. Baruchel, D. Van Dyck, J. Van Landuyt, J.P. Guigay, M. Schlenker, *Appl. Phys. Lett.*, **75**, 2912-2914 (1999).

Authors

P. Cloetens (a), J.P. Guigay (a,b), W. Ludwig (a), L. Salvo (c), M. Schlenker (b), M. Suéry (c), S. Verrier (c).
 (a) ESRF
 (b) Lab. Louis Néel, CNRS, Grenoble (France)
 (c) GPM2, ENSPG, Grenoble (France)

Atomic-resolution Hard X-ray Holography

The knowledge of atomic and molecular structure is fundamental in physics, chemistry and biology. Therefore, it is not surprising that even today, scientists try to find new techniques for structural investigations. Lately a new method, atomic-resolution X-ray holography has emerged. It is based on the same principles as traditional holography with light: a coherent wave (called the reference wave) illuminates the object and the detector surface. The intensity modulation caused by the interference between the reference wave and the wave scattered by the object (called the object wave) is recorded. This interference pattern contains both the phase and the magnitude information of the object wave. Therefore the original

wavefront can be reconstructed, giving the 3-D spatial arrangement of the objects.

In hard X-ray holography, the special feature which allows atomic-resolution is that the sources or the detectors of the hologram-forming waves are located within the sample: they are the individual atoms [1,2]. Based on the experience gained in the first two demonstration experiments [2,3], a setup was developed for synchrotron holographic studies. This work was done at **ID32**, **ID18** and **ID22** beamlines. Since there was no place in the world where this type of measurement were routinely done, even the different phases of the developments were significant scientific achievements. During this developmental phase several holograms were taken. Here, the holographic imaging of Co atoms in a CoO sample is shown as an example of what holography can give us. The quality of the data allowed the extension of the hologram to the full solid angle, using the measured symmetries. The extended hologram at 13.86 keV is shown in **Figure 122**.

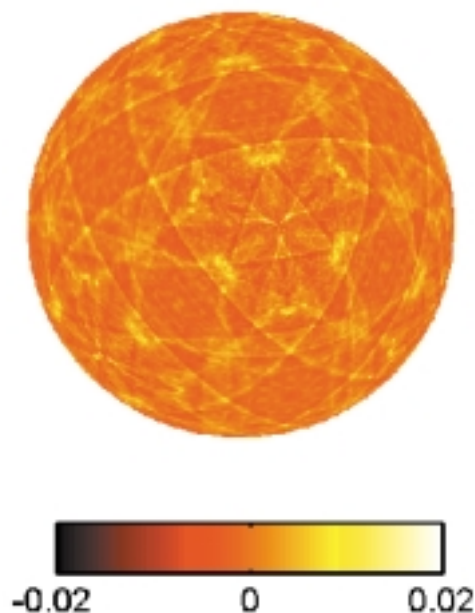


Fig. 122: Hologram of CoO taken at 13861 eV, and extended to the full solid angle. The sharp X-ray standing wave line pattern can also be seen.

In the reconstruction process the Helmholtz-Kirchhoff integral-transformation was used to obtain the 3-D real space image of the first two shells of Co atoms (**Figure 123**). It should be pointed out here that the resolution of this imaging is isotropic, and its value (0.5 Å) reached the diffraction limit. In contrast to previous measurements, the measuring time of a full data set took only a few hours. Further developments, i.e. the use of direct undulator radiation will reduce it to the minute range. This and other developments in the experimental technique and in the evaluation methods gives us hope that this novel

method will be a useful tool for structural studies in the near future.

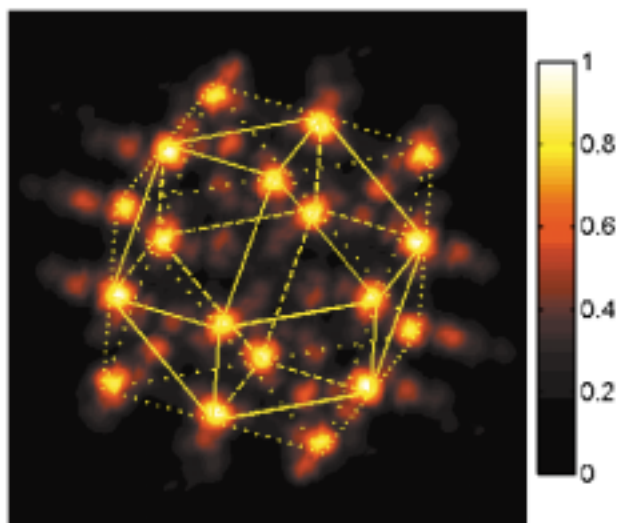


Fig. 123: The 3-D arrangement of Co atoms reconstructed from the hologram of Figure 122.

References

- [1] A. Szöke, in *Short Wavelength Coherent Radiation: Generation and Applications*, AIP Conference Proc. No 147 ed D T Attwood and J Boker (New York: AIP), 361 (1986).
- [2] T. Gog et al., *Phys. Rev. Lett.*, **76**, 3132, (1996).
- [3] M. Tegze, G. Faigel, *Nature*, **380**, 49, (1996).

Principal Publication and Authors

M Tegze (a), G. Faigel (a), S. Marchesini (b), M. Belakhovsky (b), A.I. Chumakov (c), *Phys. Rev. Lett.*, **82**, 4847, (1999).

- (a) Research Institute for Solid State Physics and Optics, Budapest (Hungary)
- (b) DRFMC-SP2M, CEA Grenoble (France)
- (c) ESRF

High-Efficiency Blazed Zone-Plate for Multi-keV Energies

The development of high-brilliance X-ray sources coupled with advances in manufacturing technologies have led to significant improvements in sub-micrometre probes for spectroscopy, diffraction and imaging applications. The generation of a small beam spot size is commonly based on three principles i) total reflection (as used in optical elements involving mirrors or capillaries), ii) refraction (such as in refractive lenses) and iii) diffraction. The latter effect is employed in Bragg-Fresnel and Soret lenses or Fresnel

zone plate lenses (FZP). These FZP lenses currently give the best spatial resolution, but their applications are traditionally limited to rather soft X-rays. In fact, the efficiencies of such FZPs are still far from unity because a significant fraction of incident beam is delivered into the (undiffracted) zero-order. At multi-keV energies, the efficiencies are usually of the order of 10-20% and cause a significant loss in the potential photon flux in the spot. This drawback can be overcome by optimising the structure profile of the zones. As theoretically shown by Tatchyn in 1970 [1], a 100% focusing efficiency can be obtained by a non-absorbing lens with a parabolic zone profile. In addition to their high efficiency, these lenses offer the advantages of low background signal and effective reduction of unwanted diffraction orders by introducing selection rules [2].

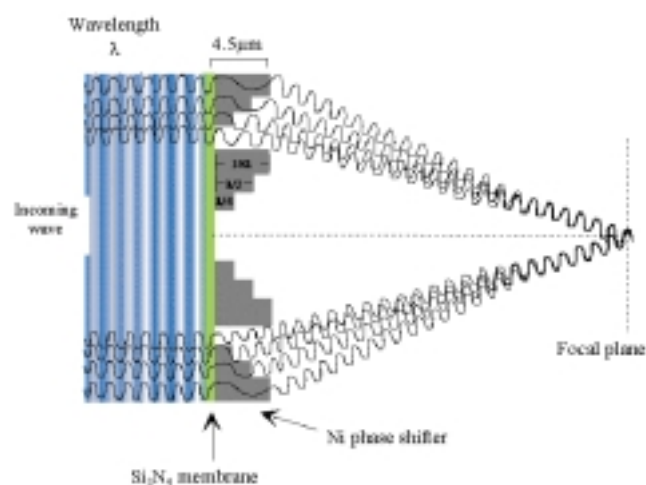


Fig. 124: The working principle of a quaternary Fresnel zone-plate: A Fresnel zone plate (FZP) consists of concentric rings designed so that the incident radiation is modulated in amplitude and/or in phase in order to interfere constructively along the optical axis at a point that represents the lens focus. In multilevel phase-shift FZPs, diffraction is performed primarily by phase modulation. Over a period, the optical path of the incident radiation increases by λ and the phase by 2π . For each zone level, an appropriate thickness of the refractive material (phase-shifter) is then added to the different X-ray optical paths to correct this phase difference.

In practice, such profiles are extremely difficult to produce with existing lithography techniques. In this work, a multi-step profile zone (Figure 124) approximated to the parabolic profile. A quaternary electroplated Nickel zone-plate – developed in collaboration with CNR-ISSS (Rome) and TASC-INFM (Trieste) – was tested on the X-ray microscopy beamline that can operate over an energy

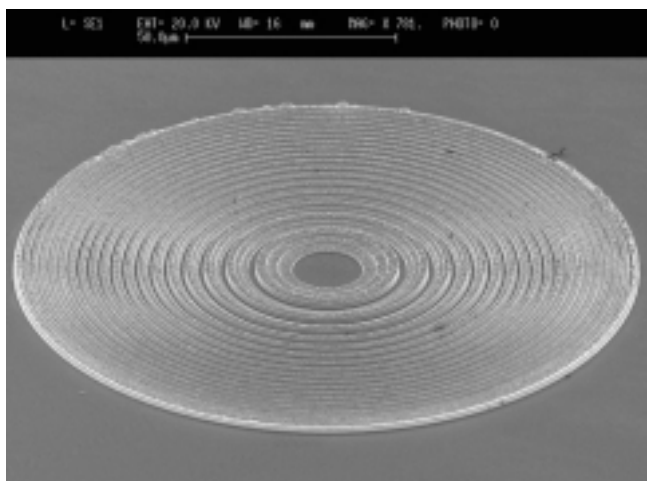


Fig. 125: Scanning electron microscope image of quaternary nickel Fresnel zone plates. The fabrication of a multilevel FZP requires the deposition and alignment of subsequent levels with an accuracy of a fraction of the desired spatial resolution. The geometrical characteristics designed for 8 keV are: focal length, 1 m; diameter, 150 μm ; number of levels, 4; and outermost zone-width of the fourth level, 500 nm. Scale bar: 50 μm .

range of 2 – 8 keV (Figure 125). The FZP efficiency measurements were performed at 5.5, 6.0, 7.0 and 8.0 keV and the efficiencies were 43%, 45%, 57% and 45%, respectively. The measured optical gain (the ratio between the photon density delivered by the FZP at the focus and the photon density impinging on the FZP) for the nickel FZP is about 2,500 at 7 keV. If we were to work at the diffraction limit by reducing the focal length, a flux gain higher than 8000 could be anticipated. These lenses should have a significant impact on techniques such as microscopy, microfluorescence and microdiffraction which require medium spatial resolution (500 – 100 nm) and high flux at fixed energies.

References

- [1] T. Tatchyn, R. O. in *X-ray Microscopy*, **43**, eds G. Schmahl, D. Rudolph, Springer Series in Optical Sciences, Springer, Berlin, 40–50 (1990).
 [2] W. Yun, B. Lai, A.A. Krasnoperova, E. di Fabrizio, Z. Cai, F. Cerrina, Z. Chen, M. Gentili, E. Gluskin, *Rev. Sci. Instrum.* **70**(9), 3537-3541 (1999).

Principal Publication and Authors

E. Di Fabrizio (b), F. Romanato (b), S. Cabrini (b), M. Gentili (c), B. Kaulich (a), J. Susini (a), R.Barrett (a), *Nature* **401**, 895 (1999).

(a) ESRF

(b) ELETTRA, Trieste (Italy)

(c) IESS/CNR, Rome (Italy)

Microfocusing with Graded Multilayers

In 1999 multilayers have been increasingly requested as optical devices. They provide monochromatic beams with a spectral bandwidth of about 1% and thus 100 times more flux than perfect crystal monochromators. Because the layer materials and spacings can be varied, multilayers can be tailored to specific requirements. More than ten different specimens were made by sputtering and have already been installed on ESRF beamlines, either permanently, or for dedicated experimental setups. The recent quality improvements resulting from both excellent substrates and deposition conditions has permitted multilayers to be used for the first time on the Topography Beamline ID19 where the slightest inhomogeneities in the beam reflected by the optics create artefacts in the images. The 100-fold gain with respect to the standard crystal monochromator allowed the users to perform experiments with much improved time resolution. Currently, the most prominent application is to microfocusing experiments with laterally graded multilayers mounted on dynamically bent substrates (see ESRF Highlights 97/98, p. 102).

Recent developments in our multilayer laboratory have aimed at two important improvements: a better control of the thickness gradient and a versatile design technique that now allows us to cover a wide range of photon energies using only one bent multilayer element. As a result, we have succeeded in reducing the error of the lateral gradient of the bilayer spacing along the mirror length of 300 mm to less than 0.5% (rms). This excellent figure is well below that of commercially available multilayers. It is also smaller than the typical energy resolution of a multilayer and therefore full reflectivity is obtained at each position of the optical element.

Focusing setups may be used for different energies without changing the geometry, for example the focal distance. In certain cases, the whole energy range available on a beamline must be covered and here one layer pair alone cannot optimally reflect the X-ray beams. Therefore, we have developed a technique to deposit two or more parallel multilayer stripes on the same substrate. Their gradients and constituent materials are usually different. However, since the optimum lateral thickness gradient of a focusing multilayer is directly related to the focal distance, the coating parameters have to be correlated precisely.

As an example, we have manufactured a focusing device for ID13 based on two Ru/B₄C multilayer stripes [1]. The two stripes were designed so that synchrotron beams of 13 keV and 20 keV can be reflected while keeping both the incident angle and the focal distance constant. Model calculations

and experimental data of the resulting gradients show excellent agreement, as illustrated in Figure 126. Thus, it is possible to switch between two energies during an experiment by a simple translation of the mirror. The 170 mm long multilayer was mounted on a standard ESRF two-moment bender. Focusing experiments were conducted on the Optics Beamline **BM5** where a focal spot size of $0.7 \mu\text{m}$ was achieved, mainly limited by the source size. The beam size before the focusing element was 1 mm and the reflectivity close to 80%. Therefore the flux gain with respect to a pinhole of the same size was about three orders of magnitude which represents a new record.

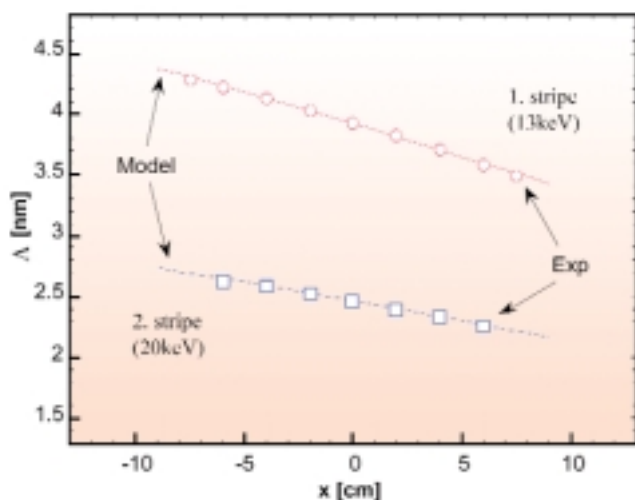


Fig. 126: Profiles of the bilayer spacing Δ of both Ru/B₄C multilayer coatings on the same substrate. Experimental data points are superimposed on the design goals (solid lines).

Reference

[1] Ch. Morawe, J.-Ch. Peffen, O. Hignette, E. Ziegler, SPIE Proceedings, **3773**, 90-99 (1999).

Authors

C. Morawe, J.-C. Peffen, E. Ziegler.
ESRF

Towards Coherence Preservation by Optical Surfaces

With the ever increasing quality of the source, i.e. smaller source size and beam divergence, the tolerances for the optical elements adapting the beam properties to the particular requirements of the experiments become more and more severe. In particular, for a certain class of

experimental techniques such as topography or tomography, it is crucial to avoid any kind of wavefront perturbation that would decrease the degree of coherence of the X-ray beams. Present-day mirror surfaces degrade the coherence properties of the source [1]. Non-ideal surfaces limit the optics performances for microfocusing experiments when attempting to decrease the focal spot size to the sub-micrometre range. At the ESRF, one strategy to microfocus X-rays is to bend flat mirror substrates [2] and presently a $1 \mu\text{m}$ spot size is achieved with this technique.

It is therefore important to continuously improve the surface quality of mirrors and multilayer substrates, i.e. the microroughness on a short spatial scale ($\sim \mu\text{m}$) and the slope errors and shape errors on the medium and long scale (mm to m). While the first should stay below 0.1 nm, the second and the third should not exceed 0.1 μrad and 1 nm, respectively (rms values). The best commercially available silicon mirrors presently exhibit 0.1 nm microroughness, 10 nm shape and 1 μrad slope error for 300 mm long flats, therefore a tenfold improvement in quality is needed.

We have recently succeeded in optimising our chemical-mechanical polishing process to achieve similar results. The art consists firstly of producing an excellent figure (low slope and shape errors) with a “hard” tool and then to preserve this flatness as far as possible when finishing with a “soft” tool to decrease the microroughness. The proper choice of the polishing pad material, the pressure, the rotation speed, the type and the supply rate of the slurry are all important parameters that must be optimised to converge to an acceptable result within a reasonable time. We can now polish a 100 mm diameter silicon specimen to a microroughness of about 0.06 nm (see Figure 127), a slope error around 1 μrad and a shape error around 10 nm in less than 8 hours.

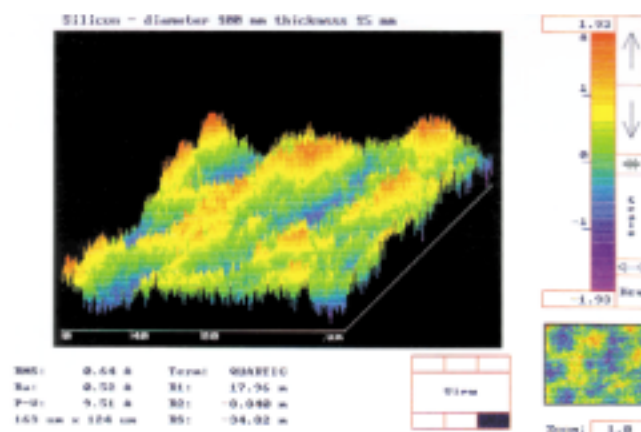


Fig. 127: Microroughness measured with a commercial optical instrument (Micromap). The height variation is given in $\text{Å} = 0.1 \text{ nm}$.

The remaining challenge is to decrease the slope and shape errors by roughly one order of magnitude. To achieve this goal, ion beam figuring is presently studied by the Optics Group in collaboration with industry where a superpolished silicon substrate can be ion beam milled. A 300 mm long substrate was micromachined or, rather, nanomachined by the company Carl Zeiss (Oberkochen), according to a surface height error map determined beforehand by precise metrology. **Figure 128** shows the surface height error of the substrate before (blue, standard deviation of 18 nm over 275 mm), and after ion beam machining (red and green, standard deviation of 1.2 nm). The corresponding slope errors were 0.88 and 0.11 μrad respectively, an improvement by a factor of eight. Significantly, the microroughness remained unaffected by the nanomachining process at a level of 0.08 nm rms!

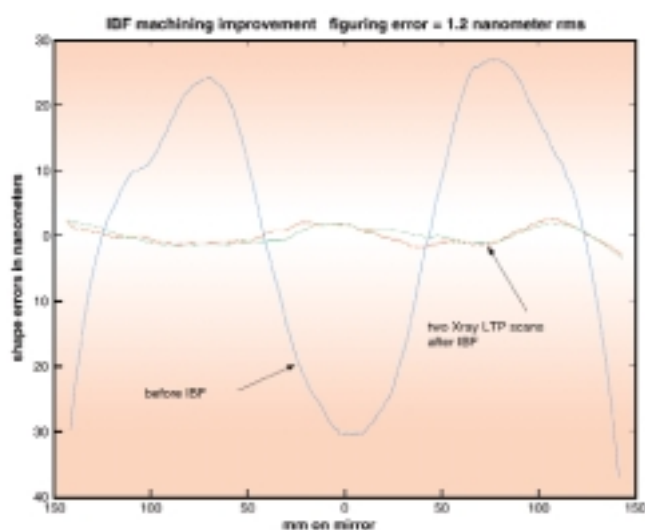


Fig. 128: The shape error obtained by X-ray profilometry over a 300 mm long silicon mirror before (in blue) and after (in red and green) ion beam figuring.

The high-precision metrology used was the X-ray long trace profiler developed earlier on the ESRF's **BM5** beamline [3]. Its precision limitations are depicted by the discrepancy between the red and green curves (Figure 128). Precision and accuracy are estimated to be around 0.3 nm and improvements are needed to provide an error map leading to a further quality gain by a second ion beam smoothing. In conclusion, with this remarkable improvement we have taken an important step forward towards our ambition of full coherence preservation by reflective optics, opening the way to new applications both for third and for fourth generation X-ray sources.

References

- [1] I. Schelokov, O. Hignette, I. Snigireva, A. Snigirev, A. Souvorov, SPIE Proceedings, **2805**, 282-292 (1996).
- [2] ESRF Highlights 1997/1998, p 102.

- [3] O. Hignette, A. Freund, E. Chinchio, SPIE Proceedings, **3152**, 277-286 (1997).

Authors

- O. Hignette (a), E. Chinchio (a), A. Rommeveaux (a), P. Villermet (a), A.K. Freund (a), H. Handschuh (b).
- (a) ESRF
- (b) Carl Zeiss Oberkochen

Performance of Synchrotron X-ray Monochromators Under Heat Load:

How Reliable are the Predictions?

The performance of an optical element can be severely degraded by exposure to intense X-ray beams. Keeping them cool is not a big issue, but the main problem is to reduce the unavoidable thermal deformation down to an acceptable minimum. For mirrors and multilayers, finite element analysis (FEA), computer simulations, and the prediction of heat load effects on the performance of optics, are straightforward. Whereas for single crystal monochromators, two complications appear. One is the diffraction angle which can be large and accordingly the penetration depth of the radiation cannot be neglected. The other is that the diffraction process of a deformed crystal is different from that of a perfect crystal, depending on the amount of strain caused by the thermal gradients.

With the steady increase in the X-ray intensity generated by modern storage ring sources we must be capable of predicting the degree to which the optical elements would limit the transfer of the flux gain downstream of the beamline to the sample and of improving the cooling schemes if necessary. For example, the X-ray transmission of a double crystal monochromator could severely suffer from the thermal deformation of the first of the two crystals. Serious discrepancies between the raw FEA results and experimental observations have been reported for cryogenically cooled crystals, fortunately in the sense that the calculations were too pessimistic [1].

As a first step towards elucidating this disagreement we wanted to examine how realistic the calculations could be for a relatively modest thermal load on an ESRF bending magnet source (Optics Beamline **BM5**) and a silicon crystal plate simply water-cooled from the behind the rear face [2]. The precise power profile of the X-ray beam was carefully measured by calorimetry with and without a 1 mm thick aluminium attenuator. Then rocking curves were taken,

recording the intensity reflected by the second (undeformed) crystal in the standard double crystal monochromator as a function of the crystal rotation angle. The incident power was changed by variation of the slit settings that defined the beam size. Any broadening of the rocking curves with increasing power load was then due to the thermal deformation of the first crystal. All the various cases were treated by finite element analysis using the program ANSYS assuming that all the power was absorbed at the surface, i.e. no depth profiling was applied. The output files were directly fed into a finite difference algorithm based on the Takagi-Taupin theory that had been specially developed for a numerical evaluation of diffraction profiles based on discrete values for deformed crystal lattices and then adapted to our present purpose [3]. Here two cases were distinguished: laterally coherent and incoherent beams. Finally, a simple geometrical model was applied where the differentiated profiles of the deformed surface obtained from ANSYS were folded with the perfect-crystal rocking curve.

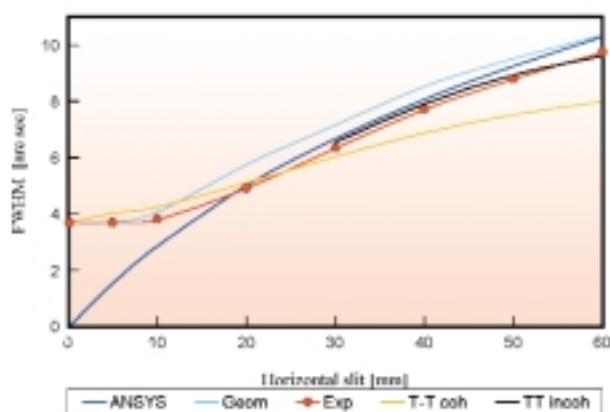


Fig. 129: Peak-to-valley thermal slope error from FEA (ANSYS) and (111)-rocking curve widths for 20 keV. Results from purely geometrical ray tracing (Geom); from Takagi-Taupin theory assuming coherent and incoherent beams, respectively (TTcoh and TTincoh), and from experiments (Exp), all FWHM, as a function of horizontal slit size and thus total power.

The results of the calculations and the experiments for the various slit settings are compared in Figures 129 and 130. Figure 129 displays the observations for the (111)-reflection and 20 keV (no Al absorber), and Figure 130 those for a superposition of the (333)- and (444)-reflection corresponding to 20 and 26.4 keV (1 mm Al in the beam), respectively. The abscissa corresponds to the horizontal slit opening that is proportional to the total power: maximum 185 W at 60 mm for Figure 129 and 132 W at 80 mm for Figure 130. The peak-to-valley thermal slope errors obtained from FEA are given as additional information only.

They cannot be directly compared with the other calculated results, because they do not include diffraction effects. The results from the simulations are quite close to the experimental values although systematic deviations are observed, in particular for the second case where penetration depth effects are much bigger.

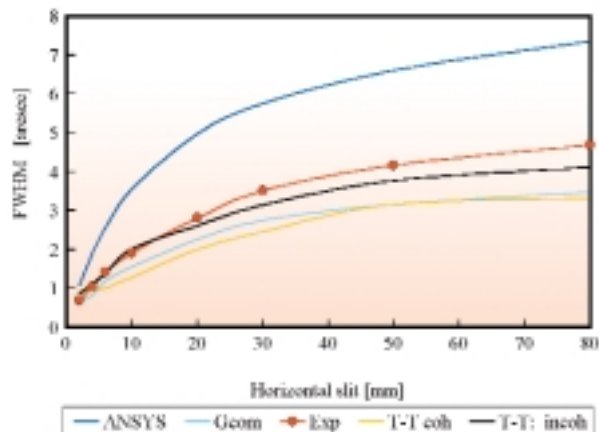


Fig. 130: Same as Figure 129, but for superimposed (333)- and (444)-rocking curves.

The main conclusions from this study are that the incoherent Takagi-Taupin approach best matches the experiments and that the overall agreement between simulation and reality is reasonably good. We proved that we have developed a simulation tool that works. The same type of calculations has recently been applied to cryogenically cooled crystals where the behaviour of the thermal deformation is more complicated due to non-linear effects. The final goal of obtaining a high level of confidence, similar to that of machine performance predictions has now been reached [4].

References

- [1] D.M. Mills, Presentation at the APS-ESRF-SPring-8 Three-Way Meeting, Argonne, April 1999.
- [2] A.K. Freund, J. Hoszowska, J.-S. Migliore, V. Mocella, L. Zhang, C. Ferrero, Proceedings of the International Conference SRI'99, Stanford, Oct. 13-15 (1999), American Institute of Physics, in press.
- [3] V. Mocella, PhD Thesis, Université Joseph Fourier, Grenoble (1999).
- [4] Results to be published at SRI 2000, Berlin, August 2000.

Authors

J. Hoszowska, J.-S. Migliore, V. Mocella, L. Zhang, C. Ferrero, A.K. Freund.
ESRF

Storage of X-ray Photons in a Crystal Cavity

The temporal structure and high brilliance of the X-ray beams produced by third-generation synchrotrons open up new possibilities in time-dependent diffraction and spectroscopy, where timescales down to the sub-nanosecond regime can now be accessed. Moreover, the properties of these beams are such that one can envisage the development of the X-ray equivalent to various optical components, such as photon delay lines and resonators. Optical resonators, like those used in lasers, are available at wavelengths from the visible spectrum to soft X-ray energies. Equivalent components for hard X-rays have been discussed for more than thirty years, but have yet to be realised. Here we report the storage of hard X-ray photons in a crystal cavity. The photons are stored for as many as 14 back-and-forth reflections, each cycle separated by one nanosecond [1].

The cavity consists of a pair of vertical plates separated by 150 mm and cut into a monolithic silicon crystal. The 111 orientation is along their surface normals as sketched in Figure 131. The plates are slightly wedge-shaped in order to vary the effective crystal thickness between 50 μm and 500 μm by a horizontal translation perpendicular to the axis of the beam. The experiment was performed at the inelastic scattering beamline ID28. The X-rays were monochromatised by a Si 888 reflection at a Bragg angle of 89.865°, providing a beam of 15.817 keV, with an energy resolution of 3.7 meV and a divergence of about 10 μrad . Photons are Bragg reflected back exactly within the divergence into the axis of the incident beam. A fast avalanche diode detector was placed behind the cavity, to measure the transmitted intensity leaving the cavity.



Fig. 131: Sketch of the cavity with the two active Bragg crystals made in a monolithic device. Photons impinging from the left can be trapped due to transmission T and reflection probabilities R . They exit the cavity with probabilities $TT, TRRT, \dots, T^2R^{2N}$ for $0, 1, \dots, N$ back-and-forth bounces at t_0, t_1, \dots, t_N . They are delayed up to N times the time of flight inside the resonator of 1.0 ns. The mean diffraction angle is adjusted to exactly 180 degrees and the beam paths of multiply reflected photons are superimposed in space.

The Bragg condition for the cavity was determined by an energy variation of the incoming photons by controlled

thermal expansion of the monochromator lattice spacing. The result of such a scan is shown in Figure 132a. The exact Bragg condition is fulfilled when the transmitted intensity has a minimum. The observed FWHM on the relative energy scale is $\Delta E/E = 7.4 \times 10^{-7}$ and the minimum transmission through the two 292 μm thick silicon plates is 17% after consideration of normal absorption.

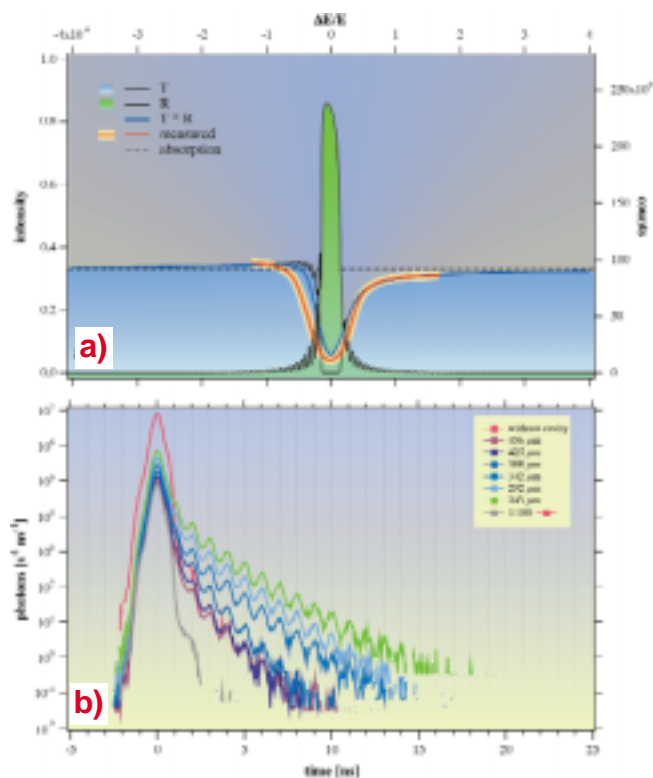


Fig. 132: a) Calculated reflection and transmission curves R and T of the cavity against energy deviation from the centre of the Bragg reflection. The monochromator delivers a similar curve to R . Thus the calculated curve for the simulation of an energy scan is the convolution $T \cdot R$. Experimental data is consistent with theory for anomalous absorption, resulting in the asymmetry around the Bragg position. b) Time pattern of stored photons at the exit of the cavity at the minimum intensity of the Bragg reflection a). Without the crystal in the beam, only a direct bunch of photons is observed at time 0 while many bunches, originating from multiple back and forth journeys inside the device, appear when the cavity is in Bragg condition.

The time dependence of the transmitted beam at the centre of the Bragg reflection is shown in Figure 132b for various crystal thicknesses. The data was obtained in the ESRF's 16 bunch mode where X-ray flashes of 100 ps duration, separated by 176 ns, allow stroboscopic timing experiments [2]. The first curve shows the time structure measured by the detector without the cavity in the beam.

There are no delayed photons and the transmitted intensity maximum defines the zero time. The time patterns with the cavity in Bragg position differ qualitatively from the first curve and show a series of sequential maxima separated by 1.0 ns with an exponential intensity decay towards longer times. The successive maxima correspond to photons trapped within the cavity for 1, 2, 3 ... N reflections from both crystal plates. When the beam impinges onto the first crystal slice, there is a probability for transmission, producing the forward diffracted beam. The same holds for the second plate and therefore yields a maximum signal at $t = 0$. But there is also a probability for reflection at each slice, permitting part of the beam to propagate back and forth and thus travelling several times the cavity length, i. e. multiples of 30 cm corresponding to a pulse separation of 1.0 ns. We observe up to 14 delayed peaks up to 14.0 ns, and even intensity beyond this for the thinnest crystals. The delayed maxima are less intense for thicker crystal slices because the transmission probability for entering and leaving the cavity goes down and one has to compromise between transmission and reflectivity.

We have demonstrated for the first time the storage of X-ray photons, with the highest energies so far of

15.817 keV, for up to 14 ns by multiple bounces in a crystal cavity. Highest ratios of 50% between neighbouring intensity peaks have been observed. Higher number of reflections were observed for thinner crystals. Discrepancies between the observed time patterns of transmitted intensity and calculations based on a simplified dynamical theory of diffraction are most likely due to a slightly distorted crystal cavity.

References

- [1] K.-D. Liss, R. Hock, M. Gomm, B. Waibel, A. Magerl, M. Krisch, R. Tucoulou, *Nature*, **404**, 371-373 (2000).
- [2] K.-D. Liss, A. Magerl, R. Hock, B. Waibel, A. Remhof, *Proceedings of SPIE*, **3451**, 117-127 (1998).

Authors

- K.-D. Liss (a), R. Hock (b), M. Gomm (b), B. Waibel (c), A. Magerl (b), M. Krisch (a), R. Tucoulou (a).
(a) ESRF
(b) Lehrstuhl für Kristallographie und Strukturphysik, Erlangen (Germany)
(c) MTU Motoren- und Turbinen-Union GmbH, München (Germany)



Highlights
1999

The X-ray Source



Introduction

During 1999, a significant effort was made to improve some of the beam's characteristics, and a number of new projects were undertaken. The main achievements include the stabilisation of fast beam motions (using global and local feedback systems), attaining a very low coupling, successful testing of an in-vacuum undulator, and development of a new high-power front-end configuration. A promising investigation was carried out on a new type of small gap ID vessel, and some of the RF systems have been upgraded. All this had to be done while the Machine was being operated continuously for the Users, and without too great a disturbance to the X-ray beam delivery (5592 hours in 1999). Hereafter, we present our results for 1999, and then describe a selection of the topics that were studied during this period by the various groups working for the ESRF's Machine Division.

Operation in 1999

During the period from 1/1/99 to 31/12/99, 686 shifts were allocated to the Users, i.e., 5488 hours (excluding the shifts for radiation tests and PSS tests). Subtracting the 189 hours due to failures (3.4%) and the 63 hours of dead time necessary for the refills (1.1%), 5236 hours of beam time were indeed delivered for experiments. This represents an average beam availability of 95.4% during 1999, a new record (Figure 133). The other figure of merit, the Mean Time Between Failures, has reached 31.9 hours, a slight improvement on that achieved in 1998 (Table 1). Thanks to a new method of testing the Personal Safety System (PSS) on the beamlines, only one shift per period of six months is dedicated to PSS tests instead of the habitual five shifts in the past.

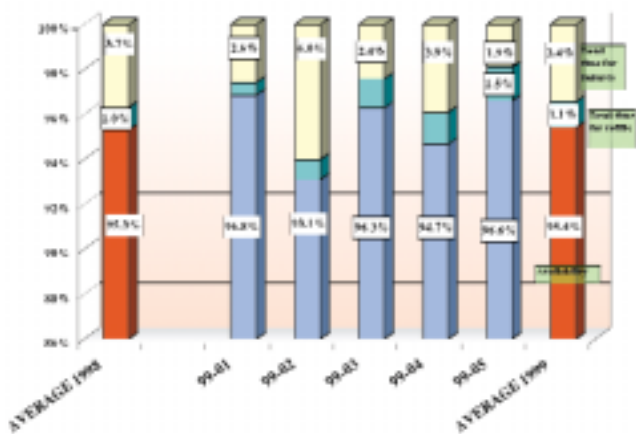


Fig. 133: Availability of the X-ray beam in 1999.

FIN NUMBER	TOTAL 99	99-1	99-2	99-3	99-4	99-5	TOTAL 99
Start		15/01/99	19/03/99	28/05/99	13/09/99	22/12/99	
End		10/03/99	19/05/99	23/07/99	13/10/99	17/12/99	
Total number of shifts	678.4	182	183	188	185	188	684
Number of USM shifts	685	117.7	148.3	138	146	156	685
Hours available for users (%)	5232.2	911.7	1104.7	1062.9	1105.6	1098.9	5236.8
Beam availability	95.3 %	95.8 %	95.1 %	96.3 %	94.7 %	95.4 %	95.4 %
Dead time for failures	3.7 %	2.9 %	6.0 %	2.4 %	3.3 %	1.9 %	3.4 %
Dead time for refills	1.0 %	0.6 %	0.9 %	1.3 %	1.4 %	1.5 %	1.1 %
Average intensity (mA)	149	179	141	125	135	137	142.3
Number of failures	179	41	49	27	28	27	172
Mean time between failures (h)	30.8	29	24.2	43.9	41.7	42.3	31.9
Mean duration of failures (h)	1.1	0.8	1.5	1	1.6	0.8	1.1

Table 1: General figures for 1999, detailed run by run.

Modes

The multibunch modes remain predominant with 65% of the time allocated to the 2/3 filling modes (Figure 134). The 1/3 filling mode has now completely disappeared and left its place to the 2/3 filling mode which, in turn, has now given up its place to the 2 x 1/3 filling mode. This new mode consists of two trains of 330 bunches spaced by a gap of 1/6th of the ring. It has all the advantages of the 2/3 filling, i.e., an intensity of 200 mA and a 65 hours lifetime whilst having the time structure needed for some experiments. Although the hybrid mode has not been abandoned, a general trend clearly is developing for separate shifts of single and multibunch modes in preference over the hybrid mode. The disappearance of the 32-bunch mode is simply explained by the fact that this mode was considered as a fallback position mode when several RF fingers problems were encountered last year. Although not fully solved at this time, the study of the RF fingers behaviour has dramatically progressed (thanks to a bench test installed on the Storage Ring) and we can once again consider working in 16-bunch mode.

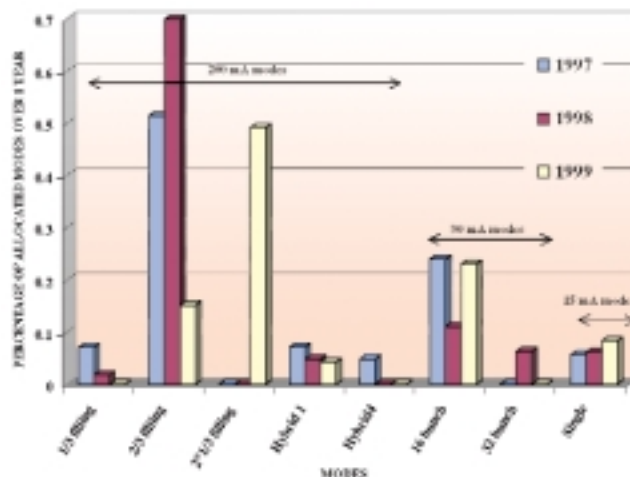


Fig. 134: Evolution of the filling modes from 1997 to 1999.

During six User Service Mode (USM) shifts, the beam was delivered at 4 GeV for the first time. This energy led to a record in low emittance values: $\epsilon_x = 1.7$ nm.rad and $\epsilon_z = 12$ pm.rad. It was possible to achieve 100 mA with a

lifetime of 10 hours. Several beamlines took advantage of the beam to perform experiments up to 30 KeV (using very high ranking harmonics from the undulator).

Failures Analysis

The longest beam interruption occurred during run 99-4: the feed through connector of an ion pump in Cell 23 broke and the corresponding cell was brought to atmospheric pressure. This incident may result from ageing combined with extreme working conditions (high voltage within a small volume of air). Fortunately, the incident happened the day before the start of a Machine shutdown. Although the repair was done in record time (12 hours), the lifetime after the intervention would have been so short (less than 1 hour) that the decision was taken not to return to USM. The full interruption therefore lasted 27 hours.

The second longest failure happened during run 99-2 and interrupted the Machine for 18 hours when an RF finger melted upstream of the in-vacuum undulator. A gap between the fingers and the sleeve, due to a mounting problem, was discovered. With the exception of this incident, the RF finger problems have almost disappeared thanks to an exhaustive control of the RF finger – by performing in situ radiogammagraphies – followed by the systematic replacement of any suspicious-looking assemblies at each vacuum intervention.

Among the eight failures which lasted more than two hours, we note five cooling problems. Although corrosion of the copper by the de-ionised water (producing copper oxide) is unavoidable, it appeared that an abnormally high rate of copper oxide was present in the water circuitry. This copper oxide accumulated on the calibrated fittings of magnets, hence reducing the water flow rate and stopping the corresponding power supply. The only short-term solution consisted of inserting special resins to trap these oxides. This proved to be efficient. However it has since been discovered that these resins saturate quickly and so their regular renewal is necessary. Since run 99-02, a test on the water circuitry is regularly carried out during Machine Dedicated Time in order to detect the first signs of blockage. This problem is partially at the origin of a degradation in the FE equipment's Mean Time Between Failure. It should also be noted that, following many problems of radiation effects on the flexible pipes, all of the magnets' and vacuum vessels' water cooling pipes have been replaced by those made of an improved radiation-proof material.

Although it remains the most fragile piece of equipment accounting for 40% of the failures, the MTBF of the Radio Frequency system has improved by 10% compared to last year.

Machine Tuning

Horizontal Focusing Optics

The virtual focusing of the electron beam downstream of the straight section of a beamline gives the possibility of further reducing the horizontal size of the photon beam at the sample. This can be achieved by operating the lattice with modified optical functions in the corresponding straight section ($\alpha_x \neq 0$, $\beta_x = 55$ m). As already reported in the 1998 issue of the Highlights, very promising results were obtained on ID6, the machine diagnostics beamline, with a gain in beam sizes by a factor of two and a significant increase in spectral flux per unit surface.

These modified optics will be implemented on ID20 at the beginning of 2000, once the 6 individual power supplies for the magnets of the straight section have been procured. In order to prepare for the changeover, the characteristics of the new optics have been fully assessed. With such a breaking of the 16 fold periodicity of the lattice optics, the challenging issues come from the requirement to maintain the performances of the standard optics (electron beam emittances, β values at the other source points, ...) without experiencing severe penalties from a one-fold symmetry lattice (energy acceptance, dynamic aperture and lifetime reduction).

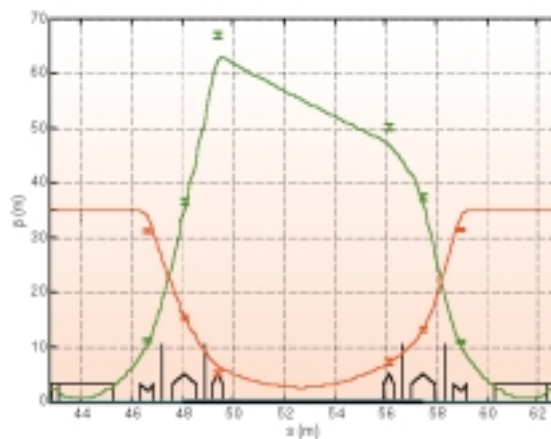


Fig. 135: Measured and predicted β functions with the horizontal focusing optics: horizontal β function in green, vertical β function in red.

All of these aspects have been carefully checked. No distortion of the optics or degradation of its characteristics could be seen. As shown in Figure 135, which gives a comparison of measured and theoretical β -values in the HFO straight section, the properties of the optics are close to those predicted. The momentum acceptance and transverse acceptance are equal to the usual values. The lifetime in multibunch mode was over 50 hours at 200 mA. This looks reasonable for operation, even if this figure is 5 to

10 hours shorter than on the periodic lattice. Further optimisation of the sextupole distribution is likely to minimise this slight drawback.

Energy Acceptance

Even if the lifetime of the machine is dominated by the Touschek lifetime in all operating modes, the request for a large momentum acceptance is crucial only for the few bunch modes of operation. With the present acceptance of 3%, the lifetime stands at 11 h in 16 bunch mode (90 mA, 1% coupling). This is mainly due to the numerous resonances on the path of Touschek scattered particles resulting from the high chromaticities ($\xi_x = 4$, $\xi_z = 8$) required to raise the transverse instability thresholds.

The first step to better understand the impact of sextupole distributions on machine performance was to refine the sextupole calibration based on magnetic measurement. The additional calibration with beam is based on the processing of measured chromaticities. By running the lattice with only chromaticity sextupoles and with one harmonic sextupole family at a time, a large amount of data could be obtained and a model was built from the fitting of the data. This reliable calibration now enables deeper comparisons of theoretical and experimental non-linear effects of sextupoles. The objective is to refine the sextupole distribution in order to optimise the tune path of scattered particles.

Low Coupling

Within a Storage Ring, the finite vertical emittance is generated by a transfer of electron motion from the horizontal to the vertical plane. For this reason it is expressed through the coupling which is the ratio between the vertical and horizontal emittance.

A record vertical emittance of 12 pm.rad was measured on ID8 and D9 X-ray pinholes at the end of 1998, with the developed correction method consisting of a response matrix modelling and minimisation of vertical beam sizes measured with the two pinholes. Following this achievement, activities in the year 1999 started with the pursuit of the limit of correction by investigating various surrounding effects.

Having seen that the optimal skew corrector strengths shifted systematically from predictions, their strengths were re-calibrated utilising the measured dispersion, as carried out previously. By taking into account local variations of the dispersion, the calibration coefficient turned out to be ~20% larger than previously estimated for most of the correctors, explaining the aforementioned discrepancy. Re-calibration

was also carried out on the pinhole camera's set up in the large coupling mode, where it was known that measured couplings give large overestimations. The new calibration managed to reproduce the expected values correctly affecting the measurement in the low coupling regime.

Since the lowest measured vertical emittance of 12 pm.rad is still notably higher than the ~5 pm.rad predicted by the model, and as the correction often saturates in a non-continuous manner, it was suspected that the correction could be limited by the influence of vertical beam motions. It was seen that the global orbit feedback that corrects the vertical beam oscillations up to 100 Hz could bring the measured vertical emittance a few picometres below the level without feedback. Similar results were obtained by reducing the integration time of the pinholes from 20 to 2 ms.

The effect of fast beam oscillations arising from resistive wall instabilities were also investigated. In uniform filling mode, the magnitude of the instability, which varies with the chromaticity, was found to be accurately reflected in the vertical emittances of the 12 pm.rad level, giving a long tail off of the effect up to the chromaticity of ~10. However, the observation appears to be in contradiction with the fact that, so far, 8 pm.rad could be achieved with 200 mA beam in 2 x 1/3 filling, despite the presence of instabilities. This puzzling issue must be investigated in more detail.

With non-uniformity revealed in the skew error distribution obtained from the response matrix analysis, an attempt was made to eliminate the two outstanding peaks in the distribution (cell 5 and 15) by moving the magnets. **Figure 136** shows the initial distribution of errors.

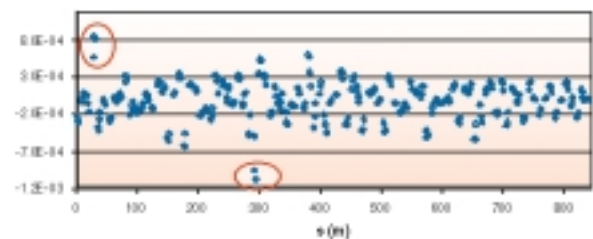


Fig. 136: Coupling errors from response matrix analysis.

As the method of localisation of error did not have a resolution high enough to identify a faulty magnet, between the two equivalent actions of rotating a quadrupole or vertically displacing a sextupole, the latter was chosen for reasons of feasibility. By displacing S22 and S24 magnets by ~0.5 mm in the proper directions, both outlying peaks were successfully removed, which enabled the standard correction to reach a slightly lower vertical emittance (~20 pm.rad).

Further efforts are underway to distinguish the sextupole

contributions to the skew errors from that of the quadrupoles. Settings were found to enable a response matrix measurement with and without a (harmonic) sextupole family turned on. Analysis of a pair of such measurements should solely identify the contribution of the selected family.

Low coupling was tentatively introduced during USM on two time-limited occasions (27 Oct ~ 1 Nov and 19 ~ 22 Nov). The correction procedure was automated and kept running in order to start the correction as soon as the measured vertical beam sizes exceeded a certain threshold following ID gap motions. Vertical emittances were mostly kept to 9 ~ 11 pm.rad with a 200 mA beam in 2 x 1/3 filling. The lifetime reduction due to the lower coupling was in the ~15 hours range (60 to 45 hours). Actual ID gap variations during USM did not bring vertical emittances beyond the ~15 pm.rad level.

Studies of Transverse Beam Instabilities

Single bunch and associated time structure modes are limited by strong vertical transverse instabilities. For operation, the vertical chromaticity is increased in order to raise the current threshold and to maintain a low vertical beam size, but the drawback of this remedy is lifetime reduction. A study – including theory, simulations and experiments – has been initiated to come to a better understanding of the instability mechanism and the associated machine impedance.

At zero chromaticity, the single bunch current is limited below 1 mA by the merging of mode 0 and mode -1. From this result, the peak of the BBR model of the impedance can be identified at high frequency (22 GHz). With the increase of the chromaticity and the large variation of bunch length with the current, the observation of successive head tail mode interacting with the impedance is also in accordance with this model. Frequency and time domain tools have been developed for the simulation of these observations.

Damping times and growth rates have also been studied using simulation and measurement data. The strong discrepancy between the two approaches needed a complementary study in order to explain the lower threshold observed. Hence, the simulation helped by showing that adjacent modes – widened by the increased current – could couple close to the threshold. This assumption was verified during machine studies.

The inefficiency of the transverse feedback is also linked to

high order modes that have low components at low frequency.

Multibunch modes are affected by smooth transverse instabilities that are produced by the low-frequency resistive wall impedance. For operation, the vertical chromaticity is also pushed to increase the current threshold and to maintain a low vertical beam size.

A systematic study has been initiated to characterise the mechanism and to prepare the installation of a transverse feedback. For the first experiments, which were made in uniform filling, only the first modes (mainly the first two) were observed. In this case, we were able to measure the relation between the beam size and the level of the excitation and to successfully apply a feedback on the first line.

Equipment Development

Fast AC Position Feedback Systems

Fast orbit correction systems have been implemented and used during normal operation of the machine since November 1998. They operate in a 0.01 to 200 Hz bandwidth with a position sampling and correction rate of 4.4 kHz.

The first system is a global feedback using 16 beam position monitors (BPM) and 16 correctors to damp the vertical beam motion all around the storage ring. The control of the global feedback has been improved (graphical user interface, diagnostics tools) in order to make its operation more robust and facilitate troubleshooting. The efficiency of the corrections has also been improved by compensating the BPM tilt which was causing a spurious mixing of the large horizontal beam motion to the vertical beam motion measurement. The correction of this effect now enables the beam motion amplitude to remain below 0.80 μm at the feedback BPM locations. The main 7 Hz frequency peak is damped by a factor 10 and the global damping factor is 2.5 when averaging all frequencies up to 100 Hz.

The second system is a local horizontal feedback implemented on the ID24 EXAFS beamline in a high β straight section. This system uses two electron BPMs to measure the horizontal electron beam position at both ends of the ID24 straight section and four fast steerer dipole magnets to produce a local correction bump (a closed bump which does not change the beam position in the rest of the machine) the residual amplitude of oscillation is damped from 13 μm down to 1 μm (rms) to be compared with the 400 μm (rms) horizontal beam size.

Following the excellent results obtained on ID24, another local horizontal position feedback was tested on ID3 to check the efficiency of the system in a low β_x straight section. The ID3 local feedback shows the same damping efficiency as achieved on the ID24 high β_x straight section. There is no apparent interaction between the ID3 and ID24 systems, when activated simultaneously. It is planned now to test the common operation of a local feedback with the ID gap opening compensation system (both systems use the same steerer magnets on both side of the straight section). In addition, a local feedback will be also implemented on ID14 after the installation of the missing BPM pick-up during the winter shutdown.

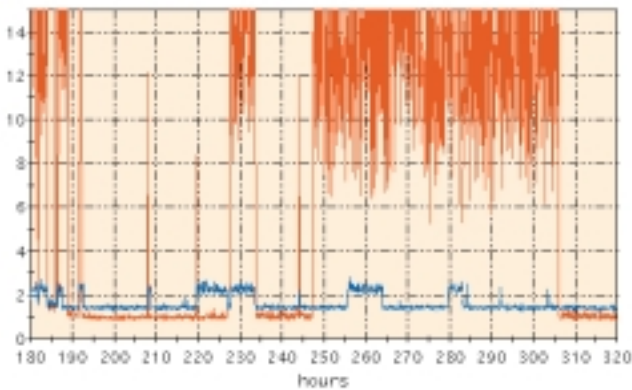


Fig. 137: Beam position (horizontal in red, vertical in blue) on the ID24 straight section with vertical global feedback and horizontal local feedback OFF and ON. These are rms values computed between 0.1 to 200 Hz and expressed in μm .

The implementation of these systems has resulted in significant improvements in beam stability. These improvements have been assessed by measurements of relevant machine parameters (position stability) as shown for instance in [Figure 137](#), and by the observation of beneficial effects on beamline operation.

Damping Device for Storage Ring Girders

A damping device, called a damping link, has been developed to attenuate the vibration of the ESRF machine girders. It consists of three parts (see [Figure 138](#)):

- a sandwich structure with Aluminium plates and ViscoElastic Material (VEM) : Al + VEM + Al
- a girder mounting fixture (GMF) which links the sandwich structure to the girder.
- a floor mounting fixture (FMF) which links the sandwich structure to the floor.

These devices link the two extremities of the girder to the floor. The mounting fixtures (GMF, FMF) should both

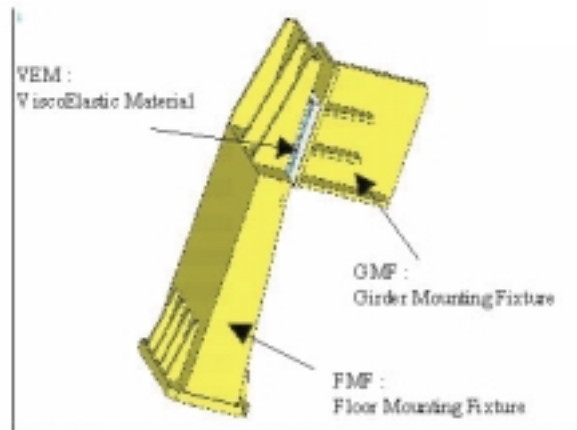


Fig. 138: Damping link and installation in SRTU.

accommodate the environment in the tunnel, and be stiff enough to transmit maximal dynamic strain energy of the magnet-girder to the layer of VEM which then dissipates this energy. The mechanical properties of the VEM are key parameters for the successful design of the damping link.

Damping links were first tested on a magnet-girder assembly installed in the experimental hall. Excellent damping results from these first tests encouraged us to continue the tests in the storage ring tunnel. Three Storage Ring girders (G10 and G20 in cell 23, G30 in cell 22) have been equipped with the damping links. Test results show that the fundamental peak (7-9 Hz) in the spectral displacement of quadrupole magnets is reduced by a factor of between 5 and 10 for the vibration in the transverse direction. The fundamental peak has been reduced to such an extent that, in some cases, the vibrations induced by the cooling water flow in the frequency range of 20-100 Hz are now noticeably significant. Compatibility tests with alignment operation were also carried out. It was shown that the damping links are compatible with alignment operation, and that girder displacement, required when re-aligning the machine, does not deteriorate the performance of the damping links.

It is now planned to bond the FMF to the floor with epoxy instead of bolts in order to facilitate installation, to compensate for the irregularity of the floor, and even to obtain a more rigid fixation of the FMF onto the floor. Additional damping devices to further attenuate the water flow-induced vibrations are also being studied by finite element modelling.

Radio Frequency Systems

Upgrading of RF Units

Since the construction of the new SRRF3 unit, an upgrade programme is under way for the three other RF units. The upgrade consists of:

- complete reorganisation of the control system, both hardware and software
- rewriting of the control software that uses all the ESRF standards and tools
- re-design of the low power electronics (RF low level, hardware interlocks...)
- re-building of klystron auxiliaries: klystron lead garage, klystron cooling system,...

The goal is to obtain complete redundancy in case of a major hardware failure so that it will be possible to:

- run the Storage Ring even if one transmitter is down
- feed the booster cavities from the SRRF2 transmitter (target for year 2000).

Following the cavity control upgrade (cavities 1 to 4), which took place in 1998, the SRRF2 transmitter was upgraded and switched to these four cavities.

The SRRF1 transmitter is currently being dismantled for its upgrade in 2000.

Improved Cavity Temperature Regulation System

An improved temperature regulation system that allows the adjustment of the individual cavity temperatures within a range of 23°C to 60°C with $\pm 0.1^\circ\text{C}$ was put into operation in January 1999. It is used to tune dangerous Higher Order Modes (HOM) of synchrotron beam resonances, thereby substantially increasing the current thresholds for Longitudinal Coupled Bunch Instabilities (LCBI). This was applied in the course of 1999 to develop new operation modes for the ESRF storage ring, for instance:

- 100 mA at 4 GeV: The natural synchrotron damping being much lower at reduced electron beam energy, the thresholds for HOM driven LCBI are about 5 to 20 mA at 4 GeV, depending on the RF voltage and the level of Landau damping that results from the partial filling of the ring. Thanks to the improved cavity temperature control, a stable working point with 4.5 MV of RF voltage was established allowing the delivery of 100 mA in 2/3 filling with a lifetime of 10h.

- 2x1/3 and uniform filling at 200 mA with a reduced RF voltage of 9 MV: the current thresholds for HOM driven LCBI are reduced thanks to the combination of an RF voltage decrease from 12 to 9 MV for higher Touschek lifetime and a symmetric filling pattern that does not provide any Landau damping. Stable operation was obtained by means of a careful temperature tuning of the cavities. As a result, the symmetric 2 x 1/3 filling pattern at 9 MV was implemented as the standard setting for 200 mA operation. Uniform filling of the storage ring at 200 mA with similar tuning has also been tested successfully and will be delivered to the users early in the year 2000.

Cavity R&D Studies and Outlook

Partial filling is one of the standard methods applied at the ESRF to avoid HOM driven LCBI. The mechanism of Landau damping, which results from a spread in synchrotron frequencies when only a portion of the storage ring is filled, has been extensively investigated and quantified in a PhD thesis within the RF group. Within this thesis, published in 1999, there was also a contribution from the ESRF to the development of a HOM free superconducting cavity for SOLEIL. The possible use of such a cavity at the ESRF is presently being evaluated. Finally, this thesis also gives the first theoretical calculations on the impact of a harmonic cavity at the ESRF. Designed to provide bunch lengthening in order to maximise the Touschek lifetime, especially for few bunch fillings with high currents per bunch, such a harmonic cavity actually reduces the current thresholds for HOM driven LCBI. In order to take these preliminary results further, a new PhD thesis started within the RF group in autumn 1999 to explore the means of controlling the bunch length at the ESRF.

Insertion Devices

More than 60 segments of Insertion Devices are now in operation around the ring. In addition to the installation of new conventional segments, 1999 has seen the successful operation of the second quasi-periodic undulator segment (on ID27), the fast switching planar/helical undulator (on ID12) and the prototype in-vacuum undulator (on ID11). This in-vacuum undulator is now operating in USM with a minimum gap of 6 mm without any perturbation to the beam lifetime in both 16 bunch and 2 x 1/3 filling modes of operation. The in-vacuum undulator technology is more expensive and less flexible than conventional technology with magnet blocks in air. However, an in-vacuum undulator produces a spectrum shifted by 1.57 (1.3) towards higher energies compared to that of a 16 mm (11 mm) gap undulator with magnet blocks in air. This makes this technology attractive for beamlines operating at high X-ray energies.

The recent operation of the ring with a 10 pm vertical emittance has resulted in a further enhancement of the brilliance which is now higher than $4 \cdot 10^{20}$ on the 5m long U34 undulator installed on ID23 (see Figure 139).

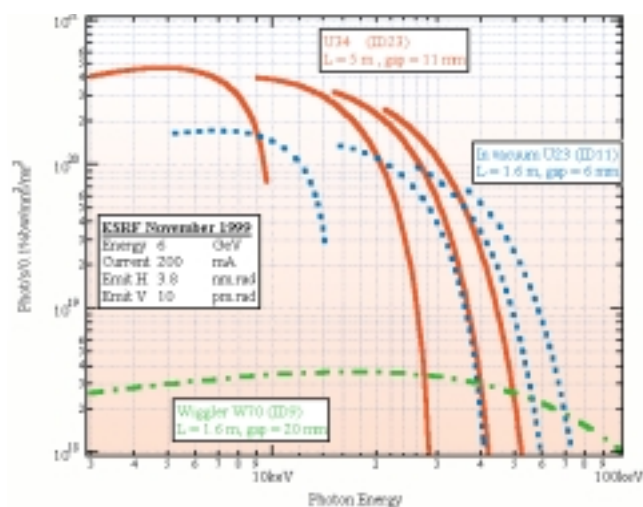


Fig. 139: Further enhancement of the brilliance.

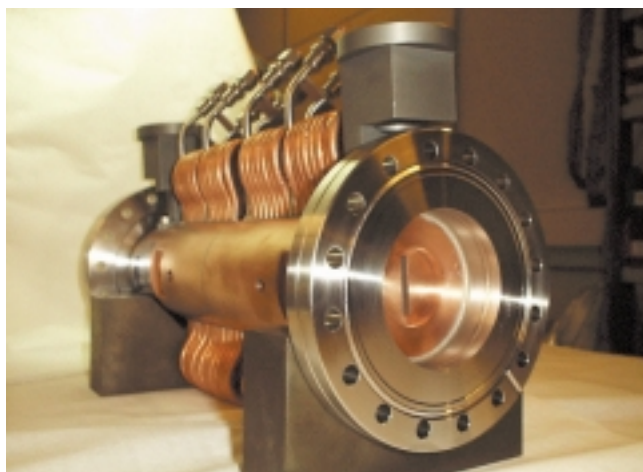
Front-Ends

Status in 1999

42 front-ends have been installed and are now connected to the storage ring : 27 are insertion device front-ends (23 for users and 4 for machine diagnostic and development) and 15 are bending magnet front-ends (14 for users and 1 for machine development).

Design, Construction and Test of a High-Power Front-End Configuration

A first prototype of a high power X-ray absorber was built in 1998 but proved to be very difficult to manufacture. Therefore, at the beginning of 1999 a second design was developed, alongside with a complete re-design of the front-end (Figure 140).



Before the summer shutdown the first prototype of the newly-designed absorber was installed and tested successfully on ID23 front end with the maximum power available (200 mA, three U34 undulator segments closed at 11 mm gap, giving a power density of 270 KW/mrad²).

After the summer shutdown a completely new front-end configuration was installed on ID23 in order to complete the tests on the absorber, to validate the new module 2 with its diamond window, and also to finalise its design. This new front-end configuration was successfully operated during the second half of the year without any problems, and it is expected to be able to operate with a larger power density (up to 400 KW/mrad²).

The new front-end configuration requires more diagnostics and different equipment. A new generation of PLC has to be used for the high-power front-ends. Preliminary tests have been carried out with the computing service group to improve the control of the existing front-ends and to make it compatible with future evolutions. The first step of this change will occur at the end of 1999.

Machine Diagnostics

The 'Thousand Turn' Extension to the Closed-Orbit BPM System

The closed-orbit BPM system consists of 214 active BPM stations distributed around the Storage Ring. It measures the closed orbit of the electron beam with high resolution and good reproducibility at a frequency of about 1 Hz. It is this measurement that is used for the so-called global orbit correction scheme.

An extension to this slow BPM system has now been conceived, installed and commissioned and it permits the measurement of the beam position, in both planes, at each BPM station, at each orbit turn, for a large number of consecutive turns.

This new functionality makes it possible, in a very short time, to extract a large number of beam and machine parameters such as local beta values, phase advance, dispersion, damping times, tune shifts and widths, phase-space diagrams etc., that are otherwise not accessible or only accessible after long and tedious manipulations and measurements.

Fig. 140: High-power front-end absorber.

The system can measure up to 2048 turns and average over a maximum of 4096 cycles. Typical results have shown a resolution of 3 μm rms for an averaging of 128 cycles (with a response time below 1 minute) on a 30 mA partially filled (200 ns) SR beam. In addition to the measurement of certain lattice parameters this system has been used to measure and optimise the closure of the injection bump.

Development and Results with the Jitter-Free Streak Camera

The development at the ESRF of a jitter-free, laser-triggered streak camera has now yielded time resolution results as short as 460 fs whilst operating in accumulating mode. The so-called jitter-free synchronisation between the laser light and the streak camera is performed through a GaAs photo-switch in a simple HV circuit that connects directly to the Streak tube's deflection plates.

The novelty of this technique is that excellent dynamic range measurements in a shot-to-shot accumulation of ultra fast (laser stimulated) events at up to 1 KHz can be obtained without degrading the time resolution.

Important insight was obtained regarding the quality of this optical synchronisation and its dependence on the laser characteristics, the switch circuit, and the structure of the GaAs switch itself. This permitted the suppression of the causes of the jitter and today the 500 fs limitation is imposed by the streak tube's intrinsic time resolution. This work was done by measuring the 3rd harmonic (i.e. 267 nm) of a 100 fs Ti:Saph laser (with Au or Pd photo-cathodes).

Important progress has also been made concerning the reliability of the photo-switch. Furthermore the problems of HV breakdown and structural degradation have been completely resolved.

Since the principal use of this system at the ESRF is in ultra-fast X-ray diffraction experiments, the exchangeable photo-cathode structure of this tube covers the entire UV-to-X-ray spectrum. The QE of various photo-cathode materials was measured in the 8-30 KeV range.

The system was used for the first time in July 1999 by external users on ID9 to measure ultra-fast surface disordering of GaAs induced by a 100 fs laser pulse at 800 nm (see [Figure 141](#)). The rapid modulation of the structure was observed by orienting a single crystal sample of GaAs to the positive side of the rocking curve of the 111 reflection. A 10 ps timescale drop in reflectivity was observed. We do not believe this to represent the ultimate time resolution of the camera but rather the timescale imposed by the experimental conditions.



Fig. 141: View of the jitter-free streak camera inside the ID9 hutch.

Support Groups

Vacuum

Storage Ring

Several new vacuum vessels were installed in the Storage Ring in 1999. The most striking item is the in-vacuum undulator which was successfully installed and commissioned during winter 1998/1999. The design of its vacuum system has proven to be reliable. Even after we were forced to vent it due to the failure of some contact fingers placed nearby, it regained a sufficiently high vacuum to allow the ID11 beamline to take beam almost immediately.

Insertion Device Chambers

A number of two and five metre long undulator chambers (made of copper plated stainless steel without pumping) of 10 mm vertical size (8 mm inner aperture) have been installed in the ring. They have undergone a number of different vacuum treatments, ex situ and in situ bake-outs but they have been found to suffer from lack of conductance and pumping speed. The main problem has been a high level of bremsstrahlung radiation in the beamline hutches and tunnel roof.

NEG-Coated Insertion Device Chambers

Based on some synchrotron radiation (SR) induced desorption measurements performed on D31, and in collaboration with CERN, we have manufactured a 5 m-long, 15 mm-high (11 mm inner aperture) extruded aluminium NEG-coated chamber. The geometry of the extrusion was chosen so that it can replace any existing 15 mm-high ID chamber in the ring. Installed and conditioned on the ID31 straight section, the indication is that the NEG-coating develops a pumping action and at the same time reduces the outgassing due to SR, confirming the many

measurements performed on samples irradiated with electrons at CERN. Moreover, the bremsstrahlung radiation measured in the experimental hutch of ID31 is five times less than that of a fully conditioned 10 mm chamber (8 mm inner aperture), a comforting sign that we are proceeding in the right direction. A graph showing the conditioning of the chamber is given in [Figure 142](#). It compares the bremsstrahlung level produced downstream of this new NEG coated aluminium vessel to those of a stainless steel vessel (devoid of pumping) and of an APS type aluminium vessel equipped with distributed NEG pumping.

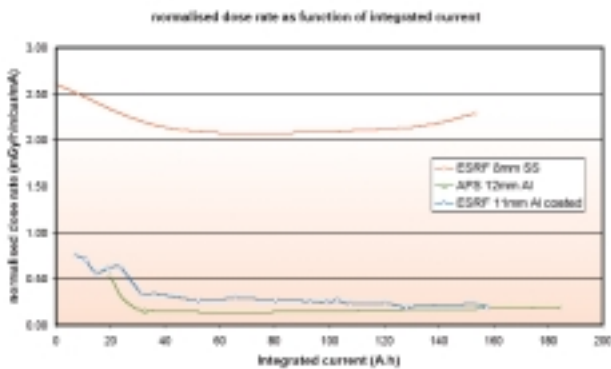


Fig. 142: Conditioning of insertion device chambers

Contact Fingers

A programme of characterisation and study of several contact finger assemblies was carried out. This was done on a dedicated test stand installed on the ID8 straight section. Using the instrumentation installed there (two infra-red sensors, two visible-light cameras, thermocouples and vacuum gauges) made it possible to identify the cause of the severe damage which had been noticed earlier, at several locations around the ring. We also tested a prototype designed by the SOLEIL project team and adopted, with modifications, by the Swiss Light Source project. We will soon install a prototype we have designed at the ESRF.

Safety

During 1999, much of the effort of the Radiation Protection group went into the preparation of the application of the Euratom Directive 96/29. Indeed, from May 2000 onwards, new radiation protection rules must be applied. In particular, these rules stipulate that the radiation limits for non-exposed people are divided by a factor of five (from 5 mSv/year down to 1 mSv/year), and that the quality factor for neutrons is increased from 10 to 20. The ESRF Radiation Protection policy is based on the fact that nobody working at the ESRF should be classified as a radiation worker. In other words,

radiation levels everywhere around the accelerators and in the Experimental Hall should be below the limits for non-exposed workers. The ESRF will continue to maintain this policy after May 2000.

Detailed radiation measurements were carried out by the Safety Group to quantify the radiation levels outside the Storage Ring tunnel associated with electron losses. These measurements have shown that, depending on the location of the obstacle for the electron beam, dose profiles outside the tunnel are observed, which peak either near the middle of the long straight section, or at the beginning of the achromat. The results also showed that the neutron dose largely dominates the photon dose. Therefore an active radiation monitoring system has been installed, based on 64 (bubble) neutron monitors - i.e. 2 per cell - which are placed on the Storage Ring tunnel roof, at those points where the radiation levels are maximum. These monitors will be interlocked to the injector in such a way that the total effective dose, integrated over four hours, will nowhere exceed the corresponding maximum level for non-exposed workers, i.e. 2 µSv per 4 hours. This radiation monitoring system, combined with the creation of restricted areas around the injection zone, will allow dose levels to be maintained below the limits for non-exposed workers everywhere around the storage ring.

Concerning the beamlines, the limiting factor comes from the scattered radiation due to bremsstrahlung. All Optics Hutches have been reinforced with typically 2 cm of lead. At the same time, radiation measurements have been taken extensively using the Safety Group's test beamline ID31 to quantify the new 5 metre long insertion device vessels. At present the new NEG-coated aluminium 11 mm internal ID-vessel is being monitored. The first results show a net decrease in radiation levels, when compared to a standard 8 mm internal stainless steel ESRF ID-vessel, which indicates a much more efficient pumping inside the vessel.

Control System

In 1999 the Machine Control System underwent some major developments such as the upgrade of the 2nd RF transmitter and the full redesign of the Front-end control. The general computing infrastructure has been completed by the installation of a wireless Ethernet link in the technical gallery allowing a portable PC to access the machine network. This installation will be extended in 2000 for the SR tunnel.

Control System Infrastructure

One major concern in system administration was the preparation of the year 2000 transition. It generated a lot of work in investigation and patching of all Unix machines, OS9 crates and PCs.

Modernisation of the System

In 1999, we began preparations for a major modernisation of the hardware and software of the control system for the next five years. Along these lines we started the design of a new control software named "TANGO". In accordance with the latest distributed software techniques, we have also started the necessary developments to replace OS9 by Linux on the VME crates. Beside we are in the process of selecting the new hardware platform based on PCI buses, which will replace VME in the next few years.

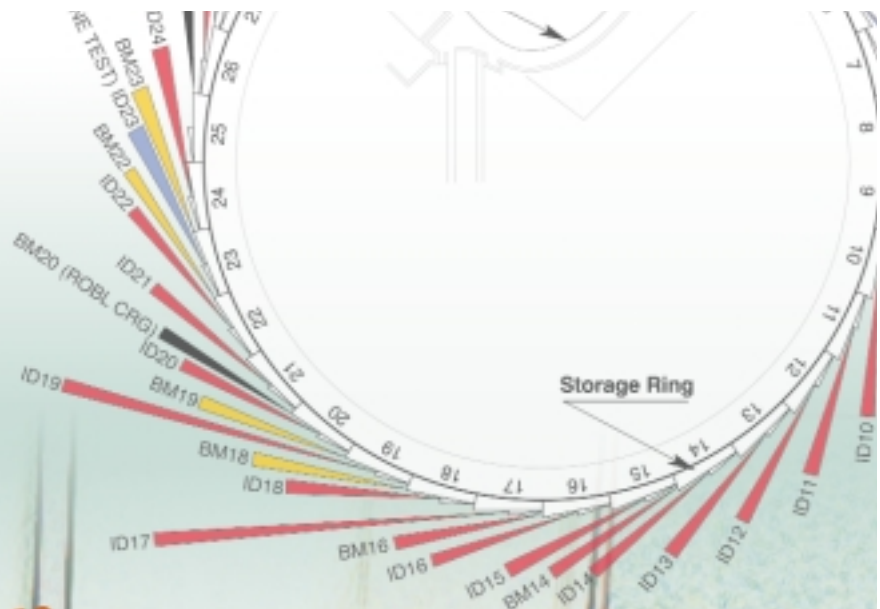
Alignment and Geodesy

After investigation, the TDA5000 motorised theodolite with automatic target recognition (ATR) was chosen as the new survey tool to be used for a complete machine survey without a substantial loss in precision. It will enable us to significantly reduce the time required to perform the machine survey during the shutdown (compared to the distivar/ecartometer pair, used until now).



Highlights
1999

Facts and figures



The Beamlines

All thirty of the ESRF's public beamlines have been operational since 1999. Four of these possess two end-stations, so there are thirty-four end-stations in total, which can be run independently. An additional fifteen beamline branches, situated on bending magnets, are devoted to Collaboration Research Groups (CRG). Ten of the CRG beamlines are now in operation (including GRAAL), the others are in the phases of planning, construction or commissioning. Figure 143 shows the location of the beamlines in the experimental hall; a list of the public beamlines is presented in Table 2; and a list of the CRG beamlines in Table 3.

Thanks to a decision by the Council in June 2000, the MAD beamline BM14 will be operated jointly by British and Spanish CRG teams until the year 2002. By then the Powder Diffraction beamline will have been transferred from a bending magnet, BM16, to an insertion device, ID31. Then BM16 will also be transformed into a MAD beamline, becoming a Spanish CRG line, while BM14 will become a British CRG line.

Additionally, there is an industrial beamline, ID27, which will be operational in the second half of 2000 for impurity analysis on silicon wafers. This line has capacity for further expansion to other fields of industrial interest.

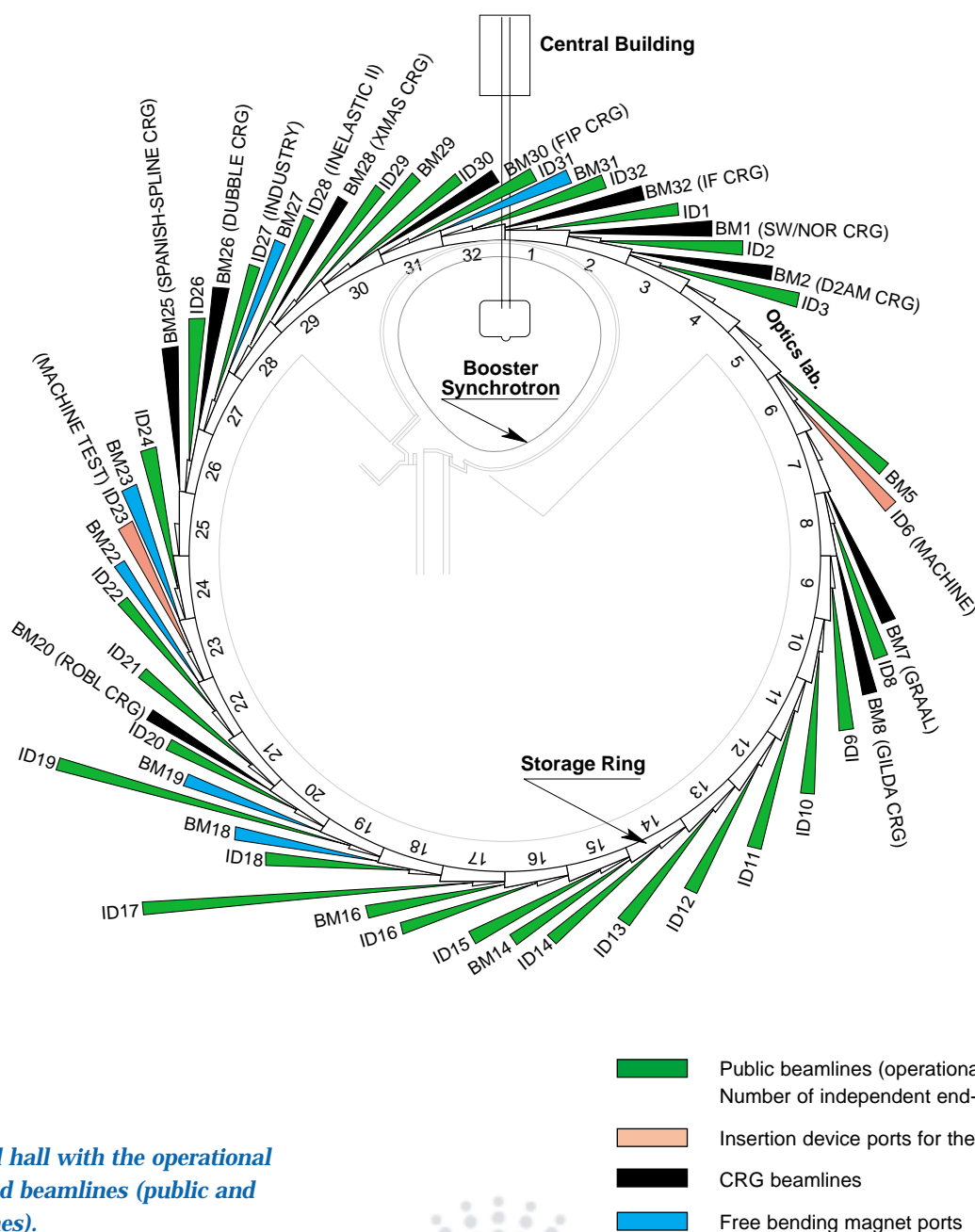


Fig. 143:
Experimental hall with the operational and scheduled beamlines (public and CRG beamlines).

SOURCE POSITION	NUMBER OF INDEPENDENT END-STATIONS	BEAMLINE NAME	STATUS
ID1	1	Anomalous scattering	Operational since 07/97
ID2	1	High brilliance	Operational since 09/94
ID3	1	Surface diffraction	Operational since 09/94
ID9	1	White beam	Operational since 09/94
ID10A	1	Troika I + III	Operational since 09/94
ID10B	1	Troika II	Operational since 04/98
ID11	1	Materials science	Operational since 09/94
ID12A	1	Circular polarisation	Operational since 01/95
ID12B / ID8	1	Dragon	Operational since 01/95 <small>Transfer to ID8, begin. 2001</small>
ID13	1	Microfocus	Operational since 09/94
ID14A	2	Protein crystallography 1, EH 1	Operational since 07/99
		Protein crystallography 1, EH 2	Operational since 12/97
ID14B	2	Protein crystallography 2, EH 3	Operational since 12/98
		Protein crystallography 2, EH 4	Operational since 07/99
ID15A	2	High energy diffraction	Operational since 09/94
ID15B	1	High energy inelastic scattering	Operational since 09/94
ID16	1	Inelastic scattering I	Operational since 09/95
ID17	1	Medical	Operational since 05/97
ID18	1	Nuclear scattering	Operational since 01/96
ID19	1	Topography	Operational since 06/96
ID20	1	Magnetic scattering	Operational since 05/96
ID21	2	X-ray microscopy	Operational since 12/97
ID22	1	Microfluorescence	Operational since 12/97
ID24	1	Dispersive EXAFS	Operational since 02/96
ID26	1	X-ray absorption on ultra-dilute samples	Operational since 11/97
ID27	1	Industry	Operational from 08/00
ID28	1	Inelastic scattering II - Electronic excitations	Operational since 12/98
ID30	1	High pressure	Operational since 06/96
ID32	1	SEXAFS	Operational since 11/95
BM5	1	Optics - Open Bending Magnet	Operational since 09/95
BM14 / ID29	1	Multiwavelength anomalous diffraction	Operational since 09/95 <small>Transfer to ID29, begin. 2000</small>
BM16 / ID31	1	Powder diffraction	Operational since 05/96 <small>Transfer to ID31, begin. 2002</small>
BM29	1	X-ray absorption spectroscopy	Operational since 12/95

Table 2: List of the ESRF public beamlines in operation.

* BM14 = British/Spanish → British in 2002
BM16 → Spanish in 2002

SOURCE POSITION	NUMBER OF INDEPENDENT END-STATIONS	BEAMLINE NAME	FIELD OF RESEARCH	STATUS
BM1	2	Swiss-Norwegian BL	X-ray absorption & diffraction	Operational since 01/95
BM2	1	D2AM (French)	Materials science	Operational since 09/94
BM7	1	GRAAL (Italian / French)	Gamma ray spectroscopy	Operational since 06/95
BM8	1	Gilda (Italian)	X-ray absorption & diffraction	Operational since 09/94
BM14	1	MAD CRG 1 *	MAD	Operational end 2000
BM16	1	MAD CRG 2 *	MAD	Design phase
BM20	1	ROBL (German)	Radiochemistry & ion beam physics	Operational since 09/98
BM25	2	SPLINE (Spanish)	X-ray absorption & diffraction	Construction phase
BM26	2	DUBBLE (Dutch/Belgian)	Small-angle scattering & interface diffraction Protein crystallography + EXAFS	Operational since 12/98 Operational from 09/00
BM28	1	XMAS (British)	Magnetic scattering	Operational since 04/98
BM30	2	FIP (French) FAME (French)	Protein crystallography EXAFS	Operational since 02/99 Construction phase
BM32	1	IF (French)	Interfaces	Operational since 09/94

Table 3: List of the Collaborating Research Group beamlines in operation, in construction or in design phase.

User Operation

The 18 months between August 1998 and January 2000, saw the opening for experiments of the full complement of 30 public beamlines, together with 8 additional beamlines operated by Collaborating Research Groups (CRGs). In parallel, requests for beam time and the number of users carrying out experiments continued to increase, as can be seen in Figure 144; this figure shows the number of applications for beam time and experiments carried out, together with the number of scientists who visited the ESRF since user operation began in September 1994.

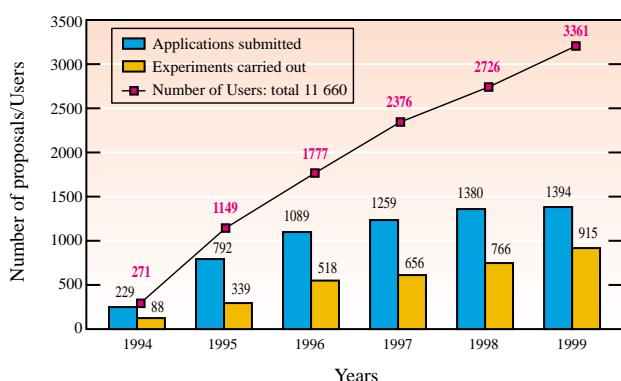


Fig. 144: Numbers of applications for beam time, experiments carried out, and users, September 1994 to January 2000.

Selection of proposals for experiments and allocation of beam time is made through peer review. Review Committees, comprising specialists from European countries, Israel, and the US, have been set up in the following scientific areas:

- chemistry
- hard condensed matter: electronic and magnetic properties
- hard condensed matter: structures
- life sciences
- methods and instrumentation
- soft condensed matter
- surfaces and interfaces

The Review Committees met three times during the period, some six weeks after the deadlines for submission of proposals (1 March and 1 September each year). They reviewed a total of 2193 applications for beam time, and selected 1076 (49%), which were then scheduled for experiments.

One feature of this period has been the dramatic increase in the number of life sciences applications, particularly for macromolecular crystallography experiments. The opening

for operation of four experimental stations on ID14, coupled with very rapid data collection times – frequently less than one shift – are opening up opportunities for user groups, and at the same time are challenging the support structure of the facility. Measures taken to assist macromolecular crystallography users include the possibility of testing crystals prior to preparing a formal application for beam time, and the introduction of a Block Allocation Group (BAG) scheme. This scheme, designed to encourage groups of users to block together their multiple requests for beam time, and likewise the scheduling of their experiments, is proving very successful.

Requests for beam time, which is scheduled in shifts of 8 hours, totalled 32,352 shifts or 258,816 hours for the period, of which 14,705 shifts or 117,640 hours (45.5%) were allocated; the distribution by scientific area is shown in Table 4.

Scientific field	Total shifts requested	Total shifts allocated
Chemistry	4 410	2 133
Hard condensed matter:		
• Electronic and magnetic prop.	6 831	3 079
• Structures	8 165	3 366
Life sciences	5 471	2 404
Methods & instrumentation	2 036	1 136
Soft condensed matter	2 481	1 211
Surfaces & interfaces	2 958	1 376
Totals	32 352	14 705

Table 4: Number of shifts of beam time requested and allocated for user experiments, August 1998 to January 2000.

This period has also seen 4655 scientists visit the ESRF under the user programme (see Figure 144); they carried out 1279 experiments. The breakdown of experiments carried out, by scientific area, is shown in Figure 145.

Experiments carried out, scheduling periods 1998 / II to 1999 / II: Total experiments: 1279

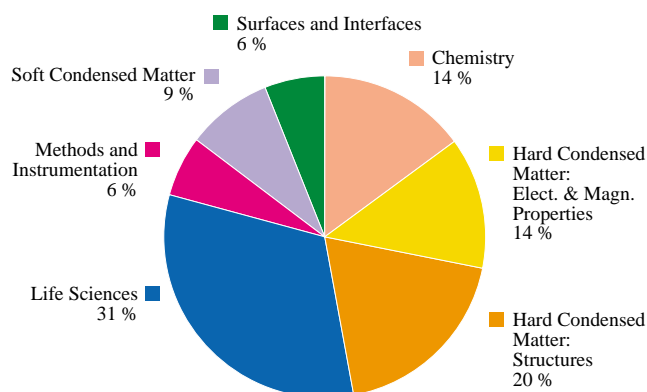


Fig. 145: Experiments carried out, from August 1998 to January 2000, by scientific area.

On average, user teams comprise 3.6 persons who stay for some 5 days. Users responding to questionnaires indicate that they particularly appreciate the quality and reliability both of the beam and of the experimental stations, together with the assistance they receive from scientists and support staff on the beamlines, and smooth administrative arrangements. Facilities on site, such as preparation laboratories, a canteen and the Guesthouse,

also make an important contribution to the quality of user support.

On the beamlines, beam time losses tended to occur because of occasional difficulties with the beamline components, computer programs, or with samples. Such beam time losses, however, remained below 5% of the total shifts scheduled for experiments during the period.

Administration and Finance

Expenditure and income 1998

	kFF		kFF
Expenditure		Income	
Site, infrastructure and buildings		1998 Members' contributions	
Personnel	26.4	Construction costs	20 843.8
Recurrent	37 206.7	Operating costs	375 156.2
Capital	23 454.1		
Infrastructure	15 029.4	Members' contribution from 1997	
Computer	8 424.7	Funds carried forward from 1997	296.0
Machine		Other income	
Personnel	29 709.0	Scientific collaboration contracts	7 078.3
Recurrent	17 113.8	Collaborating Research Groups	2 509.6
Capital	30 125.7	Discounts on invoice payments	155.0
Machine components	2 349.8	Licence agreements	134.7
Technical developments	27 775.9	Sale of beam time	1 634.0
Beamlines, instruments, experiments and in-house research		Scientific Associates	3 960.0
Personnel	107 535.5	Compensation for slab damages	6 680.0
Recurrent	37 137.1	ILL contribution to Infrastructure	5 720.3
Capital	55 505.5	Recovery of provisions	1 865.0
Beamline construction costs	10 742.7	Other third parties	2 435.3
Technical developments	44 762.8		
Technical and administrative supports			
Personnel	77 204.8		
Recurrent	13 029.3		
Unexpended committed funds			
Funds carried forward to 1999	420.3		
Total	428 468.2	Total	428 468.2

Expenditure and income 1999

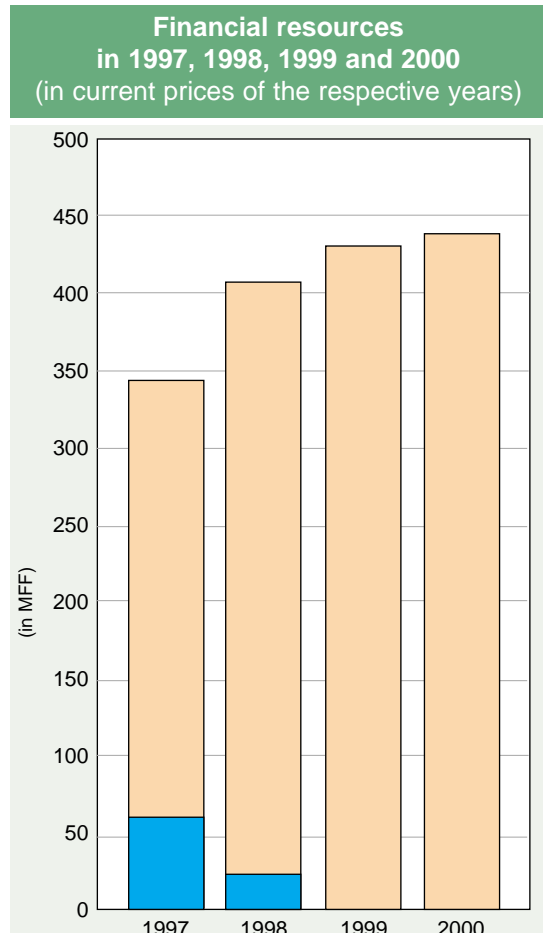
	kFF		kFF
Expenditure		Income	
Machine		1999 Members' contributions	400 000.0
Personnel	29 778.9	Funds carried forward from 1998	420.0
Recurrent	14 953.1	Other income	
Operating costs	13 012.4	Scientific Associates	9 430.0
Other Recurrent costs	1 940.7	Sale of beam time	2 644.0
Capital	21 530.9	Other sales	1 584.4
Machine developments	21 530.9	Scientific collaboration and Special projects	6 599.0
Beamlines, instruments, experiments and in-house research		Income covering expenditure in conn. activities from 3rd parties	3 660.1
Personnel	115 318.0	Financial discounts	76.9
Recurrent	37 564.8	Bank loans	2 197.9
Operating costs	20 572.0	Other	1 776.9
Other Recurrent costs	16 992.8		
Capital	44 959.3		
Beamline developments	37 012.5		
Beamline refurbishment	7 946.8		
Technical and administrative supports			
Personnel	82 763.9		
Recurrent	51 051.1		
Capital	29 986.5		
Unexpended committed funds			
Funds carried forward to 2000	482.7		
Total	428 389.2	Total	428 389.2

Expenditure 1998 by nature of expenditure		kFF
PERSONNEL		
ESRF staff	205 557.5	
External temporary staff	535.7	
Other personnel costs	8 382.5	
RECURRENT		
Consumables	38 751.4	
Services	56 220.5	
Other recurrent costs	9 515.0	
CAPITAL		
Beamlines, instruments	10 742.7	
Machine incl. insertion devices	2 349.8	
Lab. and office equipment	3 192.8	
Computer	665.3	
Buildings, infrastructure	10 180.0	
Technical developments	81 954.7	
Unexpended committed funds		
Funds carried forward to 1999	420.3	
Total	428 468.2	

Expenditure 1999 by nature of expenditure		kFF
PERSONNEL		
ESRF staff	218 302.5	
External temporary staff	586.4	
Other personnel costs	8 972.0	
RECURRENT		
Consumables	36 439.4	
Services	55 413.3	
Other recurrent costs	11 716.2	
CAPITAL		
Buildings, infrastructure	9 046.0	
Lab. and Workshops	6 212.1	
Machine incl. ID's and Fes	21 530.9	
Beamlines, experiments	43 619.4	
Computing Infrastructure	13 664.9	
Other Capital costs	2 403.4	
Unexpended committed funds		
Funds carried forward to 2000	482.7	
Total	428 389.2	

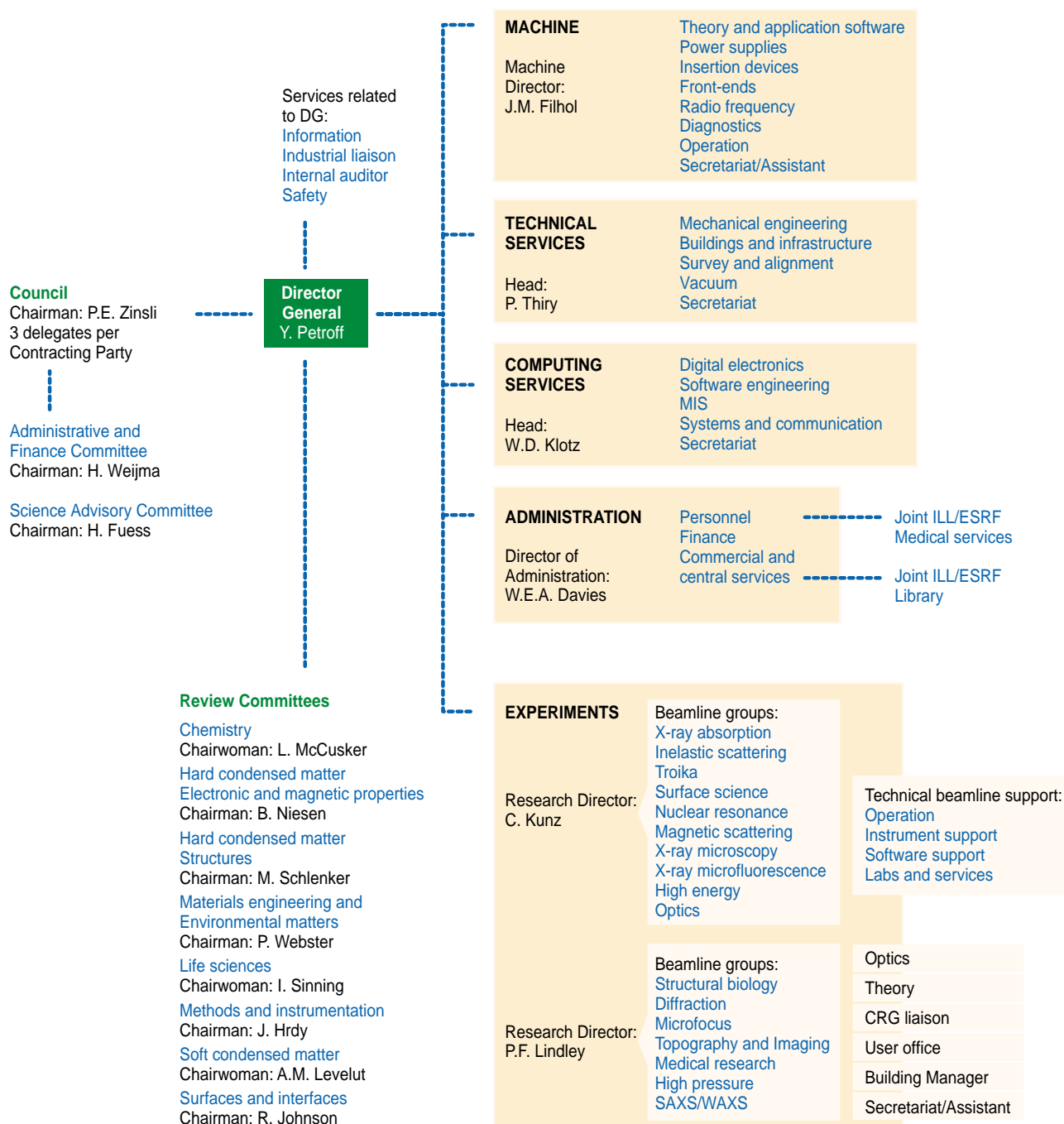
1999 manpower (posts filled at year end)				
	Cadres	Non cadres	PhD students	Total
Staff on regular positions				
Machine	22	45	1	68
Beamlines, instruments and experiments	140 (43)*	65.7	27	232.7
General technical services	38.5	69.5		108
Directorate, administration and central services	18.5	40.5		59
Sub-total	219	220.7	28	467.7
Other positions				
Peak-load staff	1	2		3
Short term contracts	9.5	33.8		43.3
Scientific collaborations	2			2
Staff under "contrats de qualification" (apprentices)		12		12
European Union grants	5			5
Temporary workers		2		2
Absences of staff (equivalent full time posts)				
				-16.7
Total	236.5	268.5	28	518.5

* Figures in brackets are the numbers of post-doc scientist posts filled.



Category	1997	1998	1999	2000
Construction costs	66	22	0	0
Operating costs	344	406	428	436

Organisation chart of the ESRF (as of May 2000)



Chief Editor

D. Cornuéjols, ESRF information officer.

Editor

G. Admans, ESRF information officer.

Layout

Pixel Project

Printing

Imprimerie du Pont de Claix

© ESRF • May 2000

Information Office

ESRF

BP220 • 38043 Grenoble • France

Tel. (33) 4 76 88 20 25 • Fax. (33) 4 76 88 24 18

<http://www.esrf.fr>

